



















4.6.2	The $\Sigma(SFR)/M_{halo}$ estimate for groups and relaxed clusters . . . .	154
4.6.3	The $\Sigma(SFR)/M_{halo}$ redshift relation . . . . .	154
<b>5</b>	<b>Discussion and Conclusions</b>	<b>159</b>
5.1	Summary . . . . .	159
5.1.1	Galaxy groups . . . . .	159
5.1.2	Galaxy Clusters . . . . .	162
5.1.3	SFR per halo mass . . . . .	163
5.2	Discussion . . . . .	164
5.2.1	SFR, Mass and sSFR as a function of group-centric distance . . . .	164
5.2.2	SFR–density relation . . . . .	168
5.2.3	The SFR-Mass plane in different environments . . . . .	170
5.2.4	Star formation rate per halo mass . . . . .	173
5.3	Conclusions: the big picture . . . . .	174
	<b>Bibliography</b>	<b>177</b>
	<b>Acknowledgements</b>	<b>195</b>
	<b>Curriculum Vitae</b>	<b>197</b>

# Zusammenfassung

Die Galaxienentwicklung ab  $z \sim 2$  ist geprägt durch die Unterdrückung (quenching) von neuer Sternentstehung (star formation, kurz SF). Vom beobachtenden Standpunkt aus wird im Allgemeinen angenommen, dass die Unterdrückung der Sternentstehung in der Umgebung von Galaxienhaufen auftritt, in der Prozesse wie Materieabtrag durch Staudruck (ram pressure stripping, Gunn & Gott 1972), Strangulierung (strangulation, Larson et al. 1980) und Galaxienbelästigung (galaxy harassment, Moore et al. 1996) besonders effektiv sind. Es wurde jedoch auch behauptet, dass die Unterdrückung von SF in Haufengalaxien in Gruppen mit geringer Masse schon vor der Haufenbildung eintritt (sogenanntes “pre-processing”, Zabludoff & Mulchaey 1998). Der Akkretionsprozess von Gruppen auf den Haufen kann selbst zur Unterdrückung der SF führen (Poggianti et al. 2004), wenn das Gas durch einen plötzlichen Anstieg der Sternentstehungsaktivität (Coia et al. 2005) schnell aufgebraucht wird. Es ist auch unklar, ob die Umgebung in dem Unterdrückungsprozess eine Rolle spielt. Peng et al. (2010) zufolge ist die massengetriebene Unterdrückung (“mass quenching”) der dominante Auslöschungsprozess für massereiche Galaxien. Da sich massereichere Galaxien in massereicheren Halos befinden, sollte ihre SF früher unterdrückt werden als in weniger massereichen. Die Auslöschung der SF wird daher eher durch innere, wie z.B. eine AGN Rückkopplung (feedback), als durch äußere Prozesse getrieben.

Im hierarchischen Strukturbildungsmodell sind Galaxiengruppen die Bausteine von Galaxienhaufen, weshalb Gruppen ein wesentlicher Bestandteil dieser Studie sind. Vom beobachtenden Standpunkt aus sind Galaxiengruppen darüber hinaus auch mit 50%-70% der Galaxienpopulation die am häufigsten vorkommende Umgebung von Galaxien im heutigen Universum (Eke et al. 2005, Geller&Huchra 1983). Wenn man bedenkt, dass die meisten Galaxien während ihres Lebens der Gruppenumgebung begegnen werden, ist demnach das Verständnis von Gruppen äußerst wichtig, um die gesamte Galaxienentwicklung zu verstehen.

Zu diesem Zweck haben wir eine Stichprobe (sample) von Gruppen aus den Feldern ECDFS, COSMOS und GOODS im Rotverschiebungsintervall  $0 < z < 1.6$  erstellt, die im Röntgenbereich detektiert wurden. Wir benutzen alle anwendbaren Indikatoren der Sternentstehungsrate, um die Sternentstehungsaktivität mit der lokalen Galaxienumgebung in Verbindung zu setzen. Wir nutzen die tiefen Beobachtungen von Spitzer MIPS und Herschel PACS, um ein exaktes Maß der Sternentstehungsrate (kurz: SFR) des Großteils der Galaxien mit SF zu erhalten. Wir verwenden Techniken zur Modellierung der spektralen Energieverteilung (SED fitting), um die stellare Masse aller Objekte und die SFR der Galaxien, die nicht mit MIPS oder PACS gefunden wurden, abzuschätzen.

Wir analysieren die Abhängigkeit der Sternentstehungsaktivität, der stellaren Masse und der spezifischen SFR von der Entfernung zum Gruppenmittelpunkt (group-centric distance) erstmals bis zu einer Rotverschiebung von  $z \sim 1.6$ . Wir finden bei keiner Rotverschiebung eine Korrelation zwischen SFR und der Entfernung zum Gruppenmittelpunkt. In Übereinstimmung damit sehen wir auch keine starke Massentrennung, was darauf hindeutet, dass Gruppen entweder eine viel kleinere Bandbreite an Akkretionszeiten gegenüber

Haufen haben, oder dass die Relaxationszeiten länger als die typischen Durchquerungszeiten (crossing times) der Gruppen sind.

Wir analysieren die Relation zwischen SFR und lokaler Galaxiendichte bis zu einer Rotverschiebung von  $z \sim 1.6$ , um zu untersuchen, ob sich diese Relation, wie in früheren Studien angedeutet, bei hohen Rotverschiebungen umkehrt. Wir finden eine Anti-Korrelation bis zu  $z \sim 0.8$ , jedoch keine Korrelation bei höherer Rotverschiebung. Wir verwenden zusätzlich einen neuartigen dynamischen Ansatz, der eine Unterscheidung zwischen X-ray Gruppenmitgliedern, Umgebungen mit mittlerer Dichte und dem Feld ermöglicht. Diese Methode erlaubt es uns, den Beitrag der Gruppen mit Halomassen  $10^{13} < M_{200}/M_{\odot} < 2 \times 10^{14}$  in der SFR-Dichte Relation zu isolieren. Auch mit diesem alternativen Ansatz sehen wir keine signifikante Umkehr in der SFR-Dichte Relation. Die Gruppengalaxien zeigen eine viel geringere mittlere SFR als jene in anderen Umgebungen bis  $z \sim 0.8$ . Bei höheren Rotverschiebungen zeigen Gruppen- und Feldgalaxien ein einheitliches Level an Sternentstehungsaktivität. Des Weiteren macht der starke Unterschied in der Entwicklung der Gruppengalaxien gegenüber den Nicht-Gruppengalaxien bei ähnlicher Dichte deutlich, dass eher Prozesse die Unterdrückung der Sternentstehungsaktivität in Gruppengalaxien unterhalb  $z \sim 1$  dominieren, die mit der Anwesenheit eines massereichen dunklen Materiehalos zusammenhängen, als reine dichteabhängige Prozesse.

Um den Grund der schnelleren Entwicklung in Gruppengalaxien gegenüber anderen Umgebungen zu verstehen, untersuchen wir die zweidimensionale Verteilung der Galaxien in verschiedenen Umgebungen in Bezug auf die sogenannte Hauptsequenz sternbildender Galaxien (“star forming galaxy main sequence”, MS, e.g. Elbaz et al. 2007). Die Gruppengalaxien liegen unterhalb der MS bis  $z \sim 0.8$  und zeigen einen größeren Anteil an nicht-sternbildenden (quiescent) Galaxien. Galaxien bei ähnlicher Dichte aber ohne Zugehörigkeit zu einer im Röntgenbereich detektierten Struktur zeigen ein Verhalten zwischen den Gruppen- und Feldgalaxien. Bei  $z > 0.8$  befinden sich die sternbildenden Gruppengalaxien auf der MS und wir finden einen ähnlichen Anteil an passiven Galaxien wie im Feld. Wir folgern daraus, dass die Gruppenumgebung anscheinend der Ort mit der effektivsten Unterdrückung von Sternentstehung ist. Das deutet darauf hin, dass es einen wesentlichen Unterschied zwischen gravitationsgebundenen (Gruppen) und ungebundenen (Galaxienüberdichten wie z.B. Filamente) Strukturen gibt, bzw. analog zwischen Halos dunkler Materie mit unterschiedlichen Massen.

All diese Resultate deuten darauf hin, dass ein signifikantes Level an “Vorverarbeitung” (“pre-processing”) in Gruppen bei  $z < 0.8$  stattfindet. Wir nutzen die Analyse von Popesso et al. (2012), um die Sternentstehungsentwicklung zusätzlich zu den in dieser Arbeit analysierten Gruppen in den zwei dynamisch aktiven Haufen Abell 1300 und Abell S0520 aus der REFLEX-DXL Stichprobe (Böhringer et al. 2001, Zhang et al. 2006) zu untersuchen. Der Vergleich macht deutlich, dass die verschmelzenden Systeme ein Level an Sternentstehungsaktivität pro Masseneinheit zeigen, das zwischen dem der Gruppen und der relaxierten Haufen liegt. Galaxienhaufenverschmelzungen könnten daher eine Rolle in der Unterdrückung oder Verstärkung der Sternentstehungsaktivität in kosmischen Strukturen spielen. Unser aktuelles Datenset liefert jedoch noch nicht die nötige Genauigkeit und Statistik, um eine definitive Aussage treffen zu können.

# Abstract

Since  $z \sim 2$  galaxy evolution is characterized by the quenching of the star formation. Much effort has been put in the understanding on the possible causes of quenching. The most popular debates are focused on the *Nature* vs *Nurture* dichotomy. The first hypothesis centers on whether the termination of star formation is established due to galaxy formation proceeding differently and faster in overdense regions, or whether it is the end product of physical processes coming into play only after galaxies have become part of a group or of a cluster. However, as De Lucia et al. (2012) recently pointed out, it is difficult, if not impossible to distinguish between *Nature* and *Nurture* since these are strictly coupled.

From the observational point of view, star formation quenching is generally assumed to occur within the cluster environment, where processes like ram pressure (Gunn & Gott 1972), strangulation (Larson, Tinsley, & Caldwell 1980), and galaxy harassment (Moore et al. 1996) are particularly effective. It has, however, also been claimed that SF quenching of cluster galaxies occurs in low-mass groups prior to cluster assembly (the so-called “pre-processing”, Zabludoff & Mulchaey 1998). The accretion process of groups onto clusters can itself lead to SF quenching (Poggianti et al. 2004), via a rapid gas consumption due to a sudden enhancement of the SF activity (Coia et al. 2005). It is also unclear whether environment plays any role at all in the quenching process. According to Peng et al. (2010), mass quenching is the dominant quenching process for massive galaxies. Since more massive galaxies reside in more massive halos, their star formation should be quenched earlier than less massive ones. Thus, the quenching of galaxy SF would be driven by some internal process, such as AGN feedback, rather than an external one.

In the hierarchical scenario of structure formation, galaxy groups are the “building blocks” of galaxy clusters, therefore these systems are a fundamental object of study. In addition, galaxy groups are also the most common environment of galaxies in the present day universe, containing 50%-70% of the galaxy population (Eke et al. 2005; Geller & Huchra 1983). Thus, given that most galaxies will encounter the group environment during their lifetime, an understanding of groups is critical to follow galaxy evolution.

For this purpose, we build an X-ray selected group sample at  $0 < z < 1.6$  in the ECDFS, COSMOS, and GOODS fields. We use several Star Formation Rate (SFR) indicators to link the SF activity to the galaxy environment. We take advantage of the extremely deep mid-infrared Spitzer MIPS and far-infrared Herschel PACS observations to have an accurate (calorimetric) measure of the SFR for the bulk of the SF galaxies. We use SED fitting technique for estimating the stellar mass of all objects and the SFR of the MIPS and PACS undetected galaxies.

We analyze the dependence of the SF activity, stellar mass and specific SFR on the group-centric distance, for the very first time, up to  $z \sim 1.6$ . We do not find any correlation between SFR and group centric distance at any redshift. Consistently, we do not observe any strong mass segregation (according which massive galaxies are located in the center of the system and less massive galaxies are at higher distances from the center). This suggests that either groups have a much smaller spread in accretion times with respect to the clusters or that the relaxation time is longer than the group crossing time.

We analyze the relationship between the SFR and galaxy local density up to  $z \sim 1.6$  in order to check whether it reverses at high redshift as suggested by some previous studies. We find an anti-correlation representing the SFR-density relation up to  $z \sim 0.8$  and no correlation at higher redshift. Thus, we do not detect the reversal of the relation as claimed by Elbaz et al. (2007) and Cooper et al. (2008). In addition to this “traditional” method, we use a novel dynamical approach, i.e. distinguishing among X-ray group members, intermediate density environments (like filaments or lower mass groups not detected in X-ray) and the field. This method allows us to isolate the contribution of groups with halo mass  $10^{13} < M_{200}/M_{\odot} < 2 \times 10^{14}$  in the SFR-density relation. Even with this alternative approach, we do not see any significant SFR-density reversal. The group galaxies show a mean SFR much lower than in the other environments up to  $z \sim 0.8$ . At earlier epochs group and field galaxies exhibit consistent levels of SF activity. In addition, the strong difference in the evolution of the group galaxies with respect to non-group galaxies at similar density, reveals that processes related to the presence of a massive dark matter halo, rather than purely density-related processes, must be dominant in the suppression of the SF activity in group galaxies below  $z \approx 1$ .

In order to understand the cause of the faster evolution in group galaxies with respect to other environments, we study also the location of the group, intermediate and low density galaxies in the SFR-stellar mass plane. In other words, we study the two-dimensional distribution of galaxies in different environments with respect to the so called SF galaxy Main Sequence (MS, e.g. Elbaz et al. 2007). The group galaxies lie below the MS up to  $z \sim 0.8$ , and they show a much higher fraction of quiescent galaxies. Galaxies at similar density but not belonging to the X-ray detected structures exhibit a somewhat intermediate behavior among the group and field galaxies. At  $z > 0.8$  the star forming group galaxies lie on the MS and show a similar fraction of quiescent galaxies as in the field. We conclude that groups seem the most efficient locus for quenching the SF. This suggests that a fundamental difference exists between bound (groups) and unbound objects (galaxy overdensity such as filaments), or between dark matter halos of different masses.

All these results suggest that a significant level of pre-processing happens in groups at  $z < 0.8$ . However, recent results of Popesso et al. (2012) based on *Herschel* data point out that the pre-processing is ruled-out in merging systems like the “Bullet” cluster. Thus, we take advantage of the analysis of Popesso et al. (2012) to study the SF evolution of the groups analyzed in this work in addition to two dynamically active clusters such as Abell 1300 and Abell S0520, observed in the REFLEX-DXL sample (Böhringer et al. 2001; Zhang et al. 2006). We first analyze the clusters individually, in order to put constraints on the time elapsed after the major merging event and to study their galaxy populations. Then we compare their star formation activity to that of the groups studied in this work and the clusters of Popesso et al. (2012). The comparison reveals that the merging systems show a level of SF activity per unit of mass intermediate between groups and relaxed clusters. Thus, merging activity could play a role in the quenching or enhancement of the SF activity in structures. However, our dataset does not provide the required accuracy or statistics for a definitive conclusion.



# Introduction

The observed properties of galaxies have long been known to depend on the environment in which they are located. According to the well known morphology-density relation (Dressler 1980) and the star formation rate (SFR)-density relation (Gómez et al. 2003), in the local universe high density regions, like groups and clusters, host mostly early type galaxies with lower star formation (SF) level than field (mostly late-type) galaxies. The environmental dependence of galaxy SFR may change with redshift, as galaxies in systems undergo significant evolution. In higher-redshift clusters, the fraction of blue galaxies is higher (‘Butcher-Oemler’ effect, Butcher & Oemler 1978a) and so is the fraction of infrared (IR) emitting galaxies (‘IR Butcher-Oemler effect’, e.g. Saintonge, Tran, & Holden 2008), where most of the IR emission is powered by SF. In addition, in recent years, observational studies have tried to assess the role of environment on galaxy evolution through large spectroscopic and photometric surveys at different cosmic epochs (e.g. Balogh et al. 2004; Cooper et al. 2006; Cucciati et al. 2006; Kauffmann et al. 2004) or through semi-analytic models (e.g. De Lucia et al. 2012). However, disentangling the environment(s) and related physical processes that are responsible for the observed trends has proved difficult, and their physical origin is still matter of debate.

Much work has focused on whether these trends are the end product of physical processes coming into play only after galaxies have become part of a group or of a cluster (the *nurture* hypothesis), or whether they are established before these events take place, due to galaxy formation proceeding differently in overdense regions (the *nature* hypothesis).

According to the *nurture* scenario, star formation quenching occurs within the cluster environment, where processes like ram pressure (Gunn & Gott 1972), strangulation (Larson, Tinsley, & Caldwell 1980), and galaxy harassment (Moore et al. 1996) are particularly effective. For example, Tran et al. (2009) observed a higher fraction of star forming galaxies in a group at  $z = 0.37$  with respect to clusters at the same redshift. It has however also been claimed that SF quenching of cluster galaxies occurs in low-mass groups prior to cluster assembly (the so-called ‘pre-processing’, Zabludoff & Mulchaey 1998). The ac-

cretion process of groups onto clusters can itself lead to SF quenching (Poggianti et al. 2004), since the gas is rapidly exhausted after a sudden enhancement of the SF activity (Coia et al. 2005). According to the *nature* hypothesis, instead, environment does not play any role at all in the quenching process. According to Peng et al. (2010) more massive galaxies residing in more massive halos should be quenched earlier than less massive ones. They name this process as “mass quenching” which identify as the dominant quenching mechanism for massive galaxies.

It is quite likely that both *nature* and *nurture* play a role in determining the properties of galaxies. Certainly collisions and mergers must play a role in the formation of cluster elliptical galaxies. It is believed, for example, that the giant elliptical galaxies seen at the centers of rich clusters are a product of the gradual accumulation of galaxies at the center of the cluster strong gravitational field (e.g. De Lucia & Blaizot 2007). On the other hand, rotation is expected to be important, especially for disk (spiral and S0) galaxies. This “bottom-up” scenario where larger galaxies formed from smaller fragments, as proposed by the current standard paradigm for structure formation, is strongly supported by current calculations of the formation of structure in the early universe. However, our picture of the formation of galaxies remains confused, and much remains to be understood.

Thus, In order to find an exit in the labyrinth of possible solutions, the best approach would be to follow the evolution of the star formation activity in structures through the different phases of structure formation. A simple way to achieve this goal is to compare the SF activity of the cluster building blocks such as galaxy groups, the subsequent merging phase in merging systems and the final relaxed massive clusters at similar redshift.

In this thesis work we follow this approach by studying the star formation activity of a large sample of galaxy groups up to redshift  $z = 1.6$  in comparison to the activity of field galaxies at the same redshifts. In addition we study the star formation of the galaxy population of two merging clusters and we compare with the mean activity of groups at the same redshift, in order to shed light on which hypothesis, *nature* or *nurture* is more suitable to explain the observations. There are two main ingredients as part of this work. First we take advantage of the deep X-ray observations of the fields such as the Extended Chandra Deep Field South (ECDFS), The Great Observatories Origin Deep Survey-South and -North fields (GOODS-S and GOODS-N, respectively) and the Cosmic evolution Survey (COSMOS) fields, for the identification of groups and galaxy clusters up to redshift 1.6. Second, we use recent very deep far-infrared observations of the same fields acquired with the *PACS* (Poglitsch et al. 2010) instrument on board the *Herschel* satellite (Pilbratt et al. 2010), launched in May 2009. Far-infrared wavelengths provide a calorimetric, thus very accurate, measure of the star formation rate estimate from the dust emission for galaxies up to very high redshift. In particular, for this work we use the *PACS* maps obtained at 100 and 160  $\mu\text{m}$  of the mentioned deep fields observed as part of the *PACS* Evolutionary Probe (PEP) (Lutz et al. 2011) and GOODS-Herschel survey (Elbaz et al. 2011).

This chapter is organized as follows. We first introduce the galaxy groups and clusters as the most massive bound gravitational systems and we characterize their environment through their X-ray properties. We then summarize past and recent results on what, if any, role has the environment in driving the evolution of the galaxy population. We, then,



introduce the *Herschel satellite* with particular focus on the *PACS* instrument. Finally, we summarize several important recent results based on *Herschel* and essential to this work.

## 1.1 Galaxy Groups

### 1.1.1 The theoretical framework

Structure formation is thought to act hierarchically from the growth of very small fluctuations (of the order of  $10^{-5}$ ) in the temperature of the cosmic microwave background (CMB) radiation. These variations, detected for the first time by the COBE satellite (Smoot et al. 1992) and later by WMAP, have been interpreted as slight variations of the gravitational potential at the surface of last scattering. According to this theoretical framework the early universe exhibits density variations with respect to the general background density of the universe and related tiny velocity perturbations with respect to the general Hubble expansion. As the universe cools down, these fluctuations attract the surrounding matter (due to the acquired stronger gravitational potential), and they start to accrete material from their surroundings as long as pressure forces are not sufficient to counteract this infall. The overdensity then increases, and its gravitational influence becomes stronger until it causes the collapse to a gravitationally bound object. The size and mass of the object depends on the scale of the fluctuation. For example, galaxies are thought to have formed out of fluctuations on a scale of  $0.5 \text{ h}^{-1} \text{ Mpc}$  while clusters of galaxies have emerged out of fluctuations on a larger scale of  $4 \text{ h}^{-1} \text{ Mpc}$ . The formation of voids fits in the same general scheme, having grown out of primordial underdensities in the matter distribution.

The total mass of the fluctuations is mostly composed by non-baryonic, “dark matter” (DM), which interacts only gravitationally. Although the constituent particles of the Dark Matter are still unknown, much argument centers on this topic. Hot dark matter (HDM) is composed by particles with a free-streaming length larger than any small density perturbations in the early universe. An example is given by neutrinos, thus relativistic particles. Given the big free-streaming length of the HDM particles, the first structures to form are the largest superclusters which would then fragment into smaller and smaller substructures resulting in clusters and individual galaxies. This scenario is also called “top-down”, since the biggest structures form before the smaller ones. However, the most popular models are based on non thermalized, non-baryonic, collisionless particles, which compose the cold dark matter (CDM). According to the CDM models, small halos form first and then merge into larger objects, following a hierarchical (or “bottom-up”) build-up of structure. In this scenario galaxies form before groups and clusters. A simple scheme of this structure formation scenario is given in Fig. 1.1, where the biggest structure formed is an elliptical galaxy.

The hierarchical structure formation scenario has been extensively investigated using N-body simulations (e.g. Angulo et al. 2012; Frenk et al. 1985, 1988; Springel & Hernquist 2003; Springel et al. 2005; White & Rees 1978; White et al. 1987; White & Frenk 1991). In the late 1990’s a “concordance” model (Ostriker & Steinhardt 1995) emerged in a scenario

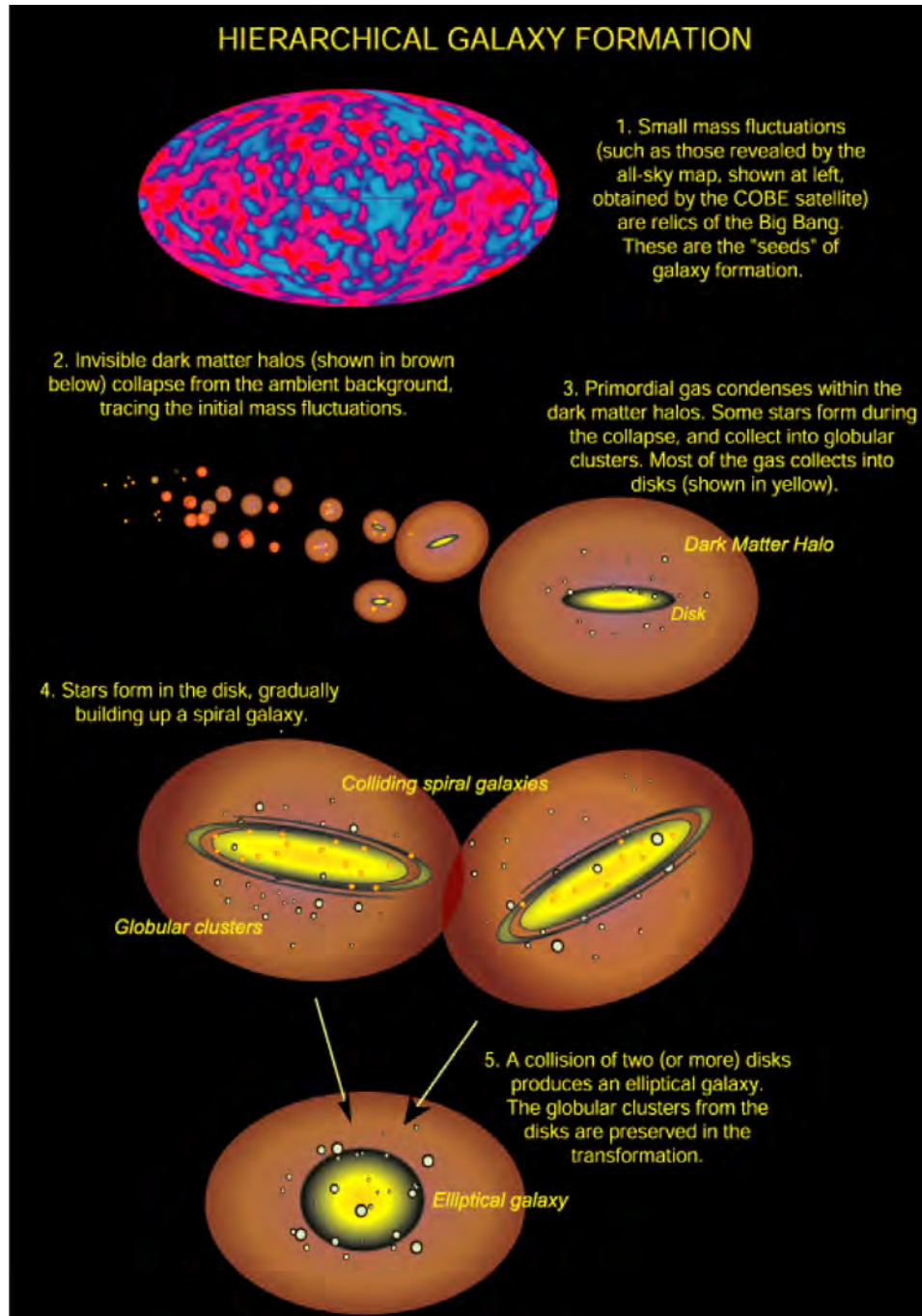


Figure 1.1: The hierarchical model of galaxy formation from Abraham & van den Bergh (2001). Structures originate from density fluctuations seen as temperature variations in the CMB. As the fluctuations grow, the baryonic matter collapse into dark matter halos, forming the first objects. In this scenario, small proto-galaxies merge to form bigger objects.

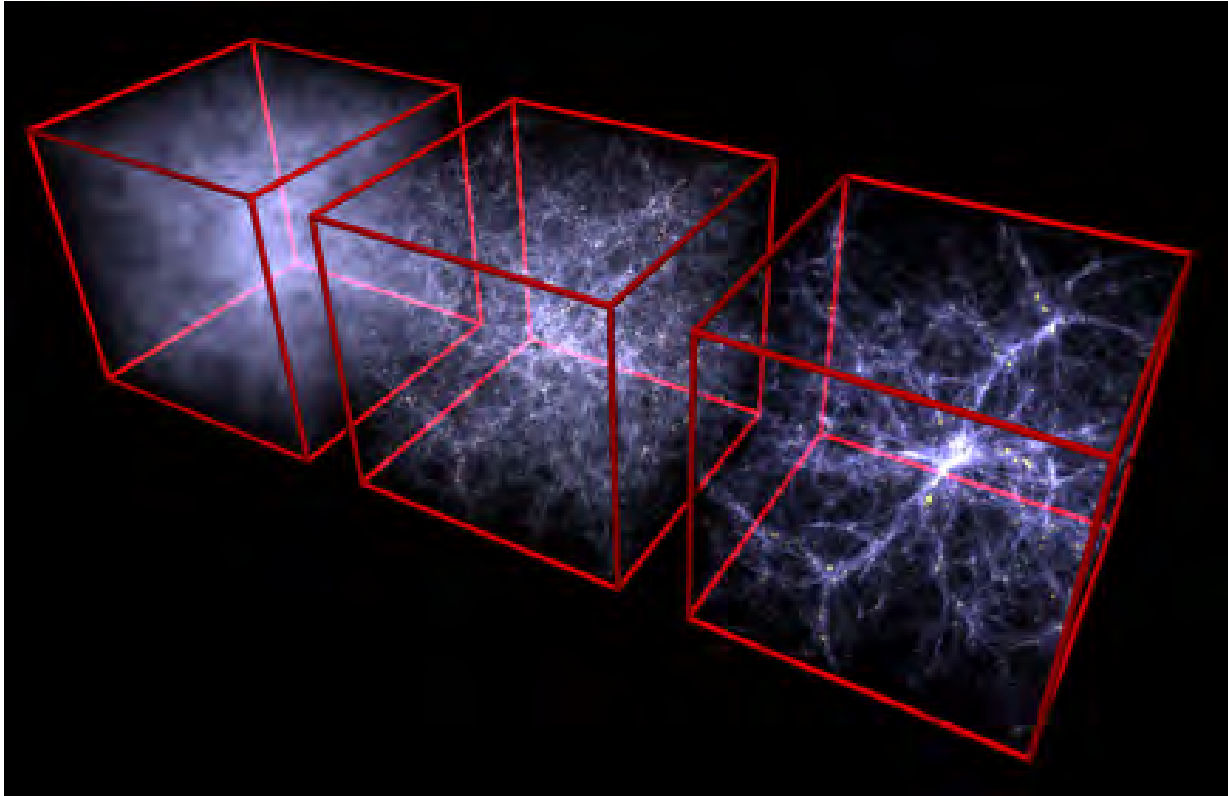


Figure 1.2: The hierarchical model of galaxy formation in the hydrodynamical simulations of Springel & Hernquist (2003). The box size is 100 Mpc and the redshift decreases from left to right, from  $z = 6$  to  $z = 0$ .

containing cold dark matter and a cosmological constant ( $\Lambda$ ). The  $\Lambda$ CDM is frequently referred to as the standard model of Big Bang cosmology, since it is the simplest model that attempts to explain the existence and structure of the cosmic microwave background, the large scale structure of galaxy clusters, and the accelerating expansion of the universe observed in the light from distant galaxies and supernovae. Fig. 1.2 reproduces the standard result of a numerical simulation of the structure evolution in the hierarchical scenario (Springel & Hernquist 2003) with a sophisticated treatment of star formation, supernova feedback and galactic outflows. The small structures, on galactic scale, collapse first and then merge to form bigger systems as galaxy clusters, which merge as well to form the so called superclusters.

The N-body simulations have become sophisticated to the point where they can reproduce observations of large scale structures with high precision. An example is given by Fig. 1.3, where we show the comparison of the filamentary structures observed in different redshift surveys (in blue) and the Millennium simulation (in red) of Springel et al. (2005).

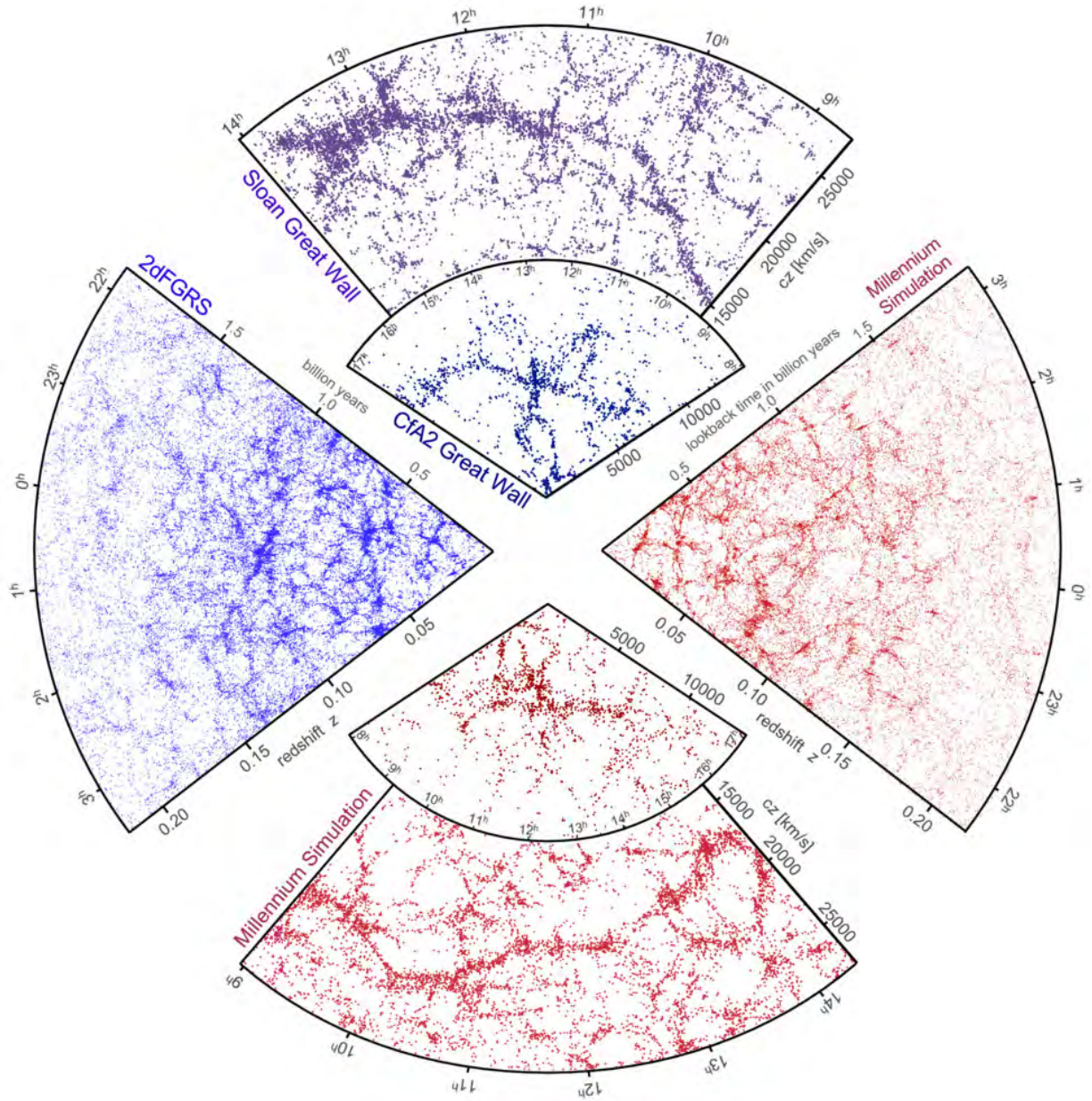


Figure 1.3: Comparison of the filamentary structures observed in different redshift surveys (in blue) and the Millennium simulation (in red) of Springel et al. (2005). The simulations reproduce with high accuracy the structures observed in the surveys.

### 1.1.2 Models of galaxy formation and evolution

After the successful reproduction of large scale structure distribution in the  $\Lambda$ CDM scenario, much work has focused on smaller scales in order to study galaxy formation into the hierarchical picture. In fact, the individual galaxies are the merger products of smaller systems, analogous clusters which form from smaller structures like groups. In such a scenario the small dark matter halos are the oldest systems in the universe and they can be seen as the building-blocks of the giant galaxies that we observe nowadays.

One successful approach has been semi-analytic models (SAMs, Kauffmann et al. 1993). These models combine N-body simulations for the study of the formation and evolution of dark matter halos with simple analytic description of the baryonic physics, using the Press & Schechter (1974) theory to predict abundances and merger rates of halos as a function of mass and redshift. These models include also the heating and cooling of gas at the center of dark matter halos, the formation of stars, and the merging of galaxies. Even though they do not make predictions on the detailed formation history of individual galaxies, the SAMs provide some useful statistical predictions on the formation epoch, the galaxy type mix, the clustering and the luminosity distribution of the galaxy population.

In the hierarchical merging scenario, galaxies end up as spirals or ellipticals depending on the details of their merger history. In particular, typical elliptical galaxies form from the merging of intermediate-mass disks at lower redshifts (e.g. Baugh, Cole, & Frenk 1996; Baugh 2006; Kauffmann, Charlot, & White 1996). As a result, the model predicts that the number of more massive galaxies should decrease with increasing redshift (that is, decreasing age) and, consequently, smaller systems should increase.

### 1.1.3 Galaxy group observations

In the hierarchical scenario of structure formation, galaxy groups are the “building blocks” of galaxy clusters, therefore these systems are a fundamental object of study. In addition to this aspect, from the observational point of view, galaxy groups are also the most common environment of galaxies in the present day universe, containing 50%-70% of the galaxy population (Eke et al. 2005; Geller & Huchra 1983). Thus, given that most galaxies will encounter the group environment during their lifetime, an understanding of groups is critical to follow galaxy evolution.

The discovery that many groups are X-ray sources has provided considerable new insights for the understanding of these important systems. X-ray observations indicate that about half of all poor groups are luminous X-ray sources. In many cases, the X-ray emission is extended, often beyond the optical extent of the group. The spatial and spectral properties of the X-ray emission suggest that the entire volume of groups is filled with hot gas. This gas component is referred to as the intra-group medium (IGM), in analogy to the diffuse X-ray emitting intra-cluster medium (ICM), found in rich clusters (e.g. Forman & Jones 1982).

To first order, groups can be viewed as scaled-down versions of rich clusters. In fact, many of the fundamental properties of groups, such as X-ray luminosity and temperature,



are roughly what one expects for a cluster with a velocity dispersion of several hundred kilometers per second. However, some important physical differences exist between groups and clusters. The velocity dispersions of groups are comparable to the velocity dispersions of individual galaxies. Therefore, some processes such as galaxy-galaxy merging are much more predominant in groups than in clusters. Other mechanisms that are important in the cluster environment, such as ram-pressure stripping (Gunn & Gott 1972) and galaxy harassment (Moore et al. 1996), are not expected to be important in groups. The spectral nature of the X-ray emission is also somewhat different in groups with respect to clusters. At the typical temperature of the intra-cluster medium, almost all abundant elements are fully ionized, and the X-ray emission is dominated by a thermal bremsstrahlung continuum. At the lower temperatures of groups, most of the trace elements retain a few atomic electrons, and line emission dominates the observed X-ray spectrum.

The existence of diffuse X-ray emitting gas is often cited as evidence that a group is a really bound and virialized system. On the other hand, optical selection favors X-ray underluminous groups (e.g. Connelly et al. 2012). These groups are usually not detected significantly in X-rays and present a higher number of substructures (Finoguenov et al. 2009). Moreover, low-luminosity, low-temperature groups tend to have irregular X-ray morphologies with the X-ray emission distributed in the immediate vicinity of individual galaxies. These X-ray morphologies suggest that these groups are still dynamically evolving and, sometimes, involved in a merger.

Many attempts have been made also to define spectroscopically selected group samples (Carollo et al. 2012; Gerke et al. 2005; Yang et al. 2007). However, dynamical studies of groups are generally hampered by small number statistics, since a typical group contains only a few luminous galaxies. For this reason, the dynamical properties of optically selected groups are always rather uncertain. In fact, many cataloged groups may not be real physical systems at all (e.g. Frederic 1995; Hernquist, Katz, & Weinberg 1995; Ramella, Pisani, & Geller 1997), but rather chance superpositions or large-scale structure filaments viewed edge-on.

In the study of the properties of groups and their galaxy population, it is necessary to take into account the effects of the group selection. X-ray selected groups are biased towards more massive, evolved, and relaxed systems, while spectroscopically selected samples are dominated by small associations of a few galaxies that would normally be undetectable in X-ray emission. In addition, undetected or faint X-ray galaxy groups tend to have a higher fraction of spiral galaxies (see Sec. 1.2.2) while bright X-ray groups are more early-type galaxy rich (Mulchaey & Zabludoff 1996; Ponman, Cannon, & Navarro 1999). Only a few studies so far have had both good membership information (which requires extensive spectroscopic programs) and X-ray data (the best indicator of a group dynamical state) and both of these are needed to obtain a comprehensive understanding of the group environment.

The best way to study galaxy groups is then, the combination of deep X-ray observations to sample the full range of the group dynamical states (from less luminous to bright systems) with a deep spectroscopic and photometric follow up. In this way it is possible to confirm the nature of these systems with the count of the spectroscopic members and the

analysis of the galaxy dynamics within the systems. Most groups are not very X-ray luminous and therefore relatively long X-ray observations are required to study these objects. For this reason, most studies have been restricted to groups that are a priori known to be X-ray bright (Mulchaey 2000). Recently, XMM-Newton studies of a few spectroscopically selected groups suggest that their properties may be quite different from those of X-ray luminous systems (Rasmussen et al. 2006).

Before the advent of the deep field surveys, this kind of approach was limited to a relatively low number of well studied groups (Rasmussen et al. 2006; Zabludoff & Mulchaey 1998). The completion of large and extremely deep multi-wavelength surveys, such as the second Canadian Network for Observational Cosmology Field Galaxy Redshift Survey (CNOC2), COSMOS, the ECDFS and the GOODS surveys, are providing now a very deep coverage in X-ray with *Chandra* and *XMM-Newton*, in the far-infrared wavelength with *Spitzer* and the *Herschel* satellite, and deep spectroscopic observations for a relatively wide area of the sky. This formidably rich multi-wavelength dataset enables for the first time:

- coverage of almost the full range of group dynamical states from faint to bright X-ray groups;
- identification of a large number of group members to study the properties of the group galaxy populations;
- study of the galaxy populations in groups over a range of cosmic epochs, up to  $z \sim 1 - 1.5$ , thus probing a large part of the group and galaxy evolutionary path.

## 1.2 Environment versus galaxy properties

In this section we introduce the main observational evidence for the relation between environment and galaxy properties, such as the “morphology-density” relation and the “star formation-density” relation. We first give an overview about the galaxy morphological type mix showing the so called “Hubble sequence”.

### 1.2.1 The Hubble sequence

Hubble (1926) classified the observed galaxies in the universe in a schematic diagram named the “tuning-fork” (Fig. 1.4) which, with minor revisions remains in use today. Hubble divided galaxies into two principal categories, Elliptical and Spiral, with a third “Irregular” category which includes all the galaxies which fail the regular classification. Elliptical galaxies, which consist of only a nuclear bulge component, are subdivided among seven ellipticity classes from E0 (circular) to E7 (cigar shaped). The ellipticity is given by  $10(a - b)/a$ , where  $a$  is the projected length of the major axis and  $b$  is the projected size of the minor axis. Similarly, spiral galaxies are classified by how tightly their arms are wound. Therefore, type  $a$  Spirals have their arms wound very tightly and have large central bulges, while type  $c$  ones have their arms wound loosely and have small central bulges. The S0

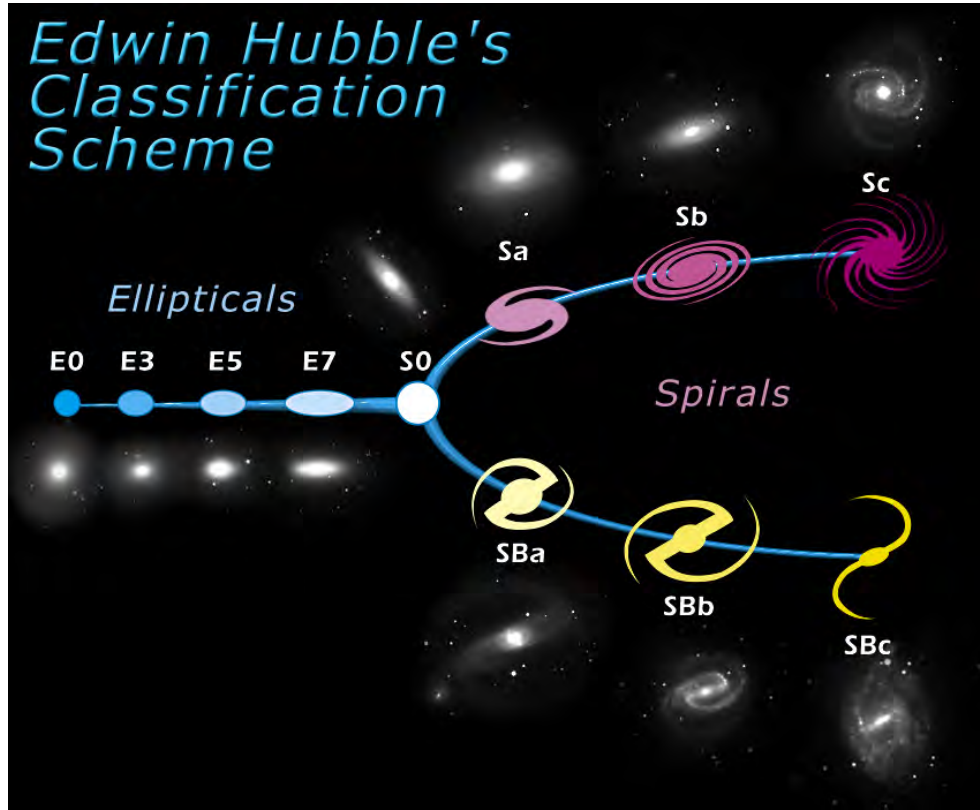


Figure 1.4: Hubble “tuning-fork” diagram for the classification of observed galaxies.

or lenticular galaxies are a transition type between elliptical and spiral galaxies. They are formed by a central bulge and a disk but they exhibit no spiral arms. The traditional classification scheme, arranged in a “tuning-fork” diagram (Fig. 1.4), comprises also two types of irregular galaxies: Irr I, with characteristics beyond those of class Sc (high gas content, dominant presence of a young population), and Irr II, which defy the normal galaxy classification because of some form of disturbance and consequent burst of star formation.

Particular attention should be dedicated to the cD galaxies. They compose a peculiar class of objects that lie at the center of rich clusters. The inner regions of cD galaxies are characterized by a surface brightness profile similar to those of normal Ellipticals, while the outer regions are defined by a diffuse halo with a slowly declining surface brightness. The external envelope of these galaxies is so luminous that it can contain as much light as the rest of the galaxy (Schombert 1987, 1988, and references therein). According to the galactic cannibalism theory (Ostriker & Hausman 1977), the cD precursor may have been the largest galaxy to form in the center of clusters (or subclusters, Merritt 1984), while the halo is the consequence of the disruption and merger of numerous smaller galaxies.



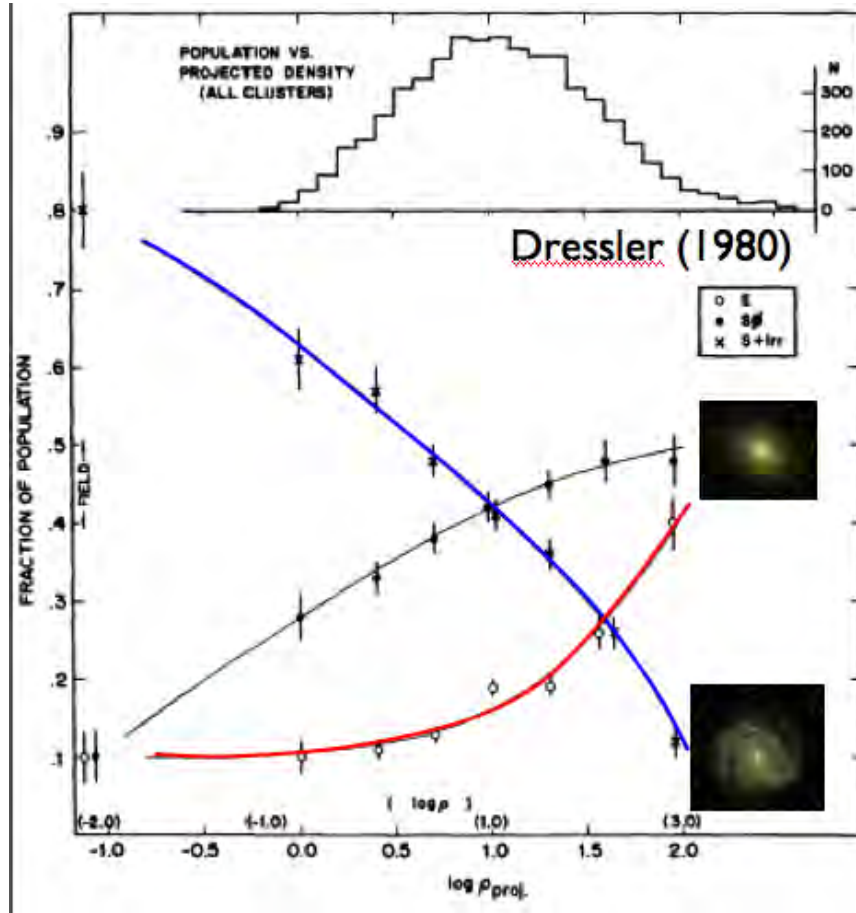


Figure 1.5: Morphology-density relation (Dressler 1980). The fraction of early type galaxies (red and black curves) increases with the density. Conversely, the fraction of late type galaxies (blue curves) decreases with the increasing density.

### 1.2.2 Morphology-density relation

Morphological types show striking differences between various environments. The most dramatic example is represented by the comparison of galaxies in rich clusters and in the field: Ellipticals and lenticular galaxies favor rich environments, while the field galaxies are mostly Spirals. This bimodality was initially measured through the morphology-density relation (Fig. 1.5), with the fraction of spirals increasing from 10 % to 80 % going from rich clusters to the field (Dressler 1980). In fact, Dressler (1980) showed that a clear dependence of galaxy morphology on the local densities exists regardless of the dynamical state of the cluster or of its concentration. Passively-evolving galaxies are preferentially found in the cluster densest regions (i.e. the cluster core), while spirals prefer the lower density environment of the outskirts.

Although the morphology-density relation is well-established in all clusters in the local

universe, its extent is less evident at high redshift, where it is clearly detected only in regular, highly concentrated clusters. Butcher & Oemler (1978a, 1984a,b) showed that a number of moderately high redshift ( $z \approx 0.4$ ) clusters contain a high fraction of blue galaxies, an effect which is not observed in nearby clusters (Butcher & Oemler 1978b). These galaxies lie at projected distances from the cluster center larger than the redder ones. After removing the redshift effects, these blue galaxies show colors similar to those of nearby spiral galaxies. The effect for which the fraction of blue galaxies in clusters increases with redshift is known as the Butcher-Oemler (BO) effect.

More recent works have confirmed the BO effect in clusters at modest redshift (e.g. Andreon, Lobo, & Iovino 2004; Dressler, Gunn, & Schneider 1985; Dressler et al. 1997; Ellingson et al. 2001; Goto et al. 2003). The blue galaxies are frequently in tight, perhaps interacting clumps (Lavery & Henry 1988). HST imaging reveals that many of the anomalous blue galaxies are normal spirals, which compose the majority of the population of these clusters. Blue colors come often from galaxies involved in merging events or tidal interaction, leading to the conclusion that the BO effect is a proxy of the transformation of spiral galaxies to Elliptical/S0. Observations at different redshifts suggest a strong evolution of galaxy type mix in clusters (Rakos & Schombert 2004; van Dokkum et al. 2000).

### 1.2.3 The SFR-density relation

Given the tight link between galaxy morphology, colors and instantaneous star formation rate (SFR), an alternative way to study the relation between environment and galaxy evolution is through the analysis of the SFR-density relation. The local relation (Gómez et al. 2003) shows an anti-correlation between SFR and density. Highly star forming galaxies, mainly gas rich spirals, prefer low density environments. Conversely, the cores of massive clusters are galaxy graveyards full of massive spheroidal systems that are dominated by old stellar populations. It has been argued that as we approach the epoch at which the early type galaxies should be forming the bulk of their stars at  $z \gtrsim 1.5$  (e.g. Rettura et al. 2010), the relation between star formation activity and environment should progressively reverse.

The existence and the behavior of the SFR-density relation at redshift  $\sim 1$  is still matter of debate. Kovač et al. (2010) show that galaxy star-formation and color transformation rates are higher in the groups than in lower density regions at  $z \sim 1$ . Elbaz et al. (2007) and Cooper et al. (2008) observe the reversal of the density-SFR relation at  $z \sim 1$  in the GOODS and the DEEP2 fields, respectively, using a spectroscopically defined density parameter. Exploring the SFR-density relation with *Herschel* PACS data, Popesso et al. (2011) show that the reversal is mainly due to an higher fraction of AGN (Fig. 1.6), which exhibit slightly higher SFR activity with respect to galaxies with the same stellar mass (Santini et al. 2012).

Caputi et al. (2009) analyzed the close environment, on 1 Mpc scales, of luminous infrared galaxies (LIRGs,  $L_{IR} = 10^{11} - 10^{12} L_{\odot}$ ) and ultra-luminous infrared galaxies (ULIRGs,  $L_{IR} > 10^{12} L_{\odot}$ ) in the zCOSMOS dataset (Lilly et al. 2007), finding that LIRGs at  $0.6 < z < 1$  are more often found in overdense environments, while ULIRGs

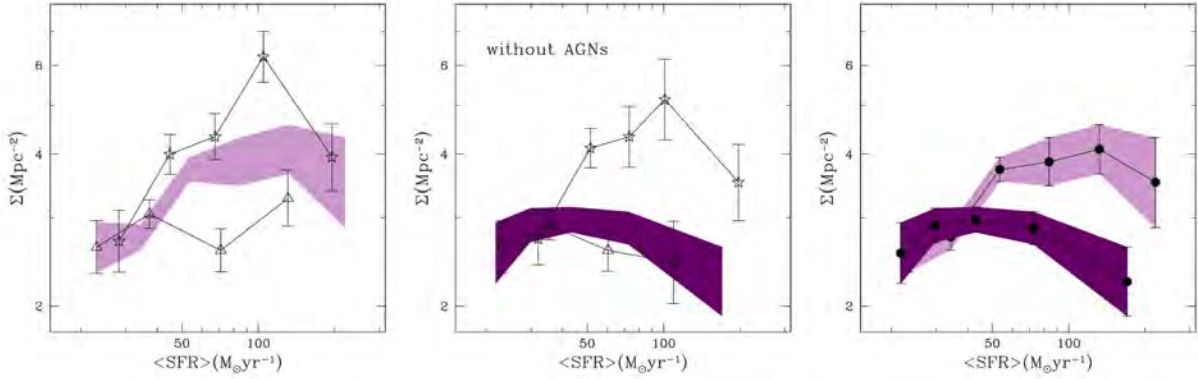


Figure 1.6: Density-SFR relation for the GOODS fields (Popesso et al. 2011). The authors show the relation obtained by including the low luminosity obscured AGNs (left panel) and the relation obtained after removing the AGNs from the sample (middle panel). In these panels the shaded regions show the global relations at  $M/M_{\odot} > 8 \times 10^9$ , empty triangles show the relation obtained in the low mass sample ( $8 \times 10^9 < M/M_{\odot} < 5 \times 10^{10}$ ), stars show the relation obtained in the high mass sample ( $M/M_{\odot} > 5 \times 10^{10}$ ). The right panel shows the comparison of the global relations obtained by inclusion (pink area) and excluding (purple area) the AGNs in the sample.

prefer underdense regions. On the other hand, Feruglio et al. (2010), using photometric redshifts to define the local galaxy density, find no dependence of the SFR and LIRG fraction on environment. The scenario is made even more complicated by the interplay of mass and density. Indeed, Scodreggio et al. (2009) reveals that already at  $z \sim 1$  mass and galaxy density are coupled with the most massive galaxies segregated in the most dense environment. Therefore, the evidence for a clear SFR-density trend could be due to the different contribution of massive and less massive galaxies favoring different density regimes. Once again much of the argument centers on whether the relation arises early on during the formation of the objects, or whether it is caused by density-driven evolution.

#### 1.2.4 Morphology modifications or simply nature?

The transformation of spiral galaxies into S0 or Ellipticals and the quenching of the star formation rate seem to be supported by several indications. Gas deficiency has been inferred from HI measurements for spirals in clusters and groups. The most deficient spirals are found in cluster cores, as a suggestion that the galaxies that come close to the dense core undergo a removal of their cold gas (Cayatte et al. 1990). A correlation also exists between the fraction of HI - deficient galaxies in a cluster and its hot gas content, measured through its X-ray luminosity (Giovanelli & Haynes 1985). This strongly suggests a dominant role for ram-pressure stripping rather than collisions. Indeed, ram pressure is efficient in very dense environments, and when the relative velocity of galaxies is high. These conditions are achieved in the core of rich galaxy clusters (Gunn & Gott 1972).

However, there is a rich literature about the types of environmental processes which could affect morphology and star formation activity in galaxies in high density regions. Indeed, several authors argue that some stripped galaxies seem to be undergoing tidal encounters, so that ram pressure is not enough to explain the star formation quenching. On the other hand, nearby spirals showing evidence for stripping exhibit evidence of tidal effects, although the combination of the two effects (such as tidal interactions and ram pressure) might make stripping happen regardless of the environment.

Nevertheless, galaxy-galaxy tidal encounters (and mergers) should be more efficient in groups than in clusters, because the velocity dispersion of a group is similar to that of an individual galaxy. A process more efficient in the cluster/group core is also the so called “galaxy harassment” (Moore et al. 1996), which consists of close multiple encounters of galaxies in high density regions. The repeated interactions with other systems would be able to progressively strip the gas from gas-rich spirals, shut down the star formation activity and leave a red remnant. Gas stripping can also be caused by the galaxies entering into a more massive dark matter halo. After loosing the gas supply, the galaxy star formation would shut down on a timescale of few Gyr (Boselli & Gavazzi 2006). This process is known as Galaxy “starvation” or “strangulation” and was proposed by Larson, Tinsley, & Caldwell (1980) to explain the transformation of spiral galaxies into lenticulars. Finally, according Birnboim & Dekel (2003) the direct collapse of gas during the accretion on a dark matter halo could induce a shock from which originates a starburst. Moreover, the gas flowing in the potential well may prevent an efficient gas removal by supernova driven winds. Despite a number of recent studies of nearby and distant clusters, it is not yet clear which processes, if any, are dominant.

A first attempt to disentangle the mass-driven and the environment driven evolution is provided by Peng et al. (2010), based on the zCOSMOS and SDSS data. With a purely empirical approach, they show that the differential effects of mass and environment are completely separable up to  $z \sim 1$ , leading to the idea of two distinct processes: “mass quenching” and “environment quenching”. The effect of environment quenching, at fixed over-density, evidently does not change with epoch to  $z \sim 1$  in zCOSMOS, suggesting that the environment quenching occurs as large-scale structure develops in the universe, probably through the cessation of star formation in 30%-70% of satellite galaxies. In contrast, mass quenching appears to be a more dynamic process, governed by a quenching rate. Mass quenching is the dominant quenching process for massive galaxies, which generally reside in massive halos like groups and clusters. Since mass quenching should occur when a galaxy reaches a limiting mass, more massive galaxies, which reside in more massive halos, should be quenched earlier than less massive ones, having reached earlier the limiting mass for quenching. Thus, the quenching of galaxy SF would be driven by an internal process, such as AGN feedback, rather than external one. This is supported observationally by the analysis of the star-formation histories of galaxies in the Virgo cluster region (Gavazzi et al. 2002), galaxies of higher H-band luminosities being characterized by shorter timescales of SF. Additional support to this scenario comes from the analysis of chemical abundances in elliptical galaxies by Pipino & Matteucci (2011).

### 1.2.5 Pre-Processing or no pre-processing?

According to the hierarchical paradigm of structure formation, cluster galaxies spend most of their life in groups of different masses, and thus in different environments, before entering the cluster regime. Thus, it is possible that, if any environmental process is acting in transforming galaxy morphology and quenching the star formation activity, this takes place during the much longer galaxy “group phase” rather than in the final state in the cluster environment. In this sense galaxies are “pre-processed” in groups before falling into cluster. This scenario has been proposed for the first time by Zabludoff & Mulchaey (1998).

Many observational studies have been carried out to investigate the importance of pre-processing in groups. However, the results of these works have been discordant. Several cluster studies strongly point on the importance of pre-processing (e.g. Fujita 2004; Haines et al. 2010; Kodama et al. 2001; Treu et al. 2003). On the other hand, other works suggest that the evolution of late-type galaxies belonging to loose structures associated with rich clusters such as Virgo are not significantly perturbed by pre-processing (Boselli & Gavazzi 2009). Moreover, using deep PACS data, Popesso et al. (2012) deny the possibility of any pre-processing showing a much higher level of star formation activity in groups than in cluster at any epoch up to  $z \approx 1.6$ .

Even theoretical simulations do not provide consistent results. Berrier et al. (2009) study the formation of fifty-three galaxy cluster-size dark matter halos formed within a pair of cosmological  $\Lambda$ CDM N-body simulations. By associating subhalos with cluster galaxies, they find that the majority of galaxies in clusters experience no pre-processing in the group environment prior to their accretion into the cluster. On average,  $\sim 70\%$  of cluster galaxies fall into the cluster potential directly from the field, with no luminous companions in their host halos at the time of accretion, and less than  $\sim 12\%$  are accreted as members of groups with five or more galaxies. Moreover, they find that cluster galaxies are significantly less likely to have experienced a merger in the recent past ( $\sim 6$  Gyr) than a field halo of the same mass. These results suggest that local, cluster processes like ram-pressure stripping, galaxy harassment, or strangulation play the dominant role in explaining the difference between cluster and field populations at a fixed stellar mass; and that pre-evolution or past merging in the group environment is of secondary importance for setting cluster galaxy properties for most clusters. However, McGee et al. (2009) perform a similar study showing that, instead, clusters at all redshifts examined exhibit a significant fraction of their galaxies accreted through galaxy groups. For instance,  $10^{14.5} M_{\odot}$  mass clusters at  $z=0$  have had  $\sim 40\%$  of their galaxies ( $M_{\text{stellar}} > 10^9 M_{\odot}$ ) accreted through halos with masses greater than  $10^{13} M_{\odot}$ . At higher redshifts fewer galaxies are accreted through massive halos. Only  $\sim 25\%$  of galaxies have been accreted through  $10^{13} M_{\odot}$  into  $10^{14.5} M_{\odot}$  mass clusters at  $z = 1.5$ . In addition, they find that the extent to which galaxies are pre-processed in groups before falling into clusters depends on the stellar mass of the infalling galaxy. For a  $10^{14.5} M_{\odot}$  mass cluster,  $73\%$  of galaxies with stellar masses greater than  $10^{10.5} M_{\odot}$  are accreted through  $10^{12} M_{\odot}$  systems, while only  $50\%$  of  $10^9$  to  $10^{10} M_{\odot}$  are accreted through the same systems. These predictions are confirmed also by De Lucia

et al. (2012), based on the Millennium simulation (Springel et al. 2005). They find that a significant fraction of group/cluster galaxies have been accreted onto their final halo as members of groups with mass  $\sim 10^{13} M_{\odot}$ . This fraction is  $\sim 27\%$  for galaxies with stellar mass  $\sim 10^9$  and  $\sim 10^{10} M_{\odot}$ , and increases to  $44\%$  for galaxies with mass  $\sim 10^{11} M_{\odot}$ . They also find that  $\sim 48\%$ ,  $\sim 43\%$  and  $\sim 23\%$  per cent of the galaxies in the same stellar mass bins are accreted onto the main progenitor of the final halo as satellite galaxies. A large fraction of group and cluster galaxies have therefore been “pre-processed” as satellites of groups with mass  $\sim 10^{13} M_{\odot}$ . Since a large fraction of the most massive galaxies we see in clusters today have been accreted as centrals, they should have been pre-processed the least.

Finally, De Lucia et al. (2012) make also a more philosophical point. According to their results, the traditional *nature* versus *nurture* debate represents subtle issues regarding “correlations” and “attribution”. It is, in principle, possible to separate nature versus nurture if they were correlated but physically uncoupled. However, their results demonstrate that the two are strongly and physically connected so that any attempt to separate them is ill-posed.

### 1.3 Infrared properties of galaxies

In the last twenty years or so, it has become more and more clear that in order to understand deeply galaxy evolution one has to take into account the energy that is absorbed by dust and re-emitted at mid- and far-infrared wavelengths. In fact, the derivation of the cosmic star formation history from ultraviolet measurements suffers from uncertainties in the obscuration corrections which must be applied to the rest frame emitted flux (e.g. Lilly et al. 1996; Madau et al. 1996). Thus, a more precise estimate of SFR is needed to investigate the SF activity at different cosmic times and environments. This possibility is offered by a calorimetric estimate coming from the mid- and far-IR emission. In the past, the two satellites *ISO* and *Spitzer* were already equipped with sensitive far-infrared detectors, although they focused on the study of local objects and luminous galaxies due to the high level of source confusion. These limitations have changed dramatically with the advent of the *Herschel* satellite.

In the next sections we describe the satellite properties, focusing in particular on the *Photoconducting Array Camera* and *Spectrometer* (PACS) instrument on board of *Herschel*. We will then present the main results existent in the literature obtained using *Herschel* data.

#### 1.3.1 The Herschel satellite

The key ingredient of our analysis is a robust estimate of the galaxy star formation activity. The rest-frame mid-infrared emission from dust in galaxies, in particular the emission detected in the  $8 \mu\text{m}$  and  $24 \mu\text{m}$  Spitzer bands, has been analyzed by a number of authors (Alonso-Herrero et al. 2006; Boselli, Lequeux, & Gavazzi 2004; Calzetti et al. 2005, 2007;

Förster Schreiber et al. 2004; Pérez-González et al. 2006; Relaño et al. 2008; Rieke et al. 2009; Roussel et al. 2001; Salim et al. 2009; Wu et al. 2005; Zhu et al. 2008), and a general correlation (but also a number of caveats) between mid-IR emission and SFR has been found. In the last two years, the *Herschel Space Telescope* opened new windows of sensitivity at even longer wavelengths than those explored by *Spitzer*, and in turn, provided even more powerful tools for probing the evolution of the rate at which galaxies have assembled their gas and dust components.

The *Herschel* satellite (Pilbratt et al. 2010) is designed to explore the “cool universe” during its expected 3.5 year mission lifetime. To achieve its scientific goals, *Herschel* is equipped with a 3.5 m main mirror and marks the beginning of a new generation of “space giants”. Bigger than any of its predecessors at approximately 7.5 m height and 4 m width, its science payload consists of three instruments: PACS and SPIRE, both cameras and spectrometers that allow *Herschel* to take pictures in six different “colors” in the far-infrared, and HIFI, a spectrometer with extremely high spectral resolution. The main instrument used in this work is PACS (Poglitsch et al. 2010), which provides *Herschel* with far-infrared imaging and spectroscopic capabilities from 60 to 210  $\mu\text{m}$ .

### 1.3.2 Photoconducting Array Camera and Spectrometer

The requested observing time of *Herschel* is largely spent on deep and/or large scale photometric surveys performed in scan map mode with the PACS photometer. Indeed, the opening of the 60-210  $\mu\text{m}$  window by PACS photometer addresses a wide range of key questions of current astrophysics concerning the origins of stars, planetary systems, galaxies, and the evolution of the universe.

The PACS photometer detectors are bolometer arrays. Each pixel of the array can be considered as a little cavity in which sits an absorbing grid. The incident infrared radiation is registered by each bolometer pixel by causing a tiny temperature difference, which is measured by a thermometer implanted on the grid. The blue channel offers two filters, 60-85  $\mu\text{m}$  and 85-130  $\mu\text{m}$  and has a  $32 \times 64$  pixel array. The red channel has a 130-210  $\mu\text{m}$  filter and has a  $16 \times 32$  pixel array. Both channels cover a field-of-view of  $\sim 1.75' \times 3.5'$ , with full beam sampling in each band. The two short wavelength bands are selected by two filters via a filter wheel. The field of view is nearly filled by the square pixels, however the arrays are made of subarrays which have a gap of  $\sim 1$  pixel in between. For the long wavelength end 2 matrices of  $16 \times 16$  pixels are tiled together. During a PACS scanmap observation, the telescope moves back and forth in a pattern of parallel scan lines that are connected by short turnaround loops. For science observations the multiplexing readout samples each pixel at a rate of 40 Hz. Because of the large number of pixels, data compression is required and hence raw data are binned to an effective 10 Hz sampling rate.

The scan technique is the most frequently used *Herschel* observing mode. Scan maps are the default to map large areas of the sky, for galactic as well as extragalactic surveys, but at the same time they are also recommended for small fields and even for point sources. Scan maps are performed by slewing the spacecraft at a constant speed along parallel lines. Available satellite speeds are 10, 20, 60 arcsec/s in PACS prime mode and 20, 60 arcsec/s

(medium, fast) in PACS/SPIRE parallel mode. The number of satellite scans, the scan leg length, the scan leg separation, and the orientation angles (in array and sky reference) are freely selectable by the observer. Via a repetition parameter the specified map can be repeated  $n$  times. During the full scan map duration the bolometers are constantly readout with 40 Hz. However, due to satellite data rate limitations, the data are compressed to a final sampling rate of 10 Hz.

### 1.3.3 The PACS Evolutionary Probe survey

Members of the PACS instrument consortium, the Herschel Science Centre, and mission scientist M. Harwit have joined forces in the PACS Evolutionary Probe (PEP) deep extragalactic survey (Lutz et al. 2011).

PEP encompasses deep observations of blank fields and lensing clusters, close to the Herschel confusion limit, in order to probe down to representative high-redshift galaxies, rather than being restricted to individually interesting extremely luminous cases. PEP is focused on PACS 70, 100, and 160  $\mu\text{m}$  observations. SPIRE observations of the PEP fields are obtained in coordination with PEP by the HerMES survey (Oliver et al. 2010). Larger and shallower fields are observed by HerMES (70  $\text{deg}^2$ ), as well as by the H-ATLAS survey (570  $\text{deg}^2$ , Eales et al. 2010), while the GOODS-Herschel program (Elbaz et al. 2011) provides deeper observation in (part of) the GOODS fields that are also covered by PEP. Finally, the Herschel lensing survey (Egami et al. 2010) substantially increases the number of lensing clusters observed with Herschel, adding about 40 clusters to the 10 objects covered by PEP.

The PACS Evolutionary Probe is one of the major Herschel Guaranteed Time (GT) extragalactic projects. It is structured as a “wedding cake” survey, based on four different layers in order to cover wide shallow areas and deep pencil-beam fields. PEP includes the most popular and widely studied extragalactic blank fields: COSMOS (2  $\text{deg}^2$ ), Lockman Hole, EGS and ECDFS (450-700  $\text{arcmin}^2$ ), GOODS-N and GOODS-S (  $\sim 200 \text{ arcmin}^2$  ). In addition, the observations of ten nearby lensing clusters offer the chance to break the PACS confusion limit thanks to the gravitational lensing (Altieri et al. 2010). PEP aims to resolve the cosmic infrared background (e.g. Berta et al. 2010 and Berta et al. 2011) and determine the nature of its constituents, determine the cosmic evolution of dusty star formation and of the infrared luminosity function, explore the relation between far-infrared emission and environment and determine clustering properties. Other main goals include study of AGN/host co-evolution, and determination of the infrared emission and energetics of known high redshift galaxy populations.

## 1.4 Herschel main science results

In this section we present the main results achieved using *Herschel* data relevant to this thesis.



### 1.4.1 The evolution of the IR SED

Before the launch of *Herschel*, the derivation of  $L_{\text{IR}}^{\text{tot}}$ , hence also of the SFR, of distant galaxies had to rely on extrapolations from either mid-IR or sub-mm photometry. Although there are many reasons to avoid the extrapolations from the mid-IR (evolution in metallicity, geometry of star formation regions, evolution of the relative contributions of broad emission lines and continuum), it has been found that these extrapolations work relatively well up to  $z \sim 1.5$ . In particular, Elbaz et al. (2010) compare  $L_{\text{IR}}^{\text{tot}}$ , estimated from *Herschel* PACS and SPIRE, to  $L_{\text{IR}}^{24}$  (the total IR luminosity extrapolated from the observed *Spitzer* mid-IR  $24\mu\text{m}$  flux density), assuming that the IR SED of star forming galaxies remains the same at all epochs, and find that they agree within a dispersion of only 0.15 dex up to  $z = 1.5$ . However, this assumption fails for bright infrared sources (LIRGs and ULIRGs) at  $z > 1.5$ , since the flux extrapolated from  $24\mu\text{m}$  or from stacking is always overestimated with respect to the one derived using *Herschel* data.

This confirms the existence of the so-called “mid-IR excess” galaxy population, first identified by comparing  $L_{\text{IR}}^{24}$  with radio, MIPS-70  $\mu\text{m}$  and 160  $\mu\text{m}$  stacking (Daddi et al. 2007a; Magnelli et al. 2011; Papovich et al. 2007). In particular, the IR luminosity derived using these data is too strong for LIRGs and ULIRGs at  $z \sim 2$  compared to local galaxies. The mid-IR excess problem has recently been confirmed with *Herschel* by Nordon et al. (2010) on a small sample of  $z \sim 2$  galaxies detected with PACS and by stacking PACS images on  $24\mu\text{m}$  priors (Elbaz et al. 2010, Nordon et al. 2010).

It has been proposed that the mid-IR excess problem could be due to the presence of unidentified AGNs affected by strong extinction, possibly Compton thick (Daddi et al. 2007b, see also Papovich et al. 2007). Indeed, at these high redshifts, the re-processed radiation of a buried AGN may dominate the mid-IR light measured in the  $24\mu\text{m}$  passband, while the far-IR emission probed by *Herschel* would be dominated by dust-reprocessed stellar light. This explanation for the mid-IR excess problem was recently called into question by mid-IR spectroscopy of  $z \sim 2$  galaxies obtained using the *Spitzer* IRS spectrograph. Surprisingly, where one would expect hot dust continuum emission (in case of a buried AGN which dominates the IR emission, Fadda et al. 2010; Murphy et al. 2009) it has been found the presence of strong PAH emission lines.

Steered by these results, after removing the AGNs from their sample, Elbaz et al. (2011), analyzed galaxies observed in the two Great Observatories Origins Deep Survey (GOODS) fields in the Northern and Southern hemispheres, detected by PACS observations at 100  $\mu\text{m}$  and 160  $\mu\text{m}$ . They show that the mid-IR excess problem is not artificially produced by imperfections that could result from the indirect stacking measurements, but instead takes place for individually detected galaxies at  $z > 1.5$  and at high  $24\mu\text{m}$  flux densities, corresponding to  $L_{\text{IR}}^{24} > 10^{12} L_{\odot}$  (Fig. 1.7).

Furthermore, Elbaz et al. (2011) do not find evidence for different IR SEDs in distant galaxies. Instead, as shown in Fig. 1.8, they find that local and distant galaxies are both distributed in two quite well-defined regimes: a Gaussian distribution containing nearly 80 % of the galaxies, which share a universal *IR8* ratio ( $= L_{\text{IR}}/L_8$ ) of  $\sim 4$ , and a sub-population of  $\sim 20$  % of galaxies with larger *IR8* values.

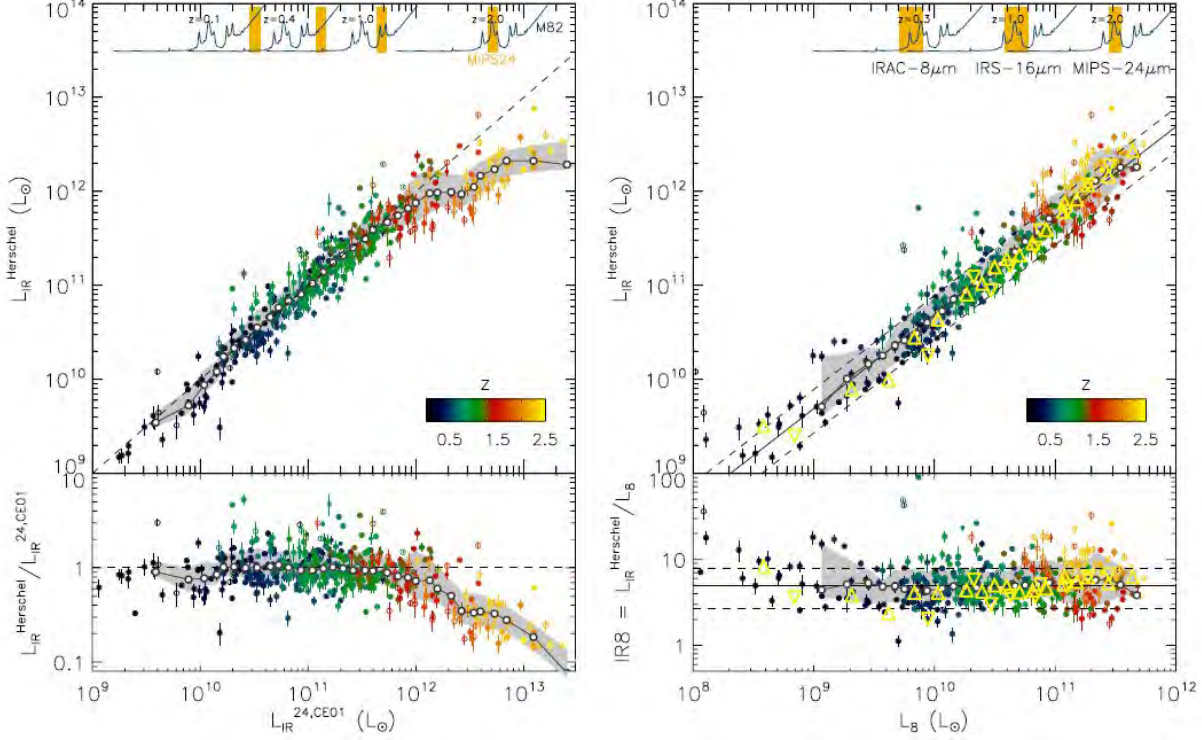


Figure 1.7: *Left panel:* Comparison of  $L_{\text{IR}}^{\text{tot}}$  (8–1000  $\mu\text{m}$ ) (Elbaz et al. 2011) as directly measured from *Herschel* ( $L_{\text{IR}}^{\text{Herschel}}$ ) with the value extrapolated from 24  $\mu\text{m}$  ( $L_{\text{IR}}^{24, \text{CE01}}$ ) using the template of Chary & Elbaz (2001). Galaxies with spectroscopic and photometric redshifts (from both GOODS–North and –South) are marked with filled and open symbols respectively. Colors range from black ( $z \sim 0$ ) to orange ( $z \sim 2.5$ ), passing through green ( $z \sim 1$ ) and red ( $z \sim 2$ ). The wavelength range sampled by the MIPS 24  $\mu\text{m}$  passband is shown in orange at the top of the figure where it is compared to the redshifted SED of M82. The dashed line in the left-hand side panels is the one-to-one correlation. The sliding median and 16th and 84th percentiles of the distribution are shown with white dots connected with a solid line and gray zone respectively. The bottom panel shows the ratio of the actual over extrapolated total IR luminosity. *Right panel:* comparison of  $L_{\text{IR}}^{\text{Herschel}}$  with  $L_8$  (rest-frame 8  $\mu\text{m}$  broadband) for “clean” galaxies. The observed bandpasses used to estimate  $L_8$  are illustrated in the top of the figure and compared to the redshifted SED of M82. The sliding scale of the median and 68% dispersion around it is shown with a gray zone which is fitted by the solid and dashed lines:  $\text{IR8} = 4.9 [-2.2, +2.9]$ . Stacked measurements combined with detections weighted by number of objects per luminosity bin are represented by large yellow open triangles (GOODS-S: upside down, GOODS-N: upward). The bottom panel shows the  $\text{IR8} (=L_{\text{IR}}^{\text{Herschel}}/L_8)$  ratio which is found to remain constant with luminosity and redshift

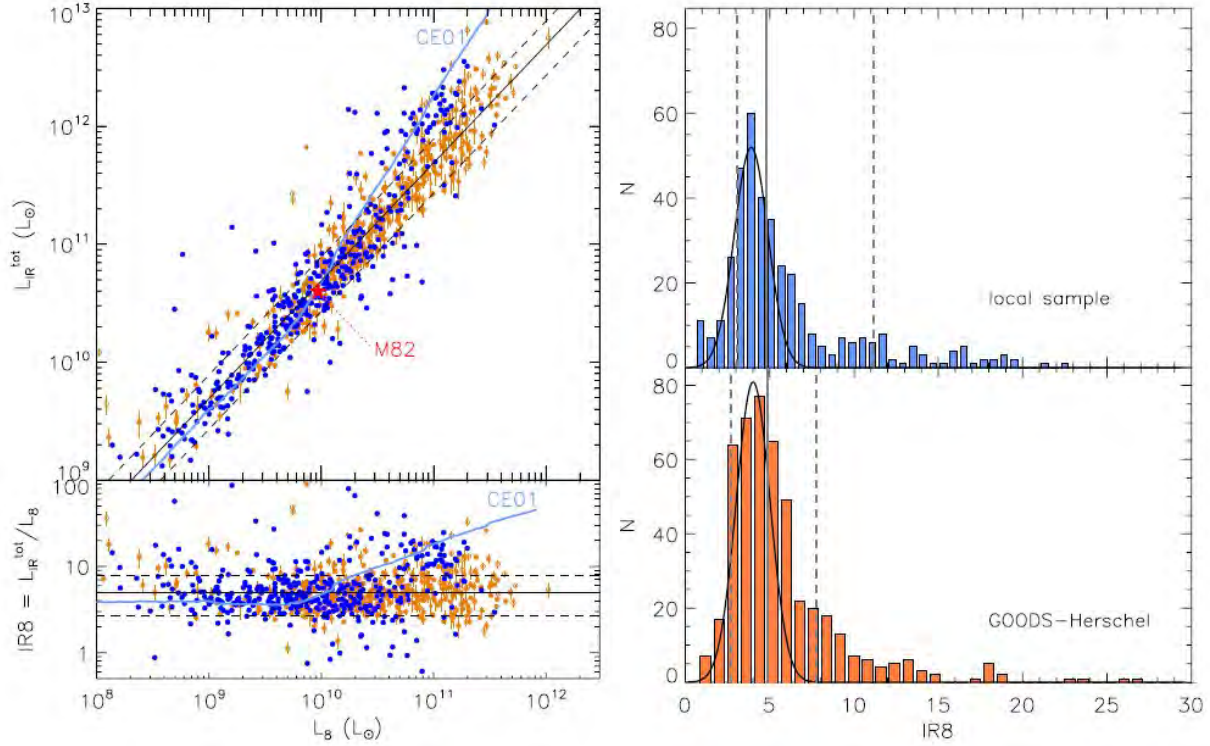


Figure 1.8: *Left:*  $L_{\text{IR}}^{\text{tot}}$  [IRAS] versus  $L_8$  for local ISO and AKARI galaxies (filled blue dots) from Elbaz et al. (2011). The GOODS-Herschel galaxies are shown in the background with lighter orange symbols together with their median (black solid line) and 68% dispersion (black dashed lines). The light blue line shows the locus traced by the CE01 SED library. *Right:* histogram of the IR8 ratios for the local galaxy sample (blue, upper panel) and GOODS-Herschel sample (orange, bottom panel). The solid curves show Gaussian fit to the distributions. The vertical gray lines indicate the median (solid) and 68% dispersion (dashed) for the full samples.

### 1.4.2 The link to the SFR-M “Main Sequence”

Deep galaxy surveys have found consistently that the star formation rate per unit stellar mass ( $M_*$ ) depends strongly on both  $M_*$  and redshift, with the bulk of star formation occurring earlier in massive galaxies than in less massive systems (e.g. Guzmán et al. 1997, Brinchmann & Ellis 2000, Juneau et al. 2005, Bauer et al. 2005, Bell et al. 2005, Pérez-Gonzalez et al. 2005, Feulner et al. 2005, Papovich et al. 2006, Caputi et al. 2006, Reddy et al. 2006). High-SFR objects are observed to be more abundant at higher  $z$  where starburst are believed to be caused by merging events.

Noeske et al. (2007a) find a defined “Main Sequence” (MS) for star forming galaxies (Fig. 1.9). This smooth sequence suggests that the same set of few physical processes governs SF in galaxies, unless quenching occurs for particular reasons. The evolution of SF along the MS appears dominated by a gradual decline of SFR in individual galaxies

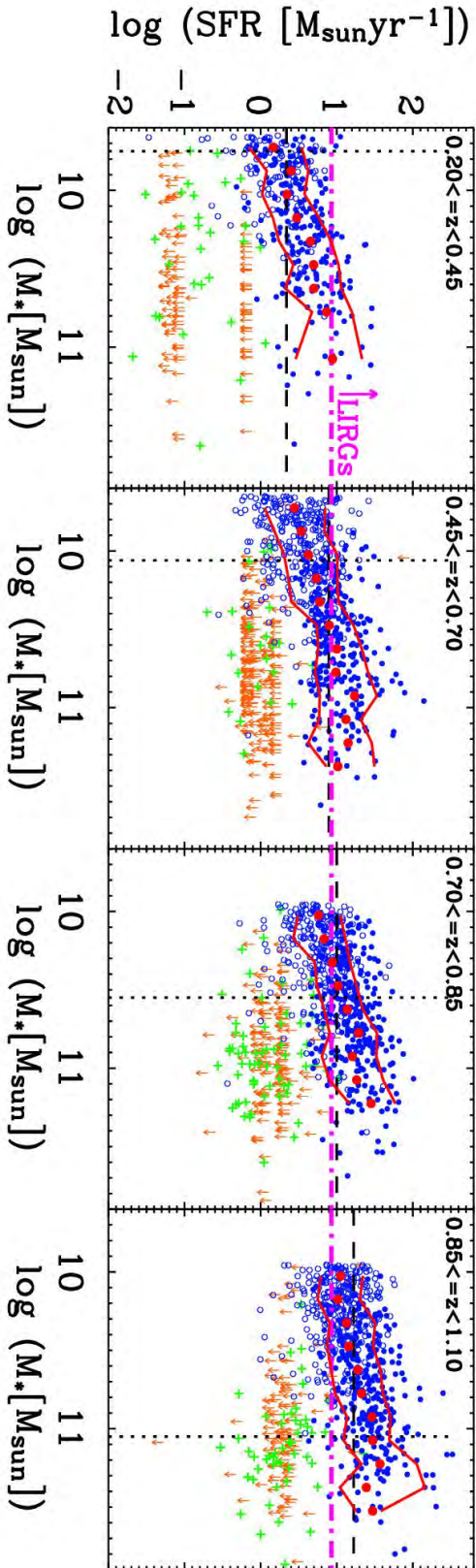


Figure 1.9: SFR vs  $M_*$  for 2905 galaxies in the EGS, in the  $M_*$  range where the data are  $> 80\%$  complete (Noeske et al. 2007a). The dotted vertical line marks 95% completeness. Filled blue circles: Combined SFR from MIPS  $24\mu\text{m}$  and DEEP2 emission lines. Open blue circles: No  $24\mu\text{m}$  detection, blue  $U - B$  colors, SFR from extinction-corrected emission lines. Green crosses: Same as open blue circles, but red  $U - B$  colors, mostly LINER/AGN candidates. Orange down arrows: No robust detection of  $f(24\mu\text{m})$  or emission lines; conservative SFR upper limits are shown. There is a distinct sequence formed by fiducial SF galaxies (open and filled circles); galaxies with little or no SF lie below this sequence. Red circles show the median of  $\log(\text{SFR})$  in mass bins of  $0.15$  dex for main sequence galaxies (blue circles). Red lines include 34% of the main sequence galaxies above and 34% below the median of  $\log(\text{SFR})$ ,  $\pm 1\sigma$  in the case of a normal distribution. Horizontal black dashed line: SFR corresponding to the  $24\mu\text{m}$  80% completeness limit at the center of each  $z$  bin.  $24\mu\text{m}$ -detected galaxies above the magenta dot-dashed line are LINERs.



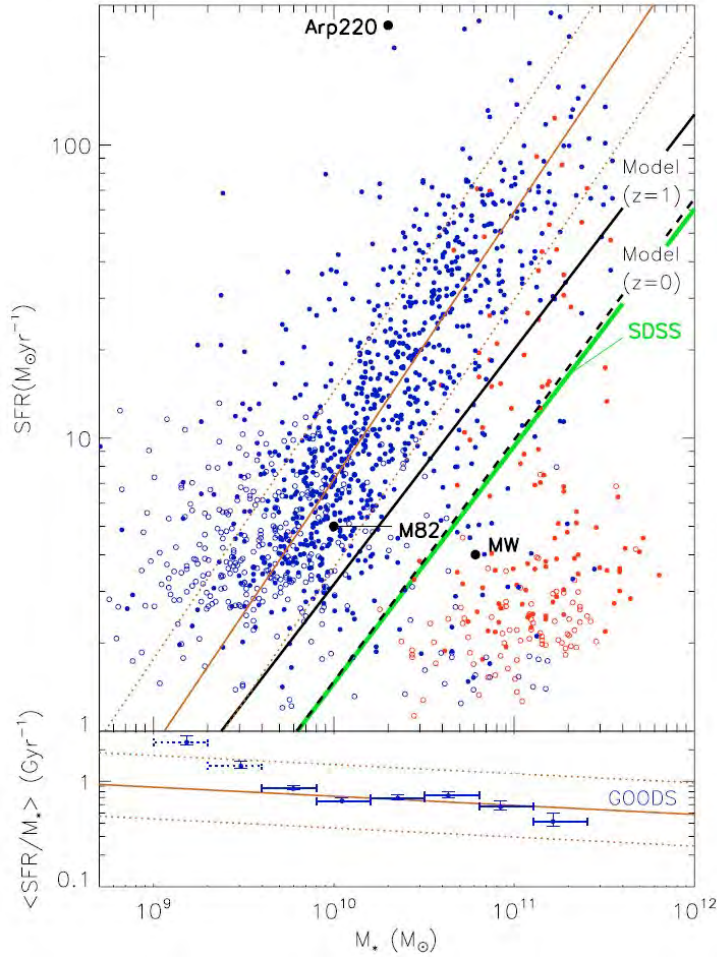


Figure 1.10: Relationship between SFR and specific SFR ( $\text{SFR}/M_*$ ) with stellar mass in  $z \sim 0.8-1.2$  galaxies from Elbaz et al. (2007). The SFR is derived from the sum of the  $\text{SFR}(\text{UV})$  and  $\text{SFR}(\text{IR})$  when galaxies are detected at  $24\mu\text{m}$  (filled symbols) and  $\text{SFR}(\text{UV})$  only otherwise (open symbols). A Salpeter IMF is assumed. Red and blue symbols are for red and blue galaxies as defined by their colors. The GOODS blue galaxies follow the relation (plain brown line):  $\text{SFR}[\text{M}_\odot \text{ yr}^{-1}] = 7.2 [-3.6, +7.2] \times (M_*/10^{10} \text{ M}_\odot)^{0.9}$  at the 68% confidence level (marked with dashed brown lines).

since  $z \sim 1$ , rather than by an evolving frequency or amplitude of starbursts. Thus, the dominant process that governs SF since  $z \sim 1$  is likely a gradual one, and a possibility could be represented by the gas exhaustion (Noeske et al. 2007a).

At somewhat higher redshift,  $z=0.8-1.2$ , Elbaz et al. (2007), using Spitzer  $24\mu\text{m}$  data, show that the tight relation (0.3 dex) between SFR and stellar mass for star forming galaxies still exists (Fig. 1.10).

By combining Spitzer  $24\mu\text{m}$  and Herschel PACS data in the GOODS fields, Elbaz et al. (2011) find the direct link between the infrared excess at  $8\mu\text{m}$  ( $IR_8$ ) and the galaxy

Main Sequence. Indeed, Elbaz et al. (2011) show that the same population of galaxies that follow a universal trend in  $L_{\text{IR}}^{\text{tot}}-L_8$  valid at all redshifts and luminosities (Fig. 1.8, right panel), follows also a main sequence in  $\text{SFR} - M_*$ . Instead galaxies exhibiting an excess  $IR_8$  ratio systematically exhibit an excess sSFR ( $=\text{SFR}/M_*$ ). In the local sample, ULIRGs are clearly members of the second population whereas  $z \sim 2$  LIRGs and ULIRGs are main sequence galaxies. It is therefore the weight of both populations that has changed with time and that is at the origin of the mid-IR excess problem. An overestimate of  $L_{\text{IR}}^{\text{tot}}$  comes up when the SED templates for local ULIRGs are used to extrapolate from  $24 \mu\text{m}$  photometry for main sequence galaxies at  $z \sim 2$ . However, one needs to keep in mind that most of the distant LIRGs and ULIRGs belong to the same main sequence as local normal star-forming galaxies.

The direct consequence of sharing the same value of  $IR_8$  for MS galaxies at any luminosities and redshift, is that most likely they share the same IR SED. Elbaz et al. (2011) divide MS from starburst (SB) galaxies on the basis of their location on the sSFR-stellar mass diagram. They use the following equation:

$$R_{\text{SB}} = s\text{SFR}/s\text{SFR}_{\text{MS}} = \tau_{\text{MS}}/\tau \quad [ > 2 \text{ for starbursts} ], \quad (1.1)$$

(where the subscript MS indicates the typical value for main sequence galaxies at the redshift of the galaxy in question) to define the starburstiness of a galaxy, which is its offset relative to the typical MS sSFR. Using this starburstiness parameter Elbaz et al. (2011) create an IR SED template for MS and SB galaxies separately. The two templates are presented in Fig. 1.11.

The typical MS IR SED in the left-hand part of Fig. 1.11 has a broad far-IR bump centered around  $90 \mu\text{m}$ , suggesting a wide range of dust temperatures around an effective value of  $\sim 30$  K, and strong PAH features in emission. Instead, the typical IR SED for SB galaxies (right panel of Fig. 1.11) presents a narrower far-IR bump peaking around  $\lambda \sim 70-80 \mu\text{m}$ , corresponding to an effective dust temperature of  $\sim 40$  K, and weak PAH emission lines. They should be considered as average SEDs, acknowledging that there is a continuous transition from one to the other with increasing  $IR_8$  or star-formation compactness (Elbaz et al. 2011).

In the further analysis we will use these new IR SED templates to derive the  $L_{\text{IR}}^{\text{tot}}$  at any redshift and luminosity.

### 1.4.3 The evolution of star formation activity per halo mass

A way of looking at the evolution of SF activity in galaxy systems is to consider a global quantity such as the star formation rate per unit of halo mass, that is the sum of the SFRs of all the galaxy in a system divided by the system total mass,  $\Sigma(\text{SFR})/M$  (e.g Popesso et al. 2012). This quantity represents a sort of sSFR for structures like groups or clusters. According to recent results (Bai et al. 2009; Chung et al. 2010; Finn, Zaritsky, & McCarthy 2004; Finn et al. 2005; Geach et al. 2006; Hayashi et al. 2011; Kodama et al. 2004; Koyama et al. 2010; Popesso et al. 2012), the evolution of  $\Sigma(\text{SFR})/M$  for clusters is rapid. The

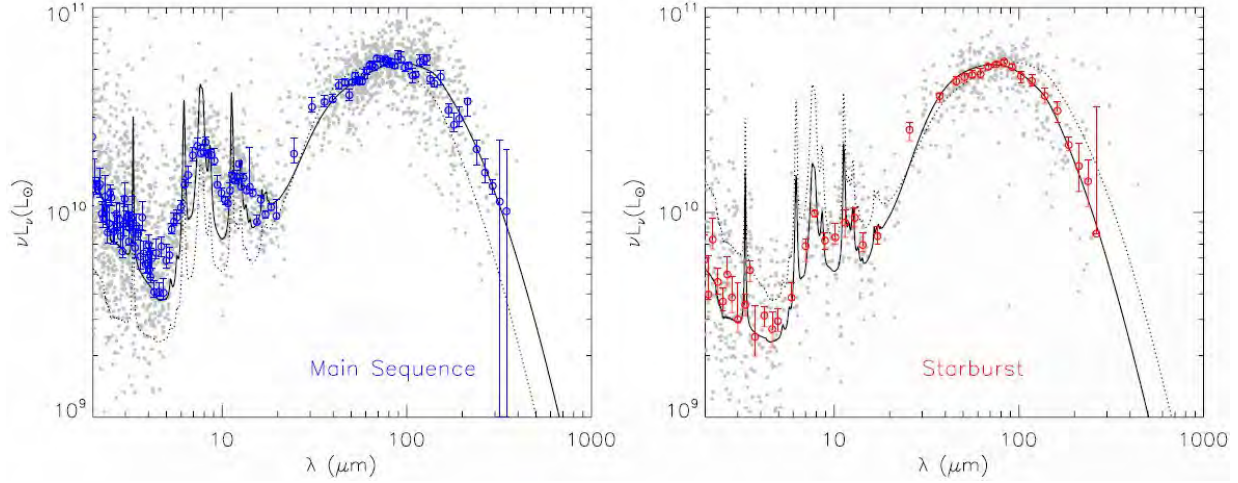


Figure 1.11: Composite spectral energy distribution of the typical main sequence galaxy (*left*;  $IR8=4\pm2$ ) and starburst (*right*;  $IR8>8$ ) from Elbaz et al. (2011). Light gray dots: individual GOODS–*Herschel* galaxies normalized to  $L_{IR}^{tot} = 10^{11} L_{\odot}$ . The large filled symbols with error bars are the median and associated uncertainty of the MS (left figure, blue dots) and SB (right figure, red dots) galaxies computed in intervals of wavelengths. The model fit to each SED is shown with a solid black line while the opposing SED (MS or SB) is shown with a dotted black line for comparison.

dependence with redshift is described by

$$\Sigma(\text{SFR})/M \propto (1+z)^{\alpha}, \quad (1.2)$$

with  $\alpha \simeq 5 - 7$ . The cluster  $\Sigma(\text{SFR})/M$  evolves faster up to  $z \sim 1$  than the fraction of IR-emitting galaxies (the IR Butcher-Oemler effect) because IR-emitting galaxies are not only more numerous in higher- $z$  clusters but also more IR luminous (Bai et al. 2009). In addition, there are some indications that  $\Sigma(\text{SFR})/M$  anti-correlates with halo mass in galaxy systems at similar redshift (Finn, Zaritsky, & McCarthy 2004; Finn et al. 2005; Homeier et al. 2005; Koyama et al. 2010). The quantity  $\Sigma(\text{SFR})/M$  thus appears to be a powerful tool for analyzing the rapid evolution of galaxies in systems of different mass.

Popesso et al. (2012) study the evolution of the star formation activity per halo mass using deep far-infrared PACS data in three different mass scales: low mass halos (field galaxies), groups, and clusters, up to a redshift  $z \approx 1.6$ . In Fig. 1.12 we show the comparison of their  $\Sigma(\text{SFR})/M$ - $z$  relation for LIRGs of galaxy systems with the corresponding relation for field galaxies from Magnelli et al. (2011) and Gruppioni et al. (2011) (light blue shaded region and blue dashed line, respectively). Black, and magenta symbols show the  $\Sigma(\text{SFR})/M$ -redshift relation for the clusters and the groups, respectively. For both samples there is evidence for a significant correlation between  $\Sigma(\text{SFR})/M$  and redshift. Groups appear to be characterized by higher  $\Sigma(\text{SFR})/M$  values than clusters, at all redshifts, i.e. they show a higher SF activity than massive clusters. The solid curves in Fig. 1.12 represent the best-fit models to the observed relations: for the cluster sample

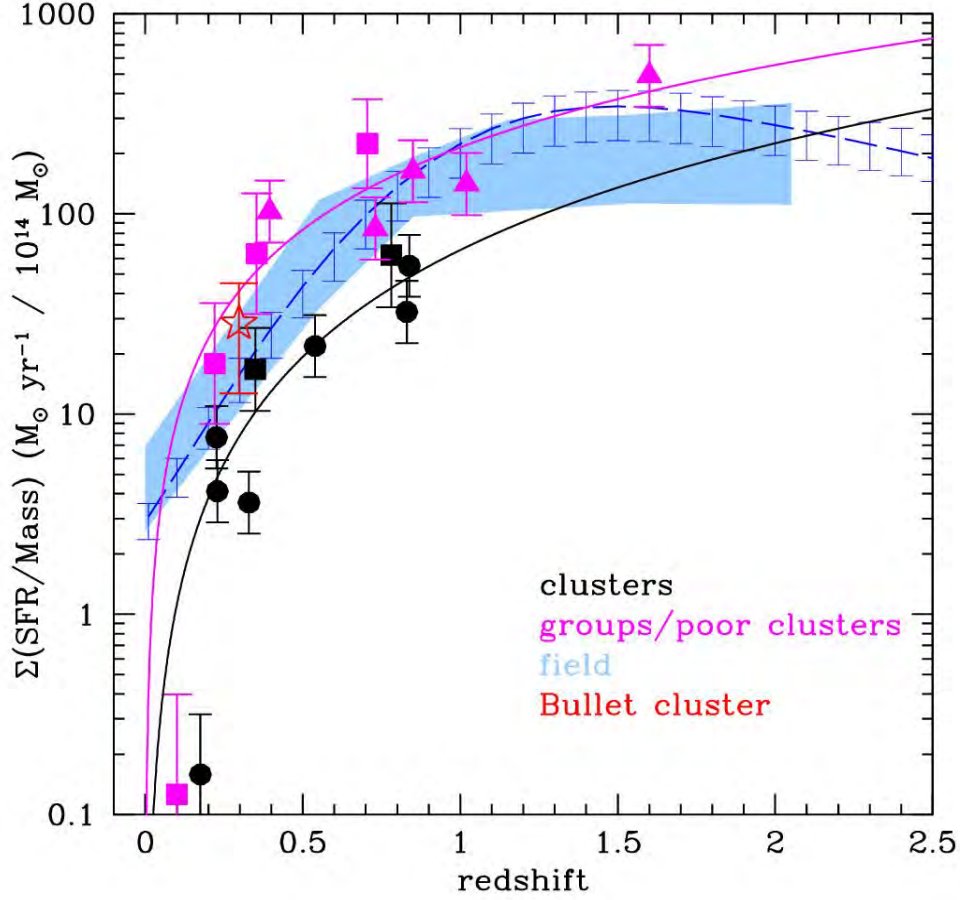


Figure 1.12:  $\Sigma(\text{SFR})/M$ - redshift relation for clusters (black symbols) and groups (magenta symbols) from Popesso et al. (2012). Square symbols, triangles, and dots identify, respectively, the COSMOS composite systems, the GOODS systems, and the remaining systems. The red star identifies the Bullet cluster. The black solid line shows the best fit  $\Sigma(\text{SFR})/M$ - $z$  relation for the cluster sample, excluding the Bullet cluster. The relation fitted to the data is of the type  $\Sigma(\text{SFR})/M \propto z^\alpha$ . The magenta solid line shows the best fit for the sample of groups and poor clusters. The field  $\Sigma(\text{SFR})/M$ -redshift relation from Magnelli et al. (2011) and Gruppioni et al. (2011) is represented by the light blue shaded region and the dashed blue line, respectively. The shading and error bars represent  $1\sigma$  confidence levels.

$\Sigma(\text{SFR})/M = (66 \pm 23) \times z^{1.77 \pm 0.36}$  and for the groups  $\Sigma(\text{SFR})/M = (213 \pm 44) \times z^{1.33 \pm 0.34}$  (Popesso et al. 2012).

Both the cluster and the group  $\Sigma(\text{SFR})/M$  increase monotonically with  $z$  while the field  $\Sigma(\text{SFR})/M$  reaches a maximum at  $z \sim 1$  and then become constant. Part of the observed evolution may come from the mass quenching (Peng et al. 2010) for which massive galaxies evolve mostly because of an internally driven process rather than an environmental influence. In fact, according to the almost linear,  $z$ -dependent, relation between galaxy



SFRs and stellar masses (Elbaz et al. 2007; Noeske et al. 2007a) most of the LIRGs are likely to be rather massive galaxies.

It is important to highlight the position of the Bullet cluster in the diagram  $\Sigma(\text{SFR})/M-z$  of Fig. 1.12. In fact, even though it is a massive cluster it has a star formation activity comparable to those of groups. Also according to Chung et al. (2010), the star formation in the Bullet cluster does not appear to be quenched. Indeed the galaxies in the infalling group (the “bullet”) show a high level of SF activity. If rapid ram-pressure stripping, acting on a very short timescale (Abadi, Moore, & Bower 1999), was a major quenching process, the group LIRGs could have had their star formation quenched already, given that the cluster-group collision happened  $\sim 250$  Myr ago (Springel & Farrar 2007). Starvation, acting on a long timescale, caused by the removal of the hot gas halo reservoirs of galaxies, is a more likely candidate as quenching process (Bekki 2009; Kawata & Mulchaey 2008). Starvation should proceed more effectively in higher (galaxy or gas) density regions, hence it should quench SF earlier in cluster than in group galaxies.

To shed light on the role of the merging activity in the evolution of the SF activity, other merging clusters at different merging stage should be considered and compared with groups and relaxed clusters.

#### 1.4.4 IR Luminosity Function

The important contribution of LIRGs ( $10^{11}L_{\odot} < L_{IR} < 10^{12}L_{\odot}$ ) and ULIRGs ( $L_{IR} > 10^{12}L_{\odot}$ ) in the evolution of the star-formation rate history of the universe is now well established up to  $z \sim 1$  (e.g. Chary & Elbaz 2001; Elbaz et al. 2002; Franceschini et al. 2001; Lagache et al. 2004; Le Floc’h et al. 2005; Magnelli et al. 2009, 2011; Metcalfe et al. 2003). Their contribution to the SFR-density of the universe, as derived from the evolution of the IR Luminosity Function (LF), increases with redshift up to  $z \sim 1$  where the bulk of the SFR-density is given by the Luminous Infrared Galaxies. The study of this evolution was possible through the use of large and accurate spectroscopic and/or photometric redshift catalogs and of deep  $24\mu\text{m}$  and  $70\mu\text{m}$  surveys obtained by Spitzer.

At  $z > 1.3$ , the SFR history of the universe has been derived by several studies (Caputi et al. 2007; Pérez-González et al. 2006) using deep  $24\mu\text{m}$  imaging and infrared bolometric correction estimated from local spectral energy distribution (SED) libraries (Chary & Elbaz 2001; Dale & Helou 2002; Lagache, Dole, & Puget 2003). All of these studies conclude that the relative contribution of Ultra Luminous Infrared Galaxies to the SFR-density of the universe increases with redshift, and may even be the dominant component at  $z \sim 2$  (see also Magnelli et al. 2009, 2011 and Fig. 1.13).

However, given to the rather uncertain extrapolation of  $L_{IR}$  from the galaxy total  $24\mu\text{m}$  flux at  $z > 1.5$ , the study of the IR LF built with PACS data at  $70$ ,  $100$  and  $160\mu\text{m}$  can well constrain the evolution of the contribution to the SFR-density of the universe of different classes of galaxies. Gruppioni et al. (2012) find that the evolution derived for the global IR LF, derived in the PEP fields, is indeed a combination of different evolutionary paths: the IR population does not evolve all together “as a whole”, as it is often assumed in the literature, but it is composed by different galaxy classes evolving

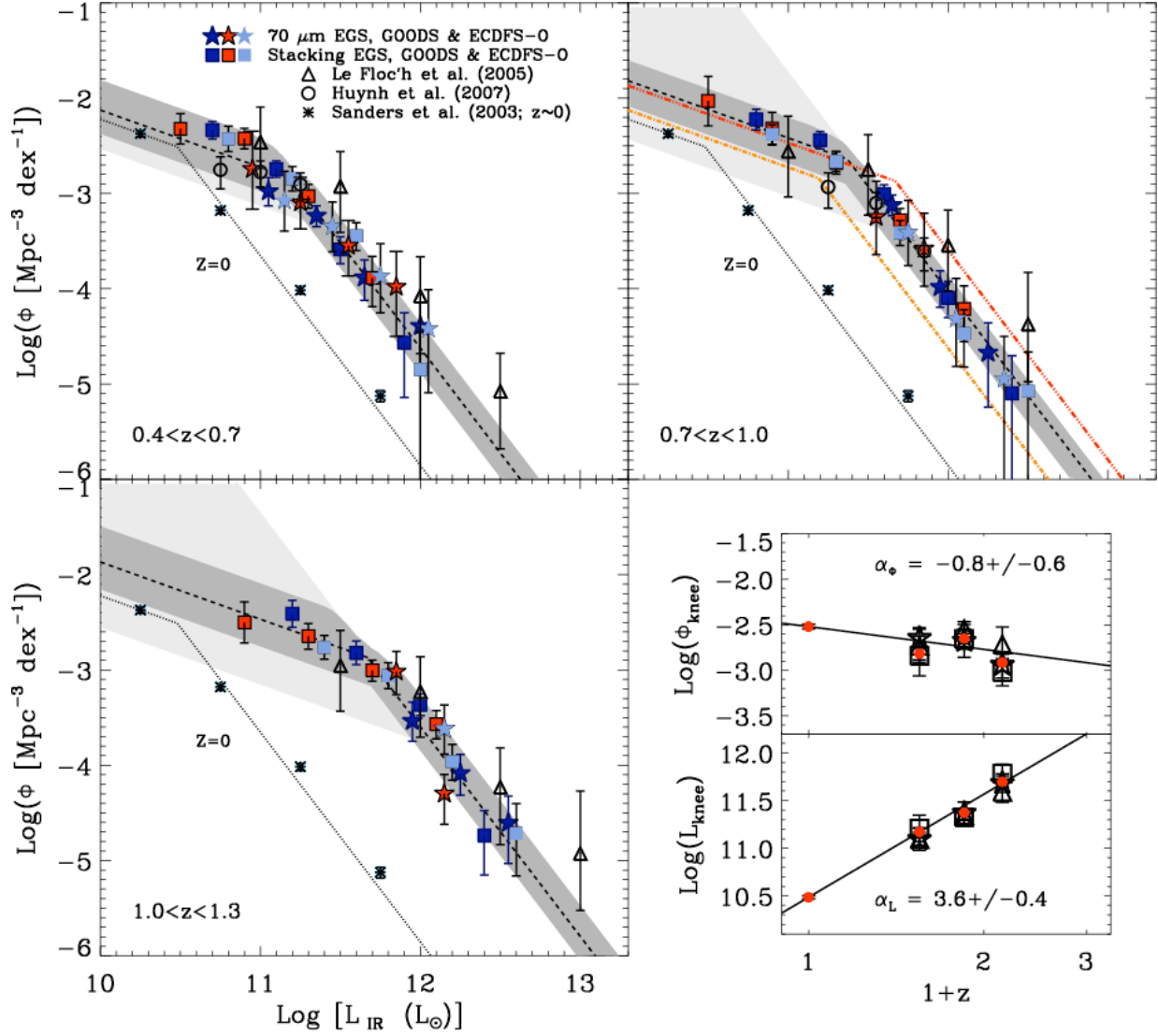


Figure 1.13: Total infrared LF estimated for three redshift bins from Magnelli et al. (2011). The red stars are obtained from the GOODS-North and South fields using Spitzer 70  $\mu\text{m}$  sources. The dark blue and light blue stars show the LF obtained from 70  $\mu\text{m}$  sources in the EGS and the ECDFS fields, respectively. The red and dark blue squares are obtained starting from 24  $\mu\text{m}$  and using the 24-70  $\mu\text{m}$  correlation (see Magnelli et al. 2009) in the GOODS and EGS fields, respectively. Asterisks show the local reference taken from Sanders et al. (2003) and the dotted line presents the fit of these data points with a double power law. The empty triangles and the empty circles are taken from Le Floch et al. (2005) and Huynh et al. (2007), respectively. The light and dark shaded area spans all the parametric solutions obtained with the minimization method and compatible, within  $1\sigma$ , with the LF measured using direct 70  $\mu\text{m}$  observations and the LF measured using the stacking analysis respectively. The inset plot represents the evolution of the  $\Phi_{\text{knee}}$  and  $\alpha_{\text{knee}}$  as function of redshift.

differently. Indeed they clarify the relative contribution of different classes of galaxies to global IR number density and luminosity density evolution ( $\rho_{IR}$ ), as shown in Fig. 1.14. Their most interesting finding is, perhaps, the derivation of the relative contribution to  $\rho_{IR}$  of galaxies on the SFR-mass Main Sequence (see previous discussion) and off-MS sources. The former always dominate, though their contribution keeps nearly constant between  $z = 0.5$  and  $z = 2.5$ , while the contribution to  $\rho_{IR}$  of the latter increases significantly with  $z$  (from 10% at  $0.5 < z < 1.2$ , to  $> 20\%$  at  $1.8 < z < 2.5$ ). A quite different evolution in the contribution to  $\rho_{IR}$  is also observed from galaxies in different stellar mass range, reflecting the downsizing scenario ( $\rho_{IR}$  peaks at higher redshift with increasing mass). Intermediate-mass objects ( $\log(M/M_{\odot}) = 10 - 11$ ) always dominate the IR luminosity density, increasing up to  $z \sim 1$ , then remaining nearly constant at higher redshifts (at least up to  $\sim 2.8$ ), while the contribution of most massive objects increases even more rapidly with  $z$  (at  $z = 2$  it was  $\sim 5$  times higher than today) and continues to grow up to  $z = 3$ .

### IR Luminosity Function versus environment

So far most of the analysis of the cluster and groups LF has been limited to Spitzer 24  $\mu\text{m}$  data. According to the analysis of Bai et al. (2006, 2009), the bright end of the IR LF has a universal form for local rich clusters, and it does not differ from field IR LFs, at least in the value of their characteristic luminosities ( $L^*$ ). These results were confirmed by Finn et al. (2010), who noted that the cluster and field IR LFs have similar shape. They also measure an increase in the fraction of luminous IR galaxies with cluster-centric distance, out to 1.5 virial radii, where it is still below the field value. Recent *Herschel* observations, instead, provide evidence of a lack of IR galaxies not only at the bright end but also the faint end of the IR LF of the nearby Virgo cluster relative to the field (Davies et al. 2010).

However, the environmental dependence of the fraction of high-SFR galaxies may not be a simple function of cluster-centric distance. Using Spitzer data, Fadda et al. (2008) detected a large scale filament in the IR (at  $z \sim 0.2$ ) where the fraction of high-SFR galaxies is larger than in other regions of the supercluster. They argue that star-formation is triggered in galaxies in the infall regions around clusters. This study is followed up by Biviano et al. (2011) who show that the IR LF changes according to the supercluster environment. Indeed, the filament hosts the highest fraction of IR-emitting galaxies at all  $L_{IR}$  while LIRGs are almost absent in the core region. The IR LF of the cluster outskirts (excluding the filament region) is intermediate between those of the filament and the core. A similar result was found using *Herschel* observations which revealed other large-scale structure filaments traced by IR-emitting galaxies (Haines et al. 2010; Pereira et al. 2010).

Groups are yet another environment characterized, as in the case of filaments, by galaxy densities intermediate between cluster cores and the field. Tran et al. (2009) investigated the infrared luminosity function of a supergroup at  $z \sim 0.37$  and found an excess of 24  $\mu\text{m}$  emitting sources in the group with respect to the field and the cluster environment. Fig. 1.15 shows their IR LFs: the cluster (open squares) exhibits a deficiency of strong IR emitting sources with respect to the supergroup (solid squares). Comparing these LFs

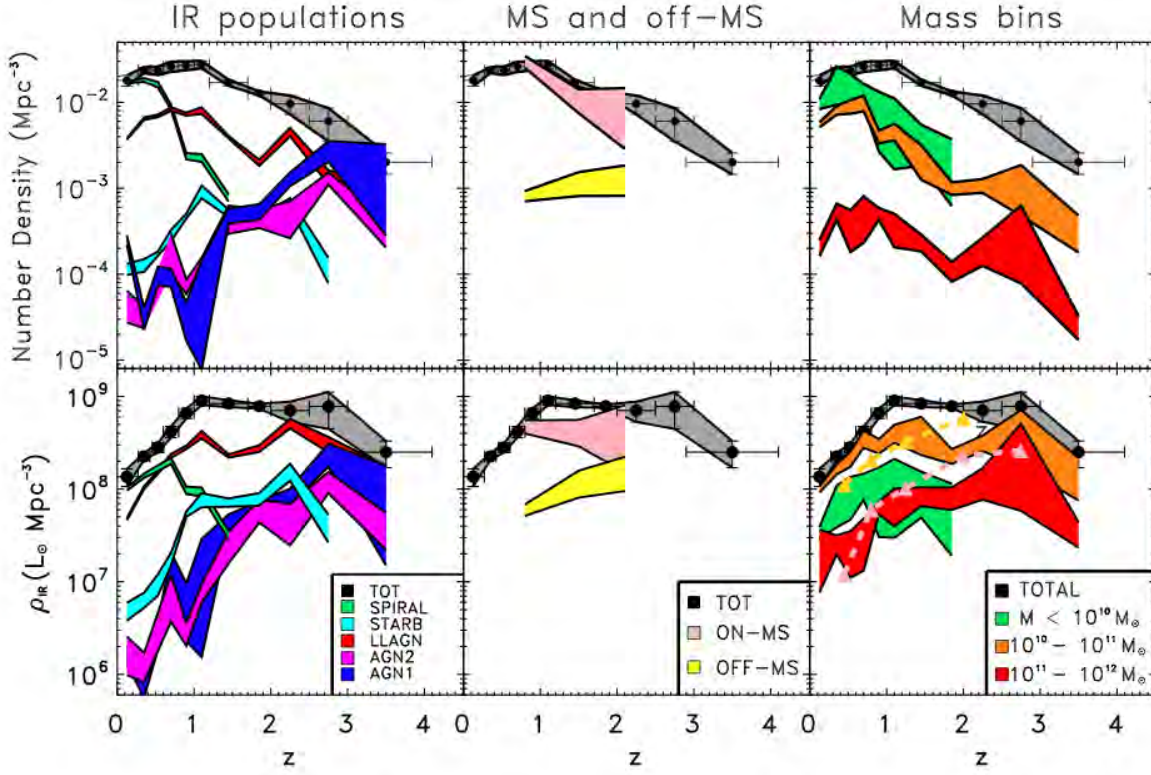


Figure 1.14: *Top*: evolution of the comoving number density of PEP sources up to redshift  $\sim 4$  (black filled circles with error-bars within  $1\sigma$  uncertainty region, represented by the gray filled area) as studied in Gruppioni et al. (2012). *Bottom*: Redshift evolution of the total IR luminosity density ( $\rho_{IR}$ ) to  $z = 4$ . The black filled circles and the gray dashed area in all the three panels represent the PEP derived  $\rho_{IR}$  and its  $1\sigma$  uncertainty region. The *left* panels show the number density (*top*) and the luminosity density (*bottom*) of the IR populations. The *middle* panels – the uncertainty regions of the relative contributions of the off- and on- SFR-mass main sequence sources. The *right* panels show the relative contribution of sources with different stellar masses.

with the field, obtained evolving the  $24\ \mu\text{m}$  LF at  $z \sim 0$  of Bai et al. (2006, dashed green curve), they find consistent results between cluster and field, but still an excess of bright ( $L_{IR} > 10^{45}\ \text{erg/s}$ )  $24\ \mu\text{m}$  sources in the supergroup. This suggests that the star formation is likely enhanced in the group environment with respect to clusters and field. On the basis of this result, Chung et al. (2010) interpreted the excess of bright IR sources in the IR LF of the Bullet cluster ( $z \sim 0.3$ ) as being due to the galaxy population in an infalling group.

Several studies take into account also the evolution of the IR luminosity function in dense regions. In fact, comparing the average IR LFs of two nearby ( $z \leq 0.06$ ) and two distant ( $z \sim 0.8$ ) clusters, Bai et al. (2009) find an evolution with redshift of both  $L^*$  and the normalization of the LF such that higher- $z$  clusters contain more and brighter IR

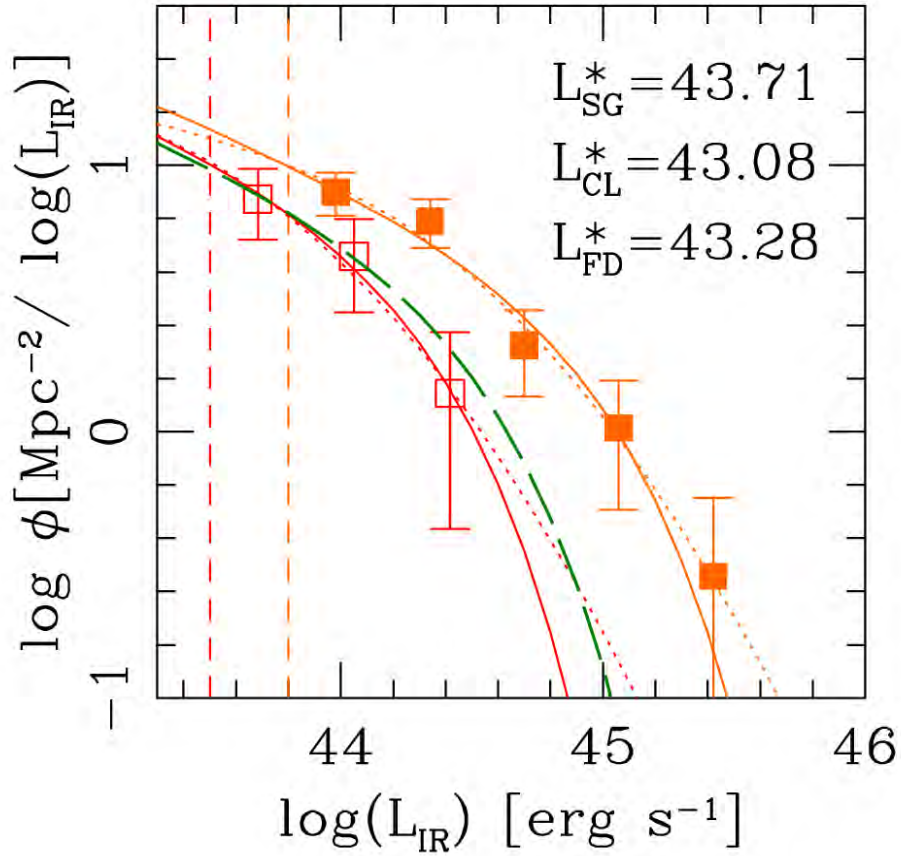


Figure 1.15: IR LF of the groups studied in Tran et al. (2009, at  $z \sim 0.37$ ). The solid squares represent the values for the supergroup (SG), while the empty squares those for the the cluster (CL) along with  $1\sigma$  error bars. The vertical dashed line correspond to 80% completeness limit of the  $24\mu\text{m}$  sources for the galaxy groups and the cluster, respectively. The IR LFs in both environments are well fitted by both Schechter (solid curve) and double-exponential (dotted curves) functions. The IR LF of the cluster galaxies is consistent with the IR LF of  $z \sim 0$  clusters evolved to  $z \sim 0.35$  (green dashed curve), but the group IR LF has an excess of bright sources.

galaxies. Biviano et al. (2011) confirm this evolutionary trend which seems to be faster at  $z \lesssim 0.4$  than the higher redshift clusters, unless the cluster at intermediate to low redshifts are a biased set of dynamically young systems, in which the presence of infalling groups biases the estimate of SFR towards higher values.

However, given the very low number of groups observed in the far infrared so far, the proper shape of the IR LF in groups, which are the most common galaxy environment in the present day universe, is still unknown. No information is yet available concerning the differences between lower density regions, such as the field, and higher density regions such as clusters. The advent of very deep surveys on the most famous blank field in the

far-infrared with *Herschel* provides for the first time the possibility to find a large number of groups up to very high redshift and, thus, to study their LF and its evolution with great detail.

## 1.5 The aim of this work

As mentioned above, much work has already been done in order to shed light on the understanding of galaxy formation and evolution and its relation to the environment. However, taking advantage of the new multi-wavelength data available and the more and more precise modeling, the picture can still be improved. Why study groups in this context? What emerges from the previous extensive introduction are the following key elements:

- the largest contribution to the the star formation rate density is provided by rather massive galaxies ( $10^{10} - 10^{11} M_{\odot}$ )
- these massive galaxies favor high density environments at least up to  $z \sim 1$  (Kauffmann et al. 2004; Scodreggio et al. 2008)
- groups are high density regions and host  $\sim 70\%$  of the present day galaxies
- the SF activity in groups could be suppressed with respect to galaxies in lower density environments

If the evolution of the SF activity is faster in group galaxies than in the field since  $z \sim 1$ , as suggested by Popesso et al. (2012), Iovino et al. (2010) and Kovač et al. (2010), then membership of a galaxy to a group could be the quenching process that causes the decline of the SFR-density since  $z \sim 1$ . Thus, we design our research strategy taking into account all these elements. Indeed the aim of this project is to analyze the evolution of the star formation activity of massive galaxies (stellar mass  $> 10^{10} M_{\odot}$ ) in groups, clusters and in the field to quantify the quenching of the SFR in star forming galaxy of groups with a link to the evolution of the galaxy type mix.

With this aim, we build a sample of X-ray selected galaxy groups at  $0 < z < 1.6$  with multi-wavelength coverage and high spectroscopic completeness. This project has three main ingredients. The first ingredient is the use of extremely deep mid-infrared *Spitzer* MIPS 24  $\mu\text{m}$  and far-infrared *Herschel* PACS data to measure with high accuracy the SFR for the bulk of the star forming population up to  $z \sim 1.6$ . The second component is the use of the X-ray emission, coming from the hot gas trapped in the group potential well, to identify bound structures with virial masses down to  $8 \times 10^{12} M_{\odot}$ . The last component is the use of multi-wavelength coverage, coupled with spectroscopic information, to define stellar masses for the whole galaxy sample and to estimate the SFR also for rather quiescent galaxies, undetected in the MIPS and PACS maps.

The thesis is structured as follows:

- we first investigate how the mean star formation and mass varies as a function of group centric-distance to check for SFR and mass segregation as observed in clusters (Balogh, Navarro, & Morris 2000);
- we then relate the mean SFR of group galaxies to intermediate and low density environment. The aim is to follow the evolution of the SFR-density relation and check whether it is reversing at high redshift as suggested by several works in the literature (Cooper et al. 2008; Elbaz et al. 2007). We study the role of different galaxy population, such as group galaxies and AGN, in shaping the SFR-density relation up to redshift  $\sim 1.6$ ;
- we also use a novel defined “dynamical” approach to isolate environments on the basis of their dynamical properties rather than galaxy local density. With this method we are able to distinguish whether quenching processes related to the galaxy membership to a massive dark matter halo are more effective than the simple galaxy-galaxy interaction (expressed by the galaxy local density);
- we analyze the two-dimensional distribution of the galaxies in groups and field in the SFR-stellar mass plane at different redshifts. The SFR-M plane allows us to study the position of the group galaxies with respect to the main sequence of star forming galaxies (e.g. Daddi et al. 2007a; Elbaz et al. 2007; Noeske et al. 2007a; Peng et al. 2010), and how this position changes with the increasing redshifts.

In order to complete this scenario, we analyze the star formation activity of two massive post-merging clusters at  $z \sim 0.3$ . This allows us to study the role of the merging activity in the quenching of SF activity, by comparing the mean SF level of the merging systems to the one of groups (the building blocks) and the relaxed clusters (final merger stage).

The outline of this thesis is described in the following: in Chapter 1 we described the state of art and introduced the topics we treat in the rest of the thesis; Chapter 2 describes the dataset and calibration for the galaxy groups of our sample; the results obtained on this sample are reported in Chapter 3; Chapter 4 outlines the analysis and results obtained on the two merging galaxy clusters; we finally summarize and discuss our results in Chapter 5.





# Dataset & Calibration: galaxy groups

## 2.1 The Surveys

This work aims at studying the evolution of the star formation activity in group and cluster galaxies and comparing it with the evolution observed in field galaxies. For this purpose, we build a dataset which combines wide area, deep photometry, and high spectroscopic coverage. This is obtained by combining galaxy catalogs from photometric and spectroscopic surveys performed on several blank fields, which are known to host a large number of X-ray selected groups. X-ray selection is necessary in order to avoid projection effects and incorrect galaxy groups identifications characteristic of optical selection techniques. On the other hand, deep and accurate multi-wavelength catalogs are necessary in order to identify the group membership and to study the properties of the group galaxy population. We identify the following blank fields with such characteristics:

- ECDFS: the Extended Chandra Deep Field South covers  $0.3 \text{ deg}^2$  (thus a medium area) allowing us to probe galaxy evolution in a wide range of environments. In addition, the deep spectroscopic coverage (Cooper et al. 2011a) allows us to study with great accuracy also high redshift groups up to  $z \sim 1$ .
- GOODS-S: the Great Observatories Origins Deep Survey-South covers a smaller area within the ECDFS. It is one of the best studied blank fields, observed very deeply in imaging and spectroscopy in many dedicated surveys. This enables us to study even higher redshift galaxy groups with respect to the ECDFS groups, such as the structure identified by Kurk et al. (2009) at  $z = 1.6$ .
- GOODS-N: the Great Observatories Origins Deep Survey-North is located in the Northern hemisphere and has similar properties to GOODS-S field (similar depth in

imaging and spectroscopy). We study two massive groups in this field in the redshift range  $0.8 < z < 1.1$

- COSMOS: the Cosmic Evolution survey covers  $2 \text{ deg}^2$ , thus it samples with higher statistics a wide range of environments. The lower spectroscopic coverage with respect to previous fields and the shallower depth of the available imaging, make this field more appropriate for the study of low redshift groups, mainly at  $z < 0.5$ .

### 2.1.1 Extended Chandra Deep Field-South

Covering  $1100 \text{ arcmin}^2$  ( $0.3 \text{ deg}^2$ ), the Extended Chandra Deep Field-South (ECDFS) survey is the Chandra survey field at the depth of 230 ks and the central region, the CDFS, is currently the deepest survey in the X-ray (4Ms). Centered on the smaller Chandra Deep Field South (CDFS,  $\alpha = 03^h32^m25^s$ ,  $\delta = 27^\circ49'58''$ ), the ECDFS has quickly become one of the most well-studied extragalactic fields in the sky with observations at a broad range of wavelengths (e.g. Giavalisco et al. 2004; Rix et al. 2004; Lehmer et al. 2005; Quadri et al. 2007; Miller et al. 2008; Padovani et al. 2009; Cardamone et al. 2010; Xue et al. 2011; Damen et al. 2011). This field has very low far-infrared backgrounds and good ALMA (Atacama Large Millimeter/submillimeter Array) visibility and hence has become one of the leading fields for infrared cosmological survey science. In particular, we highlight the Spitzer 24, 70 and  $160 \mu\text{m}$  MIPS survey of the ECDFS - FIDEL (Far-Infrared Deep Extragalactic Legacy Survey; PI: Mark Dickinson), the deep BLAST (Balloon-borne Large-Aperture Submillimeter Telescope) mapping of this region at 250, 350 and  $500 \mu\text{m}$  (PI: Mark Devlin), the more recent and deeper Herschel observations at 70 and  $160 \mu\text{m}$  with PACS (Photodetector Array Camera and Spectrometer) in the PEP (PACS Evolutionary Probe) survey (PI: D. Lutz) and at 250, 300 and  $500 \mu\text{m}$  with SPIRE (Spectral and Photometric Imaging Receiver) in the Herschel Multi-tiered Extragalactic Survey (HerMES; PI: S. Oliver), and the  $870 \mu\text{m}$  observations of the Large Apex Bolometer Camera (LABOCA)-ECDFS submm survey (PI: M. Swinbank). These are the deepest surveys at these wavelengths ever undertaken and provide sufficient sensitivity from  $24 \mu\text{m}$  to 1.4 GHz to tightly constrain the dust SEDs of thousands of galaxies and accurately measure their Star Formation (SF) activity and dust content.

In addition to the deep multi-wavelength photometric coverage, the ECDFS has been targeted by many deep spectroscopic surveys. Recently Cardamone et al. (2010) and Cooper et al. (2011a) provide a compilation of all existing high quality redshift and new IMACS (Inamori-Magellan Areal Camera & Spectrograph) spectroscopic redshifts in the ECDFS and CDFS, respectively, reaching a spectroscopic completeness down to  $\sim R = 24$  mag similar to that of smaller deep fields such as the GOODS fields (Barger, Cowie, & Wang 2008) and much higher than larger blank fields such as COSMOS (Lilly et al. 2007).

The recent extension of the CDFS survey from 2 Ms (Luo et al. 2008) to 4 Ms of exposure (Fig. 2.1, right panel, Xue et al. 2011), via a large Directors Discretionary Time project, has now provided the most sensitive 0.5-8 keV view of the distant universe. These data, complemented by the recent 3.3 Ms XMM-Newton observations in the CDFS

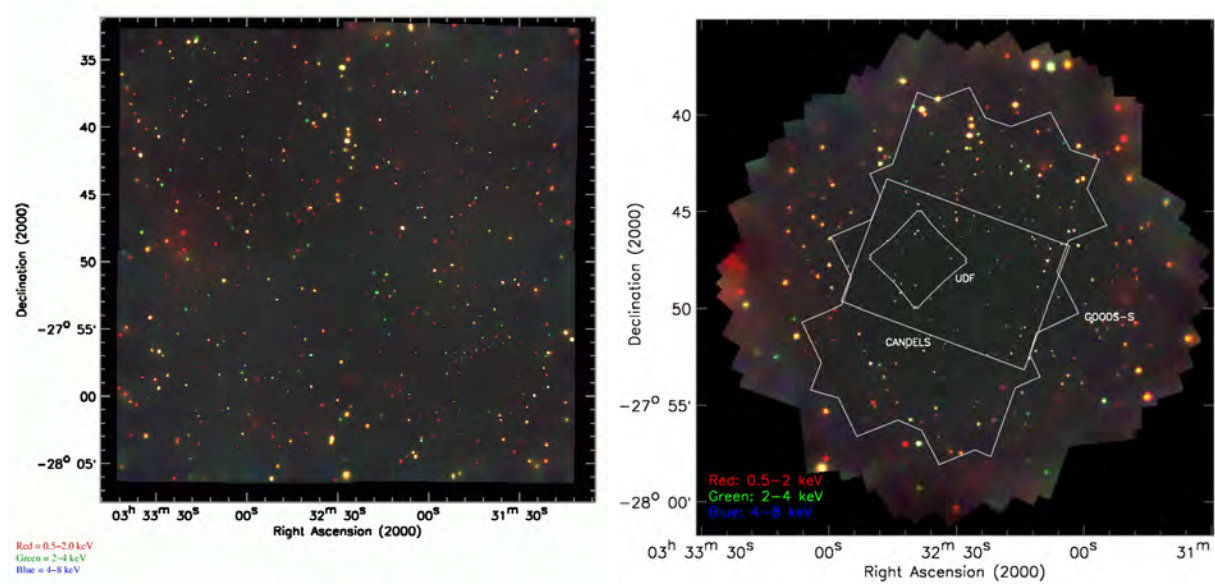


Figure 2.1: Chandra image of the Extended Chandra Deep Field South (left panel) and the smaller Chandra Deep Field South (right panel, Xue et al. 2011). The contours in the right panel show the location of other important blank fields such as the Ultra Deep Field (UDF), the Great Observatories Origins Deep Survey South field (GOODS-S) and the region covered by the CANDELS survey.

(Comastri et al. 2011), in addition to the depth of 230 ks reached in the remaining region of the ECDFS (Fig. 2.1, left panel), enable detailed studies of AGN evolution, physics, and ecology as well as the X-ray properties of normal and starburst galaxies, groups and clusters of galaxies, large-scale structures.

The combination of multi-wavelength coverage, photometric and spectroscopic depth, and areal coverage makes the ECDFS unique and probably the most important deep field for the study of the large scale structures up to very high redshift.

### The UV-IRAC photometric catalog

For the estimate of the galaxy properties derived from the SED fitting technique, we base our analysis on the ECDFS catalog released by Cardamone et al. (2010) in the MUSYC consortium. The Cardamone et al. (2010) catalog combines a total of 10 ground-based broadband images ( $U$ ,  $U38$ ,  $B$ ,  $V$ ,  $R$ ,  $I$ ,  $z$ ,  $J$ ,  $H$ ,  $K$ ), 4 IRAC images ( $3.6 \mu\text{m}$ ,  $4.5 \mu\text{m}$ ,  $5.8 \mu\text{m}$ ,  $8.0 \mu\text{m}$ ), and 18 medium-band images ( $IA427$ ,  $IA445$ ,  $IA464$ ,  $IA484$ ,  $IA505$ ,  $IA527$ ,  $IA550$ ,  $IA574$ ,  $IA598$ ,  $IA624$ ,  $IA651$ ,  $IA679$ ,  $IA709$ ,  $IA738$ ,  $IA767$ ,  $IA797$ ,  $IA856$ ). The dataset is described as follows. The  $U$   $U38$   $B$   $V$   $R$   $I$  imaging originate from the ESO archive and were combined from multiple projects using the Wide Field Imager (WFI, Baade et al. 1999) mounted on the Cassegrain focus of the ESO/MPG-2.2 m telescope at La Silla, Chile. These data were collected and calibrated as part of GaBoDS (the Garching-Bonn Deep Survey; Hildebrandt et al. 2006). The  $z$ -band data, collected as part of the MUSYC

survey, are from the Mosaic-II camera on the CTIO 4m Blanco telescope (Muller et al. 1998) and are described further by Gawiser et al. (2006b) and Taylor et al. (2009). The H-band data, taken with SofI on the ESO NTT 3.6 m telescope (Moy et al. 2003), covers 80% of the field (Taylor et al. 2009). The J and K imaging was obtained using the ISPI camera on the CTIO Blanco 4m telescope by Taylor et al. (2009). The 18-band optical medium-band photometry is taken with the Subaru telescope in the  $\sim 30' \times 30'$  ECDFS area, as part of the Multiwavelength Survey by Yale-Chile (MUSYC; Gawiser et al. 2006a). The very deep Spitzer Infrared Array Camera (IRAC) data are available as part of the Spitzer IRAC/MUSYC Public Legacy Survey (SIMPLE; Damen et al. 2011).

This catalog is publicly available and provides multi-wavelength SEDs for  $\sim 80000$  galaxies in the ECDFS down to  $R_{[AB]} \sim 27$ . For each filter in the catalog, the  $5\sigma$  depth is listed in Tables 2.1 and 2.2; for the BVR detection image, this depth is 26.8 in AB magnitudes (Cardamone et al. 2010).

The ECDFS is at high Galactic latitude and has a very low Galactic extinction. For the location of the ECDFS,  $RA = 3h32$  &  $DEC = -27^\circ48$ , Cardamone et al. (2010) calculate a value of  $E(B - V) = 0.0088$  from the  $100 \mu m$  maps of Schlegel, Finkbeiner, & Davis (1998). They calculate the expected Galactic extinction in each band, assuming  $R = 3.1$  and using the Galactic Extinction Curve of Cardelli, Clayton, & Mathis (1989) with updates in the optical region from O'Donnell (1994).

### Spectroscopic data

The study of large scale structures and the dynamical analysis of groups and clusters of galaxies require high spectroscopic coverage and quality. For this purpose we combine all high quality spectroscopic redshifts publicly available in a unique compilation. We use as a starting point the master catalog of spectroscopic redshift contained in Cardamone et al. (2010), comprising all publicly available spectroscopic redshift in the region of the ECDFS. We selected from that catalog all redshifts with high quality. More recently, other spectroscopic surveys published new spectroscopic redshifts such as Silverman et al. (2010) and the Arizona CDFS Environment Survey (ACES, Cooper et al. 2011a). Silverman et al. (2010) carried out a program to acquire high-quality optical spectra of X-ray sources detected in the ECDFS up to  $z = 4$ . They measure redshifts for 283 counterparts to Chandra sources using multi-slit facilities on both the VLT (VIMOS, using the low-resolution blue grism with a resolution  $R = 180$ ) and Keck (Deep Imaging Multi-object Spectrograph, DEIMOS; Faber et al. 2003). The Arizona CDFS Environment Survey (Cooper et al. 2011a) is a recently completed spectroscopic redshift survey of the Chandra Deep Field South conducted using IMACS on the Magellan-Baade telescope. The total number of secure redshifts in the sample is 5080 out of 7277 total, unique targets. The ACES catalog has a high number of repeated observations. These independent observations provide direct means for determining the precision of the redshift measurements for a scatter of  $\sigma z \sim 75 \text{ km s}^{-1}$  within the ACES sample when comparing repeated observations of a sizable sample of secure redshifts.

We updated the initial high quality spectroscopic redshift ( $z_{\text{spec}}$ ) compilation with the

Table 2.1: Medium Band Image Properties (Cardamone et al. 2010)

Band	FWHM ["]	$5\sigma$ depth [AB]	Zero Point [AB]
(1)	(2)	(3)	(4)
IA427	1.01	25.01	$25.10 \pm 0.11$
IA445	1.23	25.18	$25.07 \pm 0.08$
IA464	1.79	24.38	$25.30 \pm 0.03$
IA484	0.76	26.22	$25.50 \pm 0.05$
IA505	0.94	25.29	$25.34 \pm 0.02$
IA527	0.83	26.18	$25.72 \pm 0.03$
IA550	1.13	25.45	$25.88 \pm 0.06$
IA574	0.95	25.16	$25.71 \pm 0.02$
IA598	0.63	26.05	$26.02 \pm 0.03$
IA624	0.61	25.91	$25.89 \pm 0.05$
IA651	0.60	26.14	$26.15 \pm 0.03$
IA679	0.80	26.02	$26.20 \pm 0.03$
IA709	1.60	24.52	$26.02 \pm 0.03$
IA738	0.77	25.93	$26.02 \pm 0.02$
IA767	0.70	24.92	$26.04 \pm 0.02$
IA797	0.68	24.69	$26.02 \pm 0.02$
IA827	1.69	23.60	$25.92 \pm 0.04$
IA856	0.67	24.41	$25.73 \pm 0.01$

new redshifts. We clean the new compilation from redshift duplications for the same source by matching the Cardamone et al. (2010) catalog with the Cooper et al. (2011a) and the Silverman et al. (2010) catalog within  $1''$  and by keeping the most accurate  $z_{\text{spec}}$  entry (smaller error and/or higher quality flag) in case of multiple entries. Our new ECDFS  $z_{\text{spec}}$  compilation comprises 7246 unique spectroscopic redshifts.

Fig. 2.2 shows the spectroscopic completeness of the new compilation as a function of the IRAC band at  $3.6 \mu\text{m}$ . The catalog is culled of candidate stars according to the flags provided in the Cardamone et al. (2010) catalog: the SExtractor parameter (Bertin & Arnouts 1996) enables us to select the non-stellar sources (we choose  $\text{class\_star} < 0.95$ ) and the star flag indicates all the sources for which the best fitting template is the SED of a star (Cardamone et al. 2010). The spectroscopic completeness is extremely high (70%) down to  $\sim 18$  mag and it is higher than 50% up to 20 mag.

Table 2.3 lists all references from which the spectroscopic redshifts used by Cardamone et al. (2010) were obtained, including the number of spectroscopic redshifts used from the data-set, the source paper, the quality flags used and the median R-band magnitude. In order to compute accurate photometric redshifts ( $\Delta z/(1+z) \sim 0.01$ ), Cardamone et al. (2010) include the 18 medium bands and the optical and near-infrared ground based coverage in addition to the IRAC data. For the less than 1% of BVR-detected sources

Table 2.2: Other Optical and Infrared Data.

Band	FWHM ["]	$5\sigma$ depth [AB]	Zero Point [AB]	Survey
(1)	(2)	(3)	(4)	(5)
<i>BVR</i>	0.83	26.82	23.58	MUSYC
U38	0.98	25.33	21.96	GaBoDS
U	1.05	25.86	22.74	GaBoDS
B	1.01	26.45	24.38	GaBoDS
V	0.94	26.27	24.10	GaBoDS
R	0.83	26.37	24.66	GaBoDS
I	0.96	24.30	23.66	GaBoDS
z	1.07	23.69	24.47	MUSYC
J	1.48	22.44	23.53	MUSYC
H	1.49	22.46	24.15	ESO
K	0.94	21.98	24.40	MUSYC
3.6 $\mu\text{m}$	2.08	23.89	22.42	SIMPLE
4.5 $\mu\text{m}$	2.01	23.75	22.19	SIMPLE
5.8 $\mu\text{m}$	2.21	22.42	20.60	SIMPLE
8.0 $\mu\text{m}$	2.28	22.50	21.78	SIMPLE

that lie on the imaging area in fewer than 5 filters, they compute no photometric redshifts. For calibration purposes, we make use also of the Cardamone et al. (2010) photometric redshifts. Each of the redshift catalogs adopt a different selection technique for the sources for which they obtained spectra. The biggest catalogs are the one of Balestra et al. (2010, see also Popesso et al. 2009), which select galaxies at  $1.8 < z < 3.5$  for the VIMOS Low Resolution Blue grism and galaxies at  $z < 1$  in addition to Lyman Break Galaxies at  $z > 3.5$  in the Medium Resolution (MR) orange grism, and the one of Vanzella et al. (2008) which selected galaxies using color criteria and photometric redshifts at  $0.5 < z < 2$  and  $3.5 < z < 6.3$  for VLT/FORS2 observations.

### 2.1.2 The GOODS fields

The Great Observatories Origins Deep Survey (GOODS) project covers approximately 300 square arcmin divided into two fields: the Hubble Deep Field North and the Chandra Deep Field South. These are among the most data-rich portions of the sky, and are the sites of the deepest observations from Hubble, Chandra, XMM-Newton, and from many ground-based facilities. GOODS incorporates a Spitzer Legacy project designed to study galaxy formation and evolution over a wide range of redshift and cosmic lookback time. In fact, the imaging at 3.6-8  $\mu\text{m}$  with IRAC, with a mean exposure time per position of approximately 25 hours per band, reaches far deeper flux limits than any other survey, including the MUSYC survey of the ECDFS. The same fields are also observed with the

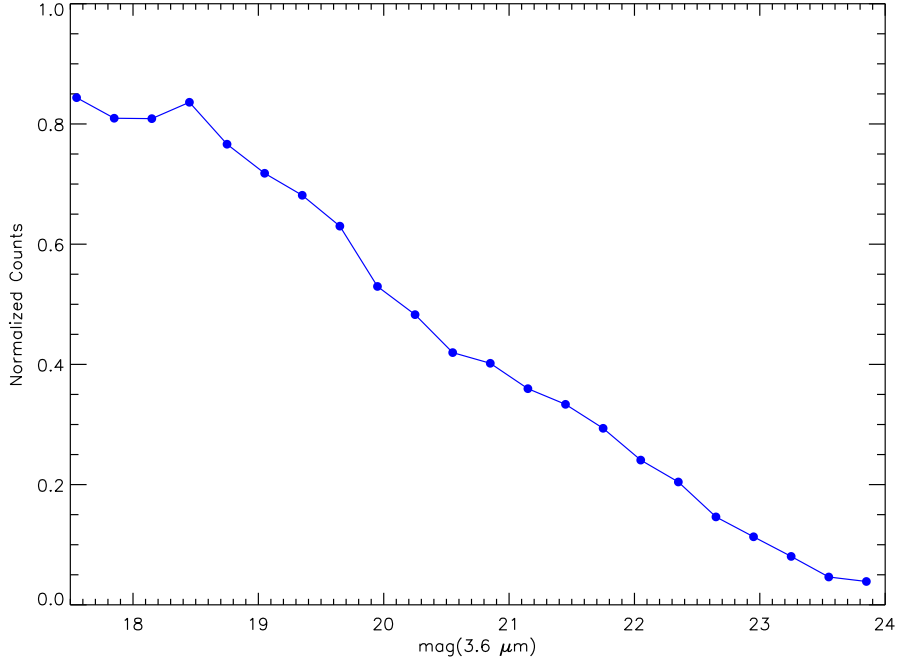


Figure 2.2: Spectroscopic completeness in ECDFS as a function of the IRAC band at  $3.6 \mu\text{m}$ . The catalog was culled of candidate stars according to the flags provided in the photometric catalog of Cardamone et al. (2010).

deepest available Spitzer MIPS maps at  $24 \mu\text{m}$ .

### A survey in a survey: GOODS-South in ECDFS

The GOODS field within the ECDFS was the target of a deep imaging campaign in the optical and near infrared with the ESO telescopes (Grazian et al. 2006). The first version of the multicolor GOODS-MUSIC sample (GOODS Multicolour Southern Infrared Catalog; Grazian et al. 2006) is extracted from the public data of the GOODS-South survey (Giavalisco et al. 2004).

A large field (20 by 20 arcmin) was covered with SOFI at shallow magnitude limits in the J, H, and Ks bands. The GOODS-CDFS is being covered by much deeper observations in the same NIR bands with the ISAAC instrument. Particularly important is the U band, which improves the photometric redshift estimate, in particular for the lowest redshift ( $z \leq 0.5$ ), when the U band still probes the blue side of the  $4000 \text{ \AA}$  break and, most important, is fundamental for identifying  $z \sim 3$  galaxies (U-dropouts). In the ESO Science Archive there are U-band images taken with the wide field imager (WFI) at La Silla (Chile),

Table 2.3: References from which the spectroscopic redshifts are obtained, including the number of spectroscopic redshifts used from the data-set, the source paper, the quality flags used and the median R-band magnitude.

# Sources	References	Quality Flags	median( $R_{AB}$ )
1239	Balestra et al. 2010	A	23
573	Vanzella et al. 2008	A,B	24
223	Le Fèvre et al. 2004	4,3	23
224	Cimatti et al. 2002	1,0	23
211	Lira et al., in prep.	3,2	22
52	Szokoly et al. 2004	3,2,1	23
9	Kriek et al. 2008	n/a	24
7	Treister et al. 2009	1	23
5	Strolger et al. 2004	n/a	25
3	Cristiani et al. 2000	n/a	24.5
3	van der Wel et al. 2004	n/a	26
2	Croom, Warren, & Glazebrook 2001	n/a	22

which are part of the EIS public survey (Arnouts et al. 2001), as well as recent images with the VLT-VIMOS imager.

The WFI images were obtained in two filters, the  $U_{35}$  and  $U_{38}$ . The  $U_{38}$  is the standard Bessel U with a peak efficiency of 50%, centered around  $\lambda_c = 3800 \text{ \AA}$ , while the  $U_{35}$  is a bit bluer,  $\lambda_c = 3500 \text{ \AA}$ , with higher efficiency ( $\sim 80\%$ ), but with a red leak at  $\lambda \geq 8000 \text{ \AA}$ , where the WFI CCD is still sensitive. The U band image of VIMOS is based on a redder filter ( $\lambda_c = 3900 \text{ \AA}$ ) and has an exposure time of 10000 seconds in total.

As already mentioned, the GOODS survey also incorporates a Spitzer Space Telescope Legacy Program to carry out the deepest observations with this facility at 3.6 to 24 microns, to study galaxy formation and evolution over a wide range of redshift and cosmic lookback time.

Table 2.4 gives detailed information for the GOODS-CDFS survey used in Grazian et al. (2006), with the wavelengths, area covered, and magnitude limits for all the filters.

A more updated version of the catalog has been released by Santini et al. (2009), who cross-correlate the catalog with available spectroscopic redshift. In addition to objects selected in the ACS  $z$  and in the ISAAC  $K_s$  bands, already present in the catalog of Grazian et al. (2006), the new catalog includes objects selected from the IRAC  $4.5 \mu\text{m}$  image, hence including sources detected at  $4.5 \mu\text{m}$  but very faint or undetected even in  $K_s$  band. Furthermore, Santini et al. (2009) remove Galactic stars and both spectroscopic or X-ray detected AGN sources. In our work we use the version of the MUSIC catalog released by Grazian et al. (2006) to keep also X-ray sources and avoid stars, which are properly flagged. The Grazian et al. (2006) catalog is then matched to our own spectroscopic master catalog of the ECDFS with the addition of GMASS redshifts (Cimatti et al. 2008)



Table 2.4: A summary of the photometric data of the GOODS-South field used in Grazian et al. (2006)

FILTER	$\lambda_c$ Å	$\Delta\lambda$ Å	EXPTIME s	FWHM <sup>a</sup> arcsec	ZP AB	AREA <i>arcmin</i> <sup>2</sup>	MAGLIM <sup>b</sup> 90%
$U_{35}$	3590	222	53654	0.90	28.520	143.2	25.5
$U_{38}$	3680	170	75100	1.10	28.755	143.2	24.5
$U_{VIMOS}$	3780	197	10000	0.80	32.500	90.2	26.5
B (F435W)	4330	508	7200	0.12	25.65288	143.2	27.5
V (F606W)	5940	1168	6000	0.12	26.49341	143.2	27.5
i (F775W)	7710	710	6000	0.12	25.64053	143.2	26.5
z (F850LP)	8860	554	12000	0.12	24.84315	143.2	26.0
$J_{ISAAC}$	12550	1499	12600 <sup>c</sup>	0.15	26.000	143.2	24.5
$H_{ISAAC}$	16560	1479	18000 <sup>c</sup>	0.15	26.000	78.0	24.3
$Ks_{ISAAC}$	21630	1383	23400 <sup>c</sup>	0.15	26.000	143.2	23.8
$CH1_{IRAC}$	35620	3797	82800	1.60	22.416	143.2	24.0
$CH2_{IRAC}$	45120	5043	82800	1.70	22.195	143.2	23.4
$CH3_{IRAC}$	56860	6846	82800	1.90	20.603	143.2	22.0
$CH4_{IRAC}$	79360	14797	82800	2.00	21.781	143.2	22.0

a) For ground-based images, *FWHM* corresponds to the seeing, while for space-based data it is the PSF of the instrument.

b) The limiting magnitudes (at 90 % completeness) are the mean values on the field, averaged on the positions and areas of every object.

c) For J, H, and Ks filters only the mean value of seeing and exposure time is reported.

to properly identify all the membership of the Kurk et al. (2009)  $z = 1.6$  structure.

## GOODS-North

The GOODS-North field centers at RA=  $12^h36^m55^s$ , Dec.=  $+62^\circ14^m15^s$  (J2000) and has become one of the most well-studied extragalactic fields in the sky with existing observations among the deepest at a broad range of wavelengths (e.g., Alexander et al. 2003; Morrison et al. 2010; Cooper et al. 2011b; Elbaz et al. 2011). GOODS-N covers an area of approximately  $10' \times 16'$  (Giavalisco et al. 2004).

We use the multi-wavelength catalog of GOODS-N built by the PEP team (Berta et al. 2010) who adopted the Grazian et al. (2006) approach for the PSF matching. The catalog includes ACS *bviz* (Giavalisco et al. 2004), Flamings *JHK*, and Spitzer IRAC data.

Moreover, MIPS  $24\ \mu\text{m}$  (Magnelli et al. 2009) and deep  $U$ ,  $Ks$  (Barger, Cowie, & Wang 2008), and spectroscopic redshifts have been added. When no spectroscopic redshifts were available, photometric redshifts (Barger, Cowie, & Wang 2008) have been derived using the EAZY code (Brammer, van Dokkum, & Coppi 2008).

We use the GOODS-North field to study two high redshift groups and the SFR-density relation. The properties of galaxies, such as SFR and stellar mass, are derived by Wuyts et al. (2011) using the dedicated software FAST (Kriek et al. 2009).

### 2.1.3 The COSMOS survey

The Cosmological Evolution survey (COSMOS) is the largest survey ever made using the Hubble Space Telescope (HST). The field is centered at RA=10h:00m:28.6s, Dec.=+02°:12':21" (J2000), where galactic extinction is low and uniform ( $<20\%$  variation; Sanders et al. 2007), but the infrared background is higher than in dark fields which are not equatorial (Scoville et al. 2007, e.g. the Lockman Hole). On the other hand, it can be observed by telescopes located both in the northern and in the southern hemisphere. In particular COSMOS has broad spectral coverage, with X-ray (Chandra & XMM-Newton), UV (GALEX), optical (SUBARU), near-infrared (CFHT), mid-infrared (Spitzer), sub-millimetric (MAMBO) and radio (VLA) imaging. Furthermore, the X-ray information provided by the 1.5 Msec observation time with XMM-Newton (53 pointings on the whole field, 50 ksec each, Hasinger et al. 2007) and the additional 1.8 Msec observations with Chandra in the central square degree (Elvis et al. 2009) enable a robust detection of galaxy groups down to  $z \sim 1.2$  (Finoguenov et al. 2007). The imaging survey is complemented by a spectroscopic program (zCOSMOS, Lilly et al. 2007) which provides 20000 spectroscopic redshifts down to  $i_{\text{AB}}=22.5$ .

The photometric and spectroscopic coverage, combined with the large area of observation, enables the study of the coupled evolution of stellar populations, AGN and dark matter throughout the cosmic time.

The COSMOS photometric catalog (Capak et al. 2007; Capak 2009) includes multi-wavelength photometric information for  $\sim 2 \times 10^6$  galaxies in the entire field. The position of the galaxies has been extracted by the deep i-band imaging obtained with Suprime-Cam mounted on the SUBARU telescope (Taniguchi et al. 2007), and the number of galaxies is in agreement with the number counts in the same band obtained in other surveys. A limit of 80% completeness is achieved at  $i_{\text{AB}}=26.5$ .

Ilbert et al. (2010) cross-match the S-COSMOS (Sanders et al. 2007)  $3.6\ \mu\text{m}$  selected catalog with the COSMOS photometric (Capak 2009) and photo- $z$  catalogs (Ilbert et al. 2009). The photo- $z$  are derived for all the sources in the COSMOS photometric catalog. The photometric fluxes are measured in 31 bands (2 bands from the Galaxy Evolution Explorer (GALEX), 6 broad bands from the SuprimeCam/Subaru camera, 2 broad bands from MEGACAM at CFHT, 14 medium and narrow bands from SuprimeCam/Subaru, J band from the WFCAM/UKIRT camera, H and K band from the WIRCAM/CFHT camera, and the 4 IRAC/Spitzer channels). The imaging data are extremely deep, reaching  $u^* \sim 27$ ,  $i = 26.2$ , and  $Ks \sim 23.5$  for a  $5\sigma$  detection in a  $3''$  aperture (the sensitivities

are listed in Capak et al. (2007) and Salvato et al. (2009). The photometric redshift are derived with an accuracy of  $\Delta z/(1+z) \sim 0.008$  at  $i < 22.5$ ,  $\Delta z/(1+z) \sim 0.011$  at  $22.5 < i < 24$ , and  $\Delta z/(1+z) \sim 0.053$  at  $24 < i < 25$ . Stellar masses, SFR and additional galaxy properties are derived through SED fitting technique by using the *Le Phare* code at  $0 < z < 2$ . In the analysis presented in the next chapter we will use the galaxy properties derived by Ilbert et al. (2010).

## 2.2 Herschel data

### 2.2.1 The deep fields

The PACS Evolutionary Probe (PEP) is one of the major Herschel Guaranteed Time (GT) extragalactic projects. It is structured as a “wedding cake” survey, based on four different layers in order to cover wide shallow areas and deep pencil-beam fields. PEP includes the most popular and widely studied extragalactic blank fields: COSMOS (2 deg<sup>2</sup>), Lockman Hole, EGS and ECDFS (450-700 arcmin<sup>2</sup>), GOODS-N and GOODS-S ( $\sim 200$  arcmin<sup>2</sup>).

The extensive multi-wavelength coverage from which ECDFS, GOODS field and COSMOS benefit, allows guided extraction based on source positions at shorter wavelengths, where the depth and resolution of the observations are higher. Furthermore this approach resolves most of the blending issues encountered in dense fields and allows straightforward multi-wavelength association (Magnelli et al. 2009, 2011). Since prior source catalogs have to contain all the sources in the PACS images, deep MIPS 24  $\mu$ m observations were used for the detection of the PACS sources. Moreover, since the 24  $\mu$ m emission is strongly correlated with the far-infrared emission, those catalogs do not contain a large excess of sources without far-infrared counterparts. This largely avoids deblending far-infrared sources into several unrealistic counterparts, as could happen when using an optical prior catalog with very high source density. The catalog was created after a PSF-fitting method using 24  $\mu$ m source positions as priors. More details on this method can be found in Magnelli et al. (2009).

### 2.2.2 The super-deep infrared survey the GOODS fields

The GOODS fields are observed by Herschel with PACS in two Surveys, the PEP survey (PI: D. Lutz) and the GOODS-Herschel Survey (GOODS-H, PI: D. Elbaz). The GOODS Herschel survey covers a smaller central portion of the entire GOODS-S and GOODS-N regions. Recently the PEP and the GOODS-H teams combined the two sets of PACS observations to obtain the deepest ever available PACS map (Magnelli et al. in preparation) of both fields. Fig. 2.3 shows the image of the part of the PEP ECDFS plus the PEP GOODS-S and GOODS-H observations (left panel) and the coverage of this image (right panel). The central squared region with super-deep coverage is given by the GOODS-H data, while at slightly lower coverage the larger region covered by the PEP survey becomes visible. The much more extended region of the ECDFS shows a PACS coverage lower by

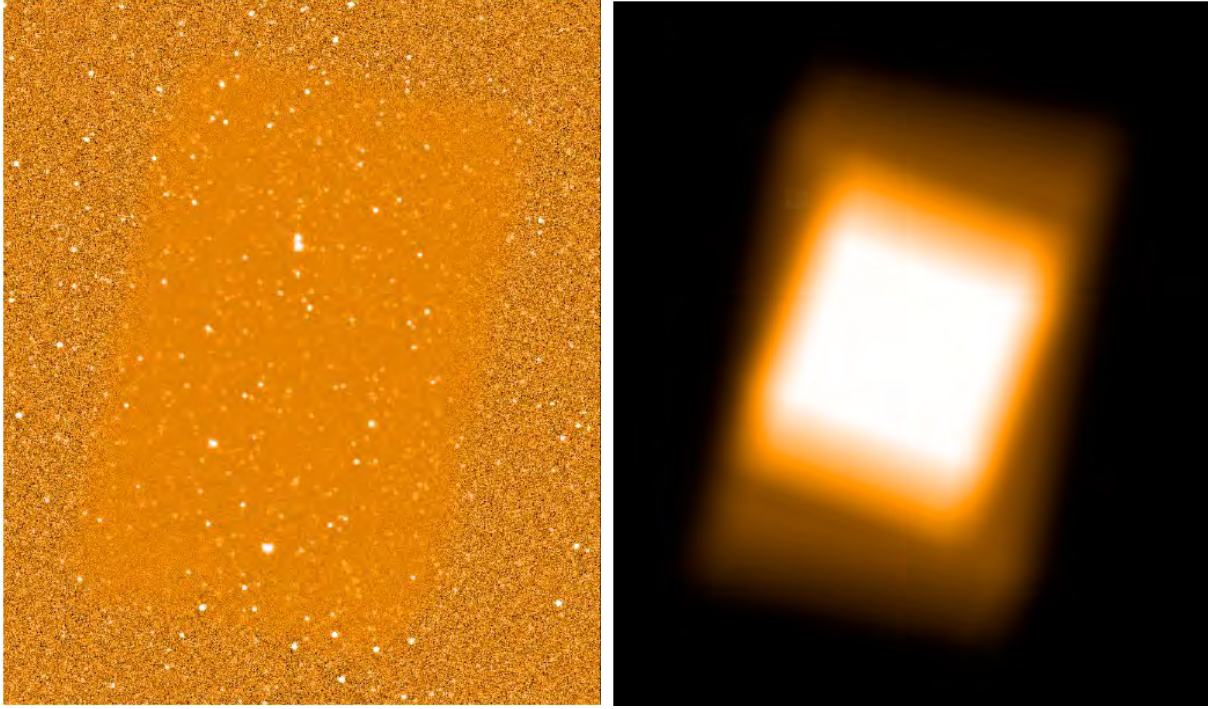


Figure 2.3: Left panel: image of the part of the PEP ECDFS plus the PEP GOODS-S and GOODS-H observations and the coverage of this image (right panel). The central squared region with super-deep coverage is given by the GOODS-H data.

several factors with respect to the center of the map.

In order to take advantage of the much higher depth of the GOODS-S field in both the PACS and the MIPS observations with respect to the larger but shallower observations of the ECDFS, we create a catalog of MIPS/PACS sources by using the PEP+GOODS-H catalog in the GOODS-S region and the PEP ECDFS catalog in the remaining ECDFS area. Before doing that we compare the fluxes at MIPS 24  $\mu\text{m}$  and PACS 100 and 160  $\mu\text{m}$  in the common GOODS-S and ECDFS area to check for consistency (Fig. 2.4). The catalog in the GOODS-S (ECDFS) field extends down to  $\sim 20 \mu\text{Jy}$  ( $\sim 50 \mu\text{Jy}$ ) at 24  $\mu\text{m}$  (Magnelli et al. 2009), to 1.2 mJy (3.9 mJy) at 100  $\mu\text{m}$  and 2.4 mJy (7.5 mJy) at 160  $\mu\text{m}$  (Berta et al. 2011; Lutz et al. 2011, Magnelli et al. in prep). We corrected the 24  $\mu\text{m}$  fluxes of ECDFS for each bin with respect to GOODS-S. This choice was driven by the fact that GOODS-S is deeper than ECDFS and that number counts of the 24  $\mu\text{m}$  flux in the ECDFS field lie below those of GOODS-S. The catalog in the GOODS-N region extends down to  $\sim 20 \mu\text{Jy}$  at 24  $\mu\text{m}$  (Magnelli et al. 2009), to 2 mJy at 100  $\mu\text{m}$  and 3 mJy at 160  $\mu\text{m}$  (Magnelli et al. in prep.).

Table 2.5 shows the main properties of the PEP fields used in this work taken from Berta et al. (2011). The first column shows the name of the blank field, the second column the PACS band in which the field is observed, the third column the effective area covered, and the fourth column the  $3\sigma$  limit in mJy.

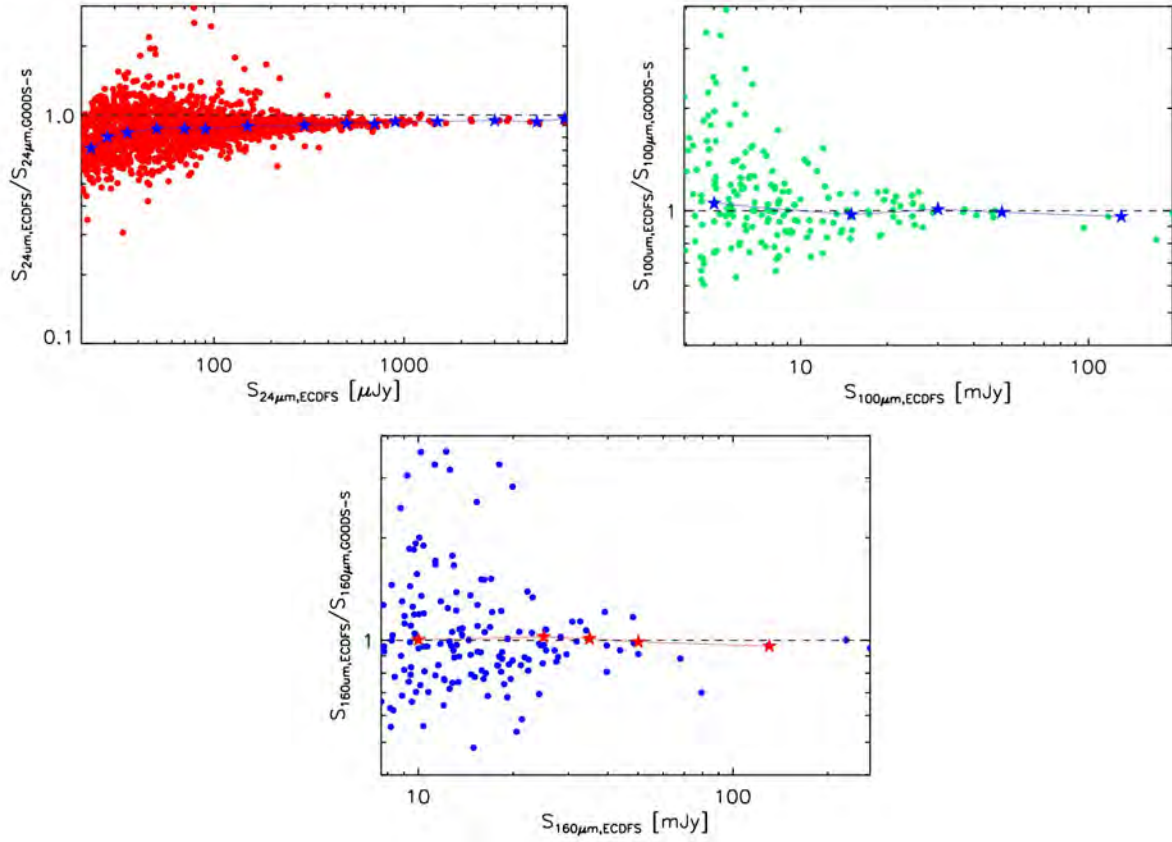


Figure 2.4: Comparison between the flux at  $24\mu\text{m}$ ,  $100\mu\text{m}$ ,  $160\mu\text{m}$  in the common area of the ECDFS and GOODS-S. The dashed line represents the value at which the fluxes of ECDFS and GOODS-S are the same, while the stars connected by a solid line represent the median of the ratio between the fluxes in the two surveys for each flux bin. The catalog in the GOODS-S (ECDFS) field extends down to  $\sim 20 \mu\text{Jy}$  ( $\sim 20 \mu\text{Jy}$ ) at  $24 \mu\text{m}$  (Magnelli et al. 2009), to  $1.2 \text{ mJy}$  ( $3.9 \text{ mJy}$ ) at  $100 \mu\text{m}$  and  $2.4 \text{ mJy}$  ( $7.5 \text{ mJy}$ ) at  $160 \mu\text{m}$  (Berta et al. 2011; Lutz et al. 2011; Magnelli et al. in prep.).

## 2.3 Computation and calibration

The aim of our analysis is to understand the impact of the environment on the evolution of the galaxy SF activity. In order to do that we need to estimate the SFR for a statistical sample of galaxies and down to a very low limit in SFR in order to consider also the passive galaxies ( $\text{SFR} \sim 0$ ). Due to the flux limit of the MIPS and PACS observation, the mid- and far-infrared data allow us to probe only the region of the normally and highly star forming galaxies that would lie on or off the SFR-Mass main sequence. To cover also the region below the main sequence in the SFR-Mass diagram we use also the information provided by the rest-frame UV emission and the SED fitting technique. Indeed, the observed rest-frame UV emission corrected for the dust attenuation and the SED fitting technique can provide

Field	Band	Eff. Area	$3\sigma$ mJy
GOODS-N	100 $\mu\text{m}$	300 arcmin <sup>2</sup>	3.0
GOODS-N	160 $\mu\text{m}$	300 arcmin <sup>2</sup>	5.7
GOODS-S	70 $\mu\text{m}$	300 arcmin <sup>2</sup>	1.1
GOODS-S	100 $\mu\text{m}$	300 arcmin <sup>2</sup>	1.2
GOODS-S	160 $\mu\text{m}$	300 arcmin <sup>2</sup>	2.4
ECDFS	100 $\mu\text{m}$	0.3 deg <sup>2</sup>	3.9
ECDFS	160 $\mu\text{m}$	0.3 deg <sup>2</sup>	7.5
COSMOS	100 $\mu\text{m}$	2.04 deg <sup>2</sup>	5.0
COSMOS	160 $\mu\text{m}$	2.04 deg <sup>2</sup>	10.2

Table 2.5: Main properties of the PEP fields included in the number counts and CIB analysis of Berta et al. (2011).

a reliable estimate of the SFR in absence of mid or far-infrared data. We use the SED fitting technique also to estimate the galaxy stellar masses. In this section we describe how we use different SFR indicators to derive the galaxy SFR and how we calibrate them to check the reliability of our SFR estimate.

### 2.3.1 Computation of IR luminosities

We compute the IR luminosities integrating the SED templates from Elbaz et al. (2011) (section 1.4.2) in the range 8-1000  $\mu\text{m}$ . The PACS (100 and 160  $\mu\text{m}$ ) fluxes, when available, together with the 24  $\mu\text{m}$  fluxes are used to find the best fit templates among the MS and SB Elbaz et al. (2011) templates. When only the 24  $\mu\text{m}$  flux is available for undetected PACS sources, we rely only on this single point and we use the MS template for extrapolating the  $L_{IR}$ . Indeed, the MS template turns out to be the best fit template in the majority of the cases (80%) with common PACS and 24  $\mu\text{m}$  detection. In principle, the use of the MS template could cause only an underestimation of the extrapolated  $L_{IR}$  from 24  $\mu\text{m}$  fluxes, in particular at high redshift or for off-sequence sources due to the higher PAHs emission of the MS template. However, the comparison between the  $L_{IR}$  estimated with the best fit templates based on PACS and 24  $\mu\text{m}$  data versus the  $L_{IR}$  extrapolated from 24  $\mu\text{m}$  flux only with the MS template, shows a very good agreement between the two estimates with a slightly underestimation (10%) only above  $z \sim 1.7$  or  $L_{IR}^{24} > 10^{11.7} L_{\odot}$ . Fig. 2.5 shows such a comparison for the GOODS fields where we have the deepest PACS coverage. In larger fields such as COSMOS and ECDFS there is a larger probability to find rare strong star forming off-sequence galaxies at  $L_{IR}^{24} > 10^{11.7} L_{\odot}$  even at low redshift. However, given the larger area of these blank fields, those sources should be captured by the Herschel observations given the very high luminosity threshold. Thus, it would not be a problem in getting a proper estimate of the  $L_{IR}$  from the best fit templates also for these rare cases.

As our final goal is to compare our results to those of Popesso et al. (2012), which are

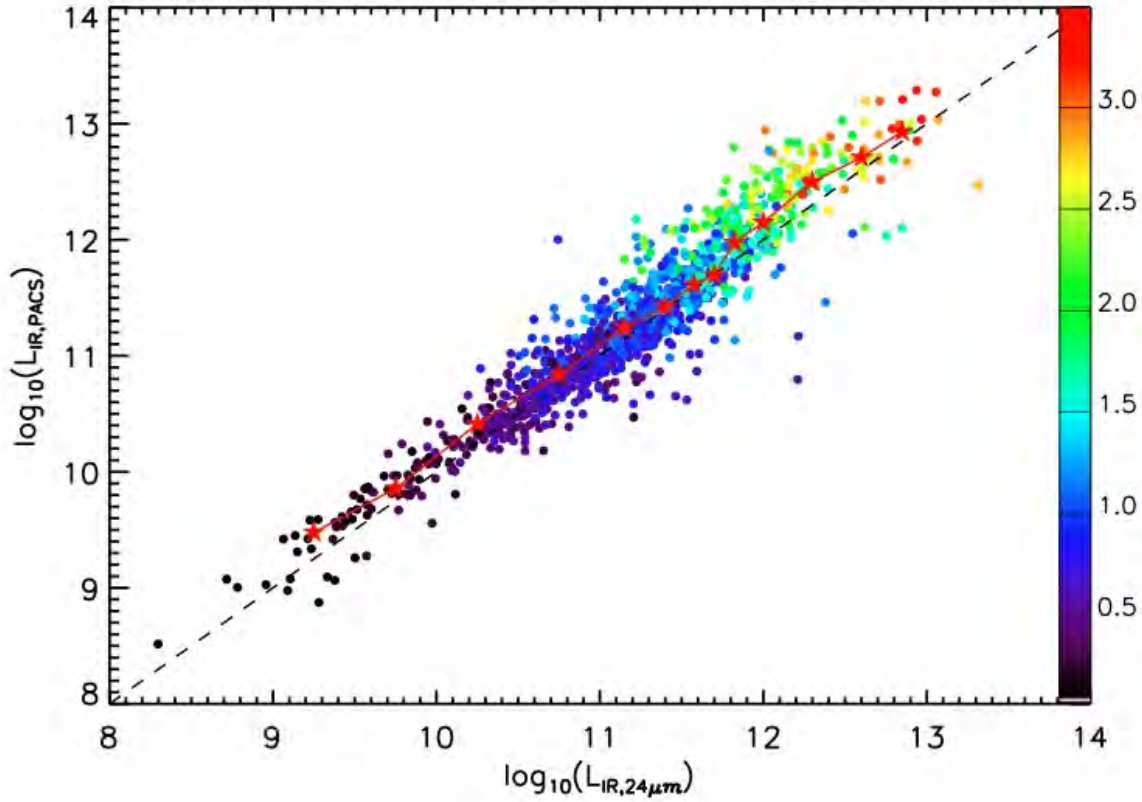


Figure 2.5: Comparison between the extrapolation of  $L_{\text{IR}}^{\text{tot}}$  from PACS (100 and 160  $\mu\text{m}$ ) versus the one from 24  $\mu\text{m}$  for the GOODS-North and -South fields as a function of redshift (color bar). The dashed line represents a one to one relation while the red stars represent the median infrared luminosity based on Herschel plus 24  $\mu\text{m}$  fluxes for each bin of  $L_{\text{IR}}^{24}$ . The luminosities are expressed in solar units.

based on the analysis of Rodighiero et al. (2010), we compare our results to those computed in the same way of Rodighiero et al. (2010) for GOODS-S (Fig. 2.6). The agreement between the luminosities computed with two different set of templates and independent methods enables us to confirm the robustness of our computation.

In the further analysis we will use the Kennicutt (1998a) relation to convert the bolometric infrared luminosity,  $L_{\text{IR}}$  into star formation rate:

$$\text{SFR} (M_{\odot} \text{ yr}^{-1}) = 4.5 \times 10^{-44} L_{\text{FIR}} (\text{ergs s}^{-1}). \quad (2.1)$$

This formula assumes a (Salpeter 1955) Initial Mass Function (IMF). We apply an offset of -0.18 dex to convert the obtained SFR in the Chabrier IMF (Chabrier 2003) which is used in our SED fitting technique for deriving the SFR of galaxies undetected in PACS or Spitzer 24  $\mu\text{m}$ .



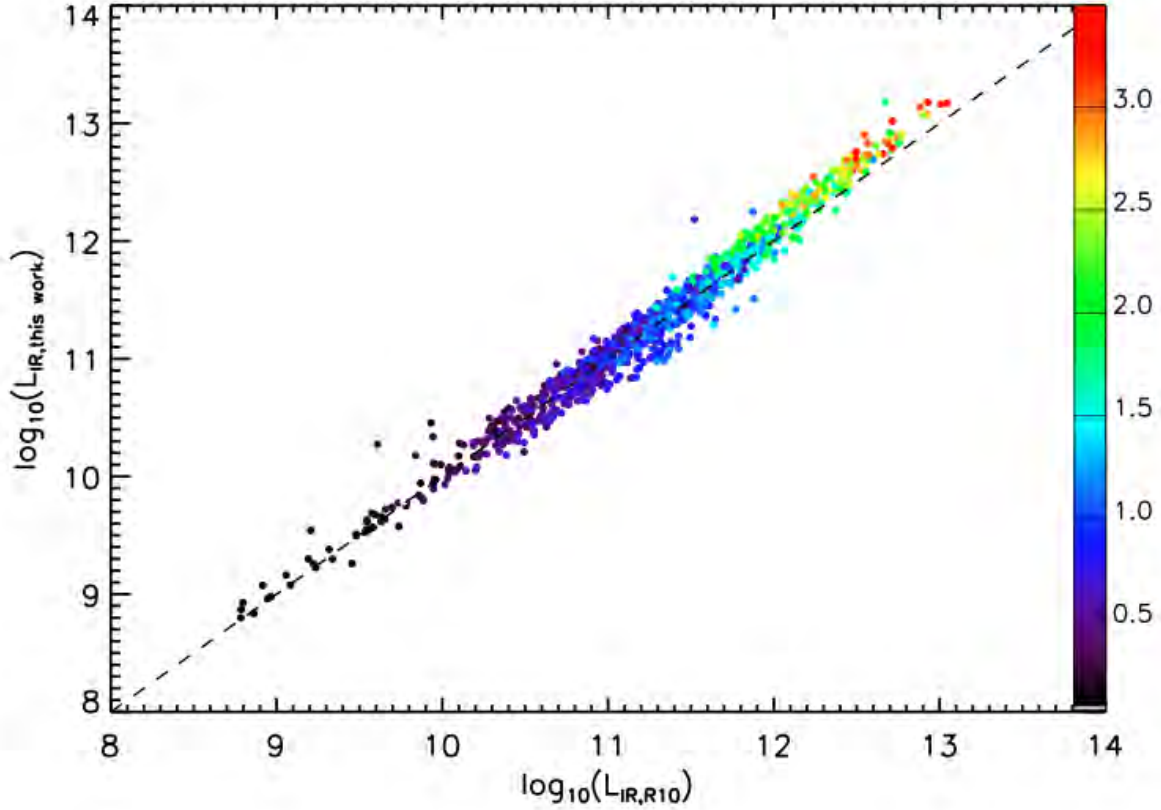


Figure 2.6: Comparison between the  $L_{\text{IR}}^{\text{tot}}$  computed in this work versus those obtained with the same method of Rodighiero et al. (2010) for the GOODS fields as a function of redshift (color bar).  $L_{\text{IR}}^{\text{PACS}}$  is computed using the best fitting template between MS and SB, while for  $L_{\text{IR}}^{24}$  we used the MS template. The luminosities are expressed in solar units.

### 2.3.2 Le PHARE and computation of SFR and Masses

*Le PHARE* (PHotometric Analysis for Redshift Estimations; Arnouts et al. 2001; Ilbert et al. 2006) is a publicly available<sup>1</sup> software based on the  $\chi^2$  template-fitting procedure. The merit function  $\chi^2$  is defined as

$$\chi^2(z, T, A) = \sum_{f=1}^{N_f} \left( \frac{F_{\text{obs}}^f - A \times F_{\text{pred}}^f(z, T)}{\sigma_{\text{obs}}^f} \right)^2, \quad (2.2)$$

where  $F_{\text{pred}}^f(T, z)$  is the flux predicted for a template  $T$  at redshift  $z$ .  $F_{\text{obs}}^f$  is the observed flux and  $\sigma_{\text{obs}}^f$  the associated error. The index  $f$  refers to the considered filter and  $N_f$  is the

<sup>1</sup>[http://www.cfht.hawaii.edu/~arnouts/LEPHARE/cfht\\_lephare/lephare.html](http://www.cfht.hawaii.edu/~arnouts/LEPHARE/cfht_lephare/lephare.html)



number of filter. *Le PHARE* estimates the photometric redshifts from the minimization of  $\chi^2$  varying the three free parameters  $z$ ,  $T$  and the normalization factor  $A$ .

Even if *Le PHARE* is usually used to compute the photometric redshifts, it is also very useful to estimate other quantities once the redshifts are known. In fact, this software can derive luminosities, star formation rates and masses given a set of SED templates.

First we need to adjust the zero-points using a spectroscopic subsample, as explained in Ilbert et al. (2006). We select a control sample with  $\sim 7000$  secure spectroscopic redshifts. Using a  $\chi^2$  minimization (Equation 2.2) at fixed redshift, we determine for each galaxy the corresponding best-fitting COSMOS templates (included in the package, see Ilbert et al. 2006). Dust extinction is applied to the templates using the Calzetti et al. (2000) law (with  $E(B - V)$  in the range 0 - 0.5 and with a step of 0.1).

For each filter  $f$ , if  $F_{obs}^f$  is the observed flux in the filter  $f$  and  $F_{pred}^f$  is the predicted flux derived from the best-fit template, the sum

$$\psi^2 = \sum_{i' \leq 21.5}^{N_{gal}} \left( (F_{pred}^f - F_{obs}^f + s^f) / \sigma_{obs}^f \right)^2$$

must be minimized leaving  $s^f$ , the estimated correction applied to the apparent magnitudes in a given filter  $f$ , as a free parameter. For normal uncertainties in the flux measurement, the average deviation  $s^f$  should be 0. Instead, Ilbert et al. (2006) notice some systematic differences. It is possible to correct the predicted apparent magnitudes from these systematic differences. Repeating a second time the procedure of template-fitting after having adjusted the zero-points, the best-fit templates may change. The offsets used to correct the apparent magnitudes are obtained after the process converges.

We apply the systematic offsets to our catalog (ECDFS and GOODS-MUSIC) and we compute the star formation rate and stellar masses using *Le PHARE*, following the recipe of Ilbert et al. (2010). The SED templates for the computation of mass and SFR are generated with the stellar population synthesis package developed by Bruzual & Charlot (2003, BC03). We assume a universal IMF from Chabrier (2003) and an exponentially declining star formation history  $SFR \propto e^{-t/\tau}$  ( $\tau$  in the range 0.1 Gyr to 30 Gyr). The SEDs are generated for a grid of 51 ages (in the range 0.1 Gyr to 14.5 Gyr). Dust extinction is applied to the templates using the Calzetti et al. (2000) law (with  $E(B - V)$  in the range 0 - 0.5 and with a step of 0.1). We apply a set of emission lines to the BC03 templates since they become more realistic (see Ilbert et al. 2010, for details).

In the whole ECDFS area we are able to compare our derived masses with those computed by Wuyts et al. (in prep., private communication). Wuyts et al. (in prep.) compute the ECDFS masses using FAST (Kriek et al. 2009), a software which searches for the best fit among different templates (and a multi-dimensional grid with different ages, extinctions,  $\tau$ ). They use the BC03 library assuming an IMF from Chabrier (2003) and the same declining star formation history we use, with a dust extinction from the Calzetti et al. (2000) law. They apply no set of emission lines to the templates. For further details see Wuyts et al. (2011).

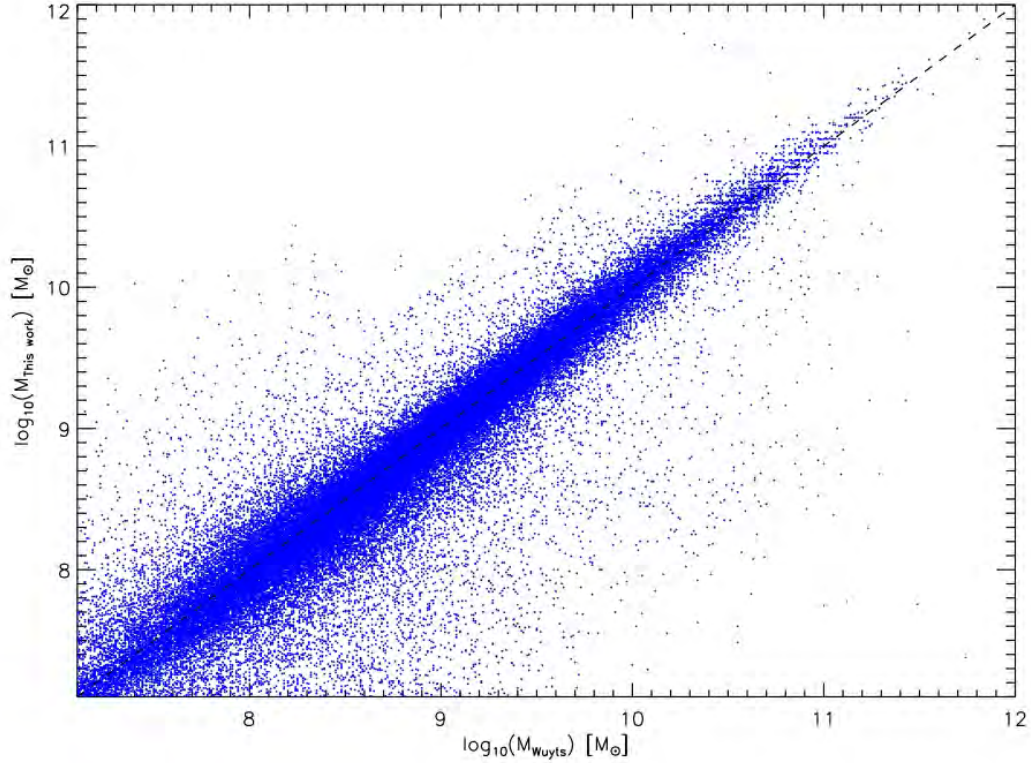


Figure 2.7: Comparison of the masses computed with our method versus those obtained by Wuyts (in prep., private communication). The values are well correlated (within a scatter of 0.34 dex) as the relation one to one shows (represented by the dashed line).

In order to compare the two results, we compute an additional set of masses and SFR using the method described above but without adding the emission lines to the BC03 templates. We find a very good agreement in the comparison of the masses we computed using *Le PHARE* with those computed by Wuyts et al (in prep.) using FAST, as we show in Fig. 2.7. In fact, the fraction of outliers above  $3\sigma$  is 2% and above  $5\sigma$  is 0.5%. We measure a spread of  $\log M = 0.34$ .

For the GOODS-S sample we use the MUSIC catalog (Santini et al. 2009) to compare the masses computed using *Le PHARE* with those of Santini et al. (2009). The authors use BC03 library assuming a Salpeter (1955) IMF. They parameterize the star formation histories with a variety of exponentially declining laws (of timescales  $\tau$  ranging from 0.1 to 15 Gyr), metallicities and dust extinctions ( $0 < E(B - V) < 1.1$ , with a Calzetti et al. (2000) or Small Magellanic extinction curve). In our computation we use the same recipe

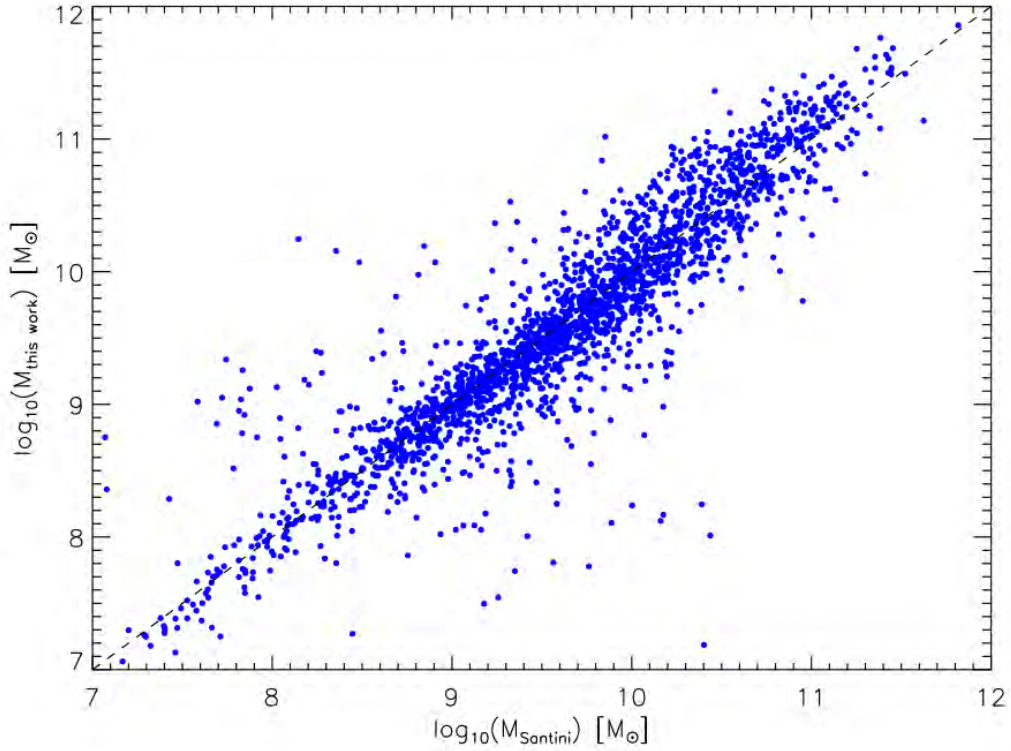


Figure 2.8: Comparison of the masses computed with our method versus those of Santini et al. (2009), rescaled to a Chabrier (2003) IMF. The values are well correlated within a scatter of 0.34 dex. The dashed line represents the relation one to one.

adopted for the ECDFS sample, thus we convert the masses of Santini et al. (2009) in a Chabrier (2003) IMF by applying an offset of -0.23 dex. Our results are in good agreement also with those of Santini et al. (2009) as we show in Fig. 2.8. We measure a spread of 0.34 dex and a fraction of outliers above  $3\sigma$  ( $5\sigma$ ) of 2% (0.4%). Thus, we consider our stellar mass estimates reliable within a factor of 2.

An additional output of *Le PHARE* is the estimate of the SFR based on the star formation history of the best fitting template. As for the masses, the SFR values are affected by the discretization of the templates. We compare our SFR estimates to those computed by Wuyts et al. (in prep., see also Wuyts et al. 2011). Fig. 2.9 shows a rather good agreement between the two quantities, which are consistent with the one to one relation. However, we notice a much higher scatter of  $\log \text{SFR} = 0.61$  with respect to the one observed for the masses, while the fraction of outliers above  $3\sigma$  and above  $5\sigma$  remains

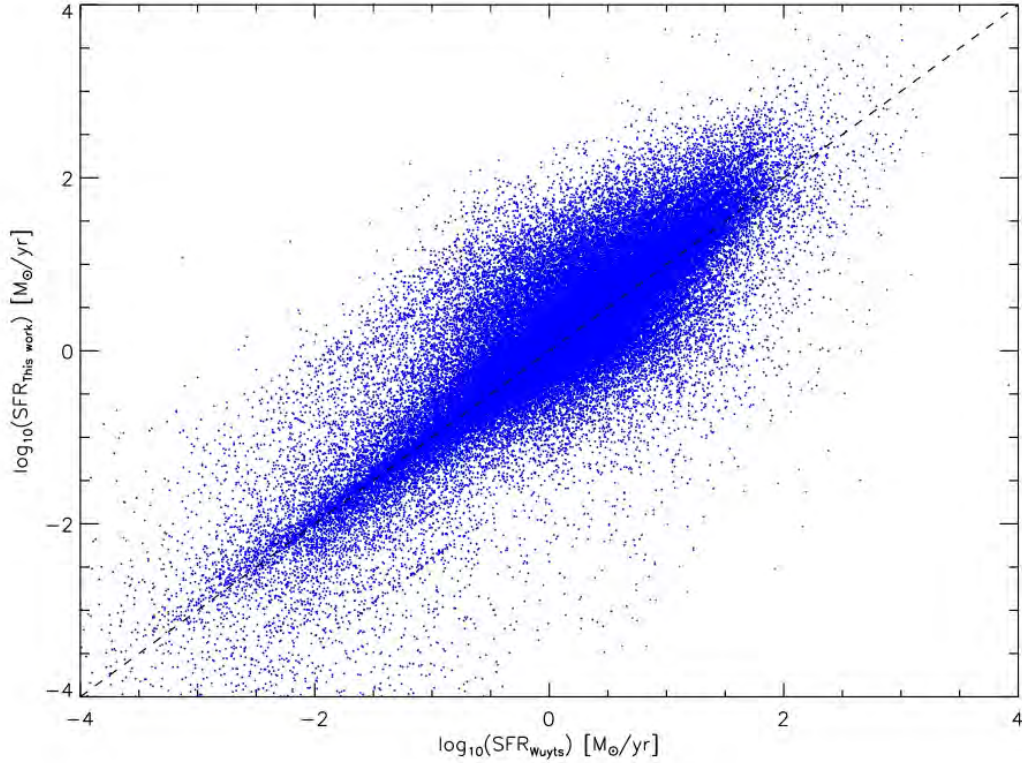


Figure 2.9: Comparison of the star formation rates computed using *Le PHARE* versus those obtained by Wuyts (in prep., private communication). The values are well correlated within a scatter of 0.61 dex. The dashed line represents the one to one relation.

unchanged. Previous studies (Papovich, Dickinson, & Ferguson 2001; Santini et al. 2009; Shapley et al. 2001, 2005) demonstrate that, while stellar masses are well determined, the SED fitting procedure does not strongly constrain star formation histories at high redshifts, where the uncertainties become larger due to the SFR-age-metallicity degeneracies. We limit the use of the SFR derived via SED fitting templates to the sources undetected in PACS and Spitzer 24  $\mu\text{m}$ , thus, only to the low star forming galaxies in most of the considered redshift bins.

Throughout our analysis we use our estimates of masses and SFR for ECDFS and GOODS-South. We use the values computed by Wuyts et al. (2011) for GOODS-North and those of Ilbert et al. (2010) for COSMOS, where there is either a very good agreement (the former case) or either we use the same code and recipe (the latter case).



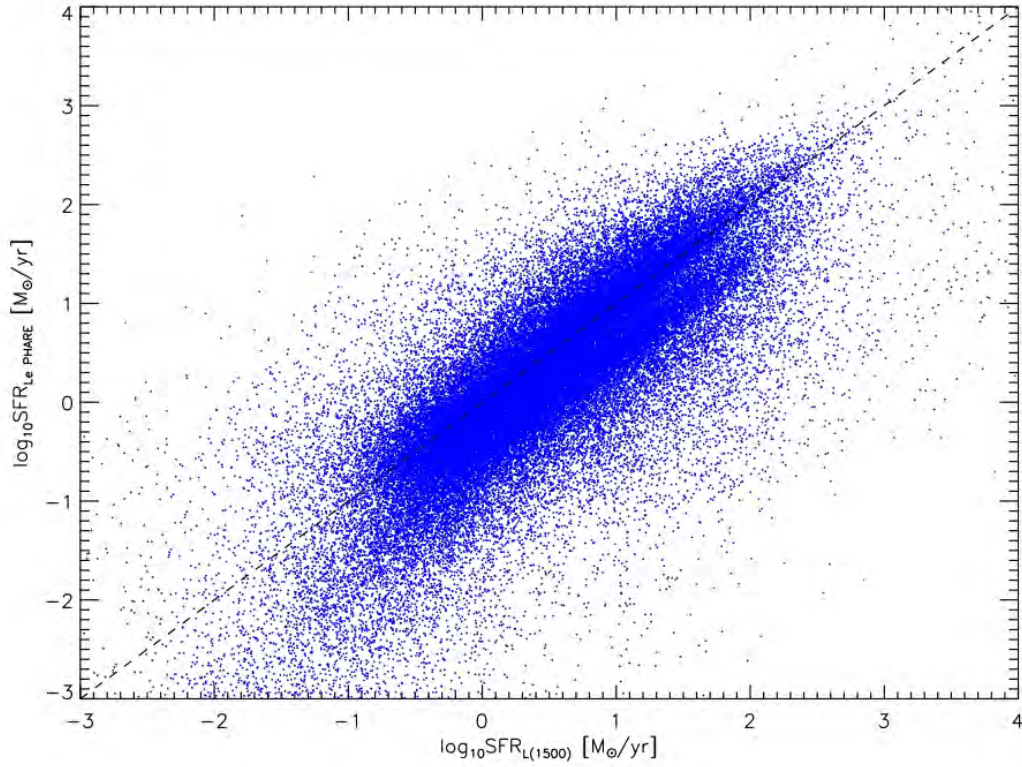


Figure 2.10: Comparison between the SFR obtained using Le PHARE versus the one derived by the luminosity at 1500 Å as in Daddi et al. (2004) for the ECDFS and GOODS-S. The values are in agreement within a scatter of 0.73 dex.

### 2.3.3 Computation of SFR from UV luminosity

As a further check we compute also the SFR using the luminosity at 1500 Å rest frame for the ECDFS and GOODS-S catalogs. The aim of this check is to test whether the UV-based SFR is more robust of the SFR extrapolated from the SED technique.

We follow the recipe of Daddi et al. (2004): they compute the SFR from the luminosity at 1500 Å applying the Calzetti et al. (2000) extinction law. However, while they derive  $E(B - V)$  applying a relation which depends on the colors of galaxies, we use the output derived from *Le PHARE* best fit template. According to the Calzetti et al. (2000) attenuation law, the value of the extinction curve at 1500 Å rest frame is  $\sim 10$ . Thus, as done in Daddi et al. (2004), we use an attenuation of  $A_{1500} = 10[E(B - V)]$  mag to obtain a reddening-corrected luminosity at 1500 Å. We finally derive the SFR applying the equation

5 of Daddi et al. (2004), i.e.:

$$\text{SFR}(\text{M}_{\odot} \text{ yr}^{-1}) = \frac{L_{1500}(\text{erg s}^{-1} \text{ Hz}^{-1})}{8.85 \times 10^{27}}. \quad (2.3)$$

This equation assumes a Salpeter IMF, therefore we apply an offset of -0.18 to convert the SFR in Chabrier IMF. We compare the SFR derived from  $L_{1500}$  with the values obtained as output of Le PHARE. The values are in agreement within a scatter of 0.73 dex, as we show in Fig. 2.10.

### 2.3.4 Calibration $\text{SFR}_{\text{SED}}$ and $\text{SFR}_{\text{UV}}$ vs $\text{SFR}_{\text{IR}}$

In order to check to what extent our estimates of the SFR based either on SED fitting technique ( $\text{SFR}_{\text{SED}}$ ) or rest-frame UV observations ( $\text{SFR}_{\text{UV}}$ ) are reliable, we calibrate these estimates versus the more robust SFR based on IR emission. Our calibration is done in 3 different redshift bins:  $0 < z \leq 0.5$ ,  $0.5 < z \leq 1$ , and  $1 < z \leq 1.6$ . Fig. 2.11 and Fig. 2.12 show the result of this comparison for the  $\text{SFR}_{\text{SED}}$  and the  $\text{SFR}_{\text{UV}}$ , respectively. We observe a consistency of the estimates, given the agreement with the one to one relation. However, we note a large amount of scatter, consistent with the one already observed in the direct comparison between  $\text{SFR}_{\text{SED}}$  and  $\text{SFR}_{\text{UV}}$  in Fig. 2.10. Indeed, we measured a scatter of 0.73 dex (0.76 dex) for the whole range of redshifts, 0.74 dex (0.99 dex) for  $0 < z \leq 0.5$ , 0.63 dex (0.79 dex) for  $0.5 < z \leq 1$ , and 0.68 dex (0.73 dex) for  $1 < z \leq 1.6$  for the  $\text{SFR}_{\text{SED}} - \text{SFR}_{\text{IR}}$  ( $\text{SFR}_{\text{UV}} - \text{SFR}_{\text{IR}}$ ) relation. The situation improves when only the spectroscopic sample is considered, probably because of the less degeneracy of the best fit templates between  $z_{\text{phot}}$  and the galaxy properties. Indeed, in this case the scatter is  $\sim 30\%$  lower in both relations and in all redshift bins. The high scatter is also due to a strong selection bias due to the flux (thus, luminosity) limit of the PACS and 24  $\mu\text{m}$  galaxy sample. This is clearly visible as a long tail towards low SFR in the distribution of residuals (see Fig. 2.13) of the two relations in any redshift bin.

We can conclude that the scatter of the  $\text{SFR}_{\text{UV}} - \text{SFR}_{\text{IR}}$  relation is always bigger (at every redshift) with respect to the  $\text{SFR}_{\text{SED}} - \text{SFR}_{\text{IR}}$  calibration. Thus, in the analysis presented in the next chapter we will use the  $\text{SFR}_{\text{SED}}$  as rough estimate of the SFR activity for PACS and Spitzer 24  $\mu\text{m}$  undetected sources.

## 2.4 Galaxy Group sample

### 2.4.1 X-ray analysis and group sample selection

As explained in details in Section 2.1, all the blank fields considered in our analysis are observed extensively in the X-ray with *Chandra* and *XMM-Newton*. Taking advantage of the better spatial resolution of *Chandra*, we use the point source catalogs derived from the Chandra maps of each field to remove point sources in the *XMM-Newton* image at lower spatial resolution. This is done by convolving the *Chandra* PSF with the

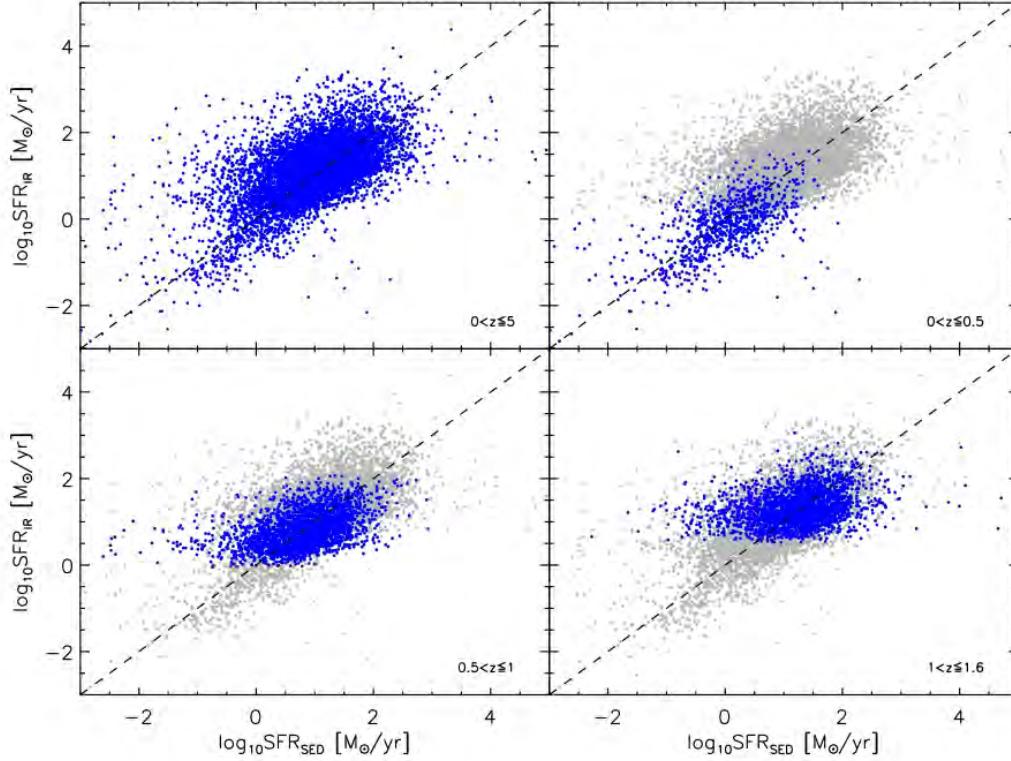


Figure 2.11: Comparison between  $SFR_{IR}$  and  $SFR_{SED}$  for the ECDFS and GOODS-S. The upper left panel shows all the sources with IR detection in the field. The same distribution is represented as gray dots in the following panels, where we show all the sources for different redshift bin with blue dots :  $0 < z \leq 0.5$ ,  $0.5 < z \leq 1$ , and  $1 < z \leq 1.6$ , respectively from left to right and top to bottom. In all panels the dashed line represents the one to one relation.

*XMM – Newton* PSF as explained in Finoguenov et al. (2009). The “residual” image, free of point sources, is then used to identify extended emission. Groups and clusters are selected as extended emission with at least  $4\sigma$  significance with respect to the background (see Finoguenov et al. (2009) for further detail on the precise definition of background and, thus, detection significance level). Finoguenov et al. (2009) and Finoguenov et al. (in prep.) assigned a redshift to each systems on the basis of spectroscopic redshift, when available, or photometric redshift. The X-ray luminosity  $L_X$  is estimated within  $R_{200}^2$  after

<sup>2</sup> $R_\Delta$  (where  $\Delta = 500, 200$ ) is the radius at which the density of a cluster is equal to  $\Delta$  times the critical density of the universe ( $\rho_c$ ) and  $M_\Delta$  is defined as  $M_\Delta = (4\pi/3)\Delta\rho_c R_\Delta^3$ .

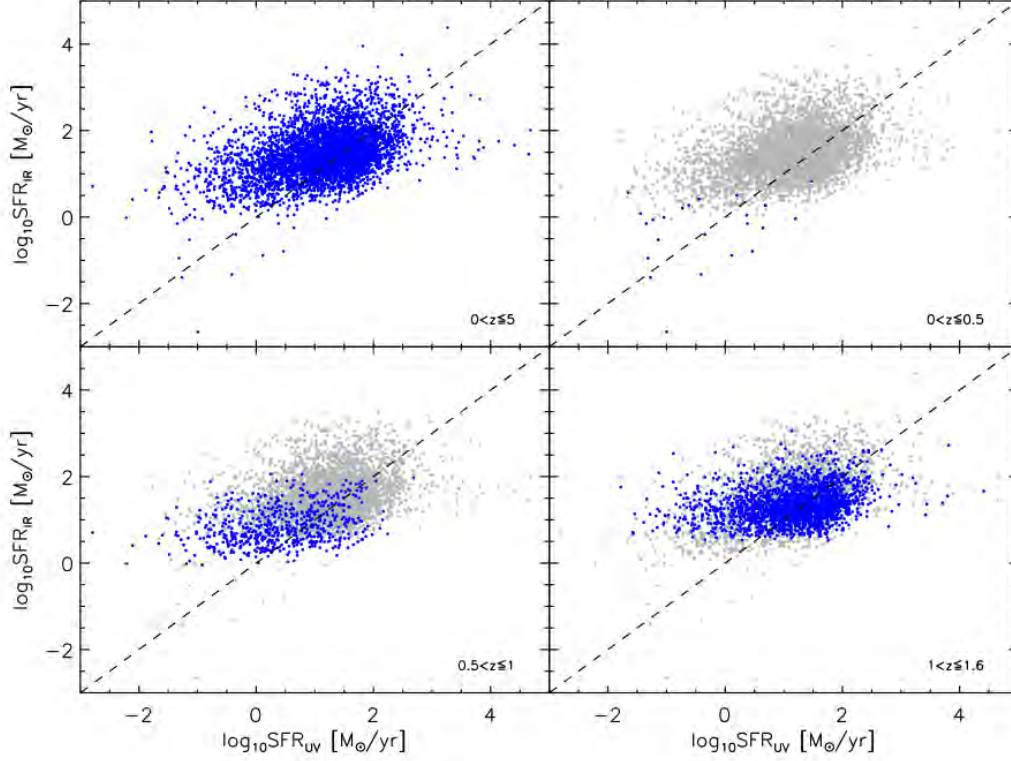


Figure 2.12: Comparison between  $SFR_{IR}$  and  $SFR_{UV}$  for the ECDFS. The upper left panel shows all the sources with IR detection and for which we have data coverage at 1500 Å rest-frame. As in Fig. 2.11, the same distribution of the upper left panel is represented as gray dots in the following panels, which represent all the sources for different redshift bin with blue dots:  $0 < z \leq 0.5$ ,  $0.5 < z \leq 1$ , and  $1 < z \leq 1.6$ , respectively from left to right and top to bottom. In all panels the dashed line represents the one to one relation.

taking into account the possible missed flux through the use of the beta-model. The X-ray masses  $M_{200}$ , within  $R_{200}$ , are estimated based on the measured  $L_X$  and its errors, using the scaling relation of Leauthaud et al. (2010) through the equation:

$$\frac{\langle M_{200} E(z) \rangle}{M_0} = A \left( \frac{\langle L_X E(z)^{-1} \rangle}{L_{X,0}} \right)^\alpha \quad (2.4)$$

where  $E(z) \equiv \sqrt{\Omega_m(1+z)^3 + \Omega_\lambda}$  is the Hubble parameter evolution for a flat metric,  $M_0 = 10^{13.7} h_{72}^{-1} M_\odot$  and  $L_{X,0} = 10^{42.7} h_{72}^{-2} \text{ erg s}^{-1}$ . The intrinsic scatter in this relation is 20% (Finoguenov et al. in prep.) and it is larger than a formal statistical error associated



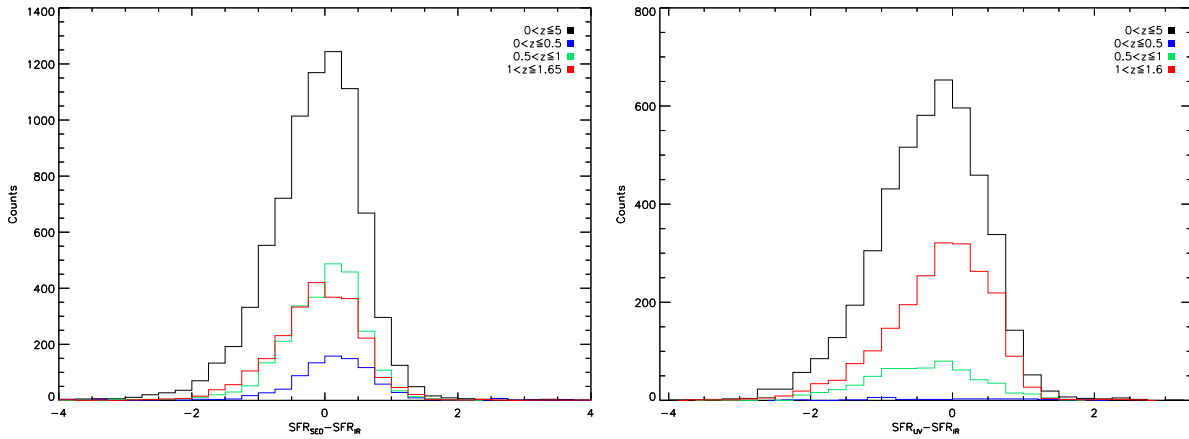


Figure 2.13: Histograms of  $SFR_{SED} - SFR_{IR}$  (on the left) and  $SFR_{UV} - SFR_{IR}$  (on the right) residuals. The different colors correspond to the same redshift bins used for Fig. 2.11. All the histograms peak around 0, meaning that our approximation is robust. We measure a scatter of 0.73 dex (0.76 dex) for the whole range of redshifts, 0.74 dex (0.99 dex) for  $0 < z \leq 0.5$ , 0.63 dex (0.79 dex) for  $0.5 < z \leq 1$ , and 0.68 dex (0.73 dex) for  $1 < z \leq 1.6$  for the  $SFR_{SED} - SFR_{IR}$  ( $SFR_{UV} - SFR_{IR}$ ) relation.

with the measurement of  $L_X$ . We use, then, the L-T relation to compute the temperature, which we used for the computation of the k-correction.

The X-ray group catalogs derived with this approach comprise 277 detections in the COSMOS field and 50 detections in the ECDFS (Fig. 2.14). However, in order to study the galaxy population belonging to each X-ray group, we need to locate precisely in redshift each detection and to identify a reasonable number of spectroscopic members (at least 10 as shown in Biviano et al. 2006) to derive velocity dispersion and possibly the dynamical mass. This process was done in Popesso et al. (2012) for the 277 COSMOS groups and in Wilman et al (in prep.) for the ECDFS X-ray groups. In both cases, we classify as insecure X-ray groups, those showing more than one peak in the spectroscopic redshift distribution along the line of sight and within 3 times  $R_{200}$  from the X-ray group center and those with a clear presence of a close companion. Indeed, in the former case the redshift associated is doubtful, and in the latter case a close companion can strongly bias the estimate of the velocity dispersion and membership. In addition, we require to identify at least 10 members. Our selection criteria lead to a final number of 28 groups in the COSMOS field and 22 in the ECDFS (see Popesso et al. 2012 and Wilman et al. in prep. for further details). We also impose a velocity dispersion cut at  $\sigma < 1200$  km/s to define a clear group catalog and to avoid contamination by massive clusters, whose galaxy population could follow a different evolutionary path, as shown in Popesso et al. (2012) This velocity dispersion cut exclude only two systems of the COSMOS group sample. We add also other 3 structures: 2 in the GOODS-N field and one in the GOODS-S field. Of the GOODS-N systems, one is X-ray detected at  $z = 1.02$  (Elbaz et al. 2007), and one system at

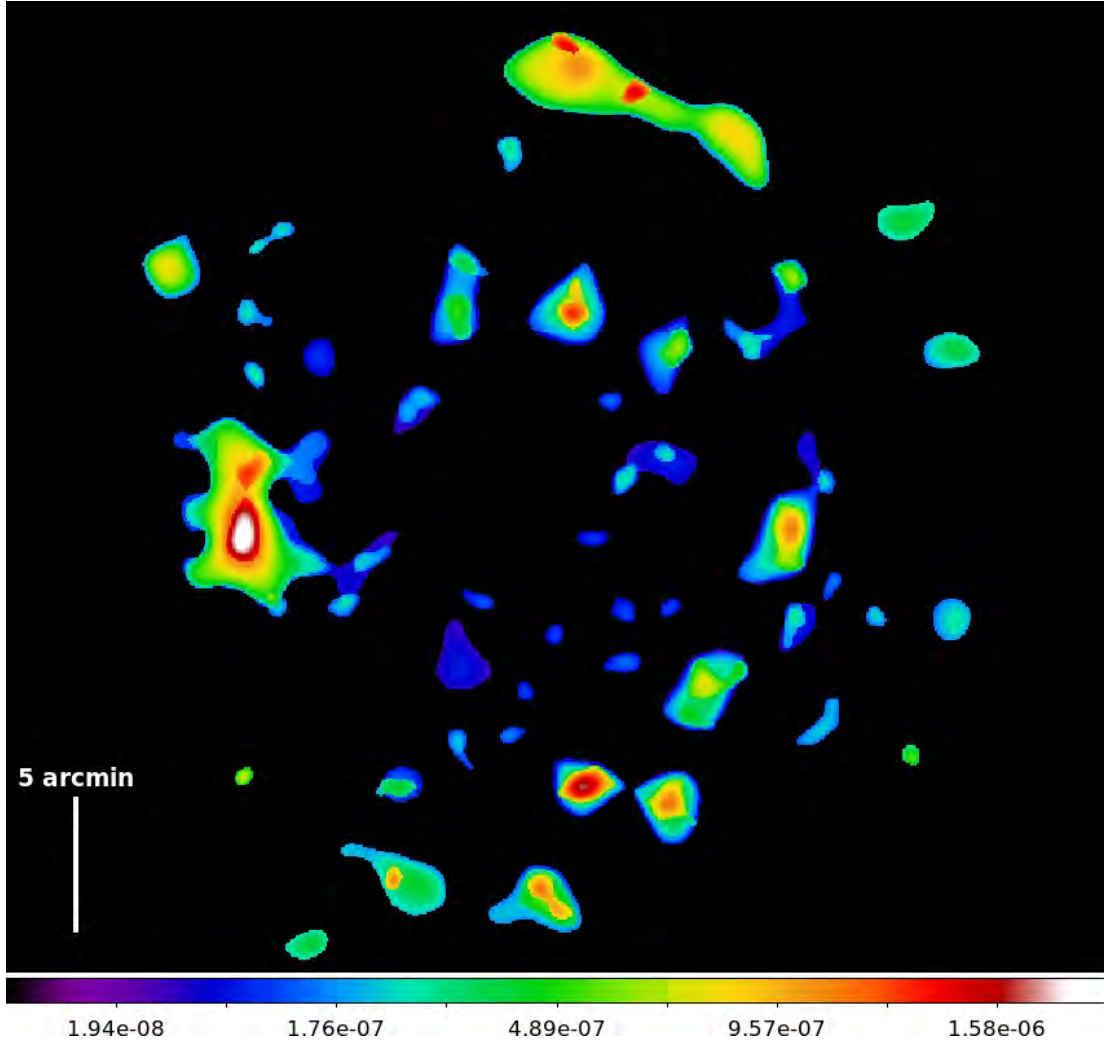


Figure 2.14: X-ray detected groups in ECDFS after a wavelet+PSF reconstruction. The units of the color bar are in  $\text{count s}^{-1} \text{pxl}^{-1}$ .

$z = 0.85$  lies close to the Chandra CCD chip gap and it is not X-ray detected (Bauer et al. 2008). These two systems are necessary to populate the  $z \sim 1$  redshift bin as shown later. We consider also a “super-group” or large scale structure spectroscopically confirmed at  $z \sim 1.6$  by Kurk et al. (2009). We devote the next section to a detailed description of this structure.

### Superstructure at $z \sim 1.6$

The structure at  $z \sim 1.6$  was first identified by Kurk et al. (2009) as a significant overdensity of galaxies at that redshift in the GOODS-S field. Popesso et al. (2012) identify 76 members dynamically related to the system using all secure spectroscopic redshift in GOODS-S and GMSS. The structure shows a clear overdensity of galaxies within  $R_{200} = 0.51$  Mpc

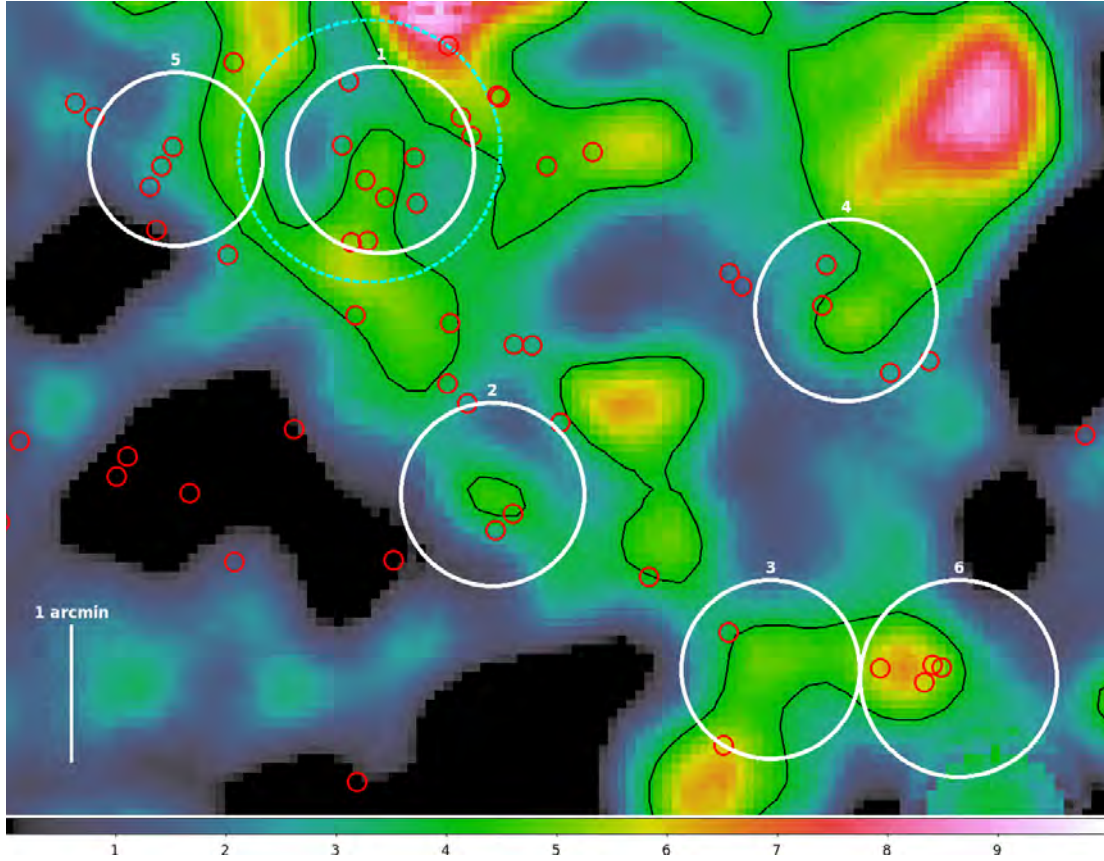


Figure 2.15: Signal-to-Noise map in a logarithmic scale of the region of the structure studied in Kurk et al. (2009). The color bar indicates the significance in  $\sigma$  units and black contours highlight the  $4\sigma$  level. We plot the position of the member galaxies with small red circles while the dashed cyan circle shows the position of the super-group with its radius representing  $R_{200}$  of the structure. The white circles identify 6 groups (Finoguenov et al. in prep.) which could be associated to the LSS of the structure studied in Kurk et al. (2009). Their radii represent  $R_{200}$  of each group and are centered on the density peaks of Kurk et al. (2009).

estimated via optical analysis, and an elongation in the galaxy density distribution towards the South, consistent with the findings of Kurk et al. (2009) based on GMASS redshift only. Kurk et al. (2009) identify also a clear red sequence of galaxies with absorption line spectra. So far only an upper limit on the X-ray emission of this structure was available. Indeed, Trevese et al. (2010) measure an upper limit of  $\sim 10^{43}$  erg/s based on the 4Ms observation of the CDFS (Bauer et al. 2008), consistent with a mass of  $\sim 10^{14} M_{\odot}$ . This mass estimate is in agreement with the optical mass estimates of Kurk et al. (2009) and Popesso et al. (2012), who report a mass of  $10^{14}$  and  $1.5 \times 10^{14} M_{\odot}$  and a velocity dispersion between 400-500 km/s, respectively. The missed secure X-ray detection of this structure suggests that it should be a non virialized structure in the process of formation.

Applying the same technique used for the COSMOS and ECDFS X-ray maps to the more recent CDFS 4 Ms observation, leads to find few X-ray emissions possibly associated to the superstructure at  $z \sim 1.6$  (Finoguenov et al. in prep.). Fig. 2.15 shows the X-ray signal-to-noise map (obtained from the CDFS map after removal of point sources) of the region covered by the structure. Finoguenov et al. (in prep.) identify 6 extended X-ray emission with a significance larger than  $3\sigma$ . The area within a preliminary rough estimate of  $R_{200}$  of each group is shown by the white circles, while the dashed cyan circle represents the  $R_{200} = 0.51$  Mpc of the structure as studied in Popesso et al. (2012). The galaxies associated to the structure according the analysis of Popesso et al. (2012) are shown by the red circles. There is consistency between the X-ray group candidate of Finoguenov et al. (in prep) and the galaxy density distribution. However, as shown in Fig. 2.15, the region of the structure is highly confused due to the presence of other three structures in foreground at lower redshift, that might contaminate and bias the estimate of the X-ray luminosity of these  $z = 1.6$  group candidates.

All these results indicate that the  $z = 1.6$  structure of the GOODS-S field is likely a “super-group” in phase of formation. Thus, it provides information about a stage of the group and cluster formation not studied before at such high redshift. Given the uncertainties of the X-ray detection in such confused region, we keep as structure parameters and membership the ones derived via the dynamical analysis of Popesso et al. (2012).

### 2.4.2 Membership and velocity dispersion estimates of galaxy systems

To define the galaxies that are members of the systems identified as described in Sect. 2.4.1, we adopt the algorithm of Mamon, Biviano, & Murante (2010), which is based on the modeling of the mass and anisotropy profiles of cluster-sized halos extracted from a cosmological numerical simulation. This algorithm is more effective than traditional approaches (e.g. Yahil & Vidal 1977) in rejecting interlopers, while still preserving cluster members. The system membership selection depends on the location of galaxies in the system-centric distance – rest-frame velocity<sup>3</sup> diagram. The peaks of the X-ray surface brightness are adopted as centers of the X-ray detected systems. The galaxy number density maxima (estimated using an adaptive kernel technique) are adopted as centers for the two systems in GOODS-N ( $z \sim 0.85$ ) and GOODS-S ( $z \sim 1.6$ ). The interloper rejection procedure is iterated until convergence.

The velocity dispersion is obtained from biweight estimates (Beers, Flynn, & Gebhardt 1990) of the system velocity dispersions along the line-of-sight,  $\sigma_v$ , as in Mauduit & Mamon (2007, see Appendix A). Furthermore, a flag is assigned to each group if there is a double peak in the redshift distribution along the line of sight. We select only well isolated groups in order to have a “clean” X-ray emission, i.e. not contaminated by other extended sources,

---

<sup>3</sup>The galaxy rest-frame velocities with respect to the system mean velocity are obtained by the relation  $v = c(z - \bar{z})/(1 + \bar{z})$  (Harrison & Noonan 1979), where  $\bar{z}$  is the system mean redshift, determined with the biweight estimator (Beers, Flynn, & Gebhardt 1990).

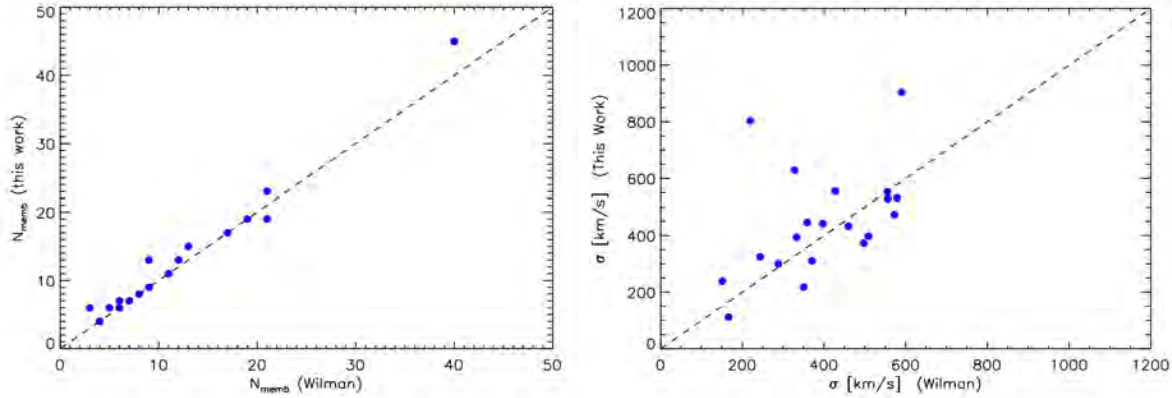


Figure 2.16: On the left: comparison of the number of members identified in our dynamical analysis versus those identified by Wilman et al. (in prep.) within  $R_{200}$  of each X-ray group in the ECDFS. On the right: comparison between the  $\sigma_v$  estimated in our work versus those estimated by Wilman et al. (in prep.).

which could bias the  $L_X$  and  $M_{200}$  estimates.

For the ECDFS groups we compare our analysis with those of Wilman et al. (in prep.). From the same X-ray catalog described in Section 2.4.1, Wilman et al. select the candidate group members within  $R_{200}$  from the X-ray center and applies a cut in velocity dispersion of  $2\sigma$ . Our dynamical analysis do not apply any cut, but we do apply them just with the aim of comparing the two results. Fig. 2.16 shows the comparison between the number of estimated group members from our analysis versus those estimated by Wilman et al. (in prep.). Our estimates are generally in very good agreement with those of Wilman et al. (in prep.). Our method is, however, more desirable than the method of Wilman et al. (in prep.) because it does not apply any cut in velocity dispersion and radii, thus, including also the galaxy group members in the infalling region. This is a fundamental point of our analysis since we want to analyze the star formation level of group galaxies in different (virialized and infalling) regions of the group environment.

### Dynamical mass estimates

As an outcome of the procedure of Mamon, Biviano, & Murante (2010), the system dynamical masses are obtained from biweight estimates (Beers, Flynn, & Gebhardt 1990) of the system velocity dispersions along the line-of-sight. For a more extensive description on the mass estimates from the dynamical analysis see also Biviano et al. (2006). The uncertainties in the system mass estimates are derived from the uncertainties in the biweight estimate of  $\sigma_v$  (Beers, Flynn, & Gebhardt 1990) via the propagation of error analysis. Fig. 2.17 shows the comparison between the mass estimates obtained from the velocity dispersion versus those obtained from the X-ray analysis. As already mentioned in Popesso et al. (2012) the mass estimates are in good agreement for COSMOS and the GOODS fields. We note much less agreement for the ECDFS groups, where the dynamical masses are on

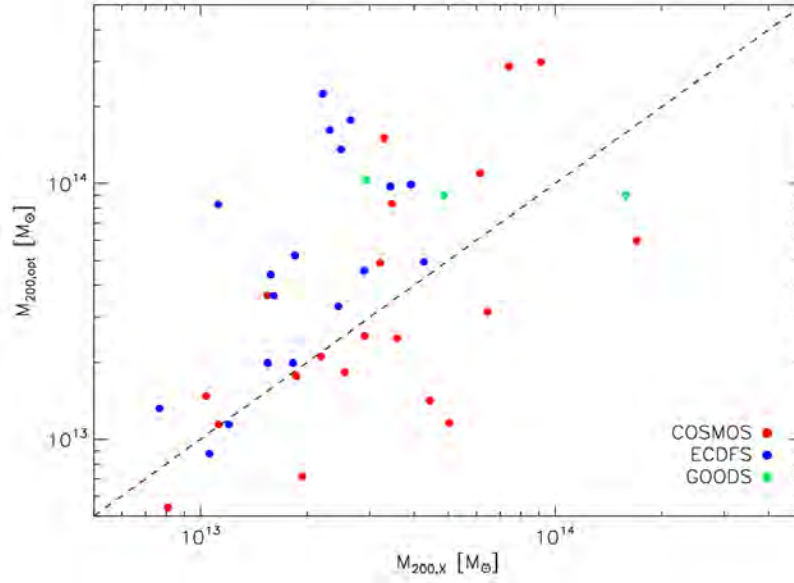


Figure 2.17: Comparison of the mass estimates for the groups obtained from the velocity dispersion versus those obtained from the X-ray analysis. Different colors represent the different surveys to which the groups belong.

average higher than the X-ray masses. This could be due to a higher level of substructures in the ECDFS groups. However, the number of members is too low to apply reliably a Dressler & Shectman (1988) test. For this reason, we choose to adopt the X-ray masses for all the systems and the dynamical masses only for the two systems without reliable X-ray information.

### Group properties

Fig. 2.18 shows the redshift distribution of the groups selected in our sample. COSMOS groups span a redshift range from  $z \sim 0$  to  $z \sim 1$ , with a peak around  $z \sim 0.3$ . ECDFS, GOODS-S and GOODS-N groups are located mainly at higher redshift, covering mostly the redshift range  $0.5 \lesssim z \lesssim 1.6$ . Our systems span a wide range of velocity dispersion and masses, from poor groups to poor clusters at any redshift thanks to the combination of large area and X-ray depth of the fields used for this analysis (Fig. 2.19). Fig. 2.20 shows the X-ray luminosity of the groups in our sample as a function of redshift. For the two groups with insecure X-ray detection, we plot an upper limit for the X-ray luminosity. COSMOS has a higher detection limit due to the shallower depth of the *XMM-Newton* X-ray observations. We divide the combined group samples in four redshift bins:  $0 < z \leq 0.4$ ,  $0.4 < z \leq 0.8$ ,  $0.8 < z \leq 1.2$ ,  $1.2 < z \leq 1.7$ .



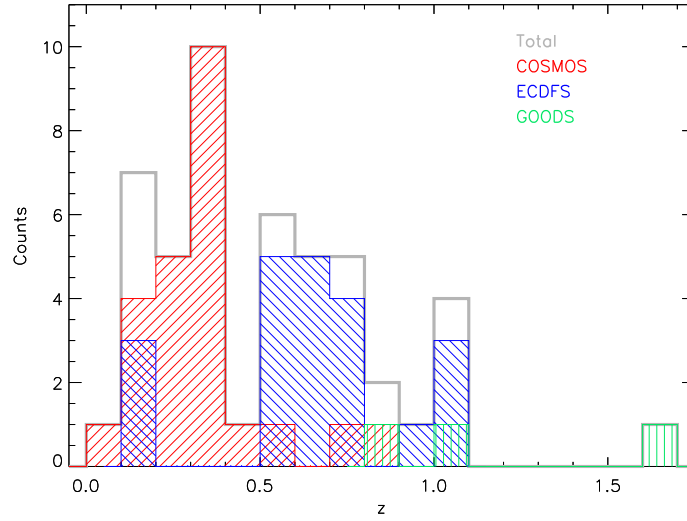


Figure 2.18: Redshift distribution of our group sample. Different colors represent the different surveys to which the groups belong.

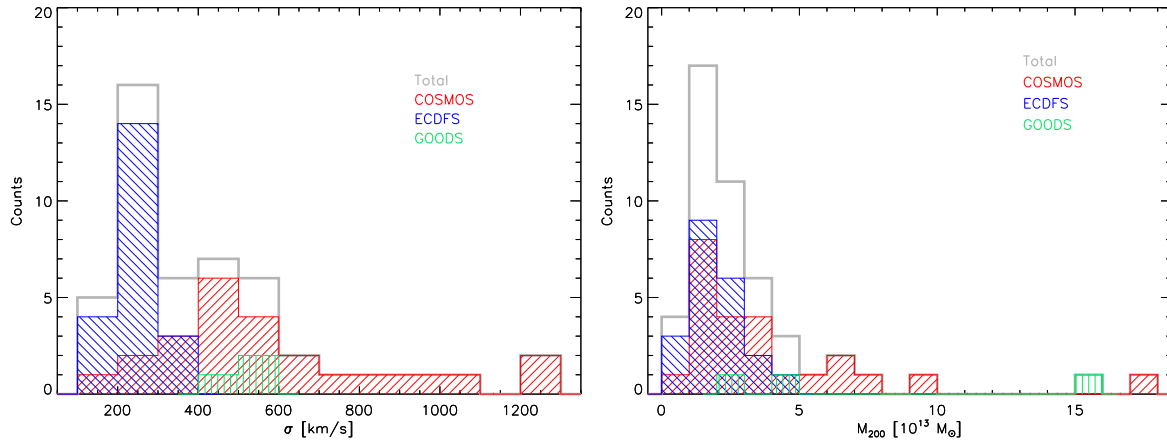


Figure 2.19: Observed velocity dispersion distribution as measured from the dynamical analysis (left panel) and observed distribution of the total masses computed from the X-ray (right panel) for our sample.

## 2.5 How to cope with spectroscopic incompleteness of the galaxy sample

For each field we create a Spitzer IRAC 3.6  $\mu\text{m}$  selected catalog. This selection criterion has the advantage to be close to a stellar mass selection up to  $z \sim 1$ . The spectroscopic

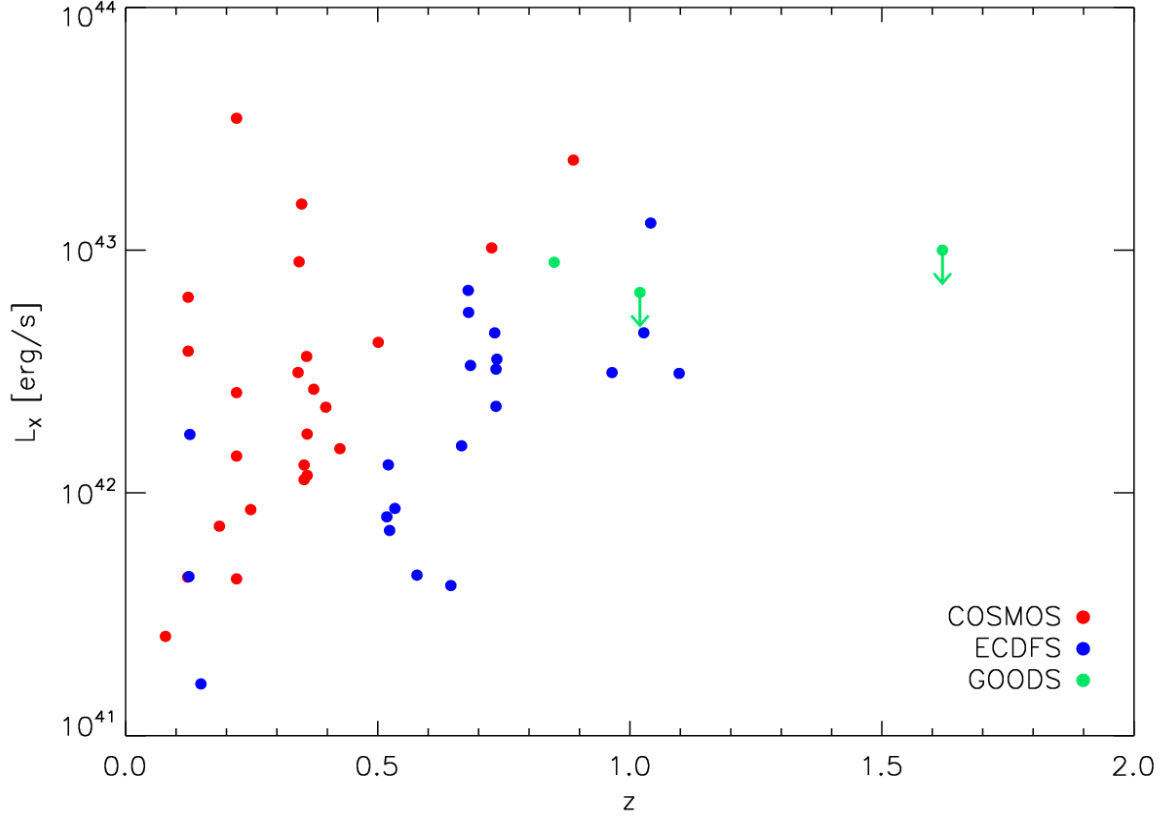


Figure 2.20: X-ray luminosities as a function of redshift of the groups in our sample. The arrows represent the upper limits of the X-ray luminosity. Different colors represent the different surveys to which the groups belong.

member catalog of each group is, then, matched to the  $3.6 \mu\text{m}$  selected catalog of the corresponding field. Since the aim of this analysis is to investigate the relation of the SF activity of the group members with respect to the field, we need first to take into account the possible selection effects due to the spectroscopic selection function, which is different from field to field. Fig. 2.21 shows the spectroscopic completeness as a function of the apparent  $3.6 \mu\text{m}$  magnitude. The left panel shows the spectroscopic completeness of the full field area for each survey. The right panel shows the mean spectroscopic completeness in the group regions. This is estimated as the mean of the completeness in the cylinder along the line of sight of each group and within  $1.5 \times R_{200}$  from the group center. This is the real completeness we must take into account in order to understand the selection biases, if any, that might affect our analysis. We divide the sample of groups per redshift bin, especially in the ECDFS area, to distinguish between the high redshift groups that happen to be mainly in the GOODS-S area with a somewhat higher spectroscopic completeness than the full ECDFS area, and the three low redshift groups that reside at the edge of



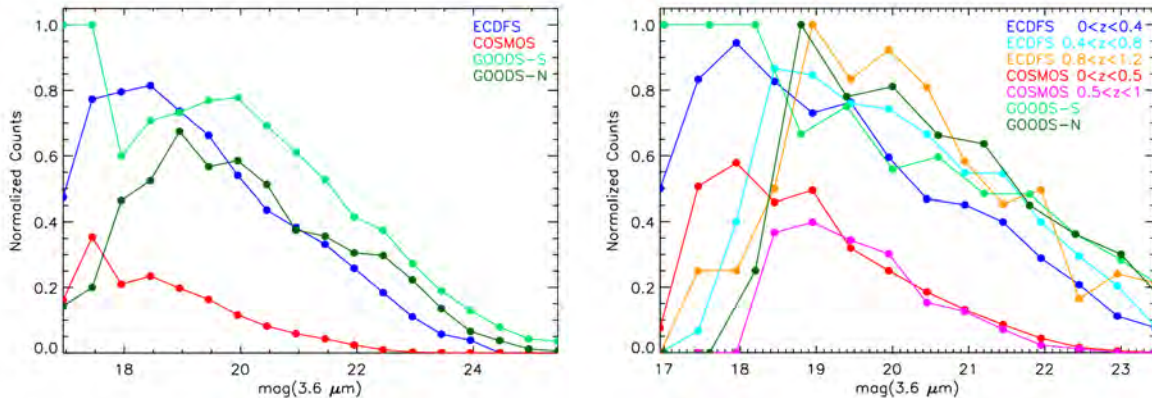


Figure 2.21: Spectroscopic completeness in the IRAC 3.6  $\mu\text{m}$  band for the field (on the left) and groups (on the right) in our sample.

the ECDFS area with a somewhat lower spectroscopic completeness. The spectroscopic completeness of the COSMOS field is much lower with respect to the other fields both in the full area and in the group area. This is mainly due to the difficulty in efficiently covering the full COSMOS area ( $2 \text{ deg}^2$ ) with a spectroscopic follow-up.

In order to estimate the errors involved in our analysis and check for possible biases due to the spectroscopic incompleteness, we design a method to use the mock catalog of Kitzbichler & White (2007) drawn by the Millennium run (Springel et al. 2005) to simulate a catalog with a spectroscopic selection function similar to the one observed in the fields considered in our analysis. We describe briefly in the next section the characteristics of the Kitzbichler & White (2007) mock catalog and our method to take into account the spectroscopic incompleteness.

### 2.5.1 The Millennium mock catalog

The Millennium simulation is a very large simulation which follows the hierarchical growth of dark matter structures from redshift  $z = 127$  to the present (Springel et al. 2005) and comprises several mock catalogs.

We choose to use the mock catalogs of Kitzbichler & White (2007) in order to estimate the errors due to the incompleteness of our spectroscopic catalogs. The simulation assumes the concordance  $\Lambda\text{CDM}$  cosmology and follows the trajectories of  $2160^3 \simeq 1.0078 \times 10^{10}$  particles in a periodic box  $500 \text{ Mpc } h^{-1}$  on a side. A full description is given by Springel et al. (2005)

The semi-analytic model in use is that of Croton et al. (2006) as updated by De Lucia & Blaizot (2007) and made public on the Millennium Simulation data download site (Lemson et al. 2006). These models include the physical processes and modeling techniques originally introduced by Kauffmann et al. (1993); Kauffmann & Charlot (1998); Kauffmann

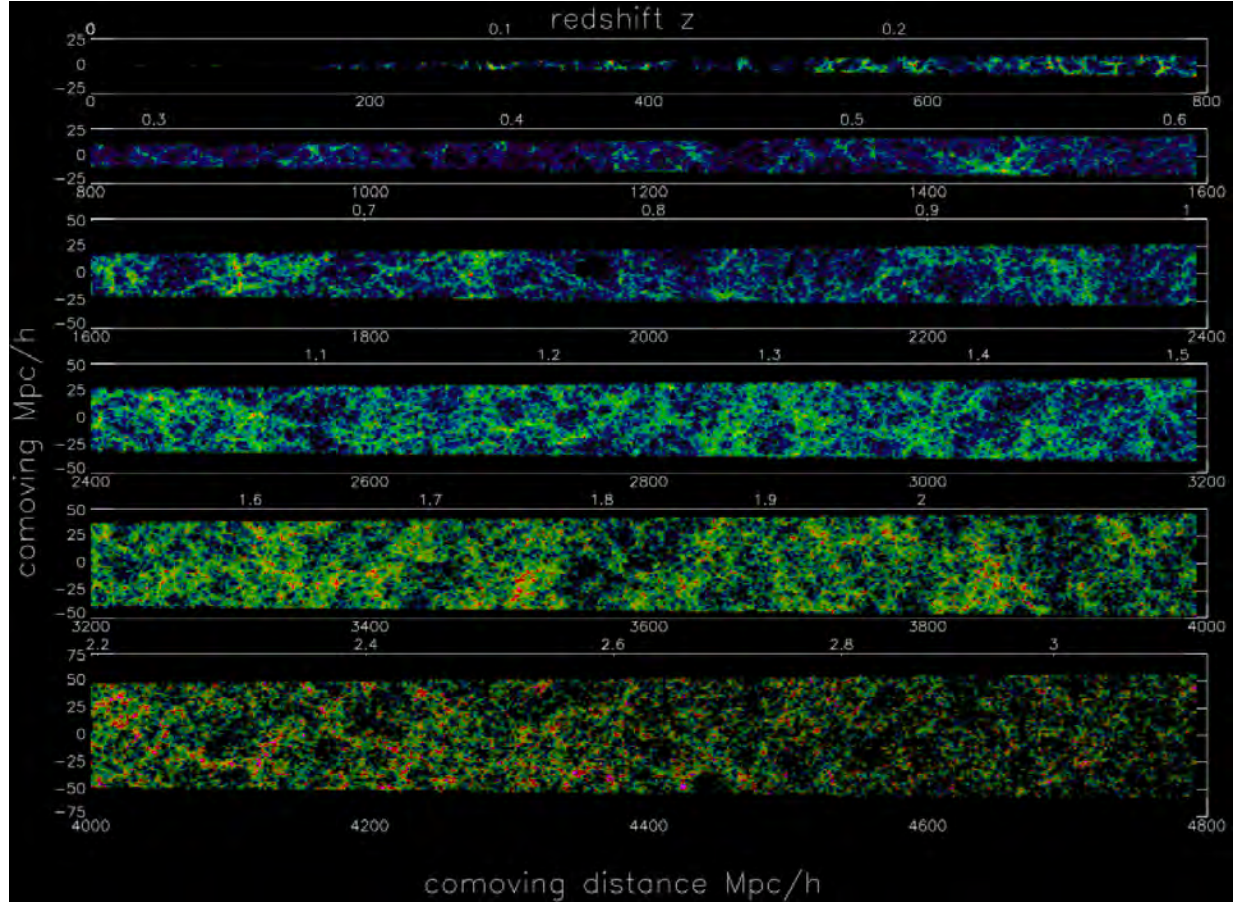


Figure 2.22: Light cone for a  $1.4^\circ \times 1.4^\circ$  field out to  $z = 3.2$  (Kitzbichler & White 2007). All galaxies above an apparent magnitude limit  $K_s(AB) < 24$  are shown, where intensity corresponds to the logarithmic density and the color denotes the offset from the evolving red sequence.

et al. (1999); Kauffmann & Haehnelt (2000); Springel et al. (2001); White & Frenk (1991) and De Lucia et al. (2004), principally gas cooling, star formation, chemical and hydrodynamic feedback from supernovae, stellar population synthesis modeling of photometric evolution and growth of super-massive black holes by accretion and merging.

For faint and distant object the most observationally accessible properties are usually fluxes in specific observer-defined bands. Quantities such as stellar mass or star-formation rate (often even redshift) must be derived from these observed properties and are subject to substantial uncertainties. Moreover which galaxies can be observed at all (and so are included in observational samples) is typically controlled by observational selection effects on apparent magnitude, color, surface brightness, proximity to other images and so on.

In order to minimize these uncertainties when drawing astrophysical conclusions about the galaxy population, it is ideal to have a simulated set of galaxies with known intrinsic

properties from which observational properties can be calculated, and to apply the same conversions and selection effects to this mock sample as to the real data. One can then assess the accuracy with which the underlying physical properties can be inferred.

For this purpose Kitzbichler & White (2007) make mock observations of the artificial universe, described above, by positioning a virtual observer at  $z \sim 0$  and finding the galaxies which lie on his backward light cone. The backward light cone is defined as the set of all light-like worldlines intersecting the position of the observer at redshift zero. Fig. 2.22 shows the simulated light cone of a deep survey (to  $K_s(AB) < 24$ ) of a  $1.4^\circ \times 1.4^\circ$  field out to  $z = 3.2$  from Kitzbichler & White (2007). The intensity in the image corresponds to the logarithmic density and the color encodes the offset from the evolving red sequence at the redshift of observation (assuming passive evolution after a single burst at  $z = 6$ ). Large-scale structure is evident and is well sampled out to redshifts of at least  $z \simeq 3$  and it is interesting that at  $z > 2$  the reddest galaxies are predicted to be in the densest regions even though many of them are predicted to be dusty strongly star forming objects.

The Millennium simulation database provides mock catalogs as explained above in six different lightcones. We use 2 of them to take into account field to field variation. We select as information from each catalog the Johnson photometric band magnitudes available ( $R_J$ ,  $I_J$  and  $K_J$ ), the redshift, the stellar mass and the star formation rate of each galaxy with a cut at  $I_J < 26$  to limit the data volume to the galaxy population of interest. In order to simulate the spectroscopic completeness observed in the region of our groups, we randomly extract for each mock catalog a subsample of galaxies by following the spectroscopic completeness of reference. Namely, we choose one of the available photometric bands and extract randomly in each magnitude bin a percentage of galaxies consistent with the percentage of systems with spectroscopic redshift in the same magnitude bin of our galaxy sample in the group region. Doing the extraction in one of the bands let us reproduce the observed completeness also in the other bands. We follow this procedure to extract randomly 50 different catalogs from each lightcone. We end up with 100 different (randomly extracted) catalogs that reproduce nicely the same characteristic of the selection function of our sample. To check this we apply the following approach. Given the very high accuracy of the photometric redshift of Cardamone et al. (2010) used for the ECDFS, we estimate a spectroscopic completeness in physical properties such as stellar mass and star formation rate of our galaxy sample (in the group region). We assume the photometric redshifts, and the physical properties based on those, as correct. Thus, we divide our sample in four redshift bins following the separation done for the groups and the analysis presented in the next Chapter. We estimate, then, the spectroscopic completeness as a function of stellar mass and star formation rate in each bin. The spectroscopic completeness is estimated as the ratio of the number of the galaxies with  $z_{spec}$  and the number of all those with  $z_{phot}$  in the considered redshift bin and per bin of stellar mass or SFR.

This procedure allows us to determine how the spectroscopic selection, based on the photometric information (e.g. color, magnitude cuts, etc.), affects the choice of galaxies as spectroscopic targets according to their physical properties. In order to check for possible biases, we follow the same approach for the randomly extracted mock catalogs. We apply the same redshift bin separation we use for the observed catalog. Then, we estimate in

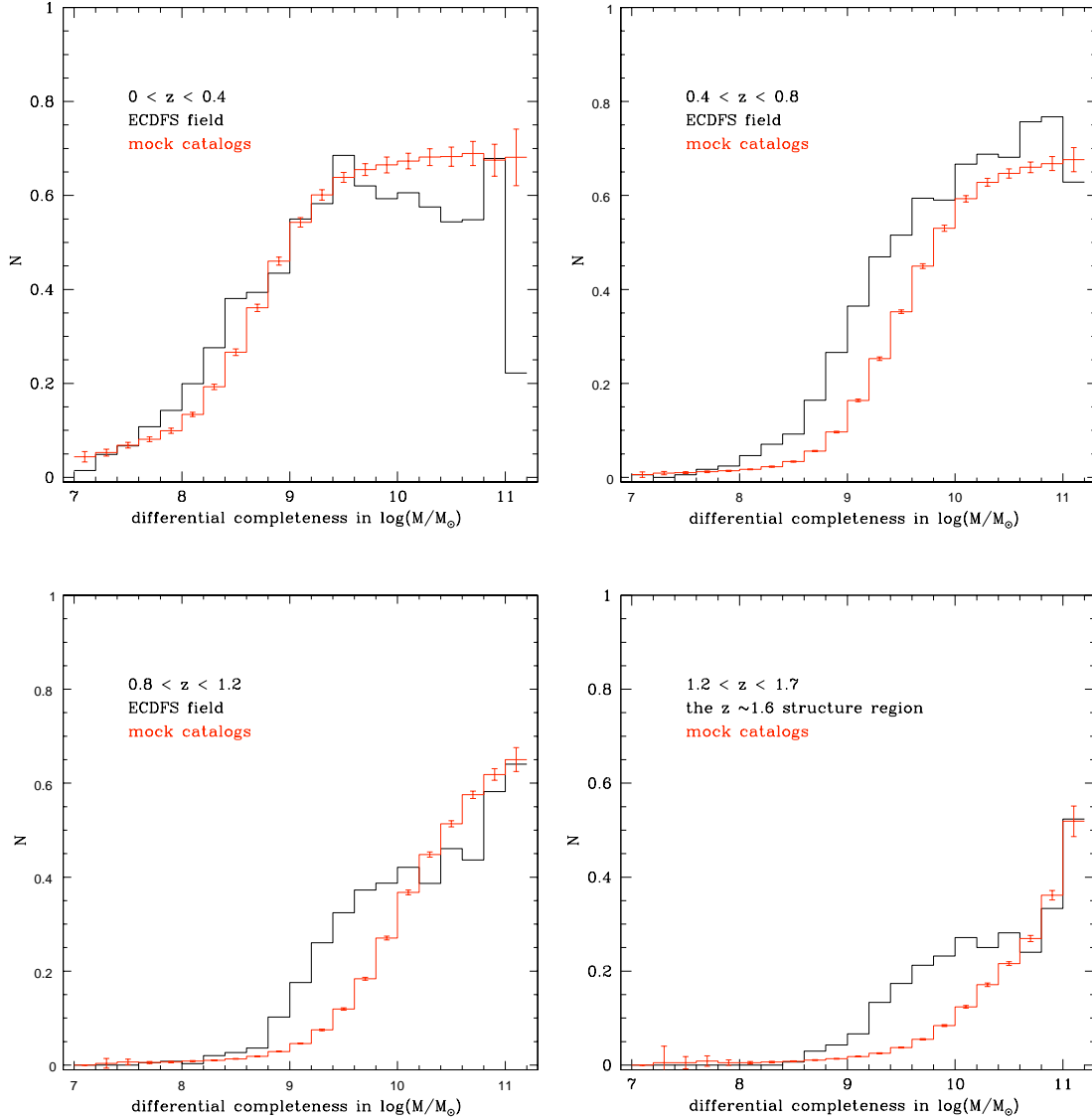


Figure 2.23: Spectroscopic completeness as a function of the galaxy stellar mass for the ECDFS (black histogram) and the mock catalogs (red histogram) in 4 redshift bins.

each bin the completeness as the ratio between the number of galaxies in that bin (and per bin of stellar mass and SFR) with respect to the number of galaxies in the parent sample (the original mock catalog of the same lightcone). The comparison between the observed completeness in ECDFS and in the corresponding mock catalogs is shown in Fig. 2.23 and Fig. 2.24. We show the mean completeness averaged over the 100 randomly extracted catalogs created following the spectroscopic completeness of the ECDFS in Johnson  $R$  band. In all panels the mock catalogs tend to reproduce the selection of massive and

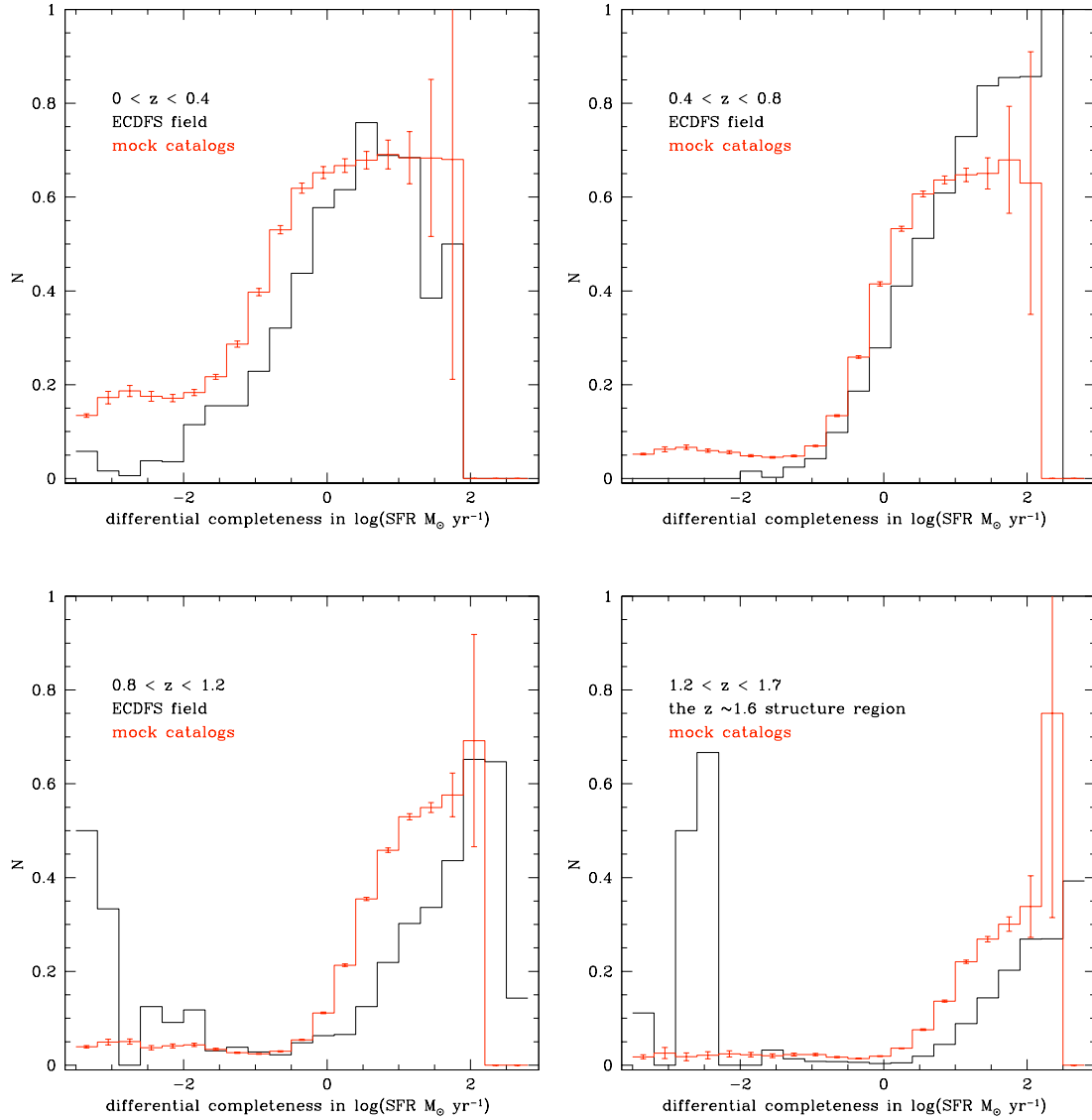


Figure 2.24: Spectroscopic completeness as a function of the galaxy star formation rate for the ECDFS (black histogram) and the mock catalogs (red histogram) in 4 redshift bins.

highly star forming galaxies observed in the real ECDFS sample. We note a significant difference only in the region of very low SFR where the completeness is much higher in the ECDFS sample than in the mock catalogs. This is due to the fact that massive early type galaxies have been targeted in dedicated observations (see Popesso et al. 2009 for more details), especially in the GOODS-S field region and at  $z > 0.5$ . This explains also why we do not see the same peak in spectroscopic completeness at low SFR in the lowest redshift bin. This feature is very difficult to reproduce in the mock catalogs. We apply the same

procedure to build randomly extracted mock catalogs with the spectroscopic completeness of the COSMOS field, which show a much lower completeness in the group region with respect to the other fields (Fig. 2.21).

In the analysis of the SF activity versus the environment we use the mock catalogs to investigate what is the effect of the spectroscopic selection on the results presented in the next Chapter. This is done by performing with the mock galaxy samples the same analysis as done on the real data and by comparing the results with those obtained with the same method from the original lightcone mock sample. The fact that the mock catalog of Kitzbichler & White (2007) fails in reproducing on average the SF activity level of high redshift galaxies, as shown in Elbaz et al. (2007), is not fundamental in our error analysis. Indeed, the aim of this error and bias analysis is to understand the relative effect of a spectroscopic selection with respect to the known parent sample and not to reproduce the observed results. The high number of the randomly extracted mock catalogs will be used to investigate the error distribution on a statistical sample. We will present our error analysis and estimate based on the mock catalogs case by case in the next Section and in Chapter 3.

## 2.6 The local galaxy density in ECDFS

The key ingredient for building a reliable density field is a very high and spatially uniform spectroscopic coverage. While a very high level of uniform spectroscopic coverage is reached in the ECDFS (see Cooper et al. 2011a and Fig. 2.25) and in the GOODS-N field (see Popesso et al. 2011), a much lower completeness level (Fig. 2.21) and a much more inhomogeneous sampling rate is available in the COSMOS field (see e.g. Kovač et al. 2010). Thus we measure the density field only in ECDFS and GOODS-N.

We reconstruct the density field around each galaxy in the ECDFS and GOODS-N field up to redshift 1.7. We compute the projected local galaxy density,  $\Sigma$ , by counting all galaxies located inside a radius of 0.75 Mpc and within a fixed velocity interval of  $\Delta v = 3000 \text{ km s}^{-1}$ , about ten times the typical velocity dispersion of galaxy group ( $\sigma_v \sim 300 - 500 \text{ km s}^{-1}$ ), and above a redshift dependent mass limit ( $M_{\text{cut}}(z)$ ), around each galaxy. Given the spectroscopic completeness in stellar mass in the four redshift bins considered in our analysis (see Fig. 2.23), we choose as stellar mass cut the  $M^*$  value where the 40-50% completeness limit is reached in each redshift bin:  $M^*/M_\odot = 10^9$  at  $0 < z < 0.4$ ,  $M^*/M_\odot = 10^{9.5}$  at  $0.4 < z < 0.8$ ,  $M^*/M_\odot = 10^{10}$  at  $0.8 < z < 1.2$  and  $M^*/M_\odot = 10^{10.5}$  at  $1.2 < z < 1.7$ . In order to take into account the effect of spectroscopic incompleteness, the density  $\Sigma$  must be corrected for the possibly missing galaxies. This correction is estimated as follows. We define for each galaxy a cylinder along the line of sight of the considered galaxy and with radius corresponding to 0.75 Mpc at the redshift of the considered source. We measure the number of sources in that cylinder with spectroscopic redshift falling into the redshift bin of the considered source and with stellar mass above  $M_{\text{cut}}(z)$  in that bin. The ratio of this number and the number of galaxies fulfilling the same requirements but with spectroscopic or photometric redshift falling in the same redshift

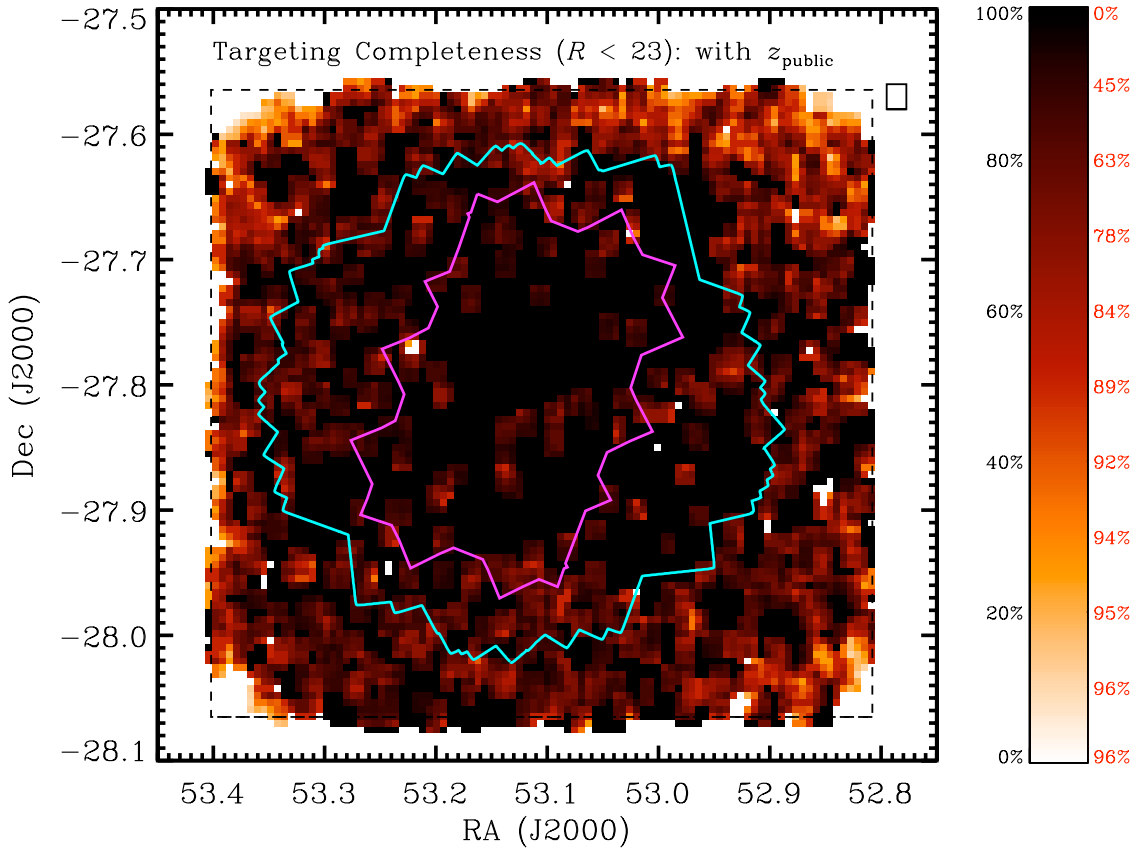


Figure 2.25: The target sampling rate at  $R_{\text{AB}} < 23$  for the CDFS galaxy population with reliable spectroscopic redshift, computed in Cooper et al. (2011a) in a sliding box of width  $\Delta\alpha = 64''$  and height  $\Delta\delta = 72''$ . The size and shape of the box are illustrated in the upper right-hand corner of the plot. The associated color bars give the mapping from color to target completeness (where black and white correspond to 100% and 0% completeness, respectively) and completeness is defined as the percentage of sources in the COMBO-17 imaging catalog with  $z_{\text{spec}}$  and all the galaxies at  $R_{\text{AB}} < 23$ . The red values to the right of the color bar show the portion of the  $30' \times 30'$  extended CDFS area (demarcated by the black dashed line in each plot) that has a target completeness greater than the corresponding level. Finally, the magenta and cyan outlines indicate the location of the GOODS *HST*/ACS and 2-Ms *Chandra*/ACIS-I observations, respectively. At  $R < 23$ , the sampling rate is exceptionally high across nearly the entire extended CDFS.

bin, provides the spectroscopic completeness level around each galaxy above the considered  $M_{\text{cut}}(z)$ . We correct for incompleteness by dividing  $\Sigma$  by this ratio. Due to the high level of mass segregation observed at least up to  $z \sim 1$  (Scodeggio et al. 2008) in the high density environment, the local density of massive galaxies around a given system should



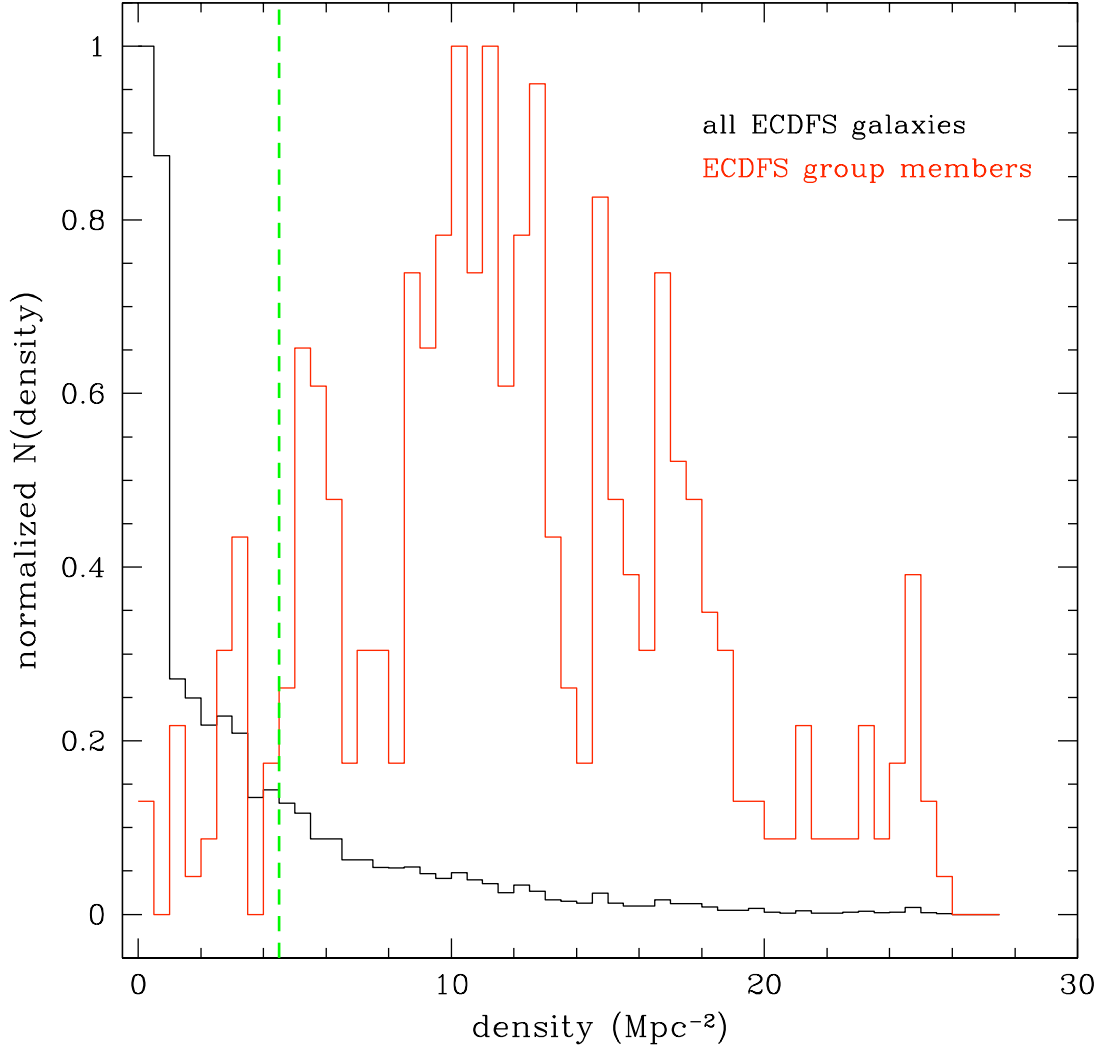


Figure 2.26: In black: density distribution around each galaxy with spectroscopic redshift in ECDFS. The red histogram shows the density of group members. The green dashed line at  $\rho = 4.5$  galaxies  $\text{Mpc}^{-2}$  nicely separates group from field galaxies. Indeed 80% of field galaxies are found at densities below this threshold and 92% of group galaxies above that.

better distinguish between low and high density regions. Indeed, Fig. 2.26 shows that our method is able to nicely discriminate field galaxies (black histogram) and galaxy identified as groups spectroscopic members (red histogram). For comparison we show in Fig. 2.27 a similar histogram obtained by Cooper et al. (2011a) and based on a different approach for the local density estimate. They estimate the local galaxy overdensity using measurements of the projected third-nearest-neighbor surface density ( $\Sigma_3$ ) about each galaxy, where the



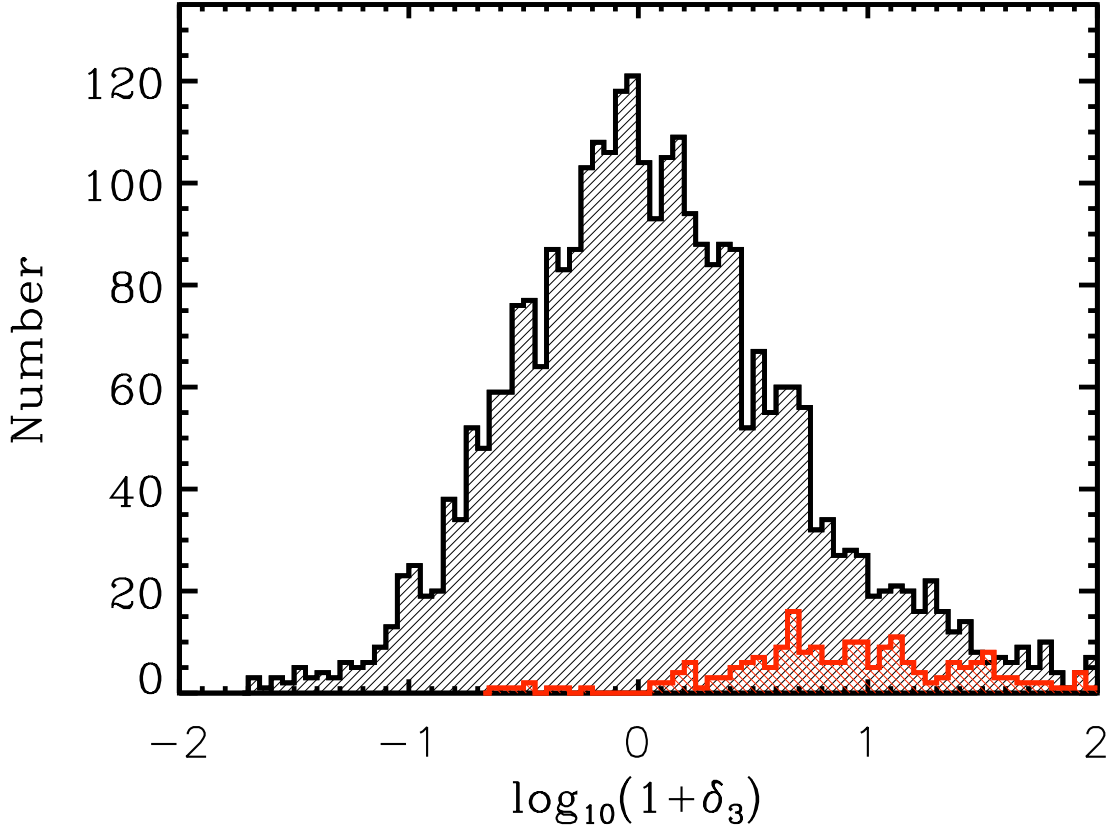


Figure 2.27: The distribution of overdensity measures for all sources with a secure redshift at  $0.2 < z < 0.8$  by Cooper et al. (2011a). The red histogram shows the environment distribution for the 210 galaxies identified as group members using the X-ray group catalog of Finoguenov et al. (in prep.).

surface density depends on the projected distance to the third-nearest neighbor,  $D_{p,3}$ , as  $\Sigma_3 = 3/(\pi D_{p,3}^2)$ . Comparing Fig. 2.26 and Fig. 2.27, our method seems to be more efficient in isolating intermediate density (or filament-like) environments.

We also identify a density threshold,  $4.5 \text{ Mpc}^{-2}$ , below which reside 80% of the field galaxies and above which we find 92% of the group galaxies. We classify as “intermediate density environment” the galaxies lying above that density threshold but not belonging to our groups. Those galaxies probably belong to filaments or sheet like structures or to groups at lower mass with respect to the mass limit imposed by the ECDFS X-ray detection limit. We will use further this classification of group, high density and field environment in the next Chapter.

In order to test the reliability of our density estimate, we measure with the same method the density field in the randomly extracted mock catalogs and compare the density obtained

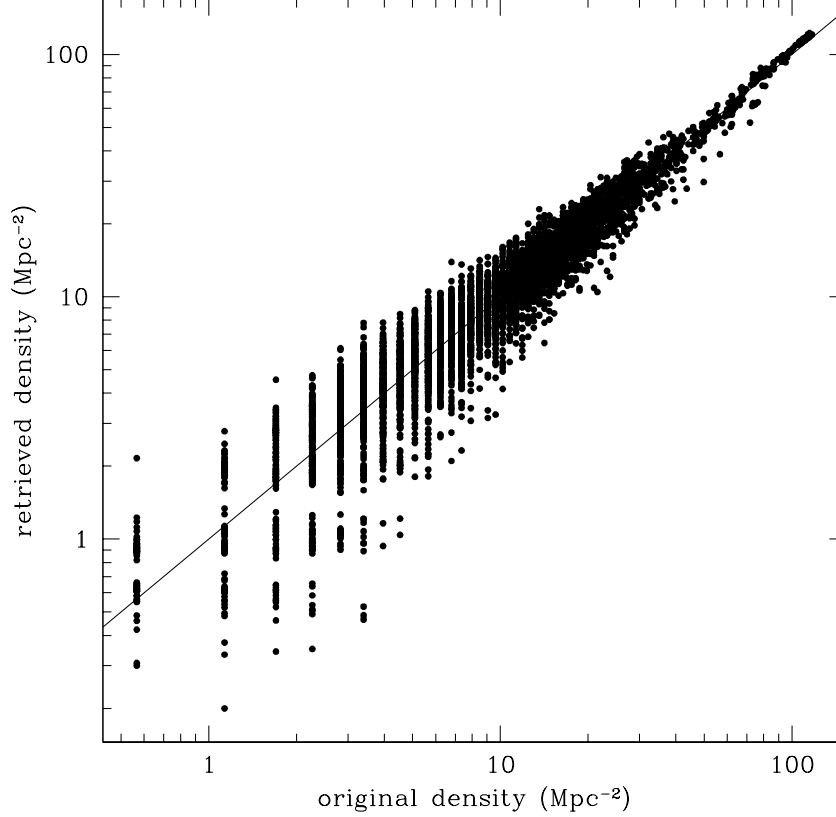


Figure 2.28: Original local density estimated in the Kitzbichler & White (2007) mock catalog versus the density retrieved in the randomly extracted catalog by following our method. The solid line shows the 1 to 1 relation.

in this way with the density measured in the parent lightcone mock catalog, free of selection biases. In order to simulate also the photometric redshift uncertainty, before estimating the incompleteness correction, we assign randomly to the redshift of the parent mock catalog galaxies (not extracted) a random error in the range  $-\Delta z < \delta z_{phot} < \Delta z$ , where  $\Delta z$  is the photometric redshift error provided by Cardamone et al. (2010). Fig. 2.28 shows the very good agreement between the original density estimated in the Kitzbichler & White (2007) mock catalog and the local density retrieved with our method. We use this approach also for estimating the error per density bin as the dispersion of  $\rho_{original} - \rho_{retrieved}$ .

# The evolution of the SF activity in groups, filament and field galaxies

## 3.1 The composite groups

This Chapter contains the results obtained from the analysis of the SFR activity in different environments. In order to tackle this issue from different points of view we define the “environment” by following two different criteria. First we use a “dynamical” approach by identifying the highest density environment as X-ray detected groups. Indeed, as explained in the Section 2.4.1, the X-ray selection of extended sources is close to a selection in total mass of the bound structures and it is much less prone to projection effects than an optical selection. In addition, the deep fields considered in our study (ECDFS, GOODS fields and COSMOS) do not contain clusters ( $M_{200} > 10^{14} M_{\odot}$ ) but only poor clusters and groups, with mean mass of  $2 \times 10^{13} M_{\odot}$ , as revealed by the X-ray analysis (see Section 2.4.1). Thus, the galaxies identified spectroscopically as group members, are considered the systems at the highest density. We use ECDFS and GOODS-N to define other two environments: intermediate density (filament-like structures) and low density environments. The identification of these two environments is based on Fig. 2.26. All galaxies with local galaxy density above a threshold of  $4.5 \text{ Mpc}^{-2}$  and not identified as spectroscopic group members or residing in the region of extended X-ray emission (including those groups not spectroscopically confirmed in our sample) are considered belonging to lower mass groups or unbounded structures like filaments. All galaxies with local galaxy density below  $4.5 \text{ Mpc}^{-2}$  are classified as systems at low density (or field galaxies). We use this approach to study the difference between the level of star formation activity in structures of different dynamical state: bound X-ray groups, lower mass groups and unbound structures such as filaments, and relatively isolated galaxies. As a second approach for defining the “environment”, we use the estimate of the local galaxy density of Fig. 2.26. This approach does not distinguish among different dynamical states (bound or unbound regions, high or

low mass groups), but it is simply sensitive to the relative vicinity of galaxies in a defined physical region. We use this approach to study the relation between SFR and density.

In order to follow the evolution of the relation between SF activity and environment, we divide our galaxy sample in four redshift bins,  $0 < z \leq 0.4$ ,  $0.4 < z \leq 0.8$ ,  $0.8 < z \leq 1.2$ ,  $1.2 < z \leq 1.7$ , according to the redshift distribution of our group sample (see Fig. 2.18). We note that the last redshift bin is populated by just one structure at  $z \sim 1.6$  (Kurk et al. 2009), which is likely a super-group or a cluster in formation as suggested by the X-ray analysis (see discussion of Section 2.4.1). Fig. 3.1 shows the caustics (cluster-centric distance versus recession velocity diagram) populated by the group galaxies in the four redshift bins. In order to put galaxies of different groups in the same diagram, the cluster-centric distance and the recession velocity are normalized to the  $R_{200}$  and the velocity dispersion of the parent group. The highest redshift bin populated by a single structure shows a much lower statistics than the lower redshift bins.

In order to limit the selection effects and, at the same time to take under control the different level of spectroscopic completeness per physical properties in the different redshift bins (see e.g. Fig. 2.23), we apply a common mass cut at  $10^{10.3} M_{\odot}$ . The uncertainties due to the spectroscopic incompleteness of our galaxy sample will be evaluated case by case with dedicated Monte Carlo simulations based on the mock catalogs of Kitzbichler & White (2007) drawn from the Millennium simulation (Springel et al. 2005).

## 3.2 SF activity within the group environment

In this section we analyze the dependence of the SF activity on the group environment. We consider all galaxies within a radius of  $1.5 \times R_{200}$  from the group center. All galaxies of the groups within the mentioned redshift bins ( $0 < z \leq 0.4$ ,  $0.4 < z \leq 0.8$ ,  $0.8 < z \leq 1.2$ ,  $1.2 < z \leq 1.7$ ) are considered all together. Their group-centric distance and recession velocity are normalized to the  $R_{200}$  and the velocity dispersion of the parent group, respectively. This is done to build a composite group per each redshift bin. We, then, analyze the dependence of the SF activity on the group-centric distance of the composite groups in each redshift bin.

### 3.2.1 SFR as a function of the group-centric distance

It is well known that in nearby rich clusters the local SF fraction or average SF activity increases linearly from the cluster core to large radii (e.g. Bai et al. 2009; Balogh, Navarro, & Morris 2000; Chung et al. 2010; Mahajan, Haines, & Raychaudhury 2010). Fig. 3.2 of Balogh, Navarro, & Morris (2000) nicely shows the increase of the mean SFR per galaxy as a function of projected distance from the cluster center, normalized to  $R_{200}$ . The solid squares correspond to the CNOC1 data averaged over radial bins and with  $1-\sigma$  jackknife error bars. The figure shows also that the average SFR per galaxy in the field is significantly higher than in clusters. Even at cluster-centric distance  $\sim 2R_{200}$ , cluster star formation rates remain suppressed by almost a factor of two relative to the field. How do group

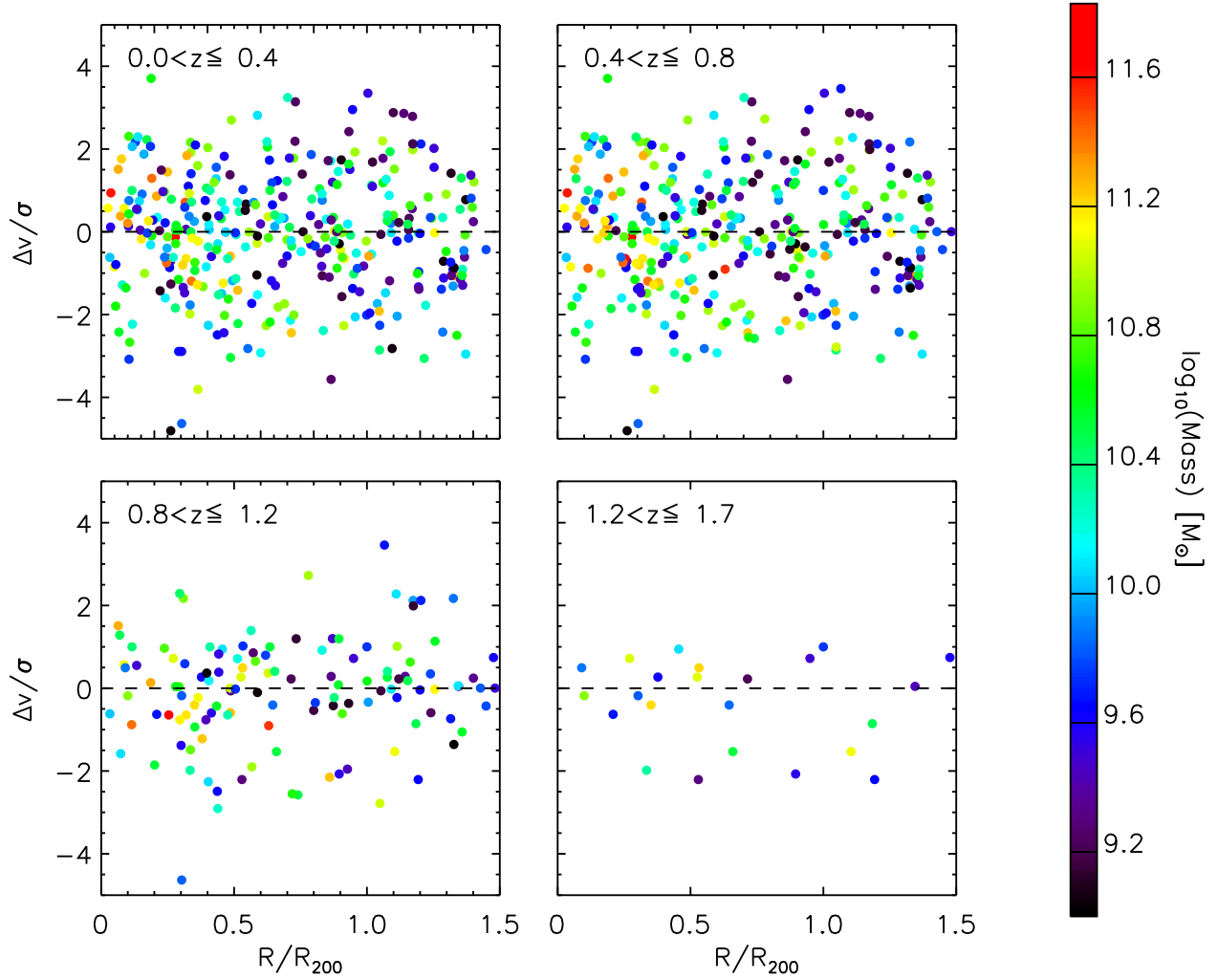


Figure 3.1: Caustic plots for all groups in the ECDFS and GOODS fields. The color shows the range of masses covered by the group galaxies. We show all the galaxies with a mass  $M \geq 10^9 M_{\odot}$  in all redshift bins (which are indicated in the legend).

galaxies behave in this respect?

Although many studies focus on star-forming (SF) galaxies in clusters (e.g. Bai et al. 2006; Bai et al. 2007; Balogh, Navarro, & Morris 2000; Chung et al. 2010; Fadda et al. 2008), such studies of groups have been lacking. Recently, Tran et al. (2009) detected an excess of  $24\ \mu\text{m}$  SF galaxies in groups compared to the field. However, their sample represents a somewhat peculiar case of a super-group in the process of forming a massive cluster.

A first attempt to quantify the dependence of the SF activity in groups as a function of the group-centric distance is done by Bai et al. (2010). In this work the authors analyze the *Spitzer* MIPS observations of a subsample of 9 groups at  $0.06 < z < 0.1$  optically selected in the 2dF spectroscopic survey and detected with XMM-*Newton* observations. The authors use as indicator of SF activity the fraction of galaxies with star formation higher than  $0.1\ M_{\odot}\ \text{yr}^{-1}$ . They compare the mean SF galaxy fraction of groups to two clusters with similar data. In contrast to the rich clusters (shown in the left panel of Figure 3.3), SF fractions in groups show no clear dependence on the distance from the group centers and remain at a level higher than the outer region of the rich clusters.

Another attempt at much higher redshift was done by Tran et al. (2010). They analyze the dependence of the SF fraction as a function of the group-centric distance in a group at  $z = 1.6$ . The X-ray observation of the structure reveals a mass of  $3 \times 10^{13}\ M_{\odot}$ . The *Spitzer* MIPS observations reveal a very high level of star formation activity. The analysis of the SFR–density relation within the structure shows that there is no relation between the two quantities. Given the tight correlation between local galaxy density and distance from the center, this is reflecting the same independence of the mean SFR from the group-centric distance as observed by Bai et al. (2010) in the nearby groups.

In this section we use our dataset to shed light on the relation of the mean SFR and the group-centric distance and to follow for the very first time its evolution up to  $z \sim 1.6$  with a homogeneous dataset. For this purpose we study the mean SFR–group-centric distance relation in the four composite groups in the  $0 < z \leq 0.4$ ,  $0.4 < z \leq 0.8$ ,  $0.8 < z \leq 1.2$ ,  $1.2 < z \leq 1.7$  redshift bins. Fig. 3.4 shows our results. We do not find any correlation between SFR and group-centric distance (as confirmed by the Spearman test) at any redshift. This is consistent with the findings of Bai et al. (2010) and confirms the different mix of the SF galaxies within the group region with respect to the clusters. Fig. 3.4 also shows that the SFR increases with redshift, consistently with the picture of Noeske et al. (2007a) and Elbaz et al. (2007), who argue that the universe was more active in forming stars in the past. The error bars in the figure are estimated by using the mock catalog of Kitzbichler & White (2007). We use the 100 randomly extracted catalogs built as explained in Section 2.5 in the following way. From each catalog we extract randomly 1000 different galaxy positions (ra, dec,  $z$ ). We use this positions as “fake group center”. For each position we measure the mean SFR ( $\text{SFR}_{\text{incomplete}}$ ) of all galaxies, with mass above the mass cut used in our analysis, within  $\pm 500(1+z)\ \text{km s}^{-1}$  and within a radius ranging from 0.1 to 1.5 Mpc from the “fake group center”. An increasing radius is used not to measure the gradient in SFR as we do in the real groups, but just to sample a larger area to increase the number of galaxies  $N_{\text{gal}}$  used to estimate the mean SFR at the completeness

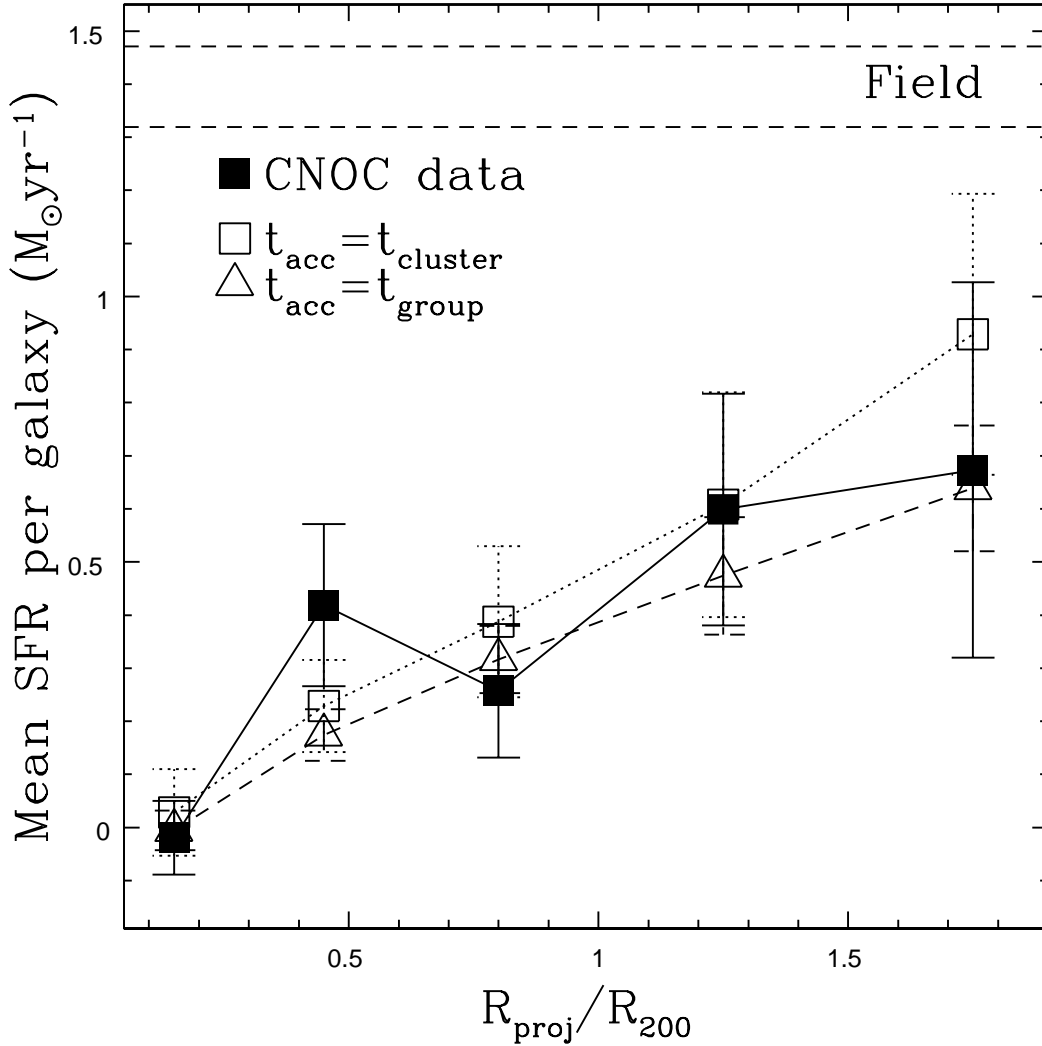


Figure 3.2: The mean SFR per galaxy as a function of projected radius for galaxies in the CNOC1 cluster sample (solid squares) compared with the model predictions of Balogh, Navarro, & Morris (2000) under the assumption that  $t_{\text{acc}} = t_{\text{cluster}}$  (open squares) and that  $t_{\text{acc}} = t_{\text{group}}$  (open triangles). The horizontal dashed lines correspond to the field SFR, bracketed by its  $1\text{-}\sigma$  dispersion. The SFR gradient in the CNOC1 clusters is accurately reproduced by the simple accretion models of Balogh, Navarro, & Morris (2000). Error bars are all  $1\sigma$ .

level of our real dataset. We measure in the exact same way the mean galaxy SFR ( $\text{SFR}_{\text{real}}$ ) in the original Kitzbichler & White (2007) mock catalog at the exact same positions. We measure, then, the difference  $\Delta_{\text{SFR}} = \text{SFR}_{\text{real}} - \text{SFR}_{\text{incomplete}}$ . We group the galaxies per redshift bin as in the real dataset and we measure the dispersion of  $\Delta_{\text{SFR}}$  as a function

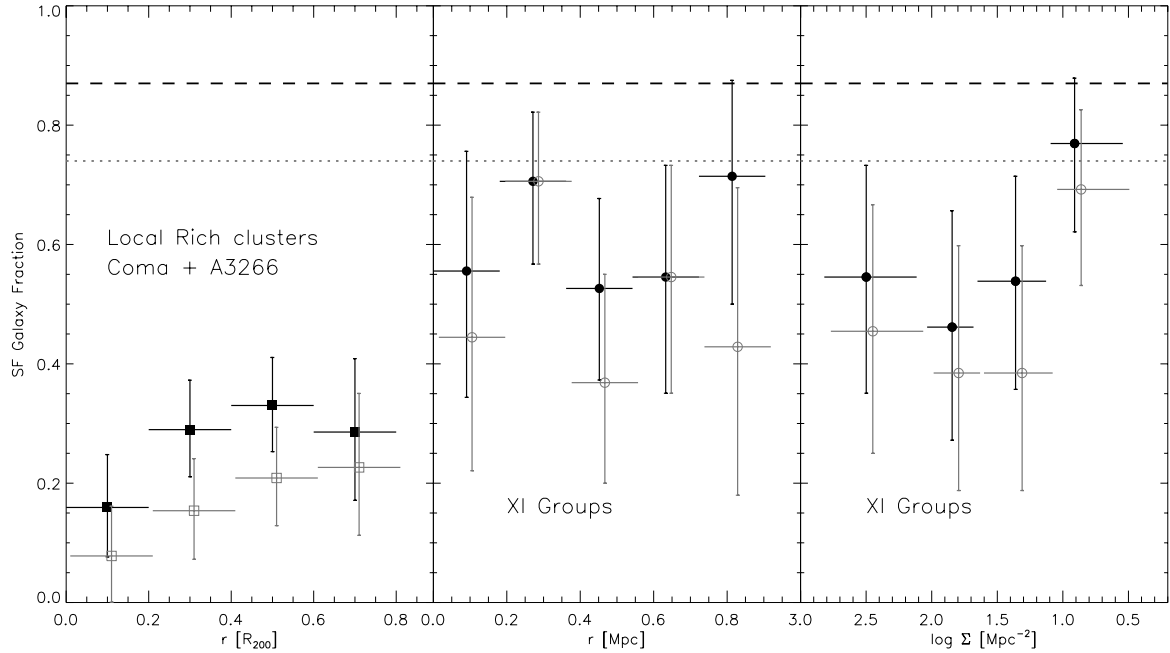


Figure 3.3: Left panel: SF galaxy fractions (filled black squares) and healthy SF galaxy fractions (gray open squares) in the nearby rich clusters Coma and A3266 as a function of projected distance (in units of  $R_{200}$ ) from the cluster center. Middle panel: SF galaxy fractions (filled black circles) and healthy SF galaxy fractions (gray open circles) in the XMM-IMACS (XI) groups as a function of projected distance from group centers. Right panel: SF fractions and healthy SF galaxy fractions in groups as a function of local projected galaxy density. In all three panels, the black dashed line is the average SF fractions in the field sample and the gray dotted line is the average healthy SF fractions in the field sample. The healthy SF fractions is defined as SF galaxies with specific SFR more than 20% of the typical specific SFR of the field galaxies.

of number of galaxies  $N_{\text{gal}}$  and per redshift bin. This provides the uncertainty due to the number of galaxies used for measuring the mean SFR and the spectroscopic incompleteness of our sample in physical quantities (SFR) at different redshifts (see Fig. 2.24). We use as error bar the error estimate at the  $N_{\text{gal}}$  and redshift bin used in the real dataset.

Bai et al. (2010) suggest that the continuously decreasing SF fractions towards the center in the cluster region could reflect a dependence of the SF properties on cluster properties that themselves depend on radius, such as local galaxy density or the density of the intra-cluster medium (ICM). If this is the case, the lack of a dependence of SF fractions on projected radius in groups could be a result of a breakdown of the correlation between galaxy density and projected distance rather than a breakdown of the correlation



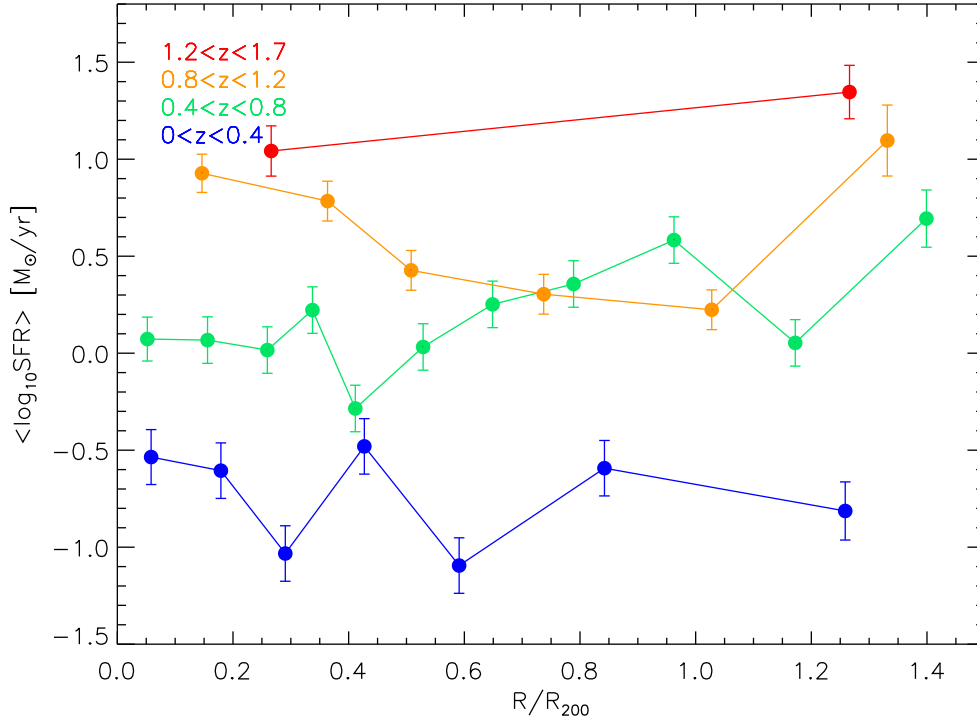


Figure 3.4: SFR as a function of group-centric distance for different redshift bin.

between SF fractions and galaxy density. To check this issue we analyze also the relation between local galaxy density, as estimated in Section 2.6, and the group-centric distance in our four composite groups. For all of them the Spearman test confirms a rather clear anti-correlation (significance higher than  $5\sigma$ ). Instead we do not find any relation between the mean SF activity and the density. Thus, our data would confirm a breakdown of the SFR–density anti-correlation within the group regime. We do not have the possibility to check the relation between the mean galaxy SFR and the gas density.

Using cluster mass accretion rates determined from N–body simulations of cluster formation in a  $\Lambda$ CDM universe, Balogh, Navarro, & Morris (2000) produce a model able to reproduce qualitative and quantitative differences in the mean star formation rates and colors between clusters and the field (see Fig. 3.2). The model demonstrates that the origin of radial gradients in these properties is the natural consequence of the strong correlation between radius and accretion times which results from the hierarchical assembly of the cluster. The absence of anti-correlation between mean galaxy SFR and the group-centric distance could reflect the much smaller spread in accretion times of low mass objects such as the groups considered in our analysis.

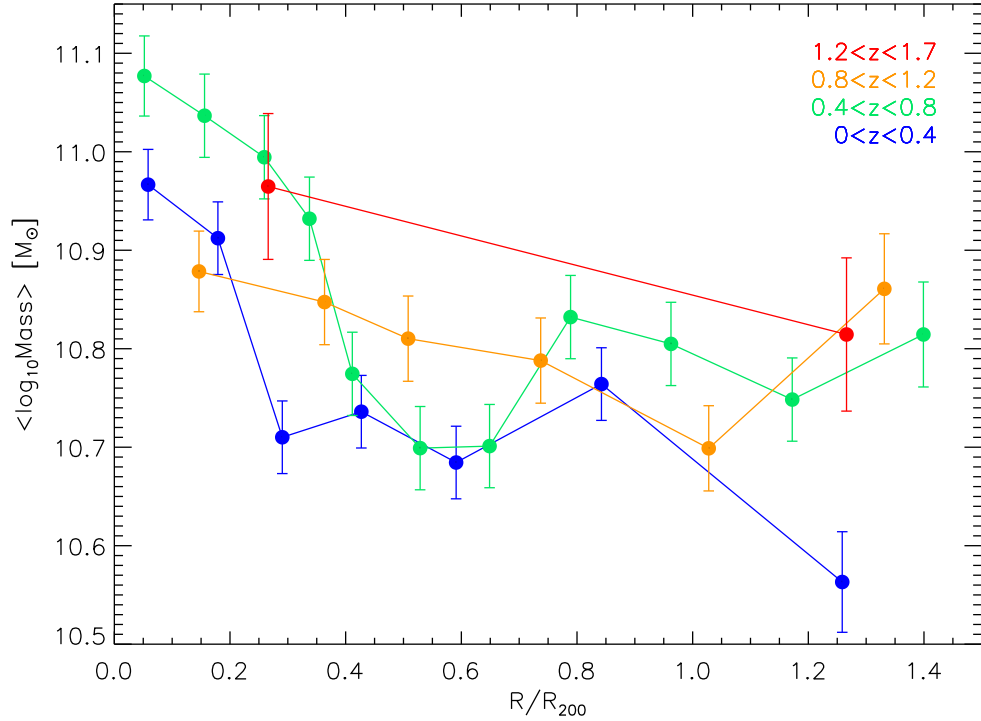


Figure 3.5: Mass as a function of group-centric distance for different redshift bins.

### 3.2.2 Is there mass segregation in galaxy groups?

The scenario described in the previous Section would be also confirmed by the rather flat relation between the mean stellar mass and the group-centric distance. Indeed, Fig. 3.5 shows that there is only a very mild ( $\sim 2.5\text{-}3\sigma$  significance level) anti-correlation between mass and distance from the center in the two lowest redshift bins and no correlation at all at  $z > 0.8$ , as confirmed by the Spearman test. Different causes can lead to the lack of a strong mass segregation in our group sample. First, we check for possible selection effects. Indeed, the very small mass range considered in our analysis ( $M > 10^{10.3} M_{\odot}$ ) can prevent us from observing a strong underlying mass segregation. To check this possibility, we analyze the stellar mass-group-centric distance relation in the lowest redshift bin with a much lower mass cut of  $10^9 M_{\odot}$ . This analysis is not possible in the higher redshift bins due to the lower spectroscopic completeness in stellar mass, as shown in Section 2.5.1. Even after considering lower mass galaxies, we observe only a marginally significant anti-correlation between stellar mass and distance.

The presence of a strong mass segregation is still matter of debate also for massive clusters. Indeed, most galaxy clusters show no significant sign of mass segregation within

the virial radius (a classical example is the Coma cluster, see White 1977). Mass segregation in bound structures is the result of relaxation or dynamical friction. In the first case, mass segregation occurs with an exchange of kinetic energy among group member galaxies with the lighter galaxies having larger velocity than the heavier galaxies. After the energy is exchanged, most massive galaxies set in the core of the cluster, while the lighter galaxies preferentially reside in the outer regions. Dynamical friction, instead, represents a kind of frictional drag which causes the galaxy motion to slow down. If the galaxy is on an orbit that makes repeated passages through the cluster or group halo, its orbit will decay over time and it will spiral in and be accreted by the larger object, thus causing that larger object to grow in mass and size. Since the timescale of dynamical friction varies as  $\sigma/\rho^3$  (where  $\sigma$  is the velocity dispersion and  $\rho$  the density of the halo), high velocity dispersion clusters do not suffer much internal dynamical evolution of their galaxy populations after their primary formation phase. Conversely, relatively low velocity dispersion groups could produce interactions and mergers on a cosmologically short timescale, even at low redshifts. Thus, if a correlation between the group-centric distance and time since the galaxy infall is expected (Gao et al. 2004; Weinmann, van den Bosch, & Pasquali 2011), radial gradients should translate into an evolutionary sequence of star formation. However, our results do not support this picture. Instead, they suggest that the relaxation or the dynamical friction timescales are not short enough to lead to a significant mass segregation at any of the considered redshifts. Our results are in agreement also with Yang et al. (2005), who do not observe a strong mass correlation in an optically selected sample of groups drawn from the 2dFGRS and the SDSS surveys, and with Presotto et al. (2012), who apply a similar analysis to a sample of optically selected clusters in the COSMOS field.

Fig. 3.5 shows also that the mean stellar mass is rather similar from low to high redshift in agreement with the mild evolution observed for the stellar mass function (e.g. Fontana et al. 2004, 2006; Ilbert et al. 2010).

As a final test we analyze also the specific SFR (sSFR)–distance relation within the group environment (Fig. 3.6). As expected due to the lack of strong relation between SFR, mass and group-centric distance, we do not observe any relation between the sSFR and the distance from the center. In Fig. 3.6 and Fig. 3.5 the error bars are estimated as in Fig. 3.4, by replacing the SFR with the stellar mass and sSFR in our error analysis.

### 3.3 SFR–density relation

The main issue about the evolution of the SFR–density relation is whether it is reversing or not at high redshift. As extensively explained in the introductory Chapter, it is well known that the SFR–density relation of the bulk of the galaxy population in the local universe is an anti-correlation (Gómez et al. 2003). Elbaz et al. (2007) and Cooper et al. (2008) claim that this relation is reversing at high redshift, indicating that the bulk of the SF activity at  $z \sim 1$  could take place in the high density regions. Both these studies are based on very small fields such as the GOODS fields (Elbaz et al. 2007) and the Groth Strip (Cooper et al. 2008). Thus, low statistics, cosmic variance, and AGN contamination could act

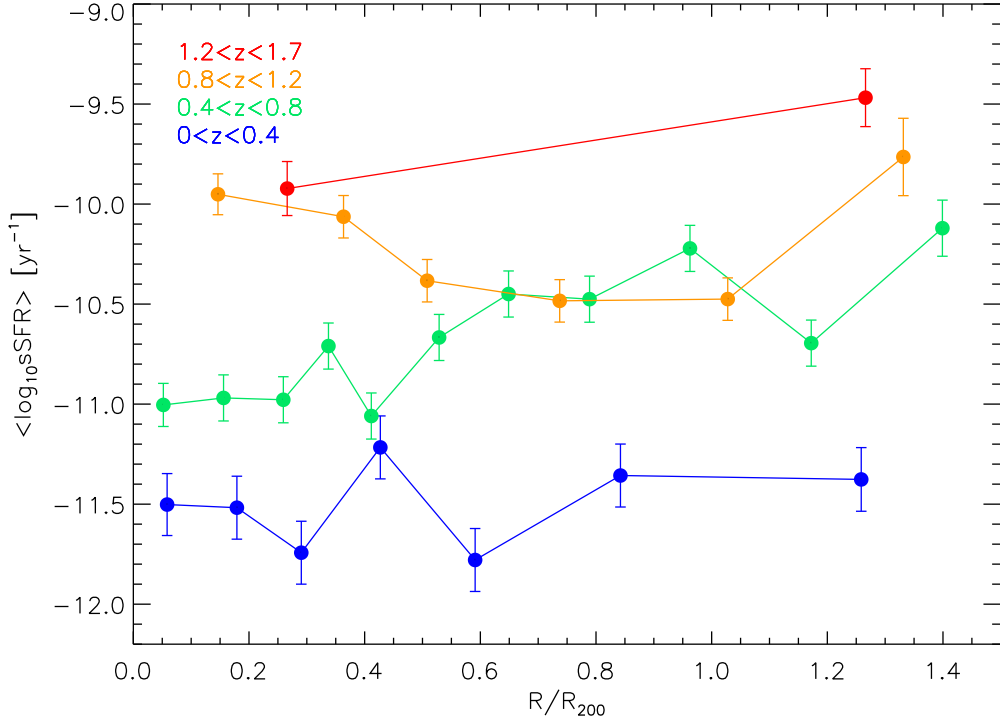


Figure 3.6: sSFR as a function of group-centric distance for different redshift bins.

against the robustness of the results. To shed light on this topic we follow the evolution of the SFR–density relation up to redshift  $\sim 1.6$  in the ECDFS and in the GOODS-N field, where the spectroscopic coverage is very high and spatially uniform, two ingredients that are essential for the aim of this analysis. The spectroscopic completeness and the sampling rate of the COSMOS field are too low and inhomogeneous, respectively, to let us perform accurately the same analysis. We build the SFR–density relation by using the density parameter estimated as explained in section 2.6 and tested against bias. First, we analyze the SFR–density relation simply studying the statistical correlation between the SFR and density parameters as usually done in the literature. This will let us compare our results with previous works. As a second approach we will use a dynamical definition of “environment” by differentiating between massive bound structures, less massive bound or unbound structures and relatively isolated galaxies. We follow the evolution of the relation in both cases up to  $z \approx 1.6$  and we test and compare our results with the predictions of simulations.

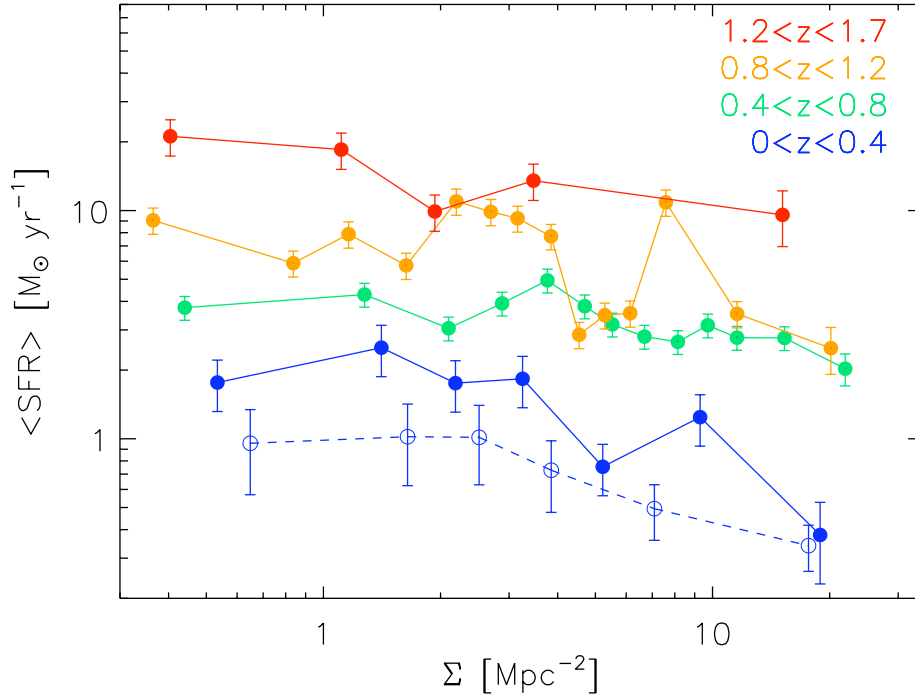


Figure 3.7: SFR–density relation for galaxies with  $M > 10^{10.3} M_{\odot}$  in different redshift bins. The dashed line represent the SFR–density relation at  $0 < z < 0.4$  with a  $10^9 M_{\odot}$  cut.

### 3.3.1 The “environmental approach”

In Fig. 3.7 we show the SFR–density relation for all galaxies with stellar mass larger than  $10^{10.3} M_{\odot}$  in the usual four redshift bins. We devote particular attention to the error analysis and the selection effects due to the spectroscopic selection. We discuss these two issues in detail in Section 2.6. We find a clear anti-correlation up to redshift  $z \sim 0.8$ , confirmed by the Spearman test at  $> 3 \sigma$  confidence level. At  $0.8 < z < 1.2$  we find an anti-correlation but with lower significance ( $2.3 \sigma$ ). In the highest redshift bin, comprising the Kurk et al. (2009) large scale structure, we do not find any significant anti-correlation ( $< 2 \sigma$  significance level). We can exclude with very high confidence level (from the Spearman test) any positive correlation in the last two redshift bins as claimed in previous works. We only observe a progressive flattening of the SFR–density relation towards higher redshifts, but no reversal of the relation.

What is the role of group galaxies in shaping the relations? In order to check this issue, we remove from the sample all galaxies associated dynamically to the X-ray extended emissions of the two fields (including the groups not included in the final group sample).

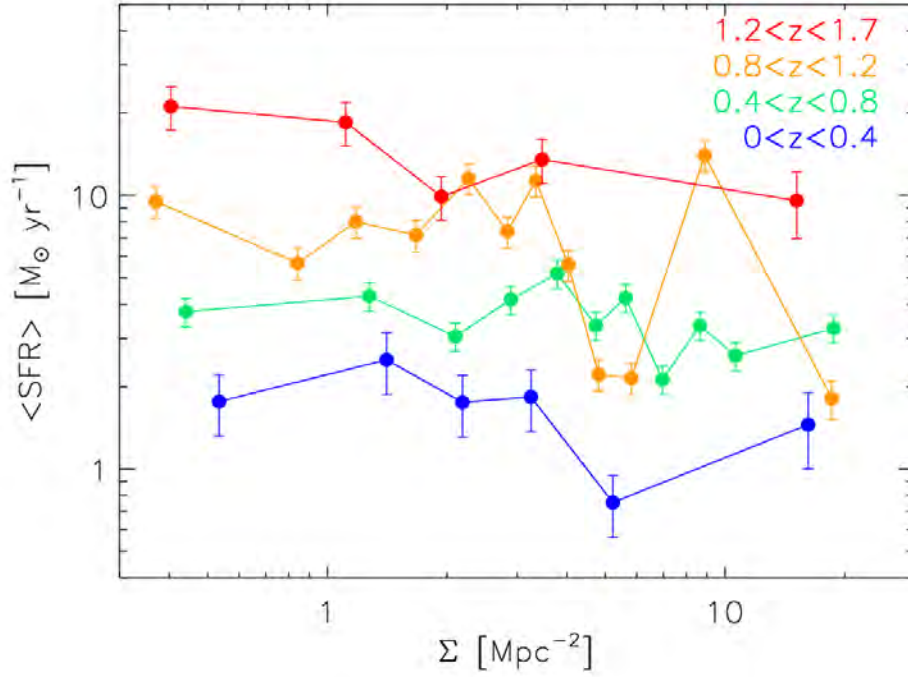


Figure 3.8: SFR–density relation for galaxies with  $M > 10^{10.3} M_{\odot}$  in different redshift bins where the group members are removed from the sample.

Fig. 3.8 shows the SFR–density relation for all the galaxies not belonging to X-ray detected groups approximately above  $M_{200} > 10^{13} M_{\odot}$ . In the two lowest redshift bins the significance of the anti-correlation decreases much below the  $3\sigma$  level. In the highest two redshift bins we still exclude a reversal but we do not see also any sign of anti-correlation. This shows clearly the dominant role of the group environment in shaping the SFR–density anti-correlation observed in the local universe and at intermediate redshift. In principle, a prominent mass segregation together with a high fraction of low star forming galaxies, typical of the group and cluster environment, could easily lead to the observed SFR–density anti-correlation observed in the local universe and at intermediate redshift. In order to check this point we explore also the stellar mass–density relation for the same sample of galaxies in the four redshift bin.

As shown in Fig. 3.9, we do not see a strong mass segregation in the galaxy sample used for the SFR–density relation analysis. The Spearman test confirms only a mild level of mass segregation at  $0.4 < z < 0.8$ . Thus, the SFR–density anti-correlation observed in the first and intermediate redshift bins are not caused by mass segregation. We can fairly conclude that the flattening of the SFR–density relation observed after excluding group galaxies, is probably caused by either a lower SF activity of group galaxies with respect to the galaxies in other environments, or to a lower fraction of SF galaxies in groups. We investigate which of these two aspects is driving the SFR–density relation in Section 3.4. However, we know

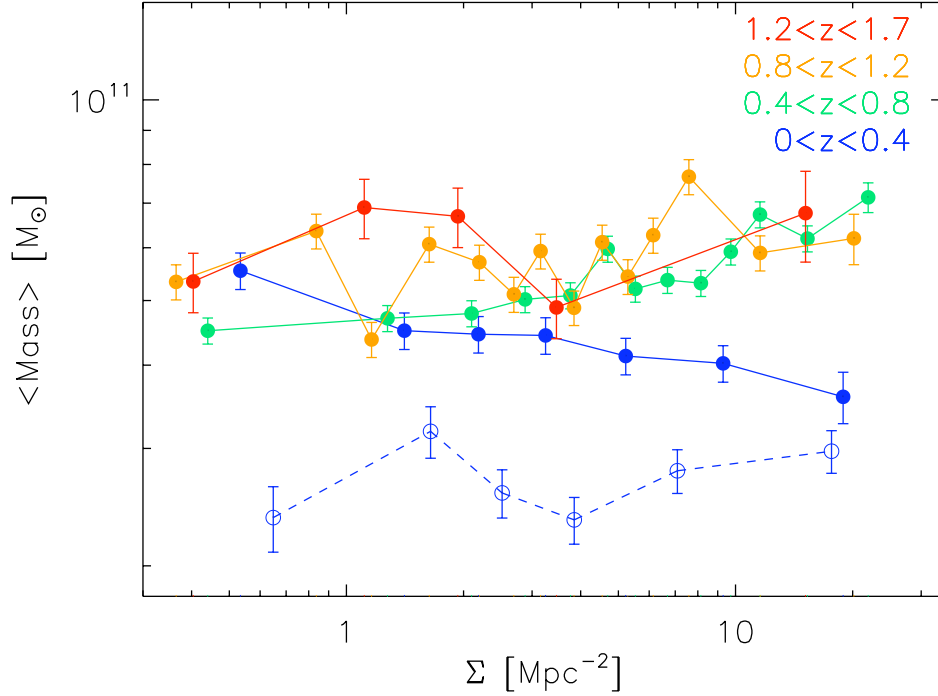


Figure 3.9: Stellar mass-density relation for galaxies with  $M > 10^{10.3} M_{\odot}$  in different redshift bins (solid lines). The dashed line represent the stellar mass–density relation at  $0 < z < 0.4$  with a cut at  $10^9 M_{\odot}$ . The lower mass cut allows to detect a significant mass segregation in the local universe in agreement with Kauffmann et al. (2004). The normalization of the dashed line is artificially increased to higher value to make it close to the blue solid line only for comparison.

that mass segregation is observed in the local universe with high significance by Kauffmann et al. (2004) on the basis of a large sample of SDSS galaxies. Are our results at odds with previous findings? The main difference with respect to Kauffmann et al. (2004) is the mass cut applied to our sample. Indeed, for spectroscopic completeness issues, we are applying a fairly high mass cut of  $10^{10.3} M_{\odot}$  while previous work applied a much lower mass cut. The dashed blue line in Fig. 3.9 shows the Mass–density relation obtained by applying a mass cut of  $10^9 M_{\odot}$  in the lowest redshift bin. This analysis is possible without strong biases only at low redshift in our sample because the spectroscopic completeness is rather high even at low stellar masses (see Fig. 2.23). The Spearman test reveals a significantly positive correlation in agreement with previous findings. This is also in agreement with the recent results of Rasmussen et al. (2012), who confirm that a significant level of mass segregation within  $10 R_{200}$  from the group center can be revealed only by including low

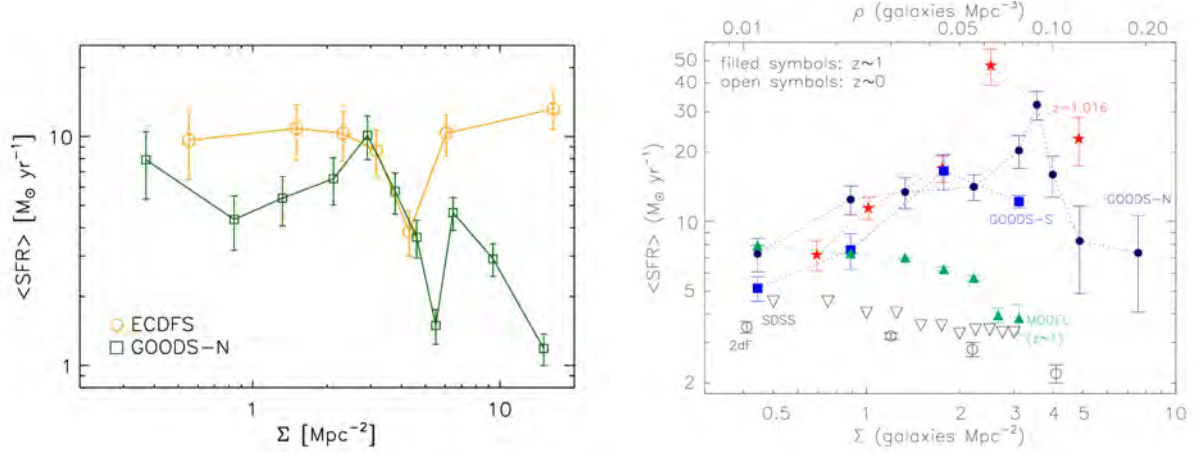


Figure 3.10: SFR–density relation for all the galaxies at  $z \sim 1$ . Left panel: we distinguish between the galaxies in the ECDFS (in orange) and GOODS-North (in green) field. Right panel: the SFR–density relation studied by Elbaz et al. (2007) in the GOODS fields.

mass galaxies. We point out that we observe an even more highly significant SFR–density relation (blue dashed line in Fig 3.7) in the lowest redshift bin after applying the lower mass cut. This probably indicates that, in a broader mass regime, mass segregation enhances the significance of the SFR–density relation.

The shape of the relations shown in Fig. 3.7 is very noisy and not even linear in log-log space. Thus it can not be fitted easily by a known fitting function. In order to quantify the steepness of the relation we simply estimate the ratio between the mean SFR at density below and above the median local galaxy density  $\Sigma$ , respectively. Below  $z \sim 1.2$ , where we see an anti-correlation, although with different significances depending on the redshift bin, the mean SFR in low density regions spans a range of 1.4-2.1 times the mean SFR of galaxies in high density regions. In the highest redshift bin we do not observe a significant difference between the SFR in low and high density regions.

The last point of our analysis focuses on understanding the disagreement between our findings and previous works claiming a reversal of the SFR–density relation at  $z \sim 1$ . The fairest comparison is with Elbaz et al. (2011) since our dataset includes the sky regions covered by their dataset. Fig. 3.10 shows on the left panel the SFR–density relation at  $0.8 < z < 1.2$  for the ECDFS and GOODS-S regions separately as obtained with our estimates of SFR and density. On the right panel we show the relation of Elbaz et al. (2007) for the GOODS-N and GOODS-S regions. Even in the GOODS-N region we observe an anti-correlation between SFR and density with high significance as confirmed by the Spearman test. We do not observe any relation between SFR and density in the ECDFS regions that contains only a very poor group at  $z = 0.96$ , differently from the GOODS-N region that comprises, in the same redshift bin, two very massive groups with masses  $M_{200} \sim 9 \times 10^{13} M_{\odot}$ . The differences with respect to Elbaz et al. (2007) can come either from the sample definition, or our recipe for the estimate of the SFR or the density. Elbaz et



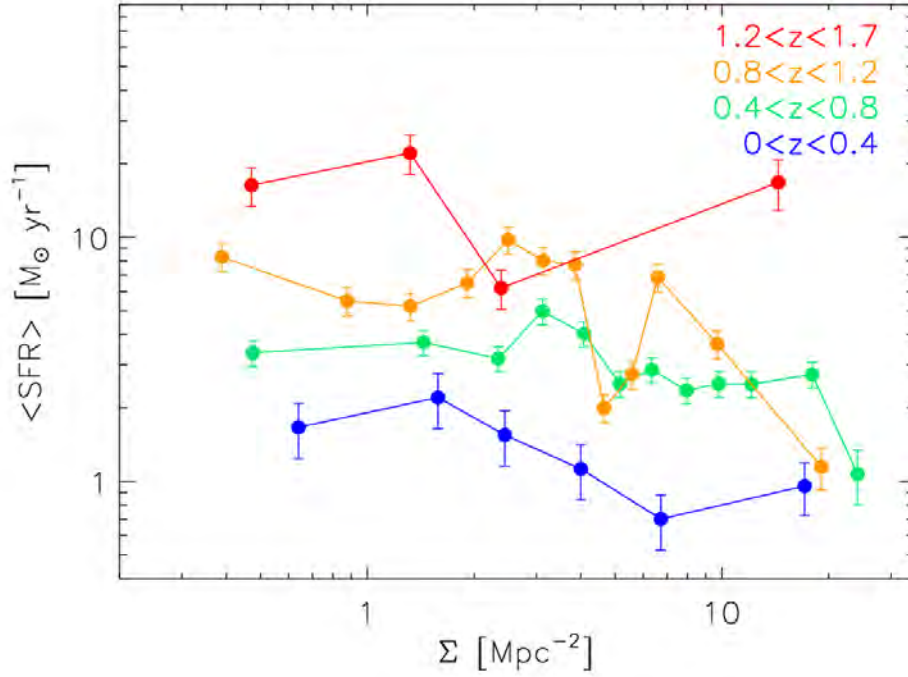


Figure 3.11: SFR–density relation for galaxies with  $M > 10^{10.3} M_{\odot}$  in different redshift bins where the AGN are removed from the sample.

al. (2007) include all galaxies with HST-ACS  $z_{AB} < 23.5$  mag without any mass cut. Given the broad redshift range considered in their work ( $0.8 < z < 1.2$ ), this apparent magnitude cut corresponds to a difference of 0.75 mag from the lowest to the highest redshift limit, thus introducing a bias with respect to our physical stellar mass selection. In addition, Elbaz et al. (2007) use Spitzer MIPS data, where available, to measure the SFR for the bulk of the SF galaxies, and UV derived SFR for all MIPS undetected galaxies. Popesso et al. (2011) show that the use of PACS data provide the big advantage, with respect to the MIPS data, of measuring without biases the SFR of AGN, whose SFR could be enhanced with respect to non active galaxies of similar stellar mass (Santini et al. 2012). Thus, given the high fraction of AGN (17%) measured at least in the highly star forming population of the GOODS-S and GOODS-N fields, Popesso et al. (2011) conclude that the reversal of the SFR observed by Elbaz et al. (2007) could be due to a bias introduced by the AGN SFR. In building the SFR–density relation, we are including all galaxies above  $10^{10.3} M_{\odot}$  with SFR much below the LIRG limit used by Popesso et al. (2011). Taking advantage of the AGN sample of Shao et al. (2010) for the GOODS-N region and the AGN sample of Lutz et al. (2010) for the ECDFS, constructed with similar criteria and X-ray flux limits, we investigate whether the AGN can bias our sample. The fraction of AGN in our sample is much lower with respect to the work of Popesso et al. (2011). Probably because, as shown also in Popesso et al. (2011), the fraction of AGN is much higher in

highly IR luminous galaxies. Thus the AGN fraction is diluted in our sample. We observe an AGN fraction of 3-5% in the ECDFS and GOODS-N region above our mass cut. If we remove the AGN from our sample, the SFR–density relation significance does not change at all (see Fig. 3.11). A further source of disagreement could be the different approach in measuring the density parameter. As explained in Section 2.6, our density estimate is based on a constant mass cut. Given the very mild evolution of the characteristic mass of the mass function (Fontana et al. 2006), this should lead to the selection of the same region of the stellar mass function at any redshift. Elbaz et al. (2007), instead, apply a simple apparent magnitude cut ( $z_{AB} < 23.5$  mag), that could lead to a strong redshift bias, as shown in Popesso et al. (2011).

We conclude that previously observed reversal of the SFR–density relations is most likely due to the combination of different selection effects due to the galaxy sample selection, a rather high fraction of AGN in the selected sample and a possibly biased definition of the density parameter, which can hide a redshift dependence.

### How robust is our analysis of the SFR–density relation?

In order to take into account all possible biases inherent to our spectroscopic selection, we study carefully the SFR–density relation in a simulated universe. For this purpose we use the mock catalog generated by the simulation of Kitzbichler & White (2007) described in Section 2.5. Fig. 3.12 shows the SFR–density relation obtained in Kitzbichler & White (2007) simulation (5 different light cones) by applying our definition of local galaxy density. We observe an anti-correlation in every redshift bins ( $> 5\sigma$  significance), including the highest redshift bin where we do not see any strong anti-correlation. Thus our results are at least qualitatively in agreement with the prediction of the Kitzbichler & White (2007) simulation but in the highest redshift bin. However, we point out that the SFR–density relations of Fig. 3.12 are observed in a sky region an order of magnitude larger than the ECDFS and the GOODS-N regions. Thus, they are sampling a much broader range of density due to the presence of massive clusters rather than only groups, as in our dataset. In order to check the implication of using a rather small area to estimate the SFR–density relation, we estimate the SFR–density relation in 1000 different regions of the Kitzbichler & White (2007) simulation with the area similar to the sum of the ECDFS and GOODS-N areas. After running a Spearman test on all datasets, we see that below  $z \sim 0.8$  we see in all cases a negative correlation with  $> 3\sigma$  significance. At  $0.8 < z < 1.2$  we see the anti-correlation in 98% of the cases and at higher redshift in 70% of the cases. The higher number of non correlation in the  $1.2 < z < 1.7$  redshift bin, is probably due to the low density of massive large scale structure predicted by the  $\Lambda$ CDM cosmology at such high redshift. Thus, cosmic variance could largely influence the significance of an anti-correlation. If we apply the same test to the incomplete catalog generated from the Kitzbichler & White (2007) mock catalog (see Section 2.5), the percentage of non correlation in the highest redshift bin increases to 45% (12%  $0.8 < z < 1.2$  and  $< 5\%$  at lower redshift). This is telling us that the small area (thus, the cosmic variance) in addition to the spectroscopic incompleteness could hide a possible anti-correlation also

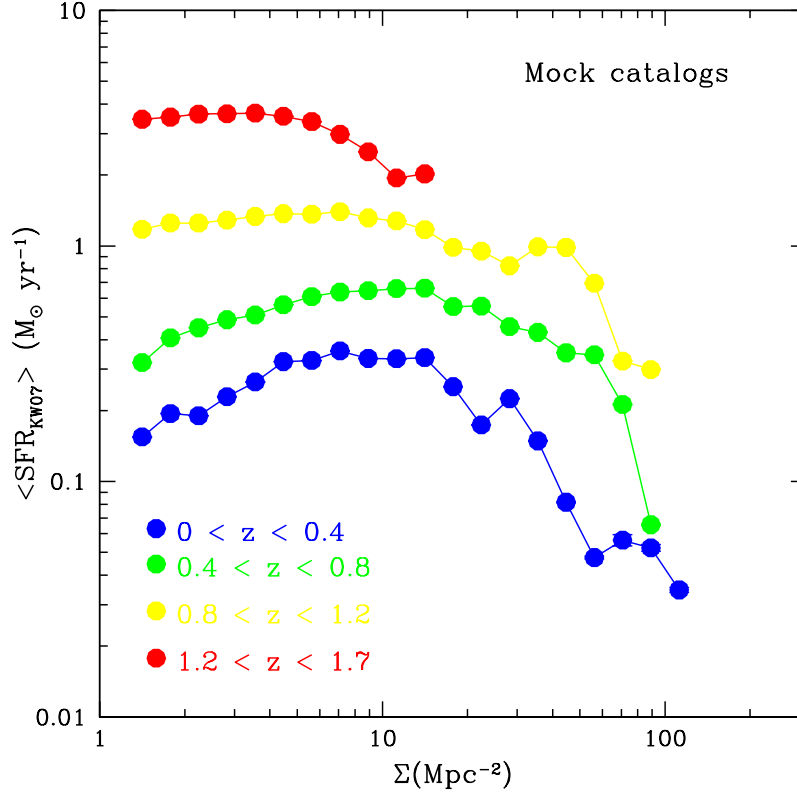


Figure 3.12: SFR–density relation at different redshift bins from the mock catalogs of Kitzbichler & White (2007).

in the highest redshift bin or reduce the significance of the anti-correlation in the lower redshift bins.

We also use the simulated incomplete mock catalog generated from Kitzbichler & White (2007) to quantify the possible bias in the estimate of the SFR–density relation due to our spectroscopic selection. We estimate the mean SFR by using the same binning in density in the incomplete catalogs and in the original complete one. This allows us to estimate the residual  $\Delta_{\text{SFR}}(\Sigma) = \langle \text{SFR}_{\text{observed}}(\Sigma) \rangle - \langle \text{SFR}_{\text{true}}(\Sigma) \rangle$ , where  $\langle \text{SFR}_{\text{observed}} \rangle$  is the mean SFR estimated in the incomplete catalog at the given density bin, and  $\langle \text{SFR}_{\text{true}} \rangle$  is the mean SFR estimated in the complete Kitzbichler & White (2007) mock catalog at the same density bin. We estimate  $\Delta_{\text{SFR}}(\Sigma)$  in the 1000 sky regions, extracted from the 5 light cones, with the area similar to the sum of the ECDFS and GOODS-N area, as explained above. This is done to take into account also the uncertainty due to cosmic variance. We estimate the mean and the dispersion of the  $\Delta_{\text{SFR}}(\Sigma)$  distribution in each density bin. The mean indicates if there is any bias in the spectroscopic selection that leads to an over- or underestimation of the mean SFR per density bin. The dispersion, instead, provides a

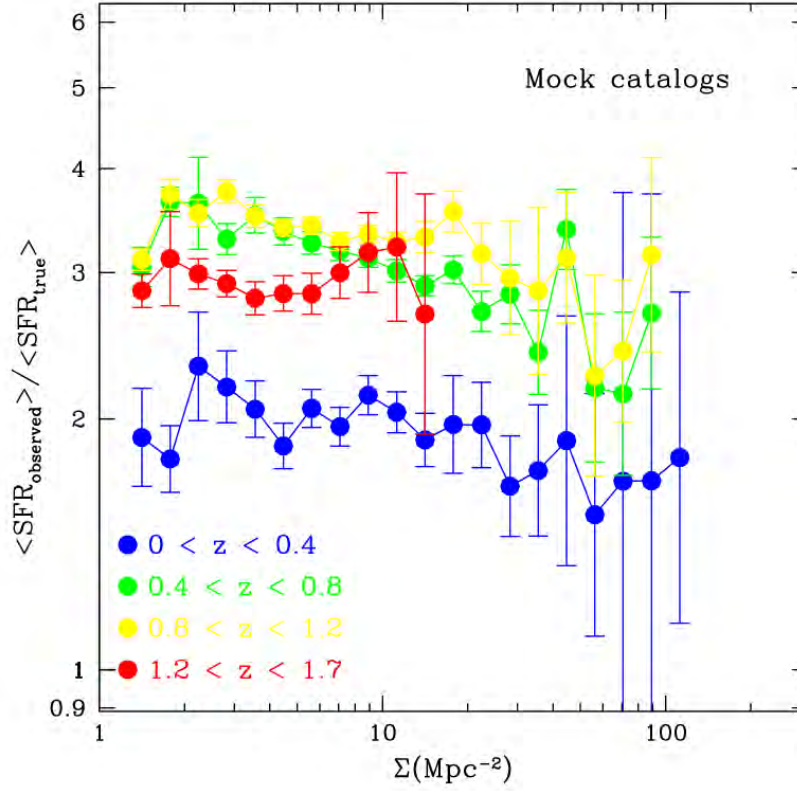


Figure 3.13: Ratio between the SFR observed and the SFR from the complete mock catalog versus density for all the four redshift bins used in this work. We do not find any bias in the slope of the SFR–density relation of Fig. 3.7.

robust estimate of the error in estimating the mean SFR per bin by using an incomplete catalog and a rather small area.

As shown in Fig. 3.13, the observed mean SFR is on average a factor of 2-4 (depending on the redshift bin) larger than the “true” one, obtained from the complete Kitzbichler & White (2007) mock catalogs, showing that the incompleteness leads to a large overestimation of the mean SFR per density bin. This is easily understandable since the simulated spectroscopic selection favors highly massive star forming galaxies (as shown in Fig. 2.23 and 2.24). The positive aspect is that, as shown in Fig. 3.13, the ratio of the observed and true mean SFR is constant as a function of the local galaxy density and is of the same order at any redshift. This implies that using our dataset we are likely overestimating the mean observed SFR in the same way at any density without biasing the shape of the relation. All these evidences convince us that our estimate of the SFR–density relation is rather robust despite the spectroscopic incompleteness which could affect the selection function of our sample. In addition we use the dispersion estimated with this procedure to

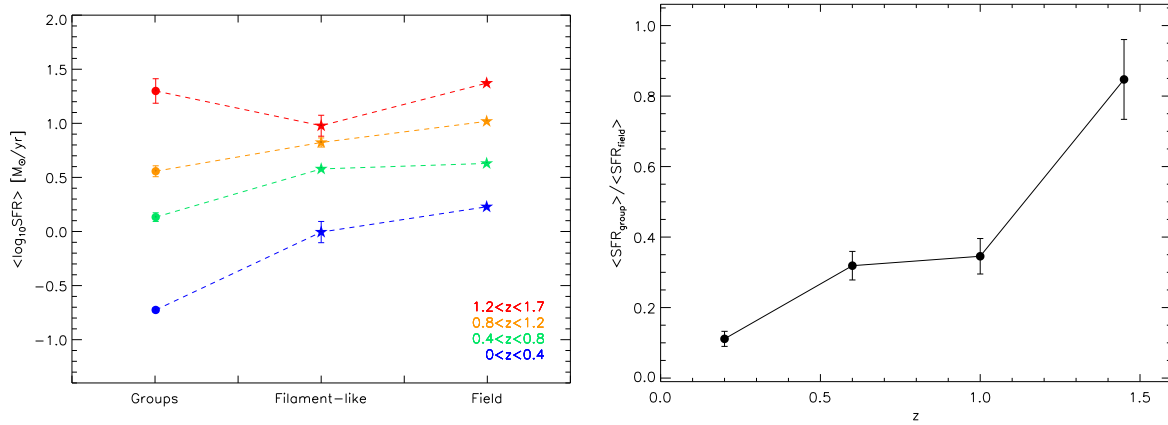


Figure 3.14: Left panel: Comparison of mean SFR among group cores (within  $R/R_{200}$ ), intermediate density (filament-like) and field. The stars represent the latter two environments. Right panel: ratio between the main properties of the field with respect to the groups as a function of redshift.

define the error bars of the observed SFR–density relation at the corresponding density.

### 3.3.2 The “dynamical approach”

As shown in Fig. 2.26, the local galaxy density of group galaxies is not completely distinguishable from galaxies likely belonging to unbound structures or dark matter halos of lower mass. Indeed, they cover the same range in local galaxy density and the distinction can be made only from the dynamical point of view, since the former belong dynamically to extended X-ray emission above the detection level (thus roughly above a mass threshold) and the latter do not. If the relative vicinity to other galaxies is the main driver in quenching the galaxy SF, we should not observe any difference in the level of SF activity between galaxies showing the same local galaxy density. If, instead, processes related to the dark matter halo play a stronger role, we should observe a difference in the level of SF activity between group galaxies and systems at high density but not related to massive dark matter halos. To check this issue, we investigate the SFR–density relation with a “dynamical” approach. In other words, we distinguish between group members, as identified via dynamical analysis, and galaxy at intermediate environment (“filament-like” environment) at the same density but not belonging to any of the detected X-ray sources (for more details see also Section 2.6). The field isolated galaxies are instead identified as the system with local galaxy density in the range of values where we do not find almost any group galaxies ( $\Sigma < 4.5 \text{ Mpc}^{-1}$ , on the left side of the green line of Fig. 2.26). Thus, we build a new version of the SFR–density relation by comparing the mean SFR in the three environments applying the usual stellar mass cut of  $10^{10.3} M_{\odot}$ .

The left panel of Fig. 3.14, shows the SFR–density relation according to our new defini-

tion. We see a strong evolution of the relative difference between mean SFR in groups and in the low density regime. Indeed, as shown in the right panel, the ratio is strongly evolving and it shows that the higher the redshift the lower the difference between the level of SF activity in groups and that in the field. This is consistent with the fact that, in the standard definition of the SFR–density relation, analyzed in previous section, the significance of the anti-correlation decreases at higher redshift until we do not find any anti-correlation at  $z \sim 1.5$ . However, in the standard SFR–density relation the mix between galaxies of different environments, but at the same densities, hides the strong evolution observed in the left panel of Fig. 3.14. Indeed, the ratio of the mean SFR between high and low density of Fig. 3.7 is rather constant and, thus, does not show any redshift dependence. This is due to the fact that the mean SFR of the intermediate (“filament-like”) environment is consistent with the mean SFR of the low density galaxies, as shown in the left panel of Fig. 3.14. Thus, for the very first time and in a robust way, we show that the estimate of the SFR–density relation based on the mere definition of the local galaxy density does not highlight the difference of the SF activity of galaxies belonging to structures in a different dynamical state. Our results also suggest that processes related to the membership of a galaxy to a massive dark matter halo must play a decisive role in the strong evolution of the SF activity of group members with respect to field galaxies.

In order to check if the strong evolution of the new defined SFR–density relation depends on a similar evolution of the Mass–density relation, we analyze with the same approach also the latter relation. Fig. 3.15 shows in the upper left panel the Mass–density relation and the right panel – the evolution of the ratio of the mean mass in group and field galaxies. We do not see strong mass segregation, in agreement with the findings of previous section. Thus, we conclude that the strong difference between group and low density regime observed at  $z < 0.8$  is likely not ascribable to a strong mass segregation. We will investigate in next section whether strong evolution of the newly-defined SFR–density evolution is due to a quenching of the SF in the SF group galaxies or to the evolution of the galaxy type mix in group and low density region.

For completeness, Fig. 3.15 shows also, in the lower panels, the evolution of the specific sSFR–density relation. This relations evolves in the same way as the SFR–density relation, since the mass–density relation is only slightly evolving.

## 3.4 The SFR-Mass plane in different environments

In this section we analyze the location of the group, “filament like” and low density galaxies in the SFR–stellar mass plane. This is done to identify the causes for the strong evolution of the SFR–density relation defined according to our “dynamical definition”.

### 3.4.1 $\Delta_{\text{MS}}$ and $f_{\text{QG}}$ evolution

As explained in the first Chapter, Noeske et al. (2007a), Elbaz et al. (2007) and Daddi et al. (2007a) find a well defined “Main Sequence” (MS) of star forming galaxies in the SFR–

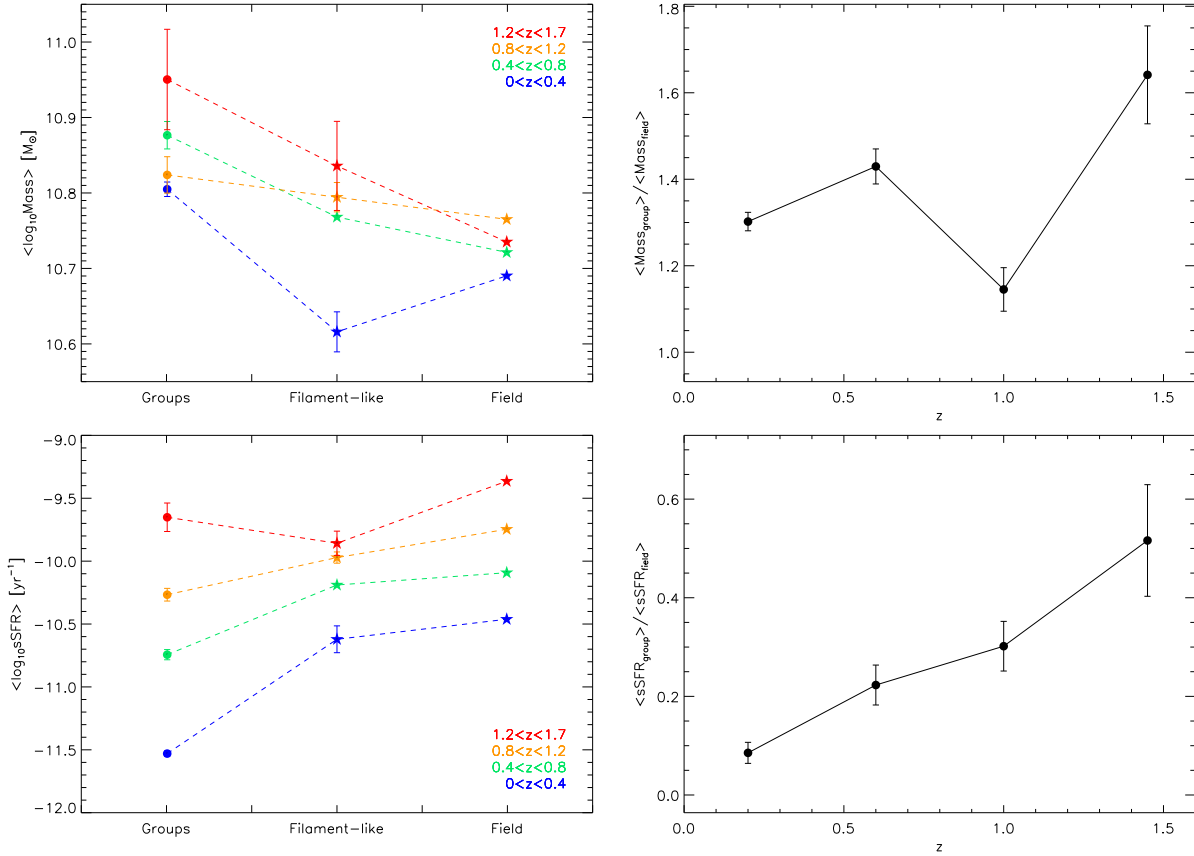


Figure 3.15: Left panel: Comparison of mean stellar mass (top panel) and sSFR (bottom panel) among group cores (within  $R/R_{200}$ ), intermediate density (filament-like) and field. The stars represent the latter two environments. Right panel: ratio between the main properties (from top to bottom stellar mass and sSFR) of the field with respect to the groups as a function of redshift.

stellar mass plane from  $z \sim 0$  up to redshift 2. The slope of the relation varies from 0.8 to 1 and shows a rather small scatter of 0.2-0.4 dex. Quiescent galaxies tend, instead, to stay below the Main Sequence in a more scattered cloud. In addition, according to Rodighiero et al. (2010), only a small fraction (10%) of outliers is found to be located above the main sequence in the starburst region.

According to Noeske et al. (2007a), this smooth sequence suggests that the same set of physical processes governs the SF activity in galaxies. If “mass quenching” is the dominant mechanism for moving a galaxy across the MS, the location of the star forming galaxies in high density environments should not be different from the bulk of the star forming galaxies regardless of their environment. If, instead, the environment plays a role in the evolution of the galaxy SF activity, the position of the group galaxies along or across the main sequence should be different with respect to the bulk of the star forming galaxies. To

check this possibility, we analyze the position of the galaxies belonging to our composite groups in the four redshift bins with respect to the main sequence of star forming galaxies of the ECDFS and GOODS-N regions in the same redshift bins at low density and at intermediate local galaxy density. In other words we follow the distinction in different environments defined in our “dynamical approach” (see Section 3.3). We do not include the COSMOS field on purpose because, although the larger statistics, the spectroscopic coverage of this field is significantly lower than the ECDFS and GOODS-N fields. We apply the following procedure. Since the Main Sequence is well studied in the literature (e.g. Daddi et al. 2007a; Elbaz et al. 2007; Noeske et al. 2007a; Peng et al. 2010), and the goal of this work is far from fitting again this relation, we use the best fit relations available in literature for the considered redshift bins. When no fit is available for our desired redshift bin, we interpolate the best fit relations of the two closest redshift bins. We define the residual  $\Delta\text{SFR} = \text{SFR}_{\text{observed}} - \text{SFR}_{\text{bestfitMS}}(M/M_{\odot})$ , where  $\text{SFR}_{\text{observed}}$  is the observed galaxy SFR and  $\text{SFR}_{\text{bestfitMS}}(M/M_{\odot})$  is the SFR given by the Main Sequence best fit at the galaxy mass. We estimate  $\Delta\text{SFR}$  for all galaxies of the ECDFS and GOODS-N field with mass above our mass cut ( $M > 10^{10.3} M_{\odot}$ ) and for the group galaxies of the composite group in the corresponding redshift bin. In order to take into account possible selection effects in populating the SFR-mass plane, in case of field galaxies, we estimate  $\Delta\text{SFR}$  for the ECDFS and GOODS-N using both the spectroscopic sample and the photometric sample, by using the photometric redshifts provided by Cardamone et al. (2010) and Berta et al. (2010), respectively. This is done mainly to check whether there is a significant lack of spectroscopic coverage in some regions of the SFR-mass plane. We stress that the MS analyzed in each redshift bin is populated mainly ( $> 80\%$ ) by PACS and MIPS detected sources. The SFR derived via SED fitting technique is efficient in populating the cloud of quiescent or low star forming galaxies below the MS.

Fig. 3.16 and 3.17 show, for each redshift bin, the SFR-Mass plane on the left panel, and the respective distribution of residual  $\Delta\text{SFR}$  on the right. In each plot, the gray points (histogram) show the MS (normalized residual distribution) of the ECDFS and GOODS-N galaxy spectroscopic sample with stellar mass above the given mass cut. The black histograms on the right panels show the normalized residual distribution of the ECDFS and GOODS-N galaxy photometric sample. The gray and black histograms are in agreement within the error bars across the whole range of  $\Delta\text{SFR}$ , showing that the spectroscopic selection function does not lead to particular biases in populating the SFR-Mass plane. Since we already observe a rather uniform spatial spectroscopic coverage across the whole ECDFS field and the GOODS fields, we conclude that also the group galaxy spectroscopic sample is not biased in the same way.

For the best fit line we use the following relations found in the literature. In the  $0 < z \leq 0.4$  redshift bin we use the MS best fit of Elbaz et al. (2007) based on SDSS star forming galaxies:

$$\text{SFR}^{[0,0.4]} [M_{\odot} \text{ yr}^{-1}] = 8.7 \times (M_{\star}/10^{11} M_{\odot})^{0.77} \quad (3.1)$$

In the  $0.4 < z \leq 0.8$  redshift bin we do not find a best fit in the literature, thus, the relation is obtained by interpolating the MS relation of Peng et al. (2010) at  $z \sim 0$  and the



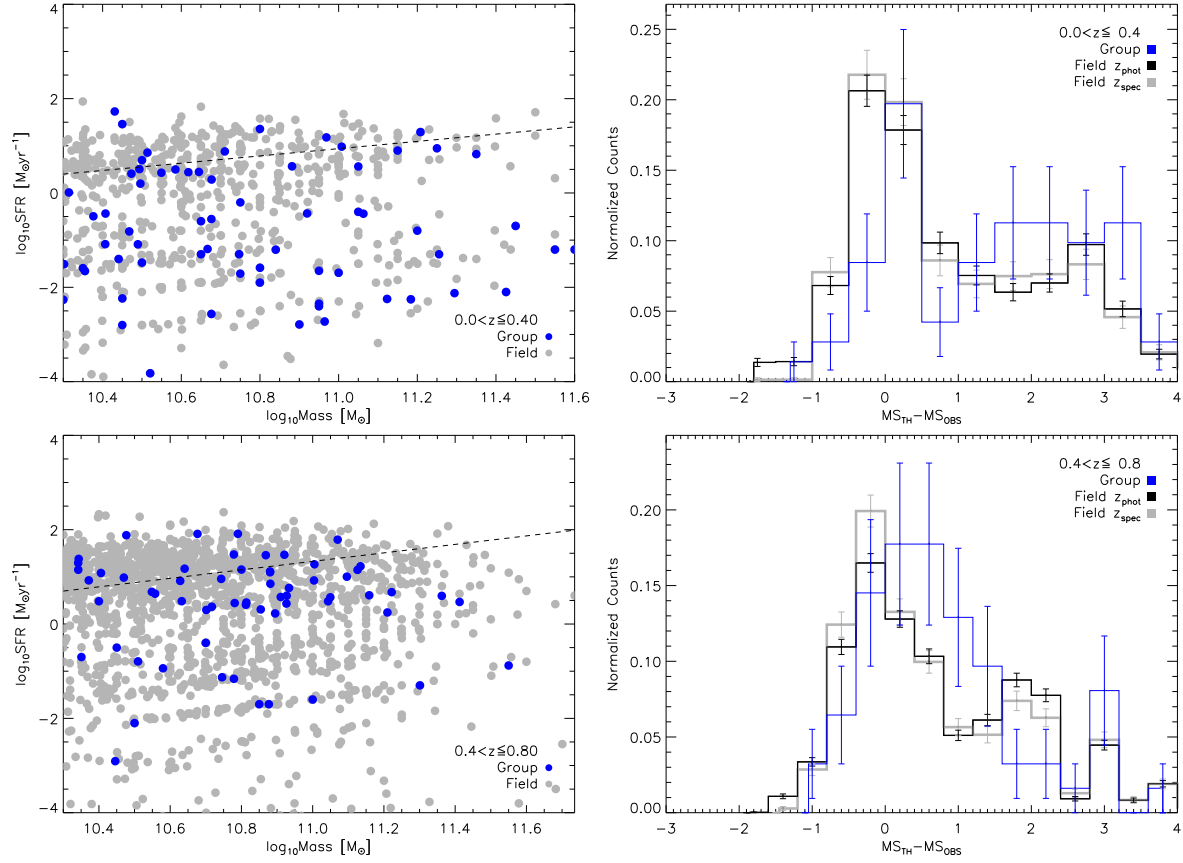


Figure 3.16: *Left column*: SFR-M diagrams for the redshift bins  $0 \leq z < 0.4$  and  $0.4 \leq z < 0.8$  for group (in blue) and field (in gray) galaxies. We over-plotted the MS relation from Elbaz et al. (2007) at  $z \sim 0$  in the top panel and the average relation between the MS of Peng et al. (2010) at  $z \sim 0$  and Elbaz et al. (2007) at  $z \sim 1$  in the bottom panel. *Right column*: residuals w.r.t. the corresponding MS relation for groups (in blue) and field (in gray for the spectroscopic sample and in black for the photometric one).

MS relation of Elbaz et al. (2007) at  $z \sim 1$  based on *Spitzer* MIPS detected star forming galaxies:

$$\text{SFR}^{[0.4,0.8]} [\text{M}_{\odot} \text{ yr}^{-1}] = 10^{8.6} \times (\text{M}_{\star}/\text{M}_{\odot})^{0.9} \quad (3.2)$$

In the  $0.8 < z \leq 1.2$  redshift bin we use the MS best fit relation obtained by Elbaz et al. (2007) at  $z \sim 1$  based on GOODS star forming galaxies:

$$\text{SFR}^{[0.8 < z \leq 1.2]} [\text{M}_{\odot} \text{ yr}^{-1}] = 7.2 \times [\text{M}_{\star}/10^{10} \text{ M}_{\odot}]^{0.9} \quad (3.3)$$

For the last redshift bin,  $1.2 < z \leq 1.7$ , the MS best fit relation is not available in the literature. Thus we interpolate between the Elbaz et al. (2007) MS relation at  $z \sim 1$  (Eq. 3.3) and the Daddi et al. (2007a) best fit MS relation at  $z \sim 2$ . We obtain the

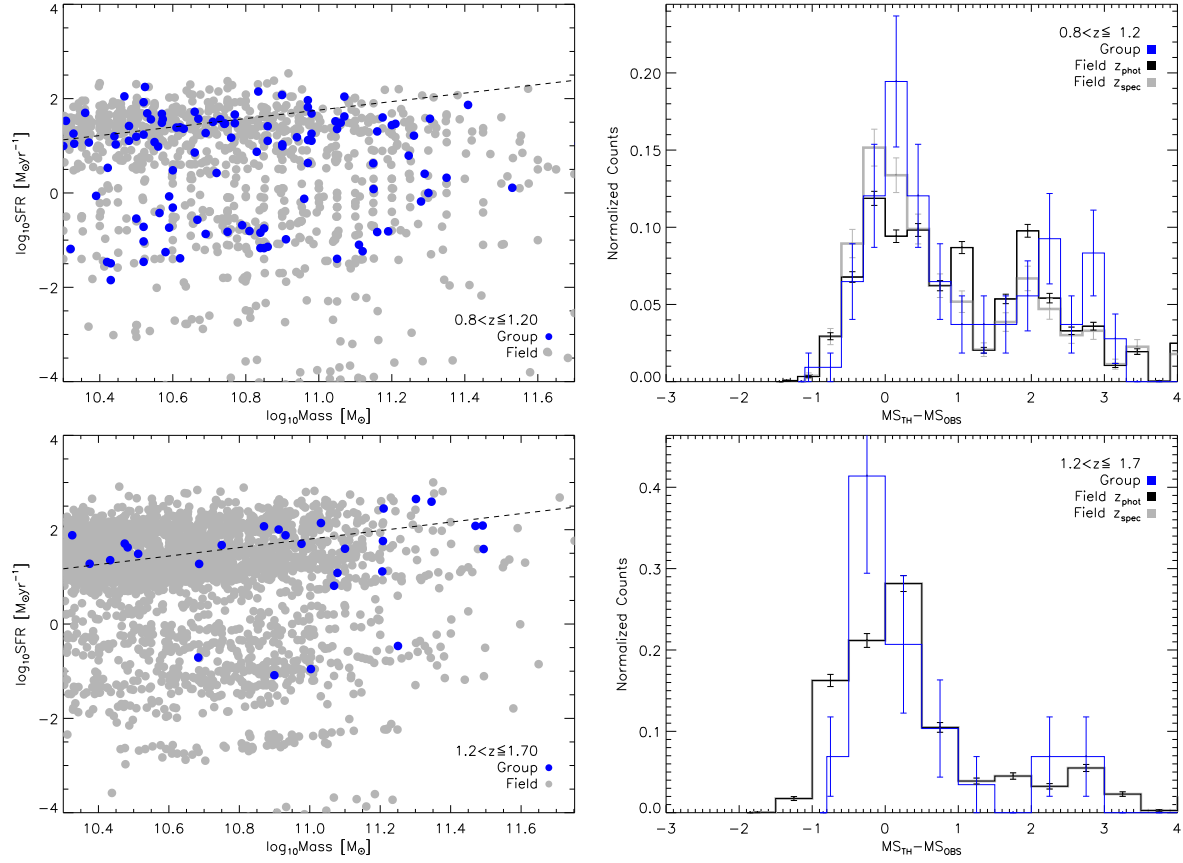


Figure 3.17: *Left column:* SFR-M diagrams for the redshift bins  $0.8 \leq z < 1.2$  and  $1.2 \leq z < 1.6$  for group (in blue) and field (in gray) galaxies. We over-plotted the MS relation from Elbaz et al. (2007) at  $z \sim 1$  in the top panel and the average relation between this relation and the one of Daddi et al. (2007a) for galaxies at  $z \sim 2$  in the bottom panel. For the last redshift bin we use the photometric sample for the field in order to have better statistics. *Right column:* residuals w.r.t. the corresponding MS relation for groups (in blue) and field (in gray for the spectroscopic sample and in black for the photometric one).

following relation:

$$\text{SFR}^{[1.2 < z \leq 1.7]} [M_{\odot} \text{ yr}^{-1}] = \log (200 \times [M_{\star}/10^{11} M_{\odot}]^{0.9}) - 0.5 \quad (3.4)$$

In all cases we find a rather good agreement between our gray data points and the best fit relations. Indeed the Gaussian distribution peaked at  $\sim 0$  in the  $\Delta_{\text{SFR}}$  residual histogram is easily visible in all panels. Only in the last redshift bin, the interpolated MS best fit is not in excellent agreement with the gray points (field galaxies). The best fit relation derived directly from our data show very large uncertainties due to the rather low statistics. Our best fit is anyhow in agreement with the interpolated MS relation. Thus, we decide to keep as reference the interpolated MS relation.

The blue points (histogram) in Fig. 3.16 and 3.17 show the position of galaxies in the SFR–Mass plane (normalized residual distribution) of the group galaxy sample in each bin. In order to identify and quantify the difference between the location across the MS of group galaxies in each bin with respect to the low and intermediate density galaxies, we apply the following procedure. The distribution of the  $\Delta_{\text{SFR}}$  of the bulk of the galaxy population (see black histograms in right panels of Fig. 3.16 and 3.17) shows a well known bimodal distribution with the Gaussian representing the MS location with peak around 0 residual, and a tail of quiescent/low star forming galaxies at high positive values of  $\Delta_{\text{SFR}}$ . This distribution is reminiscent of the bimodal behavior of the  $U - R$  galaxy color distribution observed by Strateva et al. (2001) in the SDSS galaxy sample. Following the example of Strateva et al. (2001), we identify the minimum value of the valley between the MS Gaussian and the peak of the broader quiescent/low star forming galaxies distribution. At all redshifts, the value  $\Delta_{\text{SFR}} = 1$  turns out to be the best separation between the two galaxy populations. Indeed, the observed scatter of the MS at any redshift varies between 0.2-0.4 dex (Daddi et al. 2007a; Elbaz et al. 2007). Thus, the limit at  $\Delta_{\text{SFR}} = 1$  should be consistent with a  $3\sigma$  cut from the best fit MS relation. We use this value to separate MS galaxies from quiescent/low star forming galaxies in the three considered environments. We measure the mean distance ( $\Delta_{\text{MS}}$ ) from the MS location of the galaxy population in each environments at  $-1 \leq \Delta_{\text{SFR}} \leq 1$ . By definition  $\Delta_{\text{MS}}$  should be consistent with 0 for the bulk of the MS galaxies. Indeed, the center of the Gaussian distribution (the mean) is highly consistent with 0. This confirms that our choice of the MS relation represents our data well. Only in the highest redshift bin, the low statistics prevents us from measuring accurately the  $\Delta_{\text{MS}}$  for the bulk of the MS galaxies, although our estimate is still consistent with 0 within  $1\sigma$  error. We stress once again, that given the depth of the PACS and *Spitzer* MIPS observations of the ECDFS and the GOODS fields (where all of the  $z > 0.4$  groups turn out to be located), the MS is fully sampled (80%) by IR-derived SFR with very small (10%) uncertainties. The SED fitting derived SFRs populate the region below the MS at  $\Delta_{\text{SFR}} > 1$ . Thus, our estimate of the  $\Delta_{\text{MS}}$  should not be affected by the large error (0.5-0.6 dex) in the determination of the SFR via SED fitting (see Section 2.3.2). We devote particular attention to the estimate of the error of  $\Delta_{\text{MS}}$  for field and group galaxies to take into account all possible selection effects inherent in our spectroscopic selection. Thus, we discuss in a separated section our error analysis (see Section 3.4.2).

The left panel of Fig. 3.18 shows the evolution of the  $\Delta_{\text{MS}}$  for the MS galaxies in low density environments (gray stars and line), at intermediate density (filament-like, small mass groups, green stars and line) and in groups (blue stars and line) up to redshift  $z \sim 1.6$ . In the first two redshift bins, the  $\Delta_{\text{MS}}$  of the MS group galaxies is systematically below 0 (bulk of MS galaxies) at 3-3.5 $\sigma$  level. At  $z > 0.8$  the MS group galaxies are perfectly on sequence consistently with the lower density environments. Moreover, the intermediate density MS galaxies are always placed between the low density environment and the group galaxies.

This result shows for the first time in a robust way (see also the discussion of the error analysis in next section) that at least below redshift  $\sim 0.8$  the star formation activity in group galaxies is lower than the bulk of the SF galaxies. Thus, we can not rule out

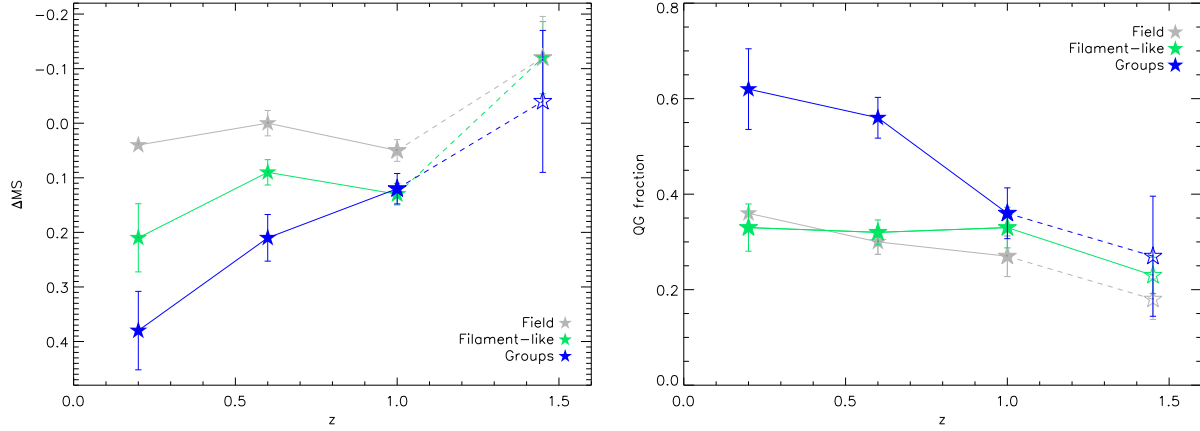


Figure 3.18: Left panel: Evolution of the Main Sequence for group and field galaxies.  $\Delta_{\text{MS}}$  represents the central value of the residuals with respect to the predicted MS for each redshift bin (right column of Fig. 3.16 and Fig. 3.17). We use the spectroscopic sample for group (blue stars), filament-like (green stars) and field (gray stars) galaxies. Right panel: Evolution of the quiescent galaxy (QG) fraction for group (blue stars), filament-like (green stars) and field (gray stars) galaxies. We define “quiescent” all the galaxies with  $\Delta_{\text{MS}} > 1$ .

completely the pre-processing scenario (galaxies are pre-processed in groups before entering in clusters). This is consistent with the result of an analogous analysis done by Bai et al. (2010) on the sample of 2dF groups already mentioned in previous discussion. Interestingly, they show that the group galaxy MS is displaced below the field MS, as in our dataset, but above the location of the MS cluster galaxies, thus, showing that a certain amount of pre-processing is happening in groups but a further quenching must happen even in the more dense cluster environment. Here we show that a certain amount of pre-processing happens even before the star forming galaxies enter in the group environment when they are falling along the filaments in the lower mass groups that will eventually merge to form the more massive groups. Thus, we show that the speed of the evolution of the SF activity in star forming galaxies depends, at least since  $z \sim 1$ , on the galaxy environment: the higher the density, the faster the evolution.

As further analysis, we investigate also the evolution of the galaxy type mix in the three different environments. The galaxy type mix is expressed in terms of level of SF activity through the fraction of quiescent galaxies ( $f_{\text{QG}}$ ). We define as quiescent galaxies all the systems with a  $\Delta_{\text{SFR}} > 1$ , that is, systems in the scattered cloud below the MS. Similarly to the  $\Delta_{\text{MS}}$  analysis, we estimate the mean  $f_{\text{QG}}$  in low density, intermediate density and group regions in the four redshift bins. The error is estimated via simulations that take into account the spectroscopic selection function and thus the related selection effects, as explained in Section 3.4.2. Right panel of Fig. 3.18 shows the evolution of the  $f_{\text{QG}}$  in the three environments. Low density (gray stars and line) and intermediate density regions (green stars and line) exhibit the same galaxy type mix at any redshift and no evolution is observed in these environments at least in the mass range considered in our analysis.

The galaxy type mix in groups shows a strong evolution at  $z < 0.8$ , where the fraction of quiescent galaxies is twice the mean fraction observed at high redshift, perfectly in line with the various evidences of the Butcher & Oemler (1978a) effect.

The two plots of Fig. 3.18 are showing us two different aspects of the role of environment in the evolution of the galaxy SF activity. Some degree of quenching is observed since we observe an “environment gradient” as a function of the distance from the MS. However, the right panel of the same figure shows that density is not responsible for the different galaxy type mix. Indeed group and “filament” like regime by definition cover the same range of local galaxy density. The main difference in the two regimes is that in the group regime galaxies belong to a massive ( $M_{200} \sim 2 \times 10^{13} M_{\odot}$ ) bound dark matter halo, while in the “filament like” regime galaxies likely belong to unbound structures, such as filaments, or lower mass halos. Thus, the different evolution of the galaxy type mix of the two environments, similar in density but not in dynamical properties, tells us that the galaxy type mix is connected to the properties of the parent dark matter halo rather than strictly on the galaxy local environment (density).

### 3.4.2 The error analysis

The aim of our error analysis is to estimate the error in  $\Delta_{MS} (f_{QG})$  by comparing the  $\langle \Delta_{MS} \rangle$  (QG fraction) derived in a galaxy sample with a spectroscopic selection function similar to the one of our dataset and a parent complete galaxy sample. Thus, we take advantage once again of the mock catalogs reproducing the spectroscopic incompleteness of our data and generated from the complete Kitzbichler & White (2007) mock catalogs (see Section 2.5). For the error estimate we apply a technique similar to the one used for the error estimate of the mean SFR (mass and specific SFR) as a function of the group-centric distance. We extract 1000 random galaxy coordinates (ra, dec) in each of the 100 “incomplete” mock catalogs derived from the Kitzbichler & White (2007) catalogs. We use those coordinates as a center of an area with radius ranging randomly from 0.05 to 0.5 deg. Sampling areas of different size allows us to sample a different number of galaxies ( $N_{gal}$ ). In this way, we can express the error on the mean distance from the MS as a function of the number of galaxies used for the estimate, since the higher the number of galaxies, the higher the accuracy in the knowledge of a mean.

Our aim is to apply the same technique used to analyze the real dataset. Thus, we need the residual  $\Delta_{SFR}$  with respect to the MS relation to measure (fit) the mean distance from the MS at  $-1 < \Delta_{SFR} < 1$ . However, the evolution of SFR-Mass plane predicted by the Kitzbichler & White (2007) catalogs is different from the one observed up the redshift considered in our work (see also Elbaz et al. 2007). Indeed simulated SF galaxies, in particular at high redshift, tend to be less star forming than in observations. Thus, the location of the MS of the mock catalog at  $z > 1$  tend to be below the observed MS in the same redshift bin. In order to cope with this problem we change the normalization of the observed MS relation (see Eq. 3.1, 3.2, 3.3 and 3.4) by keeping the observed slope, in order to match the simulated MS location. Fitting directly the simulated MS is providing similar results. This procedure provides a million of different independent estimates of the

mean distance from the MS per redshift bin and  $N_{\text{gal}}$  ranging from 5 to 200. In each area we measure, then, the mean distance from the MS at  $-1 \leq \Delta_{\text{SFR}} \leq 1$  as done in the real data ( $\langle \Delta_{\text{MS}} \rangle$ ).

We follow the same procedure in the original and complete Kitzbichler & White (2007) mock catalog at the exact same positions. We measure then the difference of the  $\Delta_{\text{MS}}$  measured in the “incomplete” mock catalogs and the original complete mock catalog ( $\delta(\Delta_{\text{MS}})$ ). This quantity tells us about the error in the estimate of the  $\Delta_{\text{MS}}$  due to the incompleteness and the spectroscopic selection function of our dataset. We bin the simulated  $\delta(\Delta_{\text{MS}})$  per  $N_{\text{gal}}$  number in each redshift bin. We check that in each redshift bin the mean of  $\delta(\Delta_{\text{MS}})$  distribution is highly consistent with 0 across the whole range of  $N_{\text{gal}}$ . Thus, the spectroscopic selection does not prevent a correct determination of the mean distance from the MS even for low values of  $N_{\text{gal}}$ . The dispersion of the  $\delta(\Delta_{\text{MS}})$  distribution provides, instead, an estimate of the error in the determination of the mean distance from the MS that takes into account both the number of galaxies involved in the estimate and the uncertainty due to the spectroscopic selection function of our dataset. For the real dataset we use as error the uncertainty obtained with this technique at the corresponding value of observed  $N_{\text{gal}}$  and redshift bin.

We apply the same technique to estimate the error in the estimate of the QG fraction by estimating in a similar way mean and dispersion of the  $\delta(f_{\text{QG}})$  distribution per redshift and  $N_{\text{gal}}$  bin.

### 3.5 Summary

We analyze the dependence of the SF activity, stellar mass and specific SFR on the group-centric distance of the composite groups in each redshift bin. In addition we study the evolution of this dependence, for the very first time up to redshift  $\sim 1.6$ . We do not find any correlation between SFR and group centric distance (as confirmed by the Spearman test) at any redshift. This is consistent with previous findings and confirms the different distribution of the SF galaxies within the group region with respect to the cluster region. The mean SFR in group galaxies increases with redshift, in agreement with the picture of Noeske et al. (2007a) and Elbaz et al. (2007), who argue that the universe was more active in forming stars in the past. Consistently with the flat SFR-distance relation, we do not observed any strong mass segregation in groups at any redshift. This could indicate a very long relaxation or dynamical friction timescale, which are usually the responsible for creating mass segregation.

By studying the SFR-density relation in the standard way, we find an anti-correlation up to  $z \sim 0.8$  but no correlation at higher redshift. Although the significance found by the Spearman test decreases as the redshift increases, we do not observe any reversal of the SFR-density relation. We check the presence of biases using the mock catalogs of Kitzbichler & White (2007), as shown in Fig. 3.13. Although we constantly overestimate the values of SFR at all redshifts, due to the spectroscopic incompleteness of our catalogs, the slope of our SFR-density relation is not affected by any bias. This allows us to

confirm the robustness of our result. We check that the role of AGN is rather marginal in shaping the relation. Instead, the anti-correlation at  $z < 0.8$  is dominated by spectroscopic group members. We check if the SFR-density relation could be driven by a strong mass segregation. However, our galaxy sample shows only a very mild mass segregation at any redshift bin.

By using the “dynamical” definition of environment, we see more clearly, for the first time and in a robust way, that the bulk of quenching happens in the groups. Indeed, group spectroscopic members show a much lower mean SFR than galaxies at similar density but not belonging to bound structures of the same mass at least up to  $z \sim 1$ . Indeed, galaxies in less massive bound or unbound structures exhibit the same level of SFR as field isolated galaxies. Group galaxies reach the same level of SF activity as field galaxies only at  $z > 1$ . However, even with this alternative approach, we do not see any significant SFR-density reversal. The ratio of the mean galaxy properties with respect to the field in the different redshift bins, reveals no big variation in the mass segregation with redshift, but a strong evolution in SFR and sSFR. Thus, we conclude that group galaxies experience a much faster evolution with respect to galaxies in other environments. In addition, the strong difference in the evolution of the group galaxies with respect to non-group galaxies at similar density reveals that processes related to the presence of a rather massive dark matter halo, rather than purely density-related processes, must be dominant in the suppression of the SF activity in group galaxies below redshift 1.

In order to understand the cause of the faster evolution in group galaxies, we study also the location of the groups, intermediate and low density galaxies in the SFR-stellar mass plane. This is done to identify if the lower mean SFR in groups at  $z < 1$  with respect to field galaxies is due to a general quenching of the SFR in all galaxies or to a faster evolution of the galaxy type mix. We find that the so called star forming galaxy Main Sequence of the groups is offset with respect to the field galaxies up to  $z \sim 0.8$ , i.e. it is shifted towards less star forming galaxies. At higher redshift the star forming group galaxies are on sequence. The intermediate density galaxies occupy at every redshift a halfway position between groups and field. This suggests that both the density- and halo-related processes are playing a role in quenching the star formation activity of active star forming galaxies. Interestingly, the quiescent galaxy (QG) fraction evolves much faster in the groups than in the other two environments up to  $z \sim 0.8$ , beyond which the fractions are comparable. This suggests that the different type mix in groups is likely the driver of the strong evolution observed in the SFR-density relation analyzed in the dynamical approach.





## The role of merging activity in the evolution of the star formation

Star formation is quenched in high density environments like clusters, where processes like ram pressure (Gunn & Gott 1972), strangulation (Larson, Tinsley, & Caldwell 1980), and galaxy harassment (Moore et al. 1996) are particularly efficient. Indeed, Tran et al. (2009) observe a higher fraction of star forming galaxies in a super-group at  $z = 0.37$  with respect to clusters at the same redshift. It has however also been claimed that SF quenching of cluster galaxies occurs in low-mass groups prior to cluster assembly (the so-called “pre-processing”, Zabludoff & Mulchaey 1998). As shown in the previous Chapter, we see some degree of quenching (i.e. the star formation is “damped” in high density environments with respect to the field) and, thus, pre-processing, in groups below  $z \sim 0.8$ . The accretion process of groups onto clusters can itself lead to SF quenching (Poggianti et al. 2004), for a rapid gas consumption due to a sudden enhancement of the SF activity (Coia et al. 2005). In order to find an exit in this labyrinth of possible solutions we must follow the evolution of the star formation activity in structures through the different phases of the structure formation. A simple way to achieve this goal is to compare the SF activity of the cluster building blocks (groups), the merging systems and the final relaxed massive clusters at similar redshift. A way of looking at the evolution of the SF activity in galaxy systems is to consider a global quantity such as the total star formation rate per unit of halo mass, that is the sum of the SFRs of all system members, divided by the system total mass,  $\Sigma(\text{SFR})/M$ . Thanks to the data collected during the Herschel GT and KT Programs PEP (P.I. D. Lutz) and GOODS-H (P.I. D. Elbaz), respectively, Popesso et al. (2012) accurately estimate the total SFRs of 9 galaxy groups, taken from our sample, with masses  $\sim 5 \times 10^{13}$ , and 9 massive clusters with mass  $\sim 10^{15} M_{\odot}$  down to  $L_{\text{IR}} = 10^{11} L_{\odot}$  and up to redshift 1.6. According to Popesso et al. (2012), groups show a higher SF activity than massive clusters at any epoch. The similarity of the field and the groups  $\Sigma(\text{SFR})/M-z$  relations suggests that the SF quenching is taking place mostly after galaxies enter the

cluster environment, and not in groups before merging, as predicted by the pre-processing scenario. Thus, galaxies experience an accelerated evolution following their accretion to more massive structures, as individuals or in groups. Interestingly, the Bullet cluster, which experienced a major merger  $\sim 250$  Myr ago (Springel & Farrar 2007), appears to lie in between the clusters and the groups. Possibly this is caused by the “contamination” due to infalling group (the “bullet”) which is actively star forming, as already suggested by Chung et al. (2010). If ram-pressure stripping, effective on short time scales, was a major SF quenching process, the Bullet cluster SF galaxies should be already quenched since the time of the major merger. However, the uncertainty in the total SFR of the Bullet cluster is too large to lead to a robust conclusion. Thus we need to increase the sample of merging systems, to investigate whether the total SFR per halo mass, and, thus, the level of SF in structures depends on the dynamical state of the system. In order to perform this analysis, we select two massive ( $M \sim 10^{15} M_{\odot}$ ) X-ray galaxy clusters at  $z \sim 0.3$ . We take advantage of the X-ray selection to identify some groups in the region encompassed by the cluster field to study how the star formation activity is affected by the presence of the groups and as a function of the dynamical state. In fact, since the “Bullet” cluster exhibits an enhanced SF activity compared to virialized clusters (Popesso et al. 2012), our aim is to investigate whether the time elapsed after the main merging event plays a role in the quenching of the star formation. The two merging systems analyzed in this Chapter are taken from the DXL survey (Zhang et al. 2006). We introduce here the DXL survey, describe the optical and X-ray data used to identify the substructures and time since the main merger event. We, then, analyze the total SFR per halo mass to locate the cluster in the Popesso et al. (2012) diagram to confirm or deny the role of the merging activity in affecting the level of SFR in structures.

## 4.1 The DXL sample

In order to understand the role of merging in the evolution of the star formation activity in clusters and in their large scale structure (LSS) environment we need a sample of galaxy clusters with small mass range and different dynamical states. With this purpose we have selected a statistically complete cluster sample drawn from the ROSAT ESO Flux Limited X-ray (REFLEX) survey (Böhringer et al. 2001). The 13 distant X-ray luminous (DXL, see e.g. Zhang et al. 2004a and Zhang et al. 2005 for details) clusters have luminosity  $L_X^{\text{bol}} = 0.5 - 4 \times 10^{45} \text{ erg s}^{-1}$ , masses  $M_{500} = 0.5 - 1.1 \times 10^{15} M_{\odot}$ <sup>1</sup> and are located within a narrow redshift interval ( $z = 0.27 - 0.31$ ). The DXL sample is a powerful instrument to investigate the mass assembly of the clusters and the evolution of galaxies therein, together with the exploration of the link between large-scale structure, substructure and galaxy population. Moreover, this snapshot of the Universe is comparable to N-body simulations including hydrodynamics (e.g. Borgani & Kravtsov 2009, ZuHone 2011), allowing us to

---

<sup>1</sup> $M_{\Delta}$  (where  $\Delta = 500, 200$ ) is defined as  $M_{\Delta} = (4\pi/3)\Delta\rho_c R_{\Delta}^3$  where  $R_{\Delta}$  is the radius at which the density of a cluster is equal to  $\Delta$  times the critical density of the Universe ( $\rho_c$ ). Throughout our analysis we adopt the X-ray estimate of  $R_{\Delta}$  (unless it is otherwise specified).

better investigate the physics that regulates cluster evolution across the cosmic web. For instance, one can understand the variation of the sub-halo mass function, traced by galaxies and the amount of substructure in clusters; estimate time scales from the dynamical state of the gas; and understand the physical processes that drive its behavior. In fact, DXL can be represented as a sequence of cluster dynamical states, starting from early stages of merging events (including several components of different mass) towards strong cool core clusters.

Most of the detailed X-ray analysis of DXL clusters has been already performed (Zhang et al. 2004a, Zhang et al. 2004b, Zhang et al. 2005, Zhang et al. 2006, hereafter referred to as Z06, Finoguenov, Böhringer & Zhang 2005). These studies, focused on the ICM, have provided valuable information on the dynamical state, AGN feedback and chemical enrichment of these clusters.

Optical analysis of the DXL sample has started in parallel. In particular, the attention was focused on two clusters with different dynamical states: an ongoing major merger (Braglia, Pierini, Böhringer 2007) and a relaxed cluster (Braglia et al. 2009, hereafter referred to as B09), in order to compare their kinematics and galaxy distributions with their X-ray properties. Braglia, Pierini, Böhringer (2007) found, associated with the merging cluster A 2744, two large-scale filaments along which blue galaxies exhibited enhanced star formation activity. This study was followed up in B09 who explored the existing link between the fraction of passively evolving galaxies and the assembly state of the cluster. Pierini et al. (2008) then suggested, from observations of three DXL clusters, that the intra cluster light has multiple origins, possibly linked to the dynamical state of the cluster.

In this chapter we present the results from the study of RXCJ1131.9–1955 (alias Abell 1300), and RXCJ0516–5430 (alias Abell S0520) at  $z \sim 0.3$ . Abell 1300 is a post-merging cluster at  $z \sim 0.3075$  with a “dumbbell” cD galaxy (Pierre et al. 1997) at its center and prominent filaments visible in the galaxy density distribution. The definition of post-merging cluster dates back to Lemonon et al. (1997) who state that this cluster has undergone a merger but the merging phase may be nearly over. Abell S0520 exhibits an X-ray elliptical morphology. It hosts 3 bright galaxies at its center, connected by a bridge of diffuse light. The central galaxies are aligned in the same direction as the elongation of the X-ray surface brightness (North-South) and a large scale filament populated by blue galaxies.

We analyze these two structures to connect the level of star formation activity to the cluster dynamical state and to check whether the merging activity can enhance or quench the galaxy star formation.

## 4.2 Observations and Data Reduction

### 4.2.1 Wide-field Imaging

Optical photometry was carried out using the Wide Field Imager (WFI, Baade et al. 1999) mounted on the Cassegrain focus of the ESO/MPG-2.2 m telescope at La Silla, Chile.

Passband	ZP	$k$	CT
B	$24.55 \pm 0.01$	$0.20 \pm 0.01$	0.24
V	$24.15 \pm 0.01$	$0.14 \pm 0.01$	-0.12
R	$24.43 \pm 0.01$	$0.09 \pm 0.01$	0.01

Table 4.1: Photometric solutions determined in this work. Column 1 gives the passband, column 2 the zero-points in the Vega magnitude system, column 3 the extinction coefficient and column 4 the color term. Two of the three quantities are reported with respective errors in the Vega magnitude. These best-fit parameters were obtained from a two-parameter fit from about 850 to 2000 measurements across the WFI field for each passband, the color term being fixed.

The data presented here were obtained as part of a heterogeneous program during MPG observing time in visitor mode (P.I.: Böhringer). The observations of A1300 and AS0520 in the B, V and R passbands were performed in 2001, between January 27th and February 1st, in photometric conditions. They were divided into sequences of 8 dithered sub-exposures for a total exposure time of 3150 s for the V band and 3600 s for the R and B bands for A1300, while for AS0520 the total exposure time was 2700 s for the V band, 4050 s for the R and 4800 s for the B band. Filter curves can be found in Arnouts et al. (2001) and on the web-page of the La Silla Science Operation Team<sup>2</sup>. Standard stars were observed in all the four nights: three Landolt fields (Landolt 1992) were targeted for a total of 35-50 standard stars per field (SA98, SA101 and SA104).

The WFI data were reduced using the data reduction system developed for the ESO Imaging Survey (EIS, Renzini & da Costa 1997) and its associated EIS/MVM image processing library version 1.0.1 (*Alambic*<sup>3</sup>). For more details on the transformation of raw images into reduced ones see Pierini et al. (2008). Source detection and photometry were based on SExtractor (Bertin & Arnouts 1996) both for standard and science images. Magnitudes were calibrated to the Johnson-Cousins system using Landolt (1992) standard stars whose magnitudes were obtained using a 10 arcsec-wide circular aperture, which were adequate as judged from determining the average growth curve of all the measured stars. Photometric standards were observed over a rather broad range of airmasses, but science frames were taken at the best airmass; in this way we were able to obtain photometric solutions (e.g. zero-points) for the calibration of reduced scientific images by merging the measurements of standard stars for each passband. The number of non-saturated Landolt stars per field did not allow independent solutions to be determined for each of the eight chips of WFI. Hence calibration had to rely upon solutions based on measurements taken across all chips. Although the EIS data reduction system includes a photometric pipeline for the automatic determination of photometric solutions, these were determined interactively using the IRAF<sup>4</sup> task *fitparams*. This choice allows the interactive rejection of

<sup>2</sup><http://www.eso.org/sci/facilities/lasilla/instruments/wfi/inst/filters>

<sup>3</sup>[http://www.eso.org/sci/activities/projects/eis/survey\\_release.html](http://www.eso.org/sci/activities/projects/eis/survey_release.html)

<sup>4</sup>IRAF is the Image Reduction and Analysis Facility, a general purpose software system for the reduction and analysis of astronomical data. IRAF is written and supported by the IRAF programming group at

Passband	ZP	$k$	CT
B	24.65	0.23	0.24
V	24.19	0.15	-0.12
R	24.47	0.12	0.01

Table 4.2: Median values for all the photometric solutions in the Vega magnitude system based on three parameter fits obtained by the ESO DPS team.

Passband	ZP	$k$	CT
B	24.81 $\pm$ 0.05	0.22 $\pm$ 0.015	0.25 $\pm$ 0.01
V	24.15 $\pm$ 0.04	0.11 $\pm$ 0.01	-0.13 $\pm$ 0.01
R	24.47 $\pm$ 0.04	0.07 $\pm$ 0.01	0.00 $\pm$ 0.00

Table 4.3: Definitive photometric solutions obtained by the 2p2 Telescope Team from observations of standard stars in perfectly photometric nights, where a bunch of standard star fields were moved around each chip of WFI. All parameters were fitted simultaneously as free parameters, with good airmass and color range, and around 300 stars per fit. The Table below gives the average solutions in the Vega magnitude system over all chips.

individual measurements, stars, and chips. Photometric solutions with minimum scatter were obtained by a two-parameter linear fit with about 850 photometric points for the B-band, about 900 for the V-band and more than 2000 for the R-band, the atmospheric extinction coefficient in each band being set equal to that listed as the median value obtained by the EIS team<sup>5</sup>. In general, zero-points and color terms are consistent with those obtained by the EIS team or by the 2p2 Telescope Team<sup>6</sup>, as can be seen by comparing Tables 4.1–4.3.

As for science images, source extraction and photometry were obtained after matching the BVR images of each target to the worst seeing (0.92'' for Abell 1300 and 0.90'' for Abell S0520, both in the V band), using the IRAF task *psfmatch*, and taking into account the weight-maps associated with the individual images, produced by *Alambic*. A common configuration file was used to produce three catalogs per target, after evaluating the seeing and the zero-point for individual images. The R-band image having the deepest exposure was used as the detection image, where sources are defined by an area with a minimum number of 5 pixels above a threshold of  $1\sigma$  of the background counts. Source photometry in individual passbands was extracted in fixed circular apertures (between 1.2'' and 10'' in diameter) or in flexible elliptical apertures (Kron-like, Kron 1980) with a Kron-factor of 2.5 and a minimum radius of 3.5 pixels. For our analysis we used the total magnitudes (Kron-like). Object magnitudes were corrected for Galactic extinction according to the

the National Optical Astronomy Observatories (NOAO) in Tucson, Arizona. NOAO is operated by the Association of Universities for Research in Astronomy (AURA), Inc. under cooperative agreement with the National Science Foundation.

<sup>5</sup><http://www.eso.org/sci/activities/projects/eis/surveys/readme/70000027>

<sup>6</sup><http://www.eso.org/sci/facilities/lasilla/instruments/wfi/zero-points>

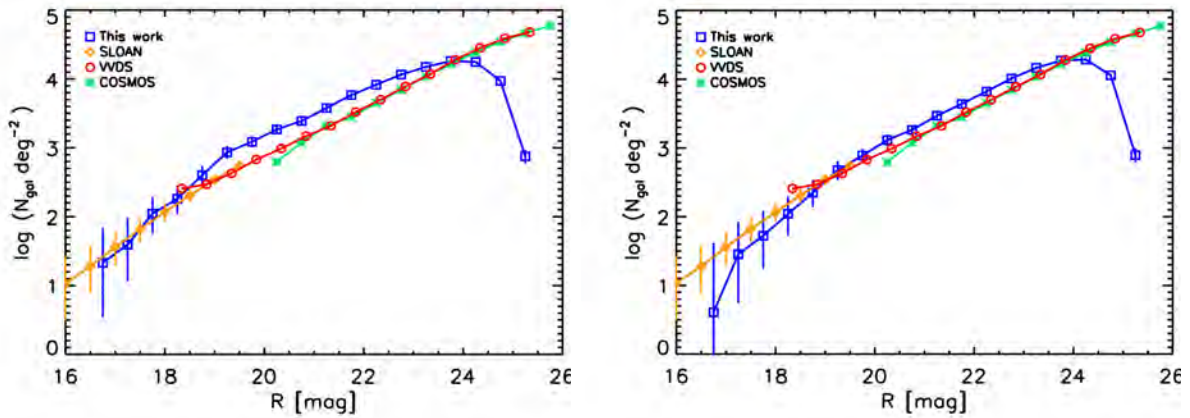


Figure 4.1: Comparison of number counts for the entire region of A1300 (on the left) and AS0520 (on the right) imaged with WFI in this work and three deep fields/wide area surveys: VVDS (red circles), COSMOS (green stars) and SDSS (orange diamonds). All errors, but those of COSMOS (for which errors were available, Capak et al. 2004), were obtained using the statistics of Gehrels (1986).

Schlegel, Finkbeiner, & Davis (1998) galactic reddening maps (from NED) and converted to the AB system according to the response function of the optical system (see Alcalá et al. 2004). The output catalogs were successively culled of fake sources by hand and by using masks before photometric redshifts were determined. In addition, stars and galaxies could be safely identified on the basis of their surface brightness profile and optical colors down to  $R = 21.5$ . Fainter than this limit, number counts are dominated by galaxies, so that all detected objects with  $R > 21.5$  are assumed to be galaxies. This assumption is supported by several tests that we run, comparing colors and magnitudes derived with different methods. Information from SExtractor flags was also taken into account in these tests.

Depth and quality of the final catalogs were also determined. Galaxy number counts in the observed field were compared with deep number counts from several surveys (i.e. VVDS, VIMOS VLT Deep Survey, McCracken et al. 2003; COSMOS, Cosmic Evolution Survey, Capak et al. 2004; and SDSS, Sloan Digital Sky Survey, Yasuda et al. 2001). All errors, but the ones from COSMOS (for which errors were available, Capak et al. 2004), were obtained using Poissonian statistics from Gehrels (1986).

Our galaxy number counts exceed those obtained from observations of deep fields such as VVDS (McCracken et al. 2003) and COSMOS (Capak et al. 2004) in the range  $18.5 \lesssim R \lesssim 23.5$  mag, as shown in Fig. 4.1. On the other hand, they begin to drop below the galaxy number counts in deep fields/wide area surveys at  $R > 23.5$ , where the number of background galaxies dominates the number of likely cluster members. The bright end is comparable with the number counts of SDSS (Yasuda et al. 2001). Assuming as a completeness limit the magnitude at which the observed counts are equal to 50% of those in

the deep fields/wide area surveys, we thus conclude that our R-band selected catalogs are complete down to  $\sim 24 \text{ mag}_{\text{AB}}$  with respect to the VVDS.

### 4.2.2 Spectroscopic Data

Multi-Object Spectroscopy (MOS) was performed at VLT between the periods of May 21-23, 2004 and January 12-19, 2005 as part of the ESO GO large program 169.A-0595 (P.I. Böhringer), carried out in visitor and service modes. The main aim of this program was to observe the largest number of galaxies lying in the same area of the sky for seven out of the 13 DXL clusters.

Low resolution ( $R = 200$ , LR-Blue grism) spectroscopy was carried out with VIMOS (VIsible Multi-Object Spectrograph, Le Fèvre et al. 2003) mounted on VLT-UT3 at Paranal Observatory (ESO), Chile. VIMOS is a wide-field imager and multi-object spectrograph operating in the visible (from 3600 to 10000 Å), with an array of 4 identical CCDs with a field of view (FOV) of  $7' \times 8'$  each and 0.205'' pixel scale, separated by a gap between each quadrant of  $\sim 2'$ .

To provide good coverage of the cluster central region and to extend the analysis to the cluster outskirts we used three pointings that partially overlap in the center and reach beyond a distance of 4 Mpc in the E-W direction from the cluster X-ray center (we present an example in Fig. 4.2).

Objects with  $I \leq 22.5$  were selected from the pre-imaging with VLT-VIMOS, corresponding to a limiting magnitude of approximately  $I^* + 3$  galaxy at the redshift of the cluster (0.3075, see Couch et al. 1998). The pre-imaging was done in the I-band in order to select targets based only on stellar mass (e.g. Worthey 1994) and avoiding any color bias. The catalog on the pre-imaging was produced running SExtractor (Bertin & Arnouts 1996) which allowed to classify galaxies with  $I \leq 20$  as bright and objects with  $20 < I \leq 22.5$  as faint, in order to observe them with two different masks (prepared using the VMMPs<sup>7</sup> tool from ESO) for the same OB. Slits of 1'' width were used for an expected uncertainty on the observed velocities of  $250 - 300 \text{ km s}^{-1}$ . Previous works (Braglia, Pierini, Böhringer 2007 and B09) have confirmed these expectations and shown that with these uncertainties it is possible to establish the membership of a galaxy and the global cluster dynamics for the massive clusters of REFLEX-DXL.

At the average redshift of the DXL ( $z \sim 0.3$ ) the LR-Blue grism samples several important spectral features: [OII], [OIII],  $\text{CaII}_{\text{H+K}}$ ,  $\text{H}_\beta$ ,  $\text{H}_\delta$  lines and the 4000 Å break. The combination of these features allows us to characterize the spectral type of galaxies (e.g. by the 4000 Å break), the present star formation rate (e.g. by the [OII] line) and nuclear activity (by the [OII]/[OIII] line ratio). The spectrum in this wavelength range does not suffer from fringing and spectroscopic redshifts up to  $z \sim 0.8$  can be determined.

The spectroscopic observations provided about 900 spectra which were reduced using the dedicated software VIPGI<sup>8</sup>. VIPGI allows to calibrate all spectra through a user-

<sup>7</sup><http://www.eso.org/sci/observing/phase2/VIMOS/VMMPs.html>

<sup>8</sup>VIPGI (VIMOS Interactive Pipeline and Graphical Interface, Scoddeggio et al. 2005). This software

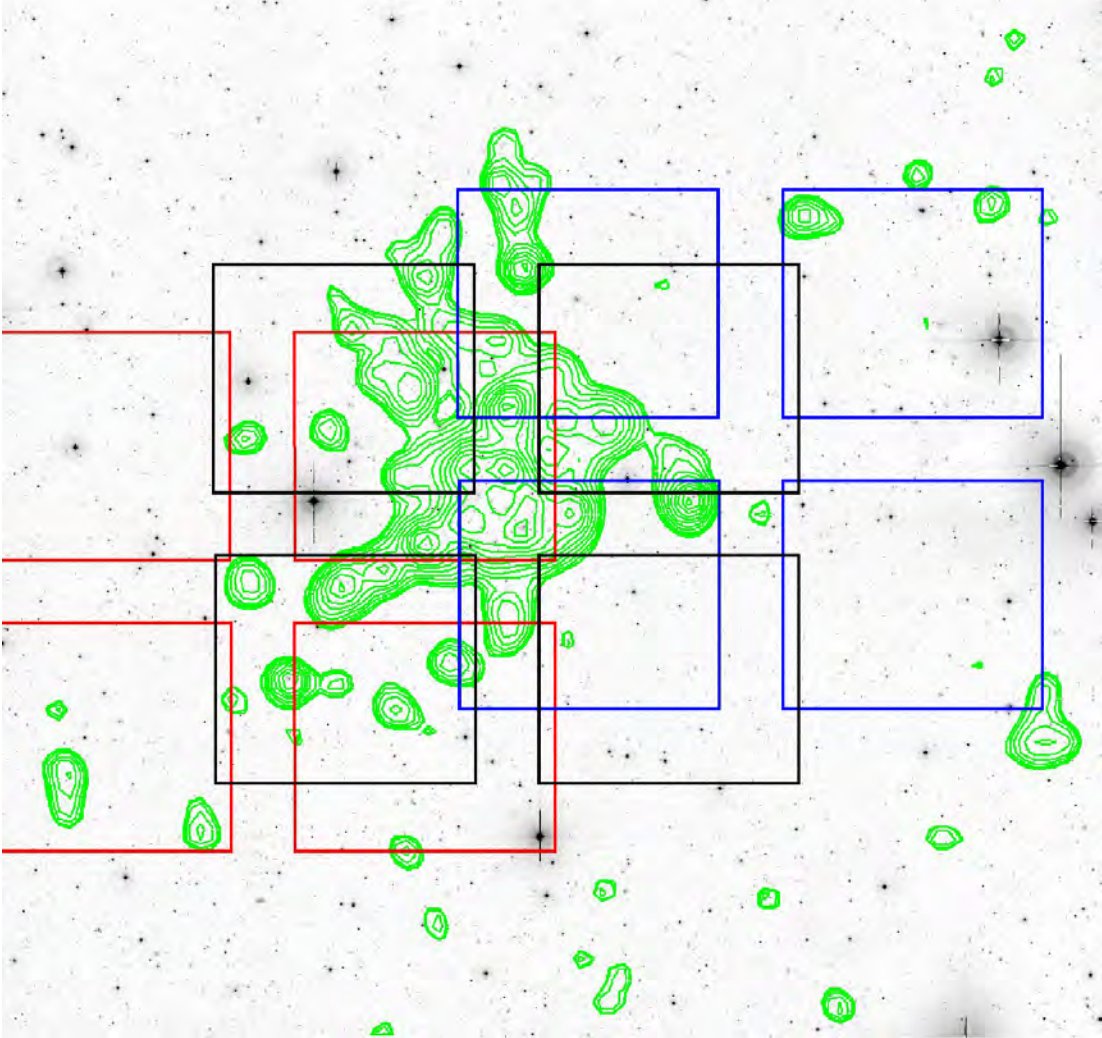


Figure 4.2: R-band image of A1300 on which are overlaid density contours (in green) and the three VIMOS pointings. Each set of four boxes with the same color represents one VIMOS pointing. This observing strategy was adopted for all the 13 DXL clusters.

friendly interface, applying flat fields corrections, sky subtraction, spectrum extraction and wavelength calibration. Data reduction followed the standard approach, as described in the VIPGI manual and in Scodeggio et al. (2005): lines were fitted and matched with available line catalogs. Furthermore, we used the template fitting procedure EZ (Easy redshift, Garilli et al. 2010), that allows fitting of spectral templates to the continuum when no evident features (e.g. emission lines) were present. Although EZ mainly relies on a  $\chi^2$  template-fitting procedure it also allows us to choose the best template after an analysis by eye. We assigned different flags to the redshifts according to their reliability:

---

was developed by the VIRMOS Consortium to handle the reduction of the VIMOS data for the VVDS (McCracken et al. 2003)



$flag = 0$  was given when it was not possible to assign a redshift,  $flag = 1$  meant a confidence in the redshift within 25%,  $flag = 2$  a reliability of the solution comprised between 25% and 50%,  $flag = 3$  between 50% and 75% and  $flag = 4$  between 75% and 100%. In order to ensure reliable cluster memberships we only use galaxies with spectral flags larger than 2 in the following.

We expanded our sample of spectroscopic redshifts with the publicly available ones on NED: for A1300 we retrieved 96 more redshifts, while for AS0520 we enlarged our sample of 108 spec-z with 34 redshifts published by Guzzo et al. (2009) and Menanteau & Hughes (2009).

### 4.2.3 Archival GALEX imaging

Galaxy Evolution Explorer<sup>9</sup> (GALEX) is a space telescope observing in far ultraviolet (FUV, extending from 1350Å to 1780Å) and in near ultraviolet (NUV, extending from 1770Å to 2730Å) (Martin et al. 2005). In these bands it is possible to constrain the recent star formation activity of galaxies as the UV light comes from massive young stars. The galaxy data archive allows to retrieve the UV data via the MultiMission Archive at Space Telescope Science Institute (MAST). Positions and magnitudes (with respective errors) were obtained from the All-Sky Imaging Survey (ASI) for which GR6 data release was available. A1300 is not well covered by GALEX observations, since just one corner of the field encompassed by WFI is available. On the other hand, AS0520 is fully sampled by the observations from this satellite.

We corrected the object magnitudes for the Galactic extinction according to the color excess provided in the GALEX catalog (in agreement with the Schlegel, Finkbeiner, & Davis (1998) reddening maps) and the mean galactic attenuation computed by the stand alone program *filter\_extinc* provided in *Le PHARE*. The program *filter\_extinc* yielded the mean galactic attenuation as a function of color excess ( $E(B-V)$ ) assuming the Cardelli, Clayton, & Mathis (1989) extinction law.

In order to take into account the GALEX PSF of 6'' and to decrease the possibility of wrong identifications, optical counterparts were searched within a radius of 7''. In case of multiple counterparts we chose the closest source with emission in the B band.

We successfully associated 1258 sources in our catalog of AS0520 with NUV and/or FUV emission, of which only 17 had a spectroscopic redshift.

As we would expect, in the color-magnitude diagram (B-R versus R), most of the galaxies with GALEX emission lie below the red sequence. However, some red sequence galaxies have UV emission.

### 4.2.4 X-ray imaging

The clusters A1300 and AS0520 were observed by XMM-Newton (Fig. 4.3 and Fig. 4.4) in AO-1 as part of the DXL cluster sample in July 2001 (Böhringer et al. 2001, Z06). The

---

<sup>9</sup>[http : //galex.stsci.edu](http://galex.stsci.edu)

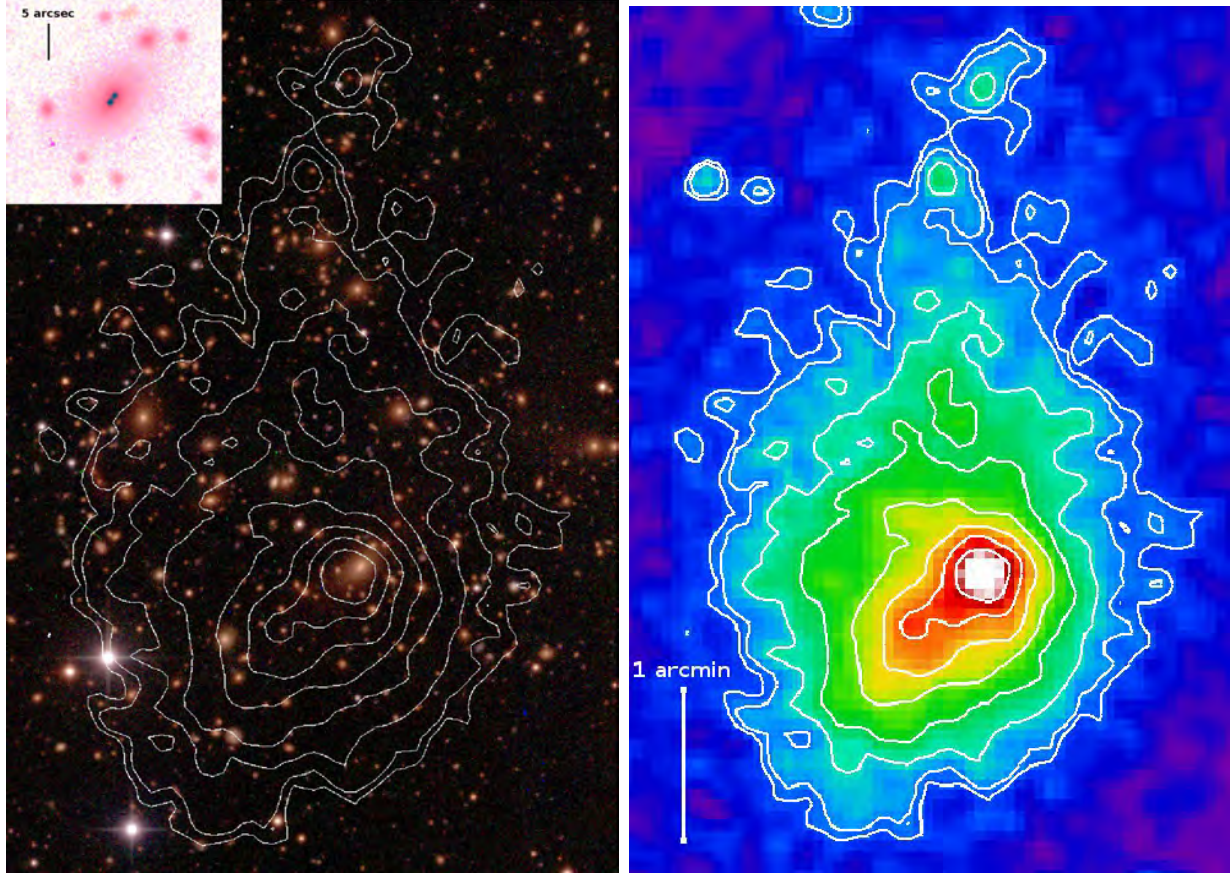


Figure 4.3: Left panel: BVR image of the central region of A1300 with an overlaid composite X-ray emission contour map. The upper left inset shows the Brightest Cluster Galaxy (BCG) for which different cuts and different scales were used for the three bands, in order to highlight the extended halo and the two nuclei separated by about  $1.2''$ . On the right: XMM-Newton image of A1300 in the 0.5-2 keV and smoothed with a Gaussian of  $\sigma = 4''$ . Z06 report a suspicious X-ray point source at the position (11:31:54.6, -19:55:43), which corresponds to the position of the BCG

observation of A1300 was subjected to a solar flare cleaning process and the observation was found to be quite clean from contamination so that almost all exposure time survived this process. For AS0520 a solar flare event was affecting large part of the data. Therefore, the observation was repeated.

The global cluster properties resulting from XMM-Newton data analysis can be found in Zhang et al. (2006). We list here those relevant to this thesis:

- bolometric X-ray luminosities of  $L = 1.80(\pm 0.15) \times 10^{45} \text{ erg s}^{-1}$  for A1300 and  $L = 0.92(\pm 0.12) \times 10^{45} \text{ erg s}^{-1}$  for AS0520,
- ICM temperature of  $T = 9.2 \pm 0.4 \text{ keV}$  for A1300 and  $T = 7.5 \pm 0.3 \text{ keV}$  for AS0520

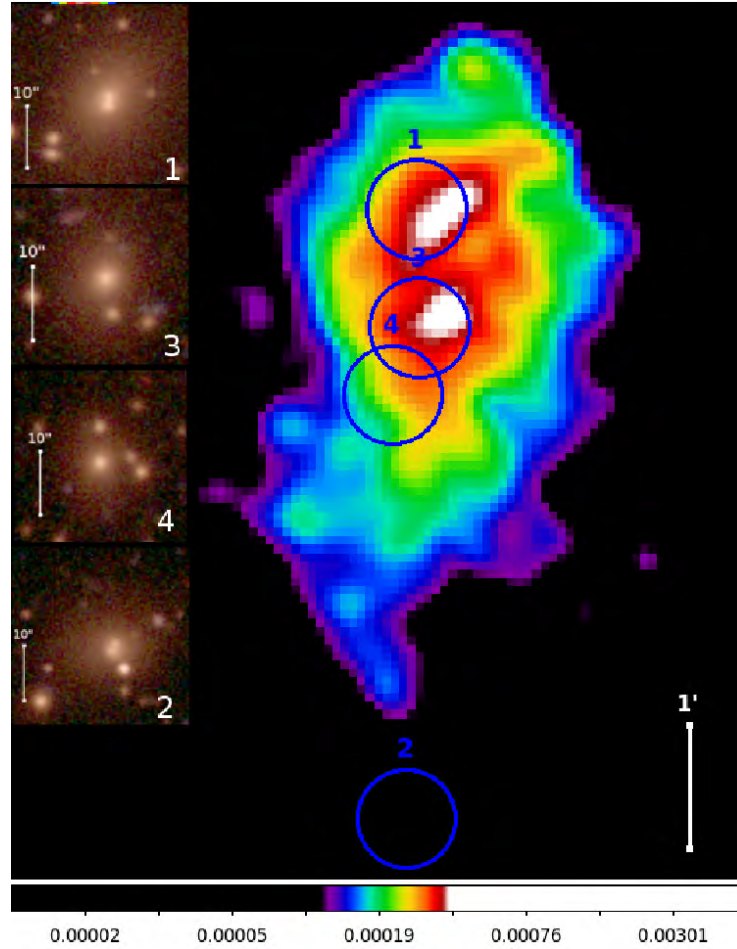


Figure 4.4: XMM-Newton image of AS 0520 in the 0.5-2 keV and smoothed with a Gaussian of  $\sigma = 4''$ . Superimposed are the region files (blue circles) of the 4 brightest galaxies ranked according to their magnitude in the R band. The units of the color bar are in counts/sec/pixel.

- total mass of  $M_{500} = 5.2(\pm 3.0) \times 10^{14} M_{\odot}$  for A1300 and  $M_{500} = 6.4(\pm 2.1) \times 10^{14} M_{\odot}$  for AS0520 (Zhang et al. 2006)
- cluster morphology is elliptical in both systems according to the classification of the dynamical state based on X-ray imaging (Jones & Forman 1992).

Fig. 4.3 and Fig. 4.4 show the XMM image in the 0.5-2 keV band, smoothed with a Gaussian of  $\sigma = 4''$ . In the case of A1300, Zhang et al. (2006) report a suspicious X-ray point source at the position (11:31:54.6, -19:55:43), which corresponds to the position of the BCG. The X-ray peak is displaced with respect to the BCG by 36 kpc. The left panel of Fig. 4.3 shows the same X-ray contours of the right panel superimposed on the BVR image of the central part of A1300 whose BCG presents 2 nuclei at its center (upper left

corner of Fig. 4.3). In the case of AS0520 (Fig. 4.4), the X-ray emission is elongated in the direction North-South and exhibits 2 peaks (in white) in the inner part, most probably due to a chip gap. We mark the positions (blue circles) of the 4 brightest galaxies in Fig. 4.4. These galaxies are aligned in the same N-S direction of the elongation of the X-ray emission. Furthermore, the most central galaxies (ID 1 and 3) are not very much displaced from the 2 X-ray peaks. The X-ray peak more accurately defined by Zhang et al. (2006) is displaced from the BCG by  $40''$  which at the redshift of the cluster corresponds to 176 kpc.

In order to obtain the maximal information from our X-ray data we performed the analysis using the method of the PSF reconstruction as explained in Finoguenov et al. (2009). In particular, after the point source removal, we computed the background estimate. This procedure allowed us to highlight not only the dynamical shape of the cluster, but also to determine the significance of the structures already seen in an appropriately smoothed X-ray image, as better explained in Section 4.4.1. This enables us to reconstruct the dynamical history of the clusters through the analysis of the groups and their link with the large scale structure.

## 4.3 Data analysis

### 4.3.1 Red sequence and blue cloud

The identification of the red sequence allows us to distinguish between likely old passively evolving objects belonging to the cluster red sequence and the likely young star forming galaxies located in the more scattered blue cloud mostly belonging to the field galaxy population. This color criterion turns out to be very successful in the SDSS galaxy sample. Indeed, at somewhat lower redshift ( $z \sim 0.15$ ), Strateva et al. (2001) show that a simple color distinction at  $u - r = 2.22$  is able to discriminate between galaxies with spectral absorption features and galaxies with emission lines, thus, star forming. This distinction is done here in order to investigate the location of the different galaxy population within the two systems and to use them to better trace the substructures.

We identify and fit the cluster red-sequence from the color-magnitude diagram (CMD, Fig. 4.5 and 4.6) of all the galaxies at  $R < 19.5$  and  $1.5 < (B - R) < 2.4$  within  $R_{200}$  of A1300 and AS0520 (1.53 and 1.62 Mpc, respectively). The best fit (dashed line in the figures), obtained through recursive  $3\sigma$  clipping, is described for the two clusters by the linear relations, respectively:

$$(B - R) = (2.823 \pm 0.090) - (0.048 \pm 0.005) \times R. \quad (4.1)$$

$$(B - R) = (2.847 \pm 0.164) - (0.057 \pm 0.009) \times R. \quad (4.2)$$

The rms scatter around the red sequence fit is  $\sim 0.09$  mag (represented by the dotted lines in Fig. 4.5 and 4.6). The best fit does not change by using either the spectroscopic or photometric sample.

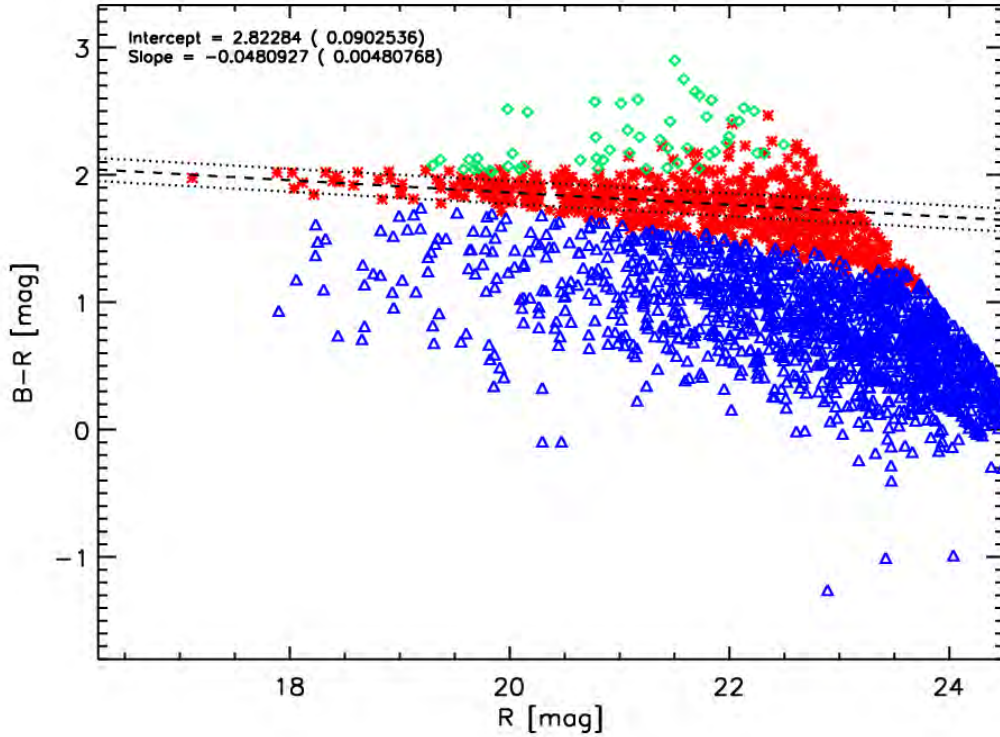


Figure 4.5: Color-magnitude diagram (B-R versus R) for all galaxies found in the field of A1300 comprised within  $R_{200}$  of the cluster. Red stars represent galaxies defining the red sequence within  $3\sigma$  from the best-fit within the photometric errors, blue triangles show the galaxies bluer than the red sequence of  $3\sigma$  within the photometric errors, green diamonds show all galaxies redder than the red sequence galaxies of  $3\sigma$  within the photometric errors. The dashed line represents the red sequence best fit and the dotted line the  $\pm 1\sigma$  scatter around the red sequence. The catalog is cut for the magnitude limit of  $B = 24.9$  and  $R = 24.5$ .

### 4.3.2 Cluster membership

Spectroscopic cluster members are identified using the same combination of techniques summarized by Biviano et al. (2006). First, we removed the obvious interlopers by excluding all galaxies with peculiar velocities in excess of  $\pm 4000 \text{ km s}^{-1}$  from the robust cluster redshift (calculated using the Beers, Flynn, & Gebhardt (1990) biweight estimators for robust mean and scale). Peculiar velocities were corrected for cosmological redshift and velocity errors and set to rest-frame using the standard recipe of Danese, de Zotti & di Tullio (1980). To the remaining galaxies we applied, first, the weighted gap selection method described by Girardi et al. (1993) and, then, the phase-space rejection criterion of den Hartog & Katgert (1996, cf. also Katgert, Biviano & Mazure 2004) to identify less evident interlopers. In all our calculations we assumed as cluster center the peak of the X-ray surface brightness map, which, in the case of A1300, lies within  $8''$  from the BCG,



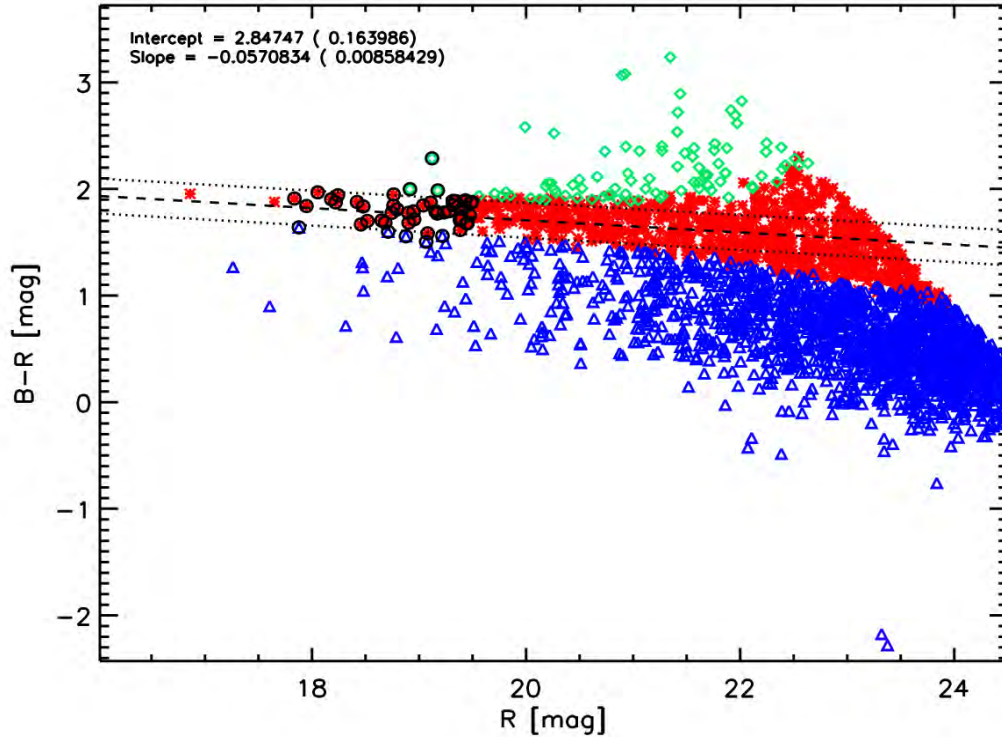


Figure 4.6: Color-magnitude diagram (B-R versus R) for all galaxies found in the region of AS0520 imaged with WFI comprised within  $R_{200}$  of the cluster. Red stars represent galaxies defining the red sequence within  $3\sigma$  from the best-fit within the photometric errors, blue triangles show the galaxies  $3\sigma$  bluer than the red sequence within the photometric errors, green diamonds all galaxies  $3\sigma$  redder than the red sequence galaxies within the photometric errors. The black circle mark all galaxies used for the fit in the three different cases. The dashed line represents the red sequence best fit and the dotted line the  $1\sigma$  scatter around the red sequence. The catalog is cut for the magnitude limit of  $B = 24.9$  and  $R = 24.5$ .

while for AS0520 within  $40''$ .

Our analysis yields a total of 230 (28) dynamically bound galaxies within a projected cluster-centric distance of  $4.5 h_{70}^{-1}$  Mpc, with a robust rest-frame velocity dispersion of  $987 \pm 101 \text{ km s}^{-1}$  ( $1064 \pm 162 \text{ km s}^{-1}$ ) for A1300 (AS0520). The errors on velocity dispersion and total mass are derived via jackknife from the catalog of confirmed cluster members. Fig. 4.7 shows the distribution of the cluster members in the phase-space while Fig. 4.8 shows the velocity distribution for the two clusters.

The spectroscopic redshifts enabled us to train the photometric redshift solutions obtained from *Le PHARE*, a software based on the  $\chi^2$  template-fitting procedure. The photometric data in three optical bands (B, V, R) allow us to trace the Balmer break of galaxies as a function of redshift up to  $z \sim 1.5$ .

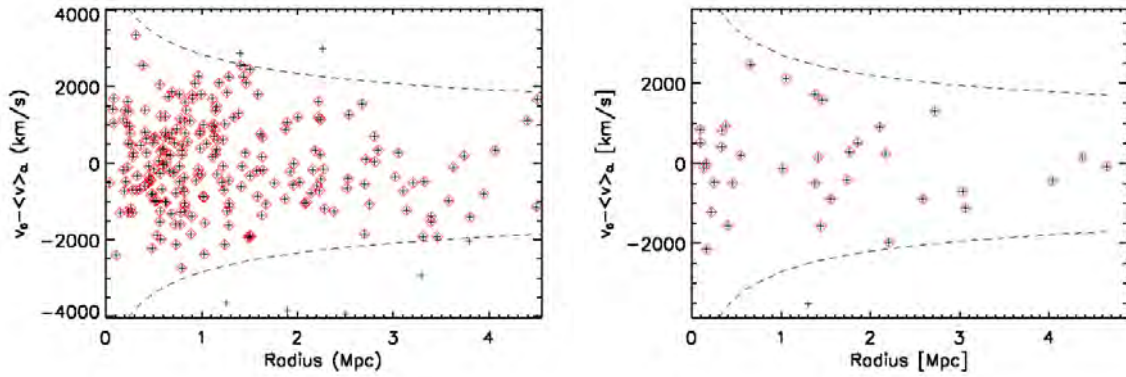


Figure 4.7: Phase-space diagram of the confirmed spectroscopic cluster members for A1300 (230 members, left panel) and AS0520 (28 members, right panel). Crosses mark the candidate cluster members prior to the interloper rejection, while red diamonds identify the confirmed cluster members. The dashed lines track the caustics defined by Katgert, Biviano & Mazure (2004) for comparison.

We adopt the included Virgo cluster template set (Boselli, Gavazzi & Sanvito 2003), from which we removed the “Blue Compact Dwarf” template, for A1300 and the COSMOS templates for AS0520, as these yield the highest quality photometric redshifts. This was defined as the smallest achievable fraction of catastrophic failures  $\eta = |z_p - z_s|/(1 + z_s) > 0.15$  (where  $z_p$  and  $z_s$  are the photometric and spectroscopic redshifts, respectively) combined with the best possible accuracy  $\sigma_{\Delta z/(1+z_s)}$  measured with the normalized median absolute deviation  $1.48 \times \text{median}(|\Delta z|/(1 + z))$  (as done in Ilbert et al. 2006), where  $\Delta z = z_p - z_s$ . The value of these parameters for all galaxies (without any selection in magnitude) and for bright galaxies ( $R < R^* + 1$ ) were respectively:  $\eta = 0.21$ ,  $\sigma_{\Delta z/(1+z_s)} = 0.07$ ,  $\eta_{\text{Bright}} = 0.07$  and  $\sigma_{\text{Bright}, \Delta z/(1+z_s)} = 0.03$  for A1300, and  $\eta = 0.19$ ,  $\sigma_{\Delta z/(1+z_s)} = 0.07$ ,  $\eta_{\text{Bright}} = 0.33$  and  $\sigma_{\text{Bright}, \Delta z/(1+z_s)} = 0.07$  for AS0520.

We use the option AUTO\_ADAPT of Le PHARE to correct our zero-points based on a sub-sample of bright galaxies and then we apply the result to the whole catalog. We choose the template set and check whether to apply extinction correction on several templates using the modified Calzetti et al. (2000) attenuation law and several others with the color excess  $E(B-V)$  values ranging between 0 and 0.3 and with a step of 0.05. Eventually, we did not use any extinction correction for A1300 as we obtained our best result using the provided observed templates of the Virgo Cluster. Concerning AS0520, we applied the Calzetti et al. (2000) attenuation law for all templates bluer than the starburst galaxy SB3<sup>10</sup> with the following color excess  $E(B-V)$  values: 0, 0.05, 0.1, 0.2, 0.3.

Ilbert et al. (2009) implemented an improved method to compute photometric redshifts

<sup>10</sup>Applying the full recipe of Ilbert et al. (2009) for the galaxy reddening (i.e. no extinction for all templates redder than the Sb template, Prevot et al. (1984) extinction law for templates comprised between Sb and SB3 and Calzetti et al. (2000) for bluer templates) gets worse our photometric redshift solutions, e.g. increasing the fraction of catastrophic failures.

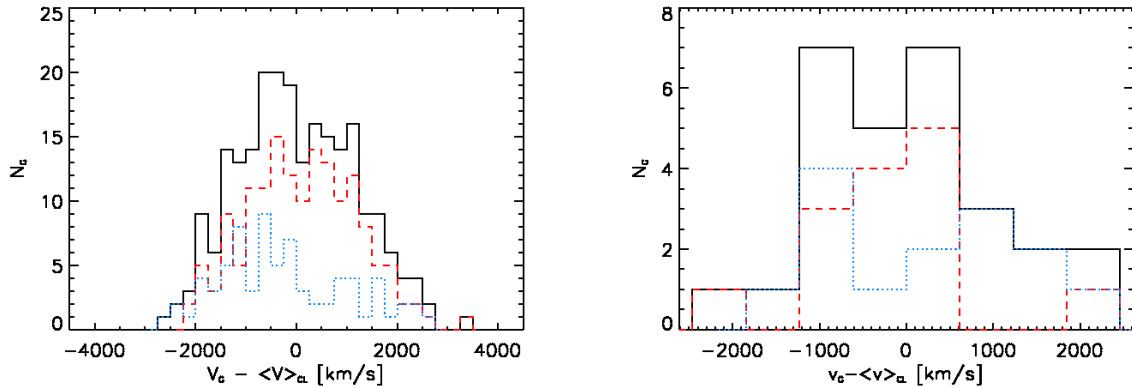


Figure 4.8: Velocity distribution of the spectroscopic cluster member galaxies of A1300 (left panel) and AS0520 (right panel). The black solid histogram shows the distribution of all cluster members; the distribution of velocities for blue and red members (as defined from their position in the color-magnitude diagram, cf. Section 4.3.2) is shown by the dashed red and dotted blue histograms, respectively.

taking into account the emission line contribution using relations between the UV continuum and the emission line fluxes associated with star-formation activity (like [OII], [OIII],  $H_\beta$ ,  $H_\alpha$ ). The authors compare the template curves with and without emission lines and found that the expected line fluxes can change up to 0.4 mag in the color. Therefore, we decided to add the emission line contributions to the SED templates after verifying an improvement in the comparison between the spectroscopic and photometric redshifts, also according to the parameters  $\eta$  and  $\sigma_{\Delta z/(1+z_s)}$ .

In Fig. 4.9 we show the comparison between  $z_s$  and  $z_p$ . The continuous line represents  $z_p = z_s$ , the two sets of dashed and dotted lines are for  $z_p = z_s \pm 0.05(1 + z_s)$  and  $z_p = z_s \pm 0.15(1 + z_s)$ , respectively. The discrepancies in the comparison between  $z_s$  and  $z_p$  is due partly to the small number (i.e. 3) of bands used for the fit and partly to the fraction of catastrophic failures provoked by the misinterpretation of some features. Braglia, Pierini, Böhringer (2007) applied their photometric redshift analysis to a simulated catalog in order to check the robustness of their  $z_p$  against the contamination of high- $z$  outliers. They found that wrong identifications mainly lay outside the cluster photometric range ( $z \sim 0.3$ ). Thus, after a visual inspection of the outliers in our catalog at  $z \sim 0.3$  we noticed that the best fit SED templates were typical of late type galaxies, for which the identification of the 4000 Å break is more problematic. Consistently, all these galaxies were classified as faint objects in the VIMOS program (section 4.2.2) and their spectra revealed some line emissions.

Photometric cluster membership is defined from the distribution of photometric redshifts of spectroscopically confirmed members: we used the biweight mean (Beers, Flynn, & Gebhardt 1990) of their photo- $z$  in order to define the center of the cluster and the scatter. For A1300 we measure a redshift interval for the cluster members of [0.23,0.35]



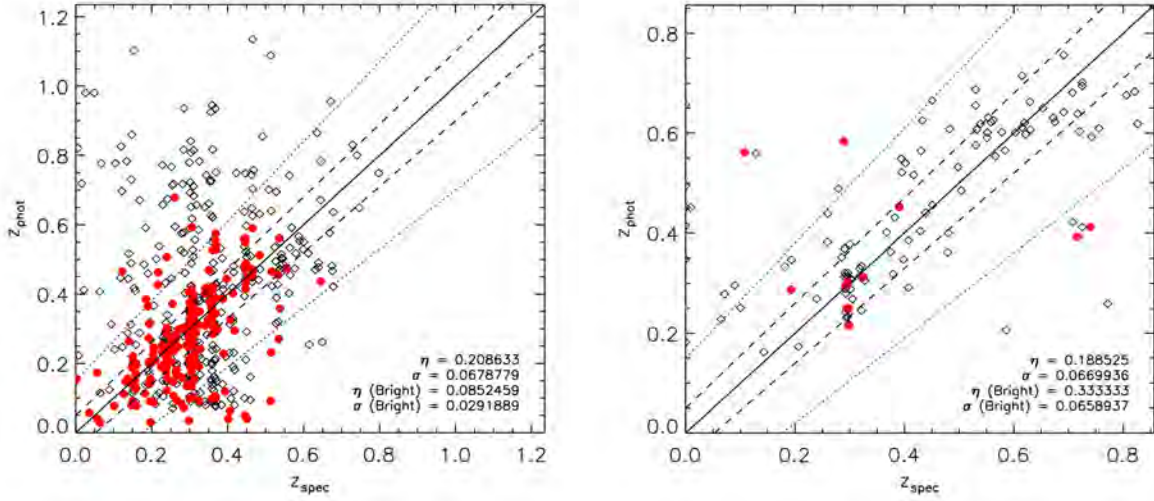


Figure 4.9: Comparison of spectroscopic and photometric redshifts for A1300 (on the right) and AS0520 (on the left). Red dots represent all galaxies brighter than  $R^* + 1$ . The continuous line is for  $z_p = z_s$ , dashed and dotted lines are for  $z_p = z_s \pm 0.05(1 + z_s)$  and  $z_p = z_s \pm 0.15(1 + z_s)$ , respectively.

and a mean of  $z_{\text{phot}} = 0.29$  (we measure a scatter of  $\sigma = 0.06$ ). Choosing this interval we had a contamination (considering the whole field of the cluster) of 42% (of which 26% in foreground and 16% in background) and we lost 35% of the spectroscopic sources (of which 18% had lower photometric redshifts and 17% higher ones with respect to the spectroscopic values). For the bright sources (marked in Fig. 4.9 as red dots) we had a contamination of 35% (of which 25% in foreground and 10% in background) and we measured losses of 18% of the spectroscopic sources (of which 14% had lower photometric redshifts and 4% higher ones with respect to the spectroscopic values). Spectroscopic redshifts were used instead of photometric ones, when available. Based on these values, we select a total of 4462 photometric cluster members, 2108 of which are classified as red galaxies and the remaining 2354 as blue, based on their position in the CMD with respect to the red sequence fit given by equation 4.1.

The mean photometric redshift of the cluster AS0520 is  $z_{\text{cl}} = 0.29$  with a scatter of  $\sigma = 0.0459$ . The redshift interval of the selected cluster members is  $[0.2427, 0.3345]$ . Choosing this interval we had a contamination (considering the whole field of the cluster) of 44% (of which 19% in foreground and 25% in background) and we lost 36% of the spectroscopic sources (of which 22% had lower photometric redshifts and 14% higher ones with respect to the spectroscopic values). Also in this case spectroscopic redshifts were used instead of photometric ones, when available. We select a total of 2483 photometric cluster members, 886 of which are classified as red galaxies and the remaining 1563 as blue, based on their position in the CMD with respect to the red sequence fit given by equation 4.2.

## 4.4 Morphological and dynamical analysis

In this section we focus on the analysis of the X-ray morphology and on the dynamical analysis of the population of the two clusters. The aim of this study is to identify which stage of the merger event the two systems are facing. Thus, we study the distribution of the ICM and its temperature and pressure maps for identifying possible shock related to the merger. We analyze in addition the distribution of galaxies in velocity and spatial distribution, to identify substructures such as infalling sub-clusters and groups through the use of statistical tests. The aim of the analysis is to quantify, if possible, the time elapsed from the merger event.

### 4.4.1 Abell 1300: the “Whirlpool” cluster

A1300 is a post-merging cluster at  $z \sim 0.3$  with a “dumbbell” cD galaxy at its center and prominent filaments visible in the galaxy density distribution. The BCG position is not coincident with the position of the X-ray emission peak, on the other hand, this cluster exhibits an elongated X-ray emission and a disturbed galaxy distribution in the optical. Finoguenov, Böhringer & Zhang (2005) named A1300 the “Whirlpool” cluster of galaxies because of the features in its temperature map which are reminiscent of a whirlpool. In the following sections we will present the results obtained for this cluster, comparing X-ray and optical information.

#### Cluster morphology and large-scale galaxy distribution

We derived the galaxy density distribution for red and blue galaxies (see Section 4.3.1 for the definition) using an adaptive kernel smoothing. This method is a refinement of the basic procedure discussed in B09 and provides a more accurate estimate of the background counts and noise, while retaining all significant information about substructure and large-scale structure, also in the outskirts of the cluster (i.e. beyond  $R_{200}$ ).

Red galaxies (red contours in Fig. 4.10) are concentrated towards the innermost region of the cluster with a mean galaxy density of  $1.57 \text{ galaxies arcmin}^{-2}$ , which is highly significant ( $> 5\sigma$ ) w.r.t. the background. Conversely blue galaxies (in blue) are more scattered and mostly located in extended structures beyond  $R_{200}$ .

The over-density information from the galaxy distribution can be used to estimate the amount of galaxy mass belonging to the cluster and compare it to that in the filamentary regions in the NE and SE. Using the X-ray peak as a reference center and  $R_{200}$  as the fiducial radius of the cluster, we find that the cumulative luminosity of all red galaxies in the NE (SE) filament is about 30% (33%) of the total. Such a high fraction of red (i.e. likely passively-evolving) galaxies beyond  $R_{200}$  suggests that the infalling galaxies may have evolved already along the large-scale structure before falling into A1300. This might have happened in the lower-mass groups through the same filaments.

Further comparing the density maps for all bright ( $R < R^* + 1$ ) and for faint ( $R \geq R^* + 1$ ) galaxies (both red and blue ones, Fig. 4.11), two different behaviors can be identified. On

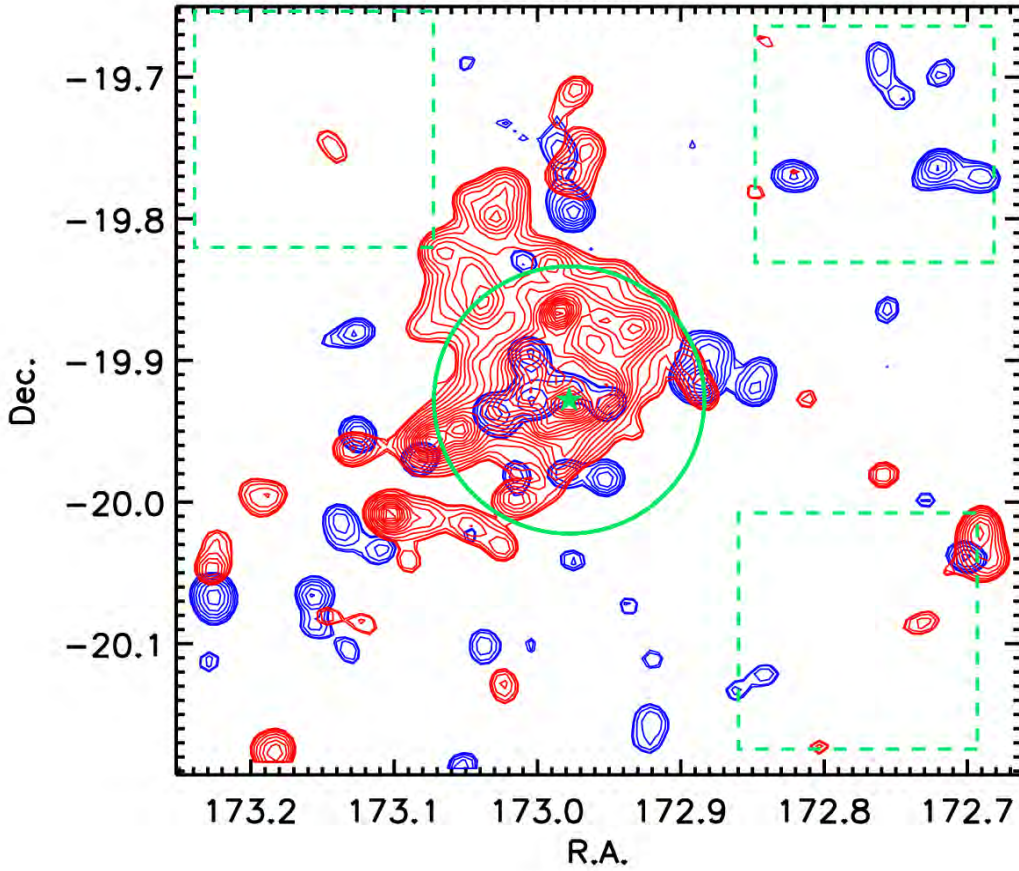


Figure 4.10: Density contours for red and blue photometric members of A1300 smoothed with an adaptive kernel. Red galaxies (in red) are more concentrated in the central regions, while blue galaxies (in blue) are preferentially located in filamentary structures. The green star shows the peak of the X-ray emission, the region of the cluster within  $R_{200}$  is marked by the green circle, while the three green dashed-lined boxes highlight the regions selected for estimating of the background. The contours have a significance of at least  $5\sigma$  w.r.t. the background and follow a square root scale.

one hand, bright galaxies are found at larger ratio close to the X-ray peak (as confirmed by the density profiles in Fig. 4.12), with some clumps following the overall direction of the filaments, while on the other hand, faint galaxies (present in larger numbers) show more over-dense clumps all across the cluster and its outskirts. Hence it seems that, while massive galaxies trace better the inner region of the cluster and the surrounding large-scale structure, faint galaxies dominate in the outskirts (at  $R \gtrsim 1.3 R_{200}$ ) and can provide insight to the substructure at the smaller scales.

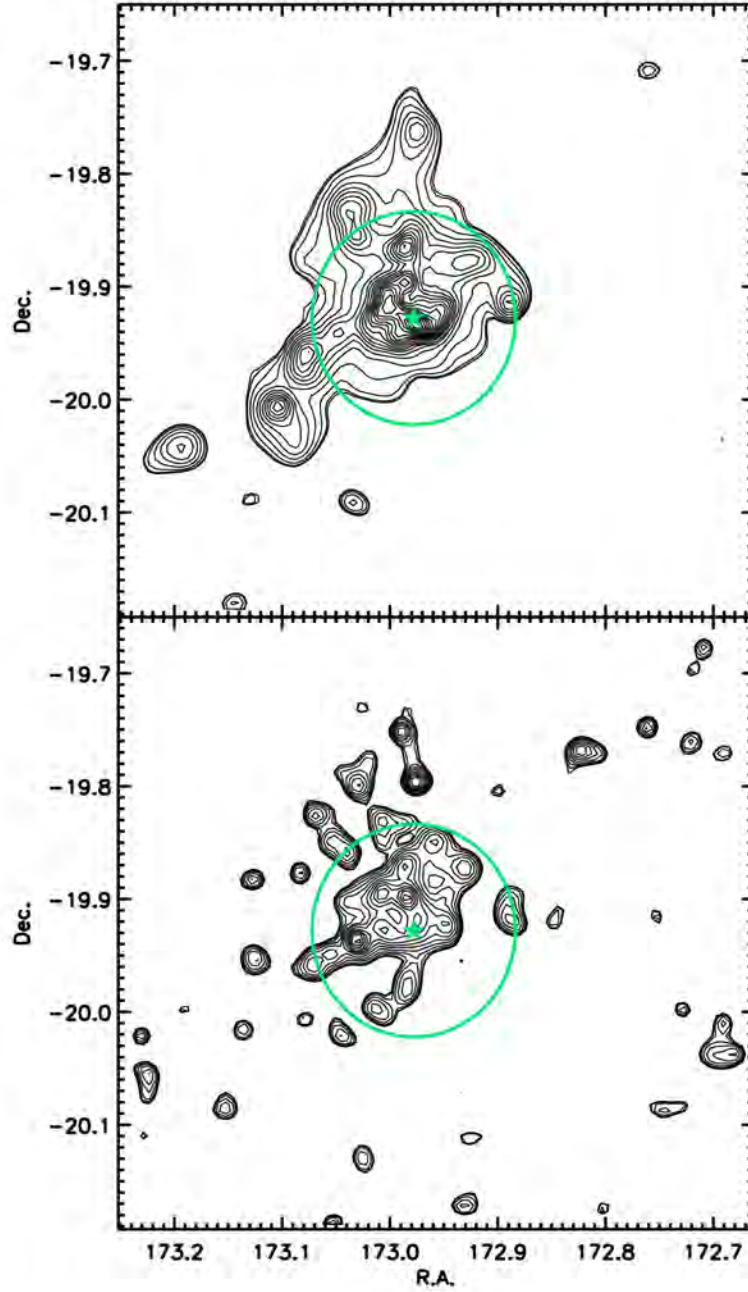


Figure 4.11: Density contours for bright ( $R < R^* + 1$ , top panel) and faint ( $R \geq R^* + 1$ , bottom panel) photometric members (both red and blue galaxies) of A1300 using an adaptive kernel method. The green star represents the peak of the X-ray emission while the region of the cluster within  $R_{200}$  is marked by the green circle. The contours have a significance of at least  $5\sigma$  w.r.t. the background (corresponding to  $0.41$  galaxies  $\text{arcmin}^{-2}$  for the bright cluster members and  $3.32$  galaxies  $\text{arcmin}^{-2}$  for the faint ones) and follow a square root scale.

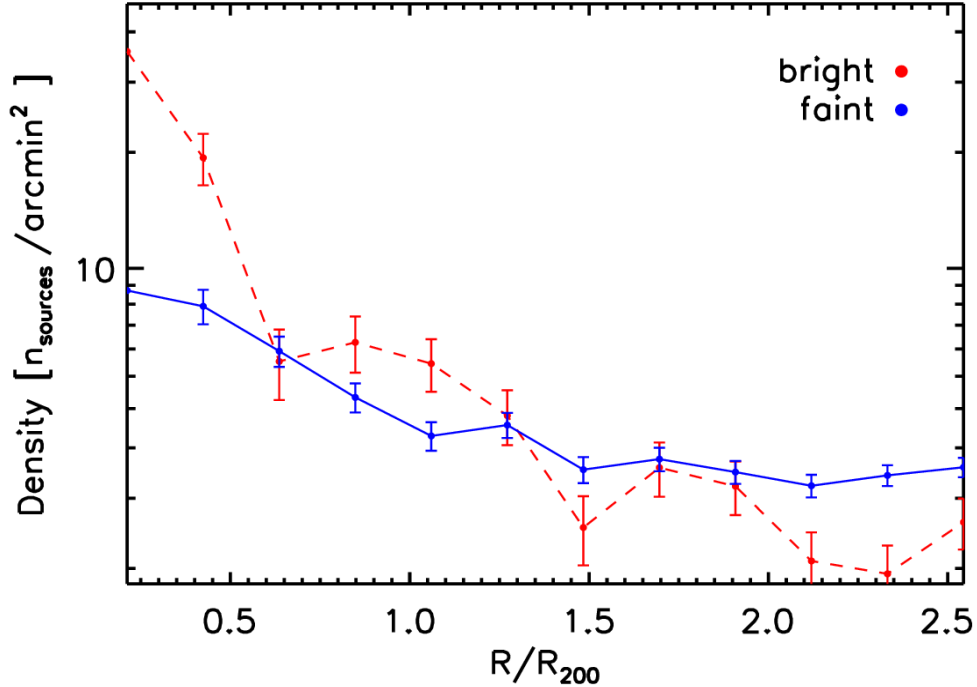


Figure 4.12: Density profile for bright (red dashed line) and faint (blue solid line) photometric members (both red and blue galaxies) of A1300. The density profile of the bright galaxies is normalized to the same total number of faint galaxies in order to compare it with that of the faint galaxies. Bright objects are mostly located in the central region of the cluster while faint ones dominate in the outskirts.

### Temperature, Pressure and Entropy

The X-ray properties for the DXL sample were first investigated in Zhang et al. (2004b). A1300 exhibits a temperature gradient and cool intra-cluster gas in the center, suggesting that cooling cores are not only found in clusters with symmetric and regular X-ray images, but can also be found in elongated, very disturbed clusters (such as A1300). An estimate of the cooling time was given in Z06:  $t_{\text{cool}} \approx 10$  Gyr, assuming a gas temperature  $T = 10^8$  K and a density  $n_p = 5.8 \times 10^{-3} \text{ cm}^{-3}$ . The region where the cooling time is smaller than the age of the Universe at the cluster redshift was found to be within a cluster-centric distance of  $27''$  ( $\sim 120$  kpc) at maximum.

A more qualitative analysis of the temperature, pressure and entropy<sup>11</sup> maps was performed by Finoguenov, Böhringer & Zhang (2005, we address the reader to their Fig. 11)

<sup>11</sup>The entropy is an important diagnostic parameter because it determines the structure of the ICM recording its thermodynamic history. We adopt the definition of Voit (2005) for the entropy:  $K = k_b T n_e^{-2/3}$ , where  $k_b$  is the Boltzmann constant,  $T$  is the temperature in keV units and  $n_e$  is the electron density.



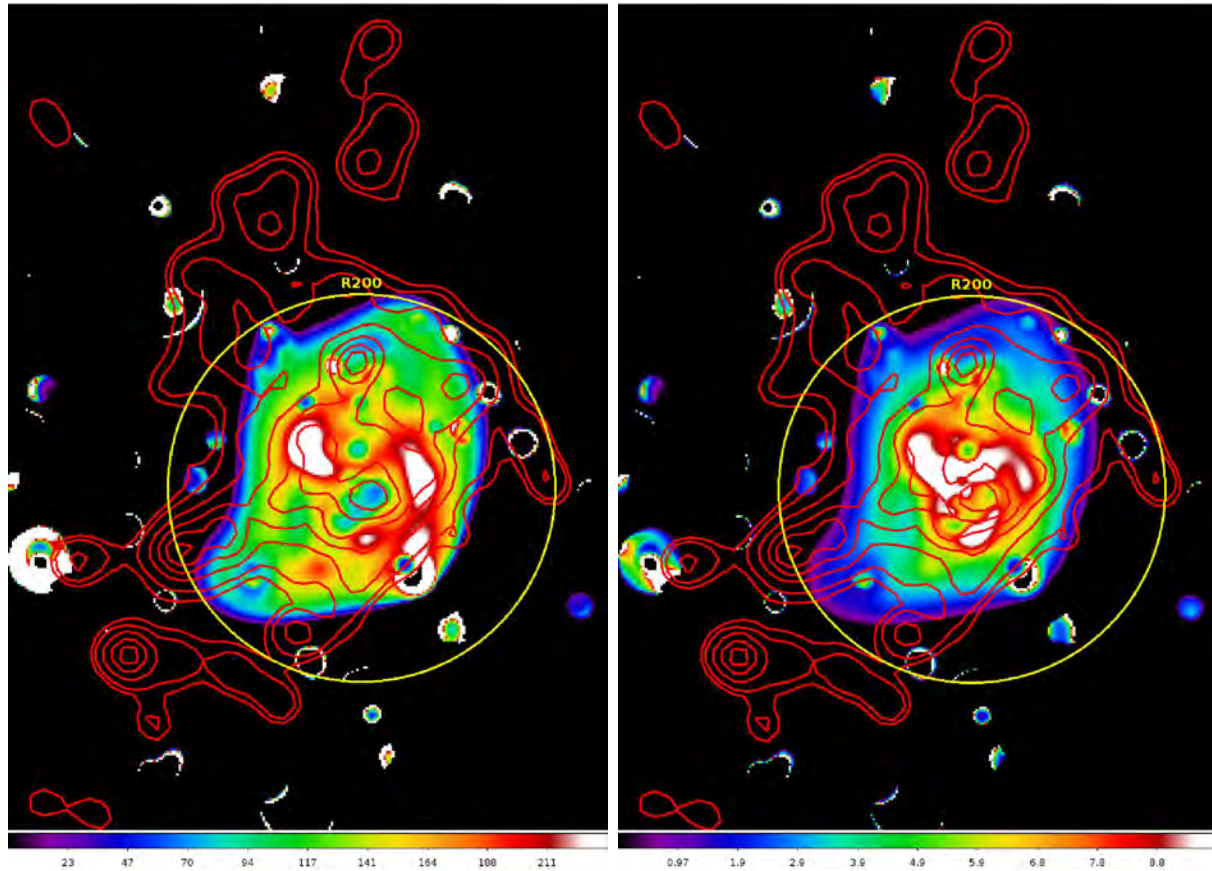


Figure 4.13: On the left: Entropy pseudo-map of A1300. The color bar is in arbitrary units. On the right: Temperature map of A1300. The color bar is in keV (For details on both pseudo-maps see Finoguenov, Böhringer & Zhang 2005). In both panels red contours outline the over-density of red galaxies while the yellow circle represents the region of the cluster within  $R_{200}$ .

who named A1300 the “Whirlpool” cluster of galaxies because of the features in its temperature map. Finoguenov, Böhringer & Zhang (2005) found a central East-West ridge of high temperature that may reflect the compression of the central region between the two main merging components. A distorted cool core, which partially preserves the characteristic low entropy, could be responsible for the complex temperature structure of the cluster. Moreover, the same authors found a large scatter in the entropy maps arguing that it reflects a high degree of substructure in the cluster.

Therefore, we compare the spatial distribution of galaxies and hot gas in order to investigate consistent behaviors of both components. In particular, the entropy map (left panel of Fig. 4.13) provides a reliable record of the gas history (Voit 2005). The distribution of the member galaxies (red in particular) follows closely the entropy features, suggesting that galaxies track the information provided by the gas in the central regions out to larger cluster-centric radii. A similar behavior can be seen in the temperature map (right

panel of Fig. 4.13) where the hot features are probably caused by shocks resulted from the collisions of different merging components. This comparison reveals a direct correspondence between the substructures traced by the gas and the galaxies. After the impact of two massive clusters it is likely that the coupled gas and dark matter components of each cluster started to swing around a common center yielding the characteristic whirlpool shape seen in Fig. 4.13.

### X-ray Surface Brightness and Identification of Substructures

In order to minimize the impact of point sources and isolate the X-ray emission due to the diffuse hot ICM, we apply a novel technique to enhance the significance of extended sources and filter out the point sources from the X-ray surface brightness map (Finoguenov et al. 2009). Although this method was originally designed for group identification in wide-field/survey areas, it proved to be also quite efficient in identifying and characterizing smaller subsystems within or close to clusters. In particular, where point sources were detected in the *XMM-Newton* maps (and confirmed by archival *Chandra* data), this technique enabled us to reduce their X-ray appearance and better remove their contribution from the extended emission (for further details and explanations see Finoguenov et al. 2009).

Figure 4.14 shows the X-ray surface brightness in the  $0.5 - 2$  keV band obtained using the wavelet+PSF reconstruction. It is possible to identify several extended sources in the proximity of the cluster (with a significance larger than  $4\sigma$  w.r.t. the background in the optical). However the X-ray emission itself is not enough to establish their membership to the A1300 system.

Comparison with the distribution of cluster members shows that a few extended X-ray sources match the position of over-densities in the galaxy distribution maps. The results of this combined analysis and identification of the groups in X-rays and optical are described extensively in Sec. 4.4.1. We mark in Fig. 4.15 all detected groups possibly related to the cluster. The black ellipses (ID numbers 4, 6 and 10) in the figures are embedded in the LSS of A1300 (detected at more than  $5\sigma$  w.r.t. the background). The green ellipses, instead, represent the extended X-ray emission with much lower significance and probably due to projection effects or confusion. The groups selected as related to the cluster are also highlighted by yellow circles in Fig. 4.14. They all lie in the outskirts of the cluster, thus providing a tool to probe the accretion regions and to investigate the large-scale dynamics of A1300.

The central region of the cluster (marked by the solid white circle in Fig. 4.14) is spherically symmetric. This region has a radius of 3.09 arcmin (corresponding to about 835 kpc at the cluster redshift) and emphasizes a possible forward shock towards SW, followed closely by the galaxy density distribution. This shock is possibly related to the candidate radio relic found in previous studies (Reid et al. 1999 and Giacintucci 2011).

Fig. 4.16 shows the 0.5-2 keV surface density radial profile extracted in the SW quadrant in the direction of the radio relic (the position of which is highlighted by the green dashed lines). We used the position of the relic to tentatively identify the curvature of the shock (as already done, for example, by Macario et al. 2011). We find an enhancement in the

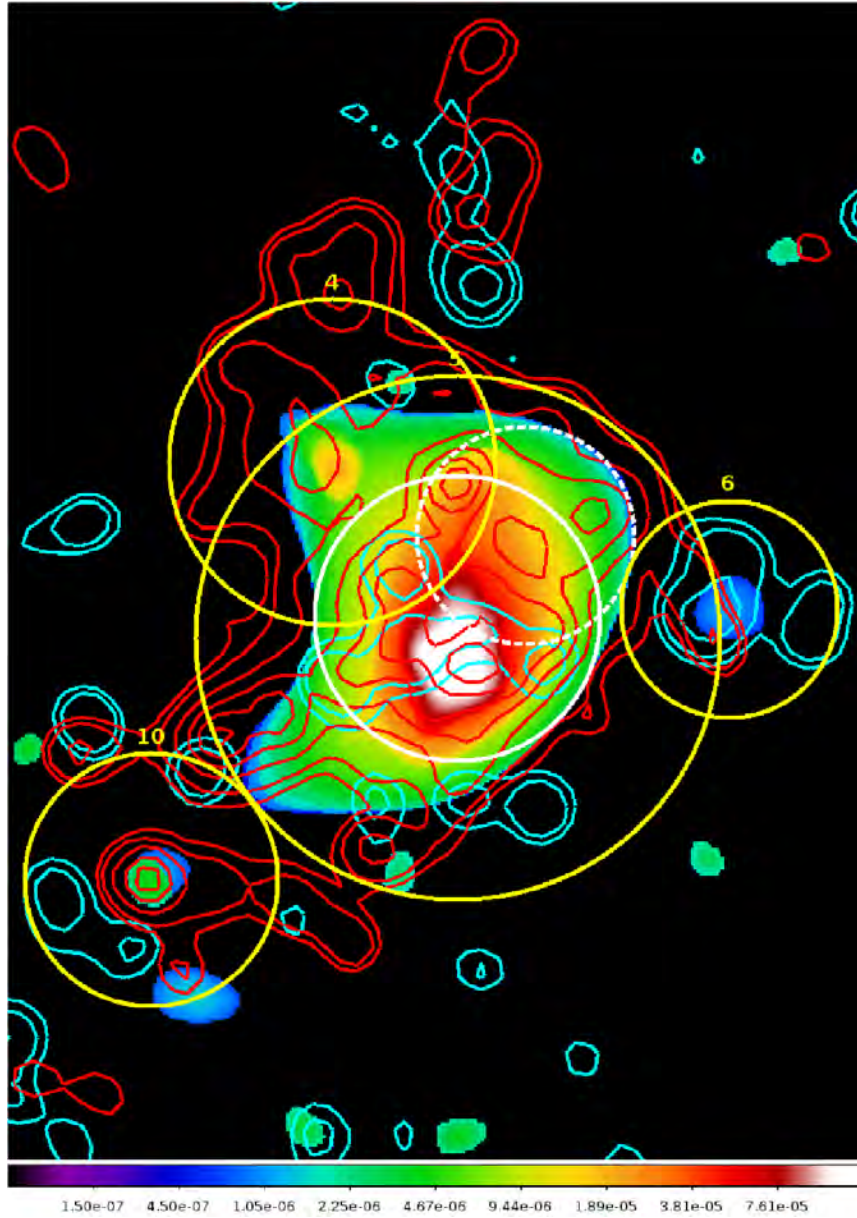


Figure 4.14: Surface brightness in the  $0.5 - 2$  keV band of A1300 using the technique described in Finoguenov et al. (2009). Several extended sources are detected around the cluster, with a significance larger than  $4\sigma$  w.r.t. the background. Superimposed are the density contours of red and blue cluster members. The yellow circles represent  $R_{200}$  of each group identified with the same ID of Table 4.4 (number 5 is A1300). The continuous white circle shows how the X-ray emission of the cluster would look like if it were spherically symmetric and the dashed white circle a possible group that disturbs the original symmetry but is now dissolved inside the cluster. The units of the color bar are in counts/sec/pixel.



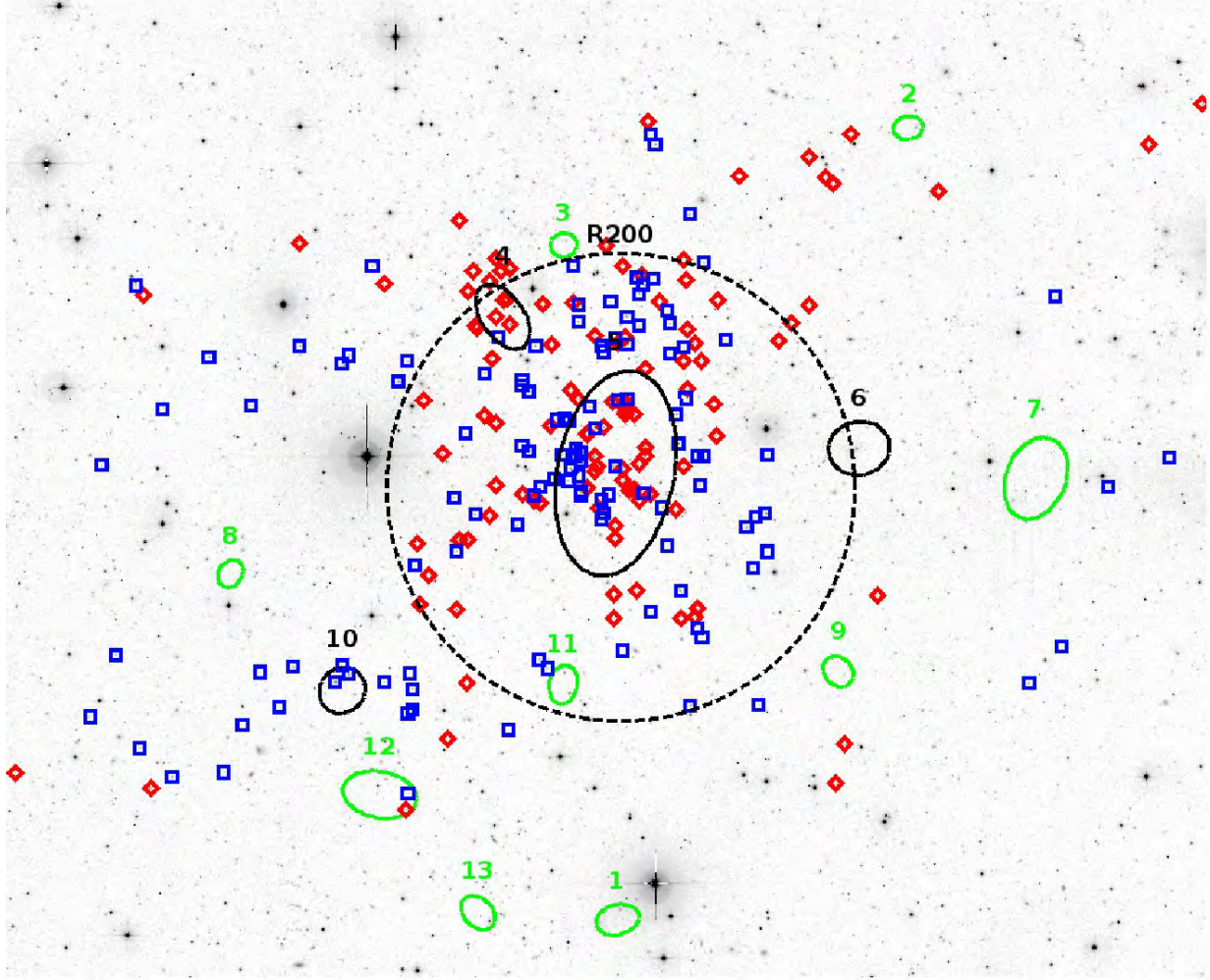


Figure 4.15: WFI R band image of A1300. The ellipses represent the groups observed in this field: the shape of all groups is related to their X-ray emission (Fig. 4.14). Black ellipse identify groups with a high probability to belong to the cluster i.e. at a significance larger than  $5\sigma$  w.r.t. the background, the green ones have a lower probability. Group number 5 is the main cluster of which region inside  $R_{200}$  is represented by the black dashed circle. The small symbols are the spectroscopic member galaxies of the cluster: the blue squares are all the galaxies approaching with respect to the observer, the red diamonds are the receding ones. Group 4 and 10 correspond to the substructures found in the DS-test (red circles in Fig. 4.18).

surface brightness coincident with the position of the relic. We use only pn data in which this enhancement is evident after masking all point sources and extended emissions outside the cluster. Our best fit model is obtained with a projected emissivity profile in which the density jump in the position of the relic is  $\rho_1/\rho_0 = 1.30 \pm 0.15$ , where  $\rho_0$  is the density of the unperturbed gas and  $\rho_1$  is the density of the gas after the shock. The density jump

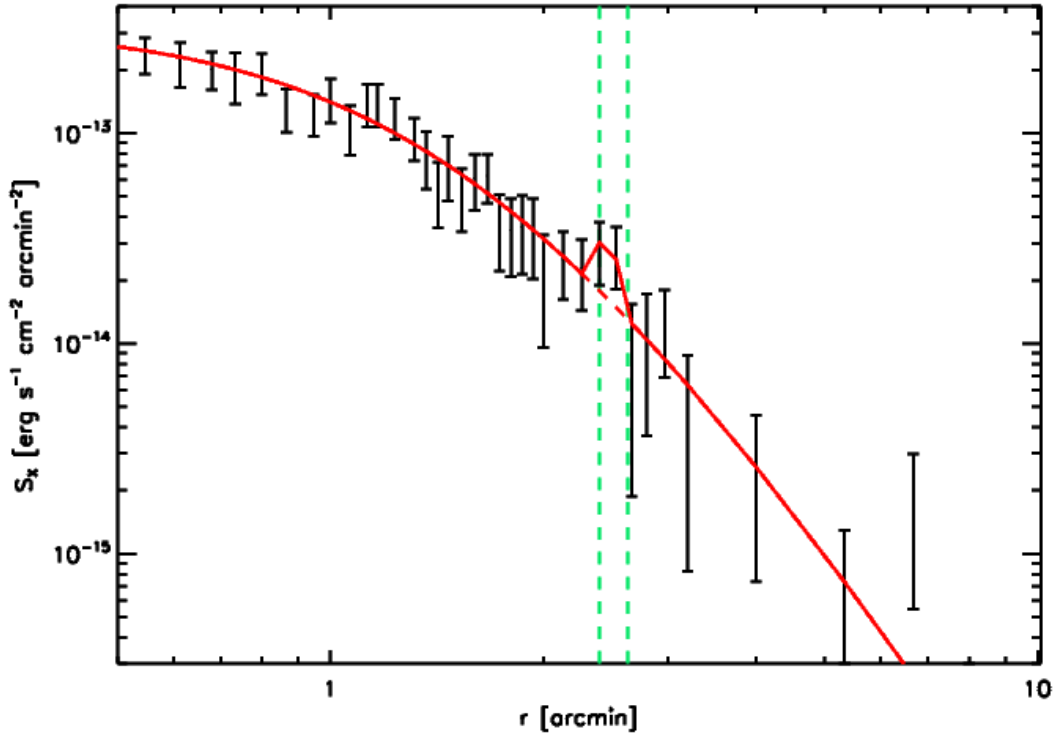


Figure 4.16: 0.5-2 keV surface brightness profile of A1300 extracted from the center of the curvature of the shock towards the SW quadrant, where the candidate radio relic was found (Reid et al. 1999, Giacintucci 2011) at the position (11:31:46.8, -19:56:44). The errors are  $1\sigma$ , the red continuous line shows the best fit model while the red dashed line shows the same model in the region of the shock without the enhancement. The green dashed lines constrain the position of the relic which corresponds to the enhancement we find in the profile.

allows us to derive an upper limit to the strength of this possible shock. Assuming a monoatomic gas with  $\gamma = 5/3$  and using equation 1 of Finoguenov et al. (2010),

$$\frac{1}{C} = \frac{3}{4\mathcal{M}^2} + \frac{1}{4}. \quad (4.3)$$

we obtain a Mach number  $\mathcal{M} = 1.20 \pm 0.10$ .

Finoguenov, Böhringer & Zhang (2005) define the cluster merging direction with the North-South on the basis of their X-ray qualitative analysis. Using X-ray and optical information (thus through a more detailed study) we are able to better define this direction. However the study of the dynamics of this cluster is not straightforward. In fact, the X-ray surface brightness map shows a more complex morphology in the outer regions of the cluster, with multiple extended structures around and beyond  $R_{200}$  and a globally asymmetric shape. This matches the distribution of photometric cluster members (cf.

Fig. 4.14), suggesting that A1300 is accreting matter along filamentary structures. In particular, the extended structure seen to the SE of the main cluster in the distribution of galaxies matches the position of Group 10, suggesting that this system may be infalling along a filament which extends from SE to NW.

In addition, we highlight with a dashed white circle in Fig. 4.14 a possible group which is now part of the cluster: its identity is lost in X-rays but it is visible in the optical image as a concentration of galaxies and in Fig. 4.14 as a density peak. To the NE of the core, the symmetry is disturbed by group 4 (shown in Fig. 4.17 with overlaid X-ray contours) which lies mostly inside the  $R_{200}$  of the cluster. Even if this group is very close to the cluster, it preserved its identity both in the X-ray and in the optical: its X-ray emission stands out even if it is already embedded with that of the cluster (Fig. 4.14). It is also possible to trace a red sequence (Fig. 4.17) and to identify a BCG in the corresponding region in the optical image. The X-ray mass of this group is  $M_{200} = 1.35 \times 10^{14} M_{\odot}$  (obtained adopting the same scaling relations of Leauthaud et al. 2010, i.e. after assuming a beta profile and removing embedded point sources, see Section 4.4.1 for details), i.e. 10% of that of the cluster. We are thus able to reconstruct the accretion pattern of A1300, which looks to be entering a phase of dynamical relaxation in its inner region, while still accreting mass in its outskirts.

### Substructures: X-ray and Optical Analysis

In the X-ray image of A1300 (Fig. 4.14), obtained by applying the technique described in Finoguenov et al. (2009), different regions with extended emission were detected around the main cluster (after removing the point sources) with a significance higher than  $4\sigma$  w.r.t. the background. These regions were compared with the 2-D distribution of galaxies in the optical catalog for the eventual identification of over-densities (groups; marked by green and black ellipses in Fig. 4.15). To assess the significance of these over-densities, we estimate the local density of galaxies at the location of each group and correct for background contamination. We thus select three square regions (highlighted in green in Fig. 4.10) at distances larger than  $R_{200}$  where no significant structures are evident in order to estimate the mean background density. Four candidate groups were dropped from the sample because the background correction exceeds the estimated density. The remaining groups have a significance of more than  $5\sigma$  above the background. The redshift information is then used to perform an X-ray analysis for all groups.

In order to assess the membership of the groups to the cluster we perform a second time the background correction using, this time, the cluster photometric member galaxies. We identify as groups belonging to the cluster all those over-densities with a significance larger than  $5\sigma$  w.r.t. the background. Of these groups we removed number 3 and number 11, since the possibility of contamination from the cluster and/or from their neighbors is high. For all remaining groups the probability to be associated with the cluster is low (given the uncertainties in our photometric redshifts the analysis is based on a qualitative approach). Where available, spectroscopic redshifts were used to confirm their membership in the cluster. The background-subtracted surface galaxy density and the significance w.r.t. the

ID	RA deg	Dec deg	$L_X$ (0.5-2 keV) $10^{42} \text{ ergs}^{-1}$	$M_{200}^X$ $10^{13} M_\odot$	$M_{200}^{dm}$ $10^{13} M_\odot$	kT keV	$R_{200}$ arcmin	Density arcmin $^{-2}$	$\sigma$	Red fr.	Blue fr.	$L_R$ $10^{11} L_\odot$	mag <sub>BCG</sub> mag <sub>AB</sub>
4	173.03195	-19.858619	$27.71 \pm 2.29$	$13.47 \pm 0.70$	$11.70 \pm 2.40$	2.06	3.53	6.75	9.3	0.89	0.11	$2.17 \pm 0.39$	18.11
5*	172.98374	-19.921704	$675.58 \pm 0.85$	$103.99 \pm 0.84$	$110.00 \pm 20.00$	8.70	6.98	8.95	15.3	0.81	0.18	$12.13 \pm 1.53$	17.11
6	172.87952	-19.911543	$4.03 \pm 1.09$	$3.92 \pm 0.65$	–	0.94	2.34	7.10	10.3	0.27	0.73	$1.12 \pm 0.19$	17.87
10	173.10082	-20.008946	$8.43 \pm 1.61$	$6.29 \pm 0.74$	$4.37 \pm 2.99$	1.25	2.74	5.43	5.8	0.56	0.44	$1.92 \pm 0.22$	17.95

Table 4.4: Properties for each group in the field of A1300. Col.1 gives the ID (ID = 5\* identifies the main body of A1300), col.2 and col.3 – the coordinates of the center, col.4 – the X-ray luminosity in the band 0.5-2 keV, col.5 – the X-ray mass, col.6 the dynamical mass, col.7 – the temperature for each group, col.8 – the value of  $R_{200}$  from X-ray analysis (for which we have adopted the same scaling relations of Leauthaud et al. 2010), col.9 – the number of galaxies per arcmin $^2$  after the background subtraction, col. 10 – the significance w.r.t. the background, col.11 and col.12 – the red and blue galaxy fraction, col.13 – the total luminosity of the group computed by summing all the single galaxy luminosities in the R band and col.14 – the R magnitude of the brightest galaxy found in the group. All the quantities listed in col.4-7 are obtained within a radius  $R_{200}$  while all those in col.9-13 within a radius  $R_{500}$ .

background of each group associated with the cluster are shown in Tab. 4.4 (col.9 and 10, respectively).

Cluster membership for each group was estimated using a number of different techniques, as only a fraction of the groups are covered by spectroscopy. For these groups we rely upon the information obtained from combining the distribution of cluster photometric members with the presence of a red sequence in the color-magnitude diagram (Fig. 4.17). Visual inspection also confirmed galaxy over-densities and the presence of a central bright galaxy.

All properties derived from this optical analysis are listed in Table 4.4, where we computed the density, the fraction of red and blue galaxies and the total luminosity within  $R_{500}$  in order to limit contamination from other groups. Snapshots and color-magnitude diagrams of the same groups are available in Fig. 4.17 with X-ray emission contours (in white).

We used the scaling relations of Leauthaud et al. (2010) described by their Equation 13:

$$\frac{\langle M_{200} E(z) \rangle}{M_0} = A \left( \frac{\langle L_X E(z)^{-1} \rangle}{L_{X,0}} \right)^\alpha \quad (4.4)$$

where  $E(z) \equiv \sqrt{\Omega_m(1+z)^3 + \Omega_\lambda}$  is the Hubble parameter evolution for a flat metric,  $M_0 = 10^{13.7} h_{72}^{-1} M_\odot$  and  $L_{X,0} = 10^{42.7} h_{72}^{-2} \text{ erg s}^{-1}$ . After deriving the value of  $R_{200}$  for each group and assuming that they lie at the same redshift of the cluster, we computed the X-ray properties for groups belonging to the LSS of the cluster, which are listed in Table 4.4. In the computation of the X-ray luminosity  $L_X$ , we have taken into account the finite size of the flux extraction area. The full  $L_X$  is estimated based on the observed counts and the expected missed flux, based on the beta-model. This is required in order to use the scaling relations which were calibrated for the full  $L_X$ . The masses are estimated based on the measured  $L_X$  and its errors. The intrinsic scatter in this relation is 20% (Finoguenov et al. in prep.) and it is larger than a formal statistical error associated with the measurement of  $L_X$ . We use the L-T relation to compute the temperature, which we used for the computation of the k-correction. Even though we report all the results obtained with the PSF reconstruction method, for the X-ray properties of the main body of A1300 (represented in Tab. 4.4 by the ID 5) we rely on those derived more accurately in Z06. The value for the total mass is in agreement with these authors.

Each group hosts at the center of its X-ray emission a very bright galaxy (identified as BGG), marked as the green star in each CMD in Fig. 4.17. The total luminosity of each group increases with the red galaxy fraction and suggests that the bulk of blue galaxies lies mostly at the faint end of the cluster galaxy population (Li et al. 2004).

In more detail, Group 4 is the most massive and the closest to the cluster among the secondary groups. It shows a red and blue galaxy fraction very similar to that of A1300 and its BGG has a spectroscopic redshift of 0.31. Its galaxy population could have evolved differently in this massive group.

Group 6 appears to be crossing  $R_{200}$ , however its galaxies are not particularly influenced in terms of their red and blue galaxy fraction. Indeed, it presents a completely different



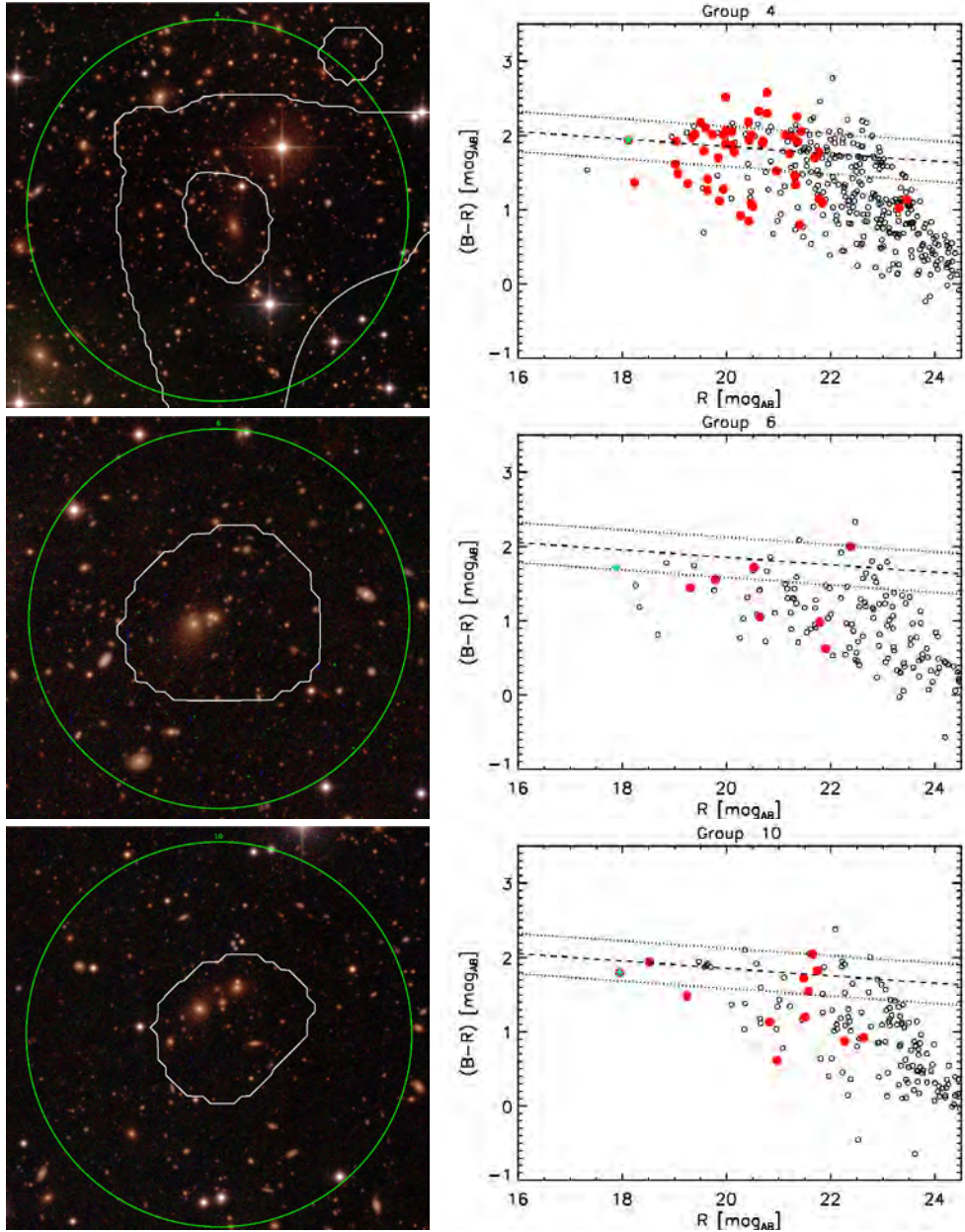


Figure 4.17: On the left: snapshots of group 4, 6 and 10 (from top to bottom respectively); the green circle is the region within  $R_{500}$  and in white are the X-ray emission contours overlaid. A smoothed (with a Gaussian of 8 pixels, or  $32''$ ) point-source-free signal-to-noise map is used for the contours. The two contour levels have a significance of  $3 \times 10^{-16} \text{ erg s cm}^{-2} \text{ arcmin}^{-2}$  (which draws the cluster X-ray shape in the top panel) and  $1 \times 10^{-14} \text{ erg s cm}^{-2} \text{ arcmin}^{-2}$ . On the right: color magnitude diagrams for each group. Black circles represent all photometric members of the cluster comprised within  $R_{500}$  of each group, red dots mark all the galaxies with spectroscopic redshifts, and the green star their BGG. The dashed line marks the best fit for the cluster red sequence the dotted line its  $3\sigma$  spread. The catalog is cut for the magnitude limit of  $B = 24.9$  and  $R = 24.5$ .

population with respect to the cluster and appears as the densest group (7.1 galaxies per arcmin<sup>2</sup>). This over-density is the most significant: its BGG (the most luminous with respect to other groups) coincides with the center of the X-ray emission and the density of the group clearly stands up at more than  $3\sigma$  above that of the background. This group could be still not part of the system or it could be so close to the cluster just for a projection effect, due to a possible large scale filamentary structure pointing towards the observer (Bower et al. 1997). As sufficient spectroscopic information is currently missing, it is difficult to obtain a definitive conclusion about this group.

Finally, Group 10 is the smallest and least dense. The spectroscopic data confirm that it is embedded in a filament and the optical image (Fig. 4.17) shows that the brightest galaxies within the X-ray emission are well aligned in the direction of the cluster (some of them, including the BGG are at the same photometric redshift as the cluster). The red and blue galaxy fractions are similar, suggesting that this group may be still relatively young and may not have experienced strong interactions with the cluster (future studies will address this). The luminosity of this group is modest in the optical but in the X-rays it is ranked as the second most luminous.

### Substructures from kinematics

We apply the kinematic DS-test Dressler & Shectman (1988) to the dataset of available spectroscopic cluster members, to identify substructures based on a combination of their position and velocity. This provides a complementary approach to detecting over-densities in the galaxy distribution and has the potential to identify substructures bound to the cluster but still retaining their kinematic identity.

The test was iterated over  $10^4$  re-samplings of the velocities and yields a DS statistics  $P_{DS} = 4 \times 10^{-4}$ , implying that the cluster has a significant degree of sub-structure (the whole test being significant at  $5.5\sigma$ ). The  $\kappa$ -test of Colless & Dunn (1996) was also run for comparison on the same dataset with consistent results. The results of the DS-test are shown in Fig. 4.18.

We identify kinematical substructures as groups of galaxies with values of the DS parameter beyond a critical value of 2.58 (calculated from the re-sampling statistics). Two groups, both with a significance above the  $3\sigma$  level, were detected.

A first group to the NE of the cluster center consists of 12 cluster members with a mean peculiar velocity of  $+1494 \text{ km s}^{-1}$  w.r.t the mean cluster redshift and a velocity dispersion of  $582 \text{ km s}^{-1}$ . This group appears quite compact on the plane of the sky, and its mean position (11:32:09.4, -19:50:43.8) is consistent with that found in X-rays for group 4. All 12 galaxies lie within the  $R_{200}$  of this group. After correcting for velocity errors, we derive a tentative mass estimate from the velocity dispersion (using the relation given by Biviano et al. 2006), finding a mass of  $(1.17 \pm 0.24) \times 10^{14} M_{\odot}$ , in good agreement with the X-ray estimate (cf. Sec. 4.4.1).

Another group of 7 galaxies to the SE of the cluster center exhibits large systematic deviations. These galaxies appear less concentrated than those identifying the previous group, however they all lie within  $R_{200}$  of group 10, their mean position (11:33:02.8, -

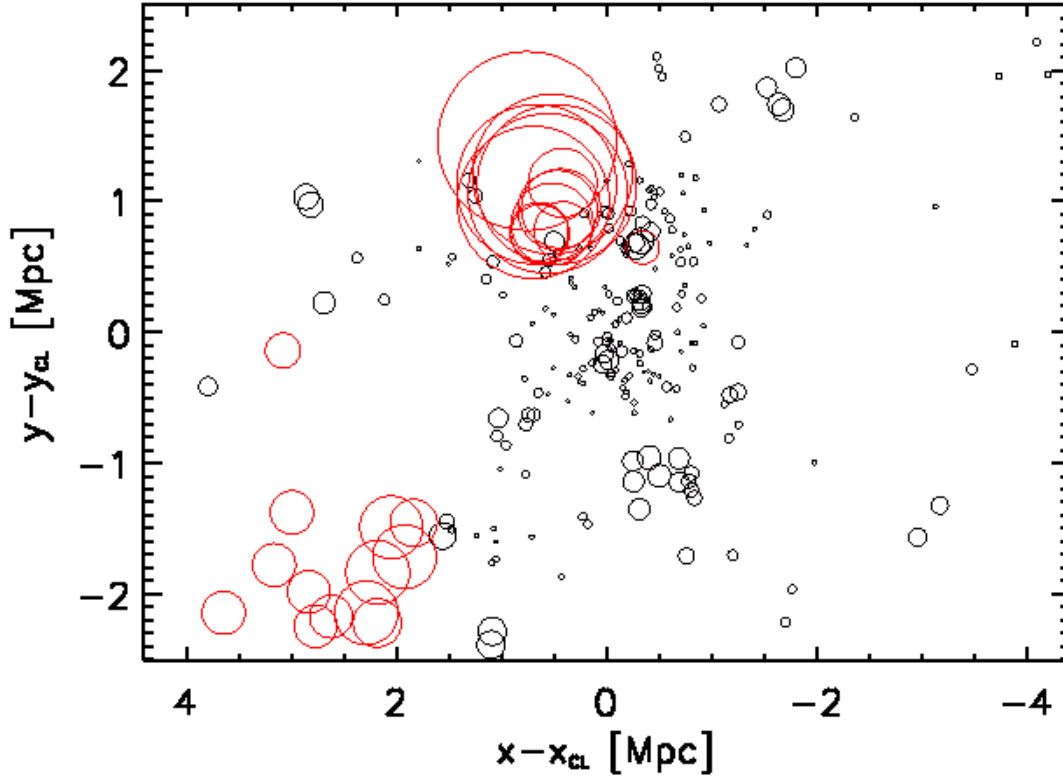


Figure 4.18: Substructure skyplot showing the results of the DS-test for the spectroscopic members of A1300. Circles are centered on the positions of member galaxies; their radius is proportional to  $e^{P_{DS}}$ , where  $P_{DS}$  is the DS deviation parameter for each galaxy. Red circles mark groups of galaxies which exhibit significant deviations ( $> 3\sigma$ ) from the local velocity distribution.

20:12:09.33) being only  $53''$  away from the X-ray peak (Table 4.4 and ellipse number 10 in Fig. 4.15). We find a mean velocity of  $-774 \text{ km s}^{-1}$  w.r.t the cluster mean velocity and a dispersion of  $452 \text{ km s}^{-1}$ , from which we infer a mass of  $(4.37 \pm 2.99) \times 10^{13} M_{\odot}$ . Although with larger uncertainty, also for this group we find an agreement with the X-ray value.

### Linking merging configuration and substructures

The combination of the X-ray, photometric and spectroscopic data enables us to investigate the dynamics of the cluster and to link them to its main substructures.

Figure 4.15 shows all spectroscopic cluster members grouped by their peculiar velocity w.r.t the cluster mean velocity: receding from the observer in red, approaching in blue. Ellipses mark the X-ray groups detected with the PSF reconstruction technique, groups encircled in black being those with a high probability to belong to the cluster. The cluster



$R_{200}$ , marked with the black dashed circle, highlights the presence of three groups (ID 4, 6, 10) entering the virialized region of the cluster.

The dynamical configuration of A1300 is quite complex, as already anticipated in the previous sections. X-ray and entropy maps reveal signs of a major merger and the presence of three X-ray groups. Two of these (ID 4 and 10) find confirmation from both the distribution of galaxies and the kinematical substructures and they seem to be accreted onto the main cluster, while a third group (ID 6) may be following a third accretion direction in a filament pointing towards the observer (unfortunately we do not have spectroscopic information to confirm it).

Northwards of the main cluster, Group 4 shows a significantly higher recession velocity by  $+1494 \text{ km s}^{-1}$ . Our findings suggest that this group may be part of the northern filament; from its peculiar velocity we can infer that the filament lies between the observer and the cluster. This is mirrored by the global velocity distribution of galaxies to the North of the cluster, which shows a systematic velocity of  $+456 \text{ km s}^{-1}$  for galaxies outside the core ( $\sim 1 \text{ Mpc}$  away from the cluster center).

Towards the South, a filamentary structure is traced by photometric spectroscopic cluster members. Group 10 is detected in the same region. It is particularly significant in X-rays and in the optical as well, showing a rich red sequence (see Fig. 4.17) and a well-defined over-density of galaxies (see Tab. 4.4). It is also detected from kinematics, with a peculiar velocity of  $-774 \text{ km s}^{-1}$ . Consistently, the overall velocity field in the southern outskirts is negative, with a mean of  $-354 \text{ km s}^{-1}$ . This suggests that the filament in which Group 10 is embedded reaches the cluster from behind.

The velocity distributions in the two regions (1 Mpc northwards of the cluster core and 1 Mpc southwards of it) are shown in Fig. 4.19. We compare the two distributions by means of a two-sided Kolmogorov-Smirnov test: this shows that the two distributions are significantly different, yielding a KS parameter of 0.018 (i.e. a significance of  $3.3\sigma$ ).

We can estimate the expected infall velocity around  $R_{200}$  for a group infalling from a large distance. Assuming a mass of  $10^{15} M_{\odot}$  for the main cluster as calculated for system 5 (cf. Sec.), we obtain a velocity of about  $2000 \text{ km/s}$  at a distance of  $2 \text{ Mpc}$  from the cluster. This allows us to estimate for each filament the angle w.r.t the plane of the sky: we find that the northern filament has an angle of about  $40^{\circ}$ , while the southern has a lower angle of about  $20^{\circ}$ . In addition, given the estimates of total luminosity for the two filaments (cf. Section 4.4.1), we estimate that A1300 will accrete about 60% of its current total mass in the next Gyr from infalling material.

### Dating the merger through simulations

ZuHone (2011) performed simulations of cluster merging starting with two cool core clusters with different masses and total mass distributions (gas and dark matter) represented by a Navarro, Frenk and White (NFW, Navarro, Frenk & White 1997) profile. The status of A1300 seems to be represented by one of the simulations where two parent clusters of approximately the same mass ( $M_{200} \sim 6 \times 10^{14} M_{\odot}$ ) are approaching one another with an initial impact parameter  $b \approx 464 \text{ kpc}$  (Fig. 4 for simulation S2 in ZuHone 2011). However,

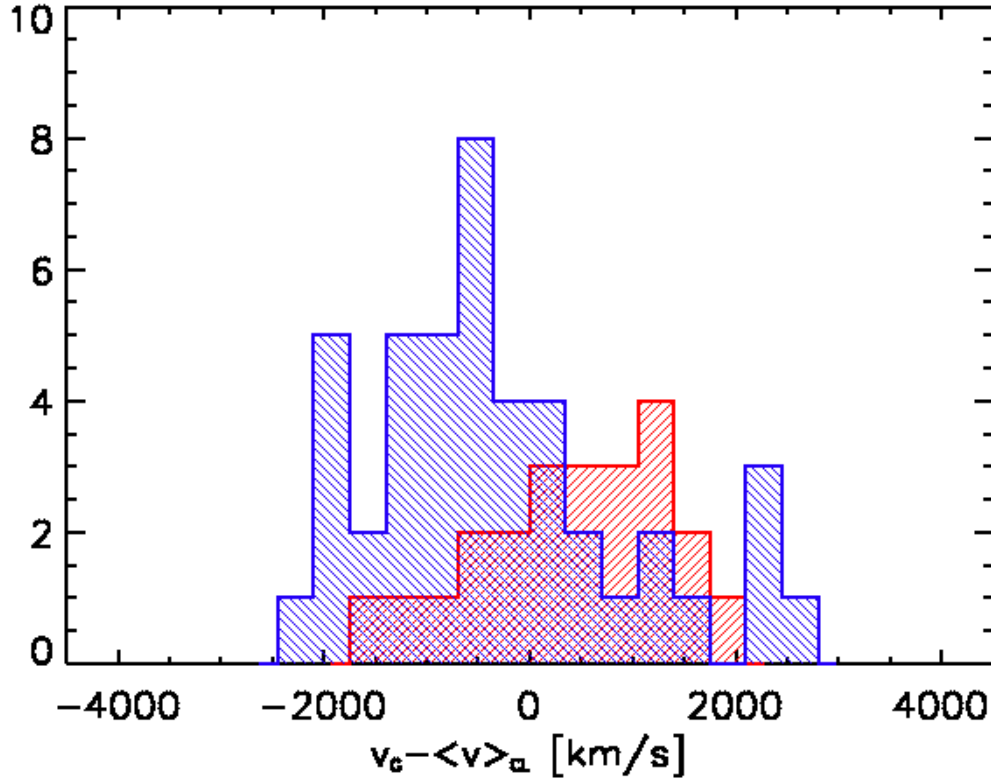


Figure 4.19: Velocity distribution for galaxies further than 1 Mpc from the cluster center. Red histogram: northern outskirts; blue histogram: southern outskirts.

we can not exclude the possibility represented by the same simulation with an impact parameter  $b \approx 932$  kpc (Fig. 5 for simulation S3 in ZuHone 2011). In these simulation the gas cores do not collide at the first core passage but sideswipe, creating a bridge of stripped, low entropy gas that stretches between the two DM cores. In fact, as high entropy gas floats and low-entropy gas sinks, the low entropy region marks the positions of the core of the cluster progenitors and the high entropy is due to the presence of shocks. The entropy map of the simulation finds a pretty good correspondence to the projected entropy map of A1300: here one plume of cold gas is located in correspondence of the BCG, showing up as a low entropy channel in the central region of the cluster, surrounded by higher entropy gas (with a characteristic whirlpool shape). The absence of a symmetric plume could be due to the fact that just one of the two cluster progenitors was a cool core (whose central part still survive at the center of A1300) similarly massive. The other entropy plume is located to the North and is not compact as the previous one. This could be an indication that A1300 is a complex system in which minor mergers played an important role in the mass assembly and the major merger happened between clusters of different dynamical states.

The comparison with these aforementioned simulations of ZuHone (2011), even if the matching is not perfect, allows us to approximately date the merging of the cluster progenitors: about  $3 (\pm 1)$  Gyr could have passed since when their regions within  $R_{200}$  touched for the first time. Tentatively tracing the previous cores in the entropy map, we can estimate the current projected impact angle which is likely to be  $\sim 130$  deg in the plane of the sky. This suggests that we are witnessing an almost face-on merging of clusters which allow us to better understand the status of the system related to the projection effects: as in the simulations, the two clusters collide with a relatively low initial impact parameter and after the first core passage the low entropy regions trace the two progenitors. Moreover, the presence of the shock found in the same position of the radio relic suggests that more than 2 Gyr passed since the merging; its weakness ( $\mathcal{M} = 1.20 \pm 0.10$ ) could constrain the age of the merging to around 3 Gyr. Furthermore, the degree of gas mixing as a function of radius (Fig. 13 for simulation S2 or S3 in ZuHone 2011) is very efficient in the off-axis merging, because the cores feel their mutual interaction and are stripped before the final merging.

The disturbed shape of the X-ray entropy, temperature and surface brightness 2-D distributions reflect a high degree of substructure in the cluster, fundamental for the interpretation of different moments of the assembly history. The surface brightness, in fact, is asymmetric (Fig. 4.14) and exhibits some excess of emission due to the influence of the filamentary structure through which groups fall. Indeed, several groups are clearly visible both in X-ray emission and in the optical galaxy distribution as clear structures.

The substructures found in A1300 likely reveals several episodes of accretion: a filament shows up in the DS-test (Fig. 4.18) and in the galaxy distribution (Fig. 4.10) we detect groups entering into the virial region of the cluster (Fig. 4.14) and over-densities in the inner part of the cluster without an X-ray counterpart. The last case refers to several peaks observed within  $R_{200}$  in the galaxy density map. This is probably due to the fact that infalling groups are stripped almost immediately of their hot gas when entering the clusters (Boselli & Gavazzi 2006). However, they can still keep orbiting around the cluster center for some time even after being captured in the deep potential well. Thus, they may retain part of their common DM halo remaining effectively bound together for longer times and appearing as galaxy over-densities. This happens mainly because of the difference in the behavior of collisional and non-collisional components of clusters or groups (galaxies and ICM respectively) as explained for example by Sarazin (2002).

The substructure analysis revealed also that the total mass of our X-ray selected groups is around 20% of that of the cluster. One of them (Group 4,  $M_{200} \approx 10^{14} M_{\odot}$ ) is already embedded in the virial region of the cluster (also in terms of gas, as it is possible to see from the X-ray emission in Fig. 4.14) and contributes alone to half of this value. This confirms the relation suggested by a recent simulation (Cohn 2012), i.e. that richness of the largest subgroup is typically 20% of that of its host cluster (even if this relation exhibits a wide scatter).

Fig. 4.3 shows the elongated shape of the galaxy distribution in the central region of the cluster, compared with the X-ray emission: the brightest galaxies, together with their satellites, trace the disturbed X-ray emission. A bit further from the central emission of

the gas we detect groups both in the X-rays and in the optical bands (as galaxy concentration). The X-ray surface brightness (better investigated in the PSF reconstructed image, Fig. 4.14) appears elliptical at the center but a projected filament to the South suggests the direction of a past accretion event. The X-ray surface brightness appears elongated towards the direction of the filaments in which the infalling groups are embedded, thus the ongoing mergers will modify again the shape of the cluster as it happens in the North-East.

Combining all the available information and comparing them with simulations, we conclude that A1300 could have been the result of the merging of two clusters of similar mass approximately 3 Gyrs ago. The collision happened most likely with a small impact parameter (as inferred from the entropy and the temperature maps) and this shock heated the gas, yielding all the features visible in X-rays. The cluster is still dynamically active and it is undergoing a strong phase of accretion of infalling groups and galaxies from the surrounding filaments.

#### 4.4.2 Abell S0520: the “Mermaid” cluster

AS0520 is an X-ray luminous cluster at  $z \sim 0.3$  with a dominant “dumbbell” galaxy at its center. This central galaxy is connected by a filament of diffuse stellar light to another bright elliptical. The morphology of the X-ray surface brightness is elliptical (Jones & Forman 1992, Zhang et al. 2006) and elongated in the same direction of the ICL filament. The PSF+wavelet reconstruction technique highlights the central part of the cluster connected to an extended emission which is reminiscent of a mermaid profile. In the following sections we describe the results obtained on AS0520 combining optical, UV and X-ray information.

#### ICM and Galaxy distribution

Fig. 4.4 shows the four central brightest red galaxies ranked according to their R magnitude<sup>12</sup>. The brightest and the second brightest galaxies exhibit 2 nuclei: the BCG is a “dumbbell” cD galaxy with 2 nuclei of approximately the same dimensions (see insets in Fig. 4.4) while Galaxy 2 exhibits two nuclei of different sizes, probably because of a projection effect. The similar red colors of the Galaxies 1 and 2 makes the two brightest red sequence galaxies good candidates to be the former BCGs of the cluster progenitors.

The 3 central galaxies are connected by a bridge of diffuse light as if tracking their path towards the minimum of the cluster gravitational potential. Fig. 4.20 shows the R band image of AS0520 cluster core. The colors and the scales used allow us to highlight the low surface brightness regions, e.g. the filament of diffuse light connecting the central brightest galaxies.

Moreover, we plotted in Fig. 4.20 the position of the GALEX NUV emitting sources, as they should trace the presence of young stars. We notice no particular NUV emission in the central region of the cluster, meaning that the stripped stars are mainly old, consistently with a predominantly dissipationless merging scenario for the build up of the BCG (De

<sup>12</sup>The galaxy number 4 is in fact the fifth brightest galaxy within  $R_{200}$ . The fourth brightest galaxy lies at a distance  $\sim R_{200}$  North-East from the X-ray peak.

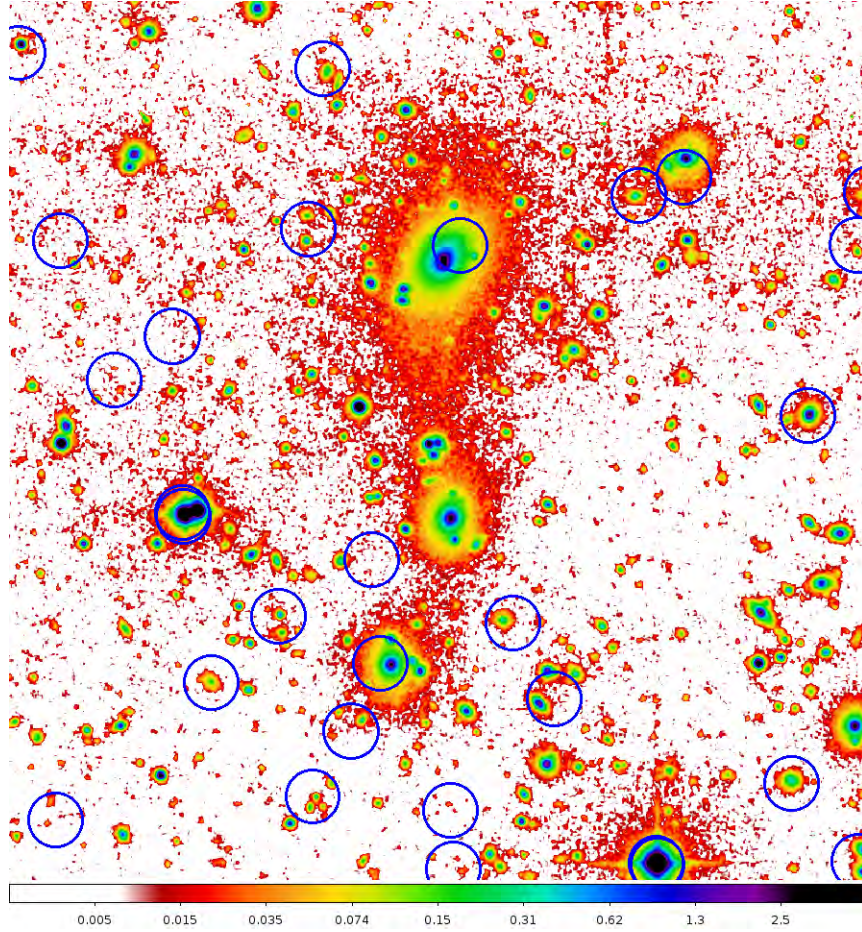


Figure 4.20: R band image of AS0520 cluster central region where the intensity of the sources increases from white to back in a logarithmic scale. The blue circles represent the GALEX emitting sources.

Lucia & Blaizot 2007). This result agrees with the AS0520 ICL colors, since we do not observe such a bright filament of diffuse light in the B and V band.

We analyze the galaxy distribution using the same technique as in A1300, in order to investigate the color and luminosity segregation towards the center. Red galaxies (red contours in Fig. 4.21) are concentrated towards the innermost region of the cluster, as expected. Conversely blue galaxies (in blue) are more scattered and mostly located beyond  $R_{200}$ . The red galaxy distribution shows several peaks in the direction North-South as an indication of the main infalling direction, as suggested by the elongation of the X-ray emission. However, a quite isolated peak just North-Eastern outside the area within  $R_{200}$  is prominent in the galaxy distribution. The distribution of blue galaxies reveals a filamentary structure in the South-East departing from the compact distribution of red galaxies. The analysis of the spatial distribution of bright and faint galaxies (defined as for A1300) reveals a strong luminosity segregation (Fig. 4.22). Bright galaxies populate the



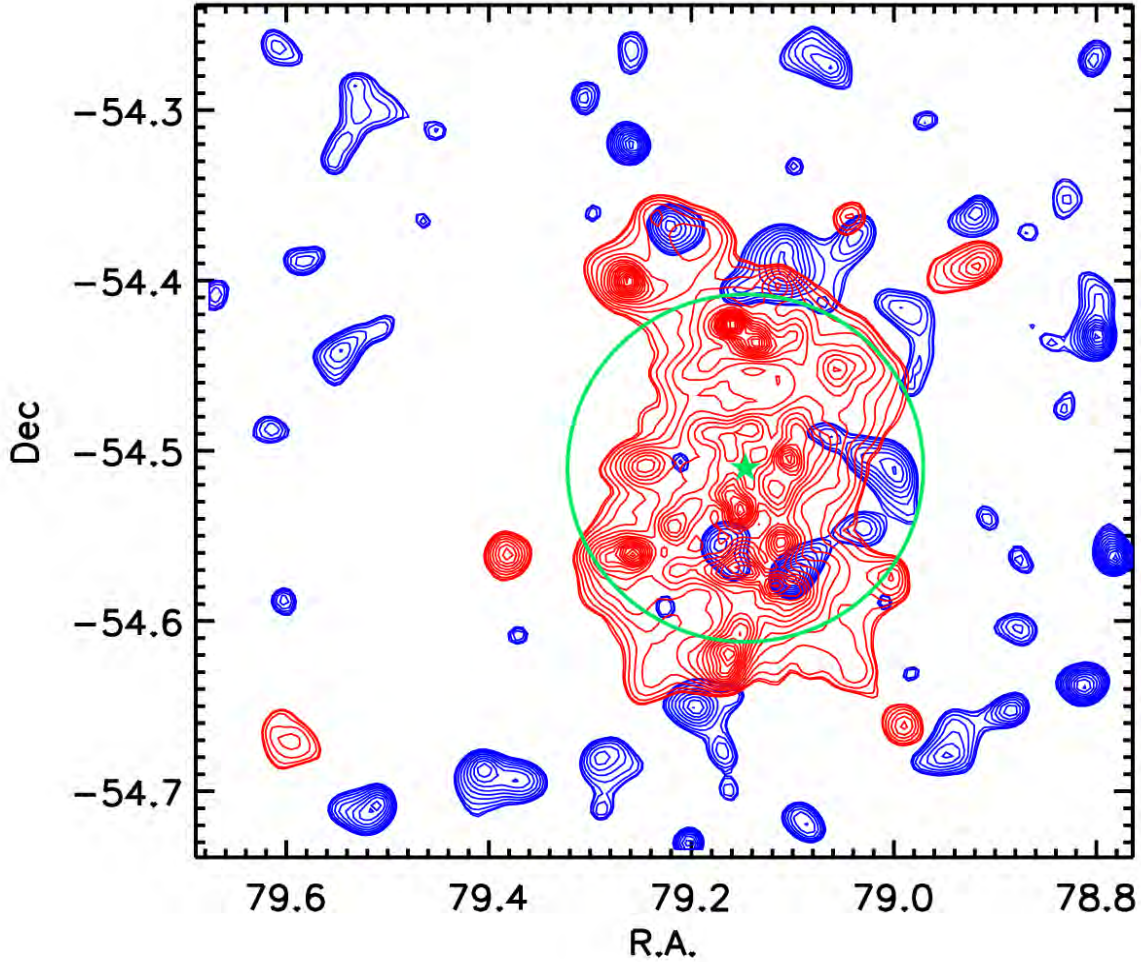


Figure 4.21: Density contours for red and blue photometric members of AS0520 smoothed with an adaptive kernel. Red galaxies (in red) are more concentrated in the central regions, while blue galaxies (in blue) are preferentially located in the outskirts. The green star shows the peak of the X-ray emission while the region of the cluster within  $R_{200}$  is marked by the green circle. The contours have a significance of at least  $5\sigma$  w.r.t. the background (corresponding to  $0.59 \text{ galaxies arcmin}^{-2}$  for the red galaxies and  $1.60 \text{ galaxies arcmin}^{-2}$  for the blue ones) and follow a square root scale.

cluster core, while faint galaxies favor the outskirts (i.e. the filamentary structure in the South-East region). The density profile (Fig. 4.23) is consistent with the one of A1300.

As for A1300, we use the PSF+wavelet reconstruction technique to highlight the outskirts of the cluster and to investigate the presence of extended emissions associated to candidate groups. Starting from large scales, the comparison of the X-ray morphology with the projected galaxy distribution (Fig. 4.24) reveals a common elongation North-

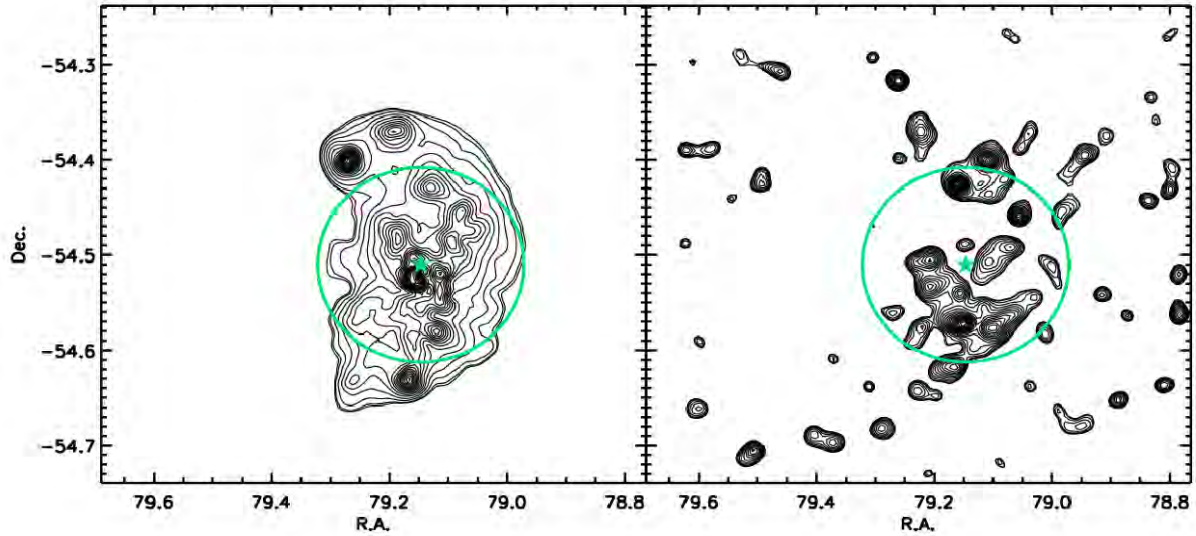


Figure 4.22: Density contours for bright ( $R < R^* + 1$ , top panel) and faint ( $R \geq R^* + 1$ , bottom panel) photometric members (both red and blue galaxies) of AS0520 using an adaptive kernel method. The green star represents the peak of the X-ray emission while the region of the cluster within  $R_{200}$  is marked by the green circle. The contours have a significance of at least  $5\sigma$  w.r.t. the background (corresponding to  $0.20 \text{ galaxies arcmin}^{-2}$  for the bright cluster members and  $2.10 \text{ galaxies arcmin}^{-2}$  for the faint ones) and follow a square root scale.

South between ICM and galaxy distribution (which exhibits several peaks aligned in the same North-South direction). In the South, GALEX selected (star forming) galaxies are concentrated mainly in 2 blobs: the main peak is coincident with one of the central overdensities of the red galaxies, very close to the third brightest galaxy (cf. Fig. 4.4), while the southern blob points toward a candidate filament of blue galaxies. In the North, a prominent peak of red galaxies is dominating and no significant number of NUV galaxies is visible in this area.

### Dating the merger time

AS0520 does not show peculiar X-ray and optical features to be compared with simulations as we do for A1300. Thus, we can not use simulation for dating the merger of AS0520. For this purpose we adopt a different technique. Smith et al. (2010) shows that the amplitude of the magnitude gap between the BCG and the second brightest galaxy can be related to the dynamical state of the system. More generally, large luminosity gap clusters are relatively homogeneous, with elliptical/diskly brightest cluster galaxies (BCGs), cuspy gas density profiles (i.e. strong cool cores), high concentrations and low substructure fractions. In contrast, small luminosity gap clusters are heterogeneous, spanning the full range of boxy/elliptical/diskly BCG morphologies, the full range of cool core strengths and dark

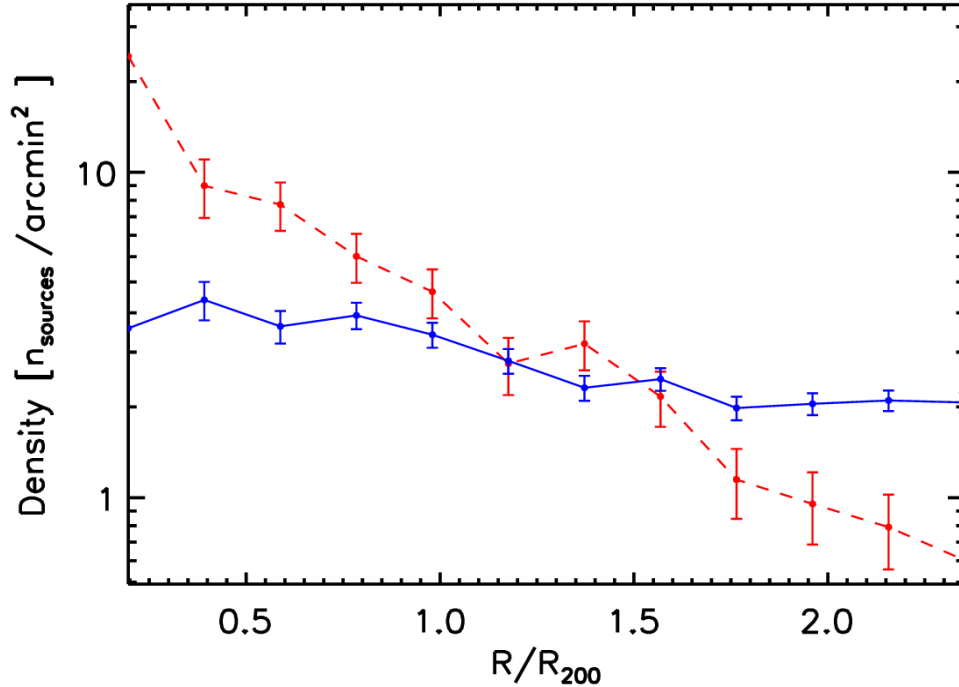


Figure 4.23: Density profile for bright (red dashed line) and faint (blue solid line) photometric members (both red and blue galaxies) of AS0520. The density profile of the bright galaxies is normalized to the same total number of faint galaxies in order to ease the comparison. Bright objects are mostly located in the central region of the cluster while faint ones dominate in the outskirts.

matter concentrations, and have large substructure fractions. Taken together, these results imply that the amplitude of the luminosity gap is a function of both the formation epoch and the recent infall history of the cluster. “BCG dominance” is therefore a phase that a cluster may evolve through and is not an evolutionary “cul de sac” (Smith et al. 2010).

For this purpose, we use the red sequence best fit obtained as described in Section 4.3.1, for identifying the BCG and the second brightest cluster galaxies. This allows us to measure the magnitude gap  $\Delta m_{1,2}$ . Table 4.5 lists the  $\Delta m_{1,2}$  values for AS0520 (RXCJ0516.7-5430), A1300 (RXCJ1131.9-1955) and other two DXL clusters (RXCJ0014.3-3022 and RXCJ2308.3-0211) studied by Braglia et al. (2009). According to Braglia et al. (2009), RXCJ0014.3-3022 is undergoing a phase of merging while RXCJ2308.3-0211 is a relaxed cluster. Indeed, these clusters exhibit the smallest and largest magnitude gap, respectively, in the DXL sample. AS0520 and A1300 show very similar magnitude gap ( $\Delta m_{1,2}$  of AS0520 being somewhat higher) and are classified as post-merger phase. This suggests that they should have a similar amount of time elapsed since the merger event. We stress that the best fit red sequence relations of all four clusters are in very good agreement, as it is expected since all systems are at the same redshift. This indicate that our measurement



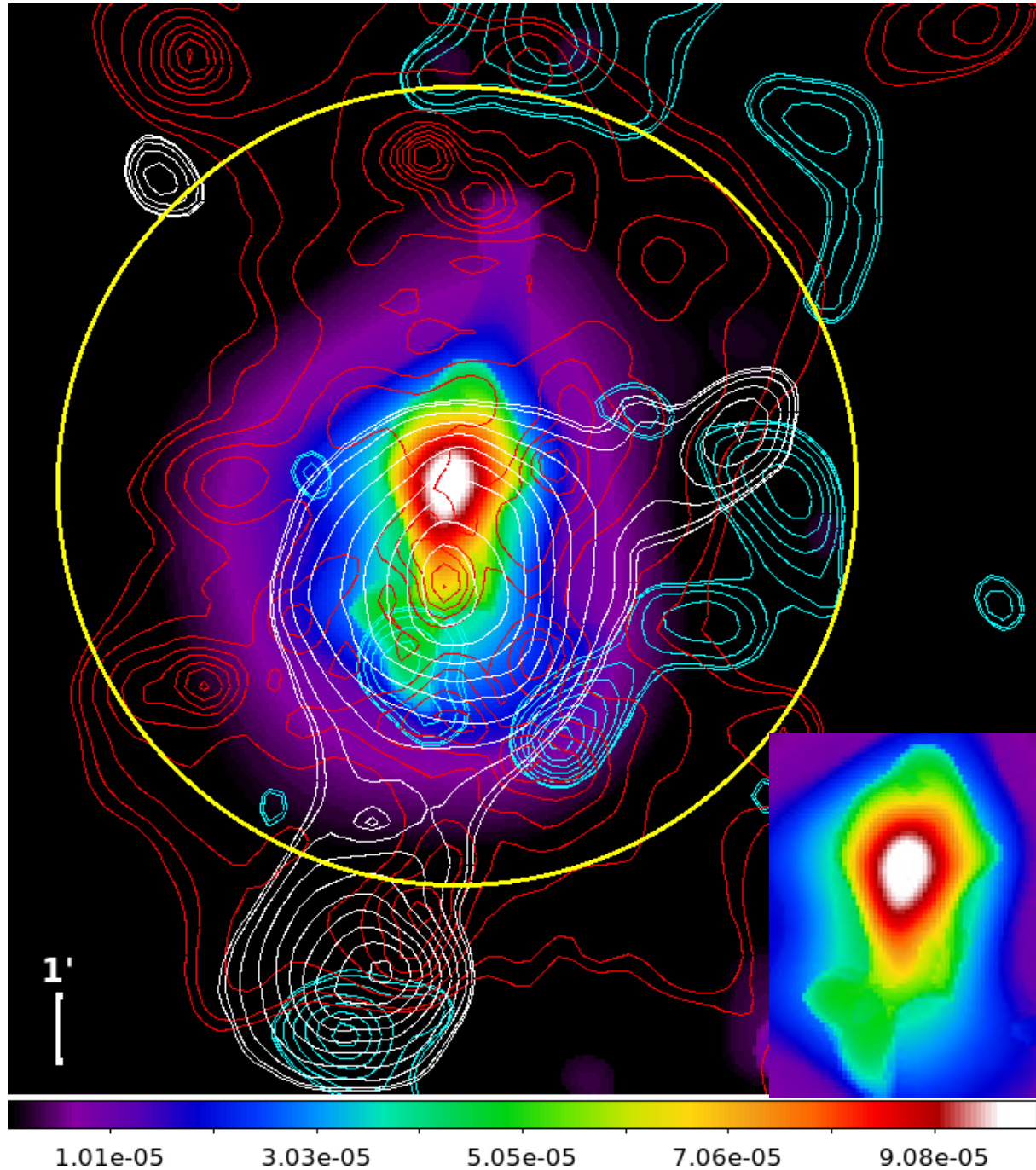


Figure 4.24: X-ray PSF reconstructed image of AS0520. Superimposed are the density contours of red and blue cluster members (in red and cyan respectively). The white contours represent the distribution of cluster members with NUV emission. The yellow circle represent the region within  $R_{200}$ . The units of the color bar are in counts/sec/pixel. Inset on the bottom right: details of the central part of the cluster. The PSF reconstruction highlights an extended emission which could be associated to a recently merged group.

RXCJ	name	a	b	$\Delta m_{1,2}$	Dynamical State
0014.3 –3022	A2744	$-0.037 \pm 0.003$	$2.935 \pm 0.238$	$\sim 0.1$	Merging
1131.9 –1955	A1300	$-0.048 \pm 0.005$	$2.823 \pm 0.090$	$\sim 0.8$	Post-merging
0516.7 –5430	AS0520	$-0.057 \pm 0.009$	$2.847 \pm 0.164$	$\sim 1.0$	Post-merging
2308.3 –0211	A2537	$-0.038 \pm 0.003$	$2.933 \pm 0.323$	$\sim 1.1$	Cool core

Table 4.5: Optical properties for 4 DXL clusters: col.1 gives the name of the cluster as in the REFLEX catalog, col.2 and col.3 – the fit parameters of the best red sequence fit (where the fit is represented by the equation  $y = ax + b$ ), col.4 – the gap between the two brightest galaxies and col.5 – the dynamical state.

of the  $\Delta m_{1,2}$  should be very robust.

Dubinski (1998) analyzed a dark matter simulated cluster with mass  $M = 1 \times 10^{14} M_{\odot}$  starting from  $z = 2$  to  $z = 0$ . Within 3 Gyr from the start of the simulation the four most massive galaxies merge to form an object resembling to an elliptical galaxy. Three of them fall down a line that can be identified as the primordial filament in the early formation of the dark matter cluster. In this context, AS0520 exhibits a bridge of diffuse stellar light (see e.g. Zibetti et al. 2005) between the two central galaxies (Fig. 4.20), similar to Rasmussen et al. (2010), and a less evident elongated feature continues towards the galaxy 4. Pierini et al. (2008) pointed out that the diffuse stellar emission follow the distribution of the dark matter (and the ICM) in relaxed (or close to relaxation) clusters. Following the magnitude gap statistics (Tab. 4.5), we support this conclusion when we compare Fig. 4.20 and Fig. 4.4. Moreover, according to De Lucia & Blaizot (2007) the BCG is built up by a series of dissipationless merging, therefore we would expect to find an old stellar population in the diffuse light surrounding the central galaxy. Consistently, the ICL observed in AS0520 has red colors and not particularly NUV emission (which trace young stars). This suggests that no recent merging events rejuvenated the diffuse light which traces the path along the gravitational cluster potential.

## 4.5 SFR computation and calibration

The two clusters considered here do not have the rich multi-wavelength coverage of ECDFS, GOODS-N and COSMOS fields. Thus, in order to get the most reliable estimate of the SFR for the cluster members we adopt the following approach. We base our SFR on the available photometry and use a subsample of ECDFS galaxies at the same redshift ( $0.28 < z < 0.32$ ) as a reference sample. The ECDFS galaxies have a calorimetric estimate of the SFR based on infrared data, and they are observed with similar photometry as for the clusters at the considered wavelengths. Thus, we check the effect of using only the B,V and R photometric band for estimating the SFR by comparing the  $SFR_{B,V,R}$  with the SFR based on infrared data. For A1300, which has a rich spectroscopic coverage, we compare this estimate of the SFR also with the estimate based on the [OII] flux line at  $\lambda = 3727 \text{ \AA}$ .

### 4.5.1 SFR from UV emission at 1500 Å

The only way to get an estimate of the SFR from the restricted photometry for A1300 and AS0520, is to use the SED fitting technique to extrapolate the flux from the rest frame UV emission at 1500 Å. Indeed the bluest band of our photometry, the WFI B band, is fairly close to the redshifted observed UV emission, but we still need an extrapolation. Since we already know the best fit template from the analysis described in Sec. 4.3.2, we use this information to derive an estimate of the dust attenuation provided in output by *Le PHARE* for the best fit solution. We use the best fit of each galaxy to extrapolate the rest-frame UV flux and we correct it for dust absorption. We use the corrected UV emission for estimating the SFR with the Daddi et al. (2004) recipe. It is clear, that the limited photometry can provide only a roughly estimate of the dust attenuation and, thus, the SFR. However we can estimate how rough this estimate is by taking advantage of the ECDFS galaxy reference subsample at the same redshift of the clusters.

We identify 248 galaxies at  $0.28 < z < 0.32$  in ECDFS, very close to the cluster redshift, with available SFR derived from the infrared emission. We use the same template set (the COSMOS templates) used in Sec. 4.3.2 to best fit the B, V, and R photometric bands of the subsample. We estimate, then, the SFR in the same way as in the clusters. Fig. 4.25 shows the comparison between the SFR derived with this procedure and the one based on IR emission. We see a clear bias in this estimate. Indeed, the best fit to the  $\text{SFR}_{\text{UV}} - \text{SFR}_{\text{IR}}$  comparison in the log-log space is a linear fit with slope  $1.06 \pm 0.11$  and intercept  $0.49 \pm 0.12$ . This means the our estimate of the SFR, based on the extrapolated UV emission, is underestimating the real SFR by half an order of magnitude. Nevertheless, the scatter of the relation is 0.45 dex. This is still consistent with the uncertainty retrieved in Sec. 2.3.2 in the  $\text{SFR}_{\text{UV}} - \text{SFR}_{\text{IR}}$  comparison, where the  $\text{SFR}_{\text{UV}}$  is based on the full ECDFS multiwavelength photometry. Thus, we use the  $\text{SFR}_{\text{UV}} - \text{SFR}_{\text{IR}}$  relation as a calibration to correct the underestimated SFR estimated with our approach.

### 4.5.2 SFR from [OII]

In order to double check the robustness of our method, we derive the SFR of the A1300 members from the [OII] doublet line flux. The [OII] doublet emission line is coupled to the H II regions, the sites of star-formation inside galaxies. The [OII] luminosity from the [OII]  $\lambda$  3726, 3729 doublet is less-directly coupled to the ionizing flux from young stars as, for example,  $\text{H}\alpha$  line. Thus it suffers larger uncertainties as a SFR indicator. However, since our spectra are detected using a low resolution blue grism, with a range of wavelength of 3700-6700 Å, the  $\text{H}\alpha$  line is not sampled at the redshift of the cluster ( $z \sim 0.3$ ). Thus, only [OII] can be used.

To estimate the [OII] line flux, we use the same definition as Balogh et al. (1999) for the continuum definition, which is measured as a linear regression between the blue and red continuum points. We estimate the line flux by summing up the flux above the continuum level in the wavelength range 3700-3755 Å. We estimate the luminosity from the flux and, finally, we compute the SFR corrected for the extinction and metallicity applying

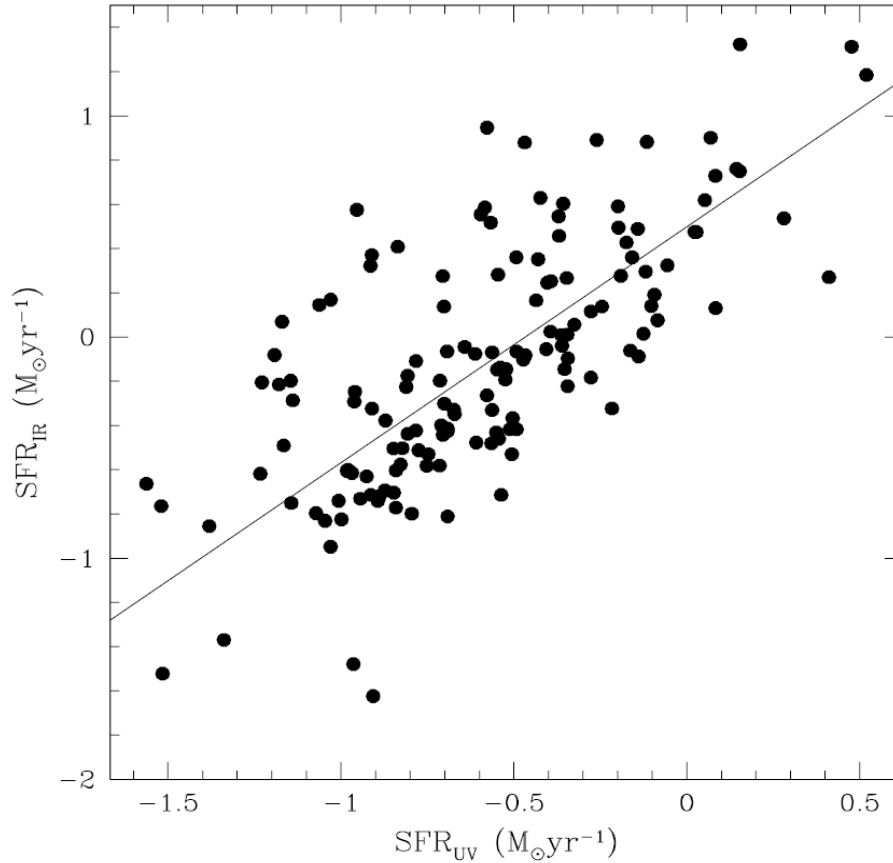


Figure 4.25: Comparison between the SFR derived from the flux at 1500 Å and the SFR derived from the infrared emission for a sample of galaxies at  $0.28 < z < 0.32$  in the ECDFS. The solid line represents the linear fit of the two sets of SFRs.

the empirical formula derived by Gilbank et al. (2010) at  $z = 0.1$ :

$$SFR_{emp,corr} = \frac{SFR_0}{a \tanh[(x - b)/c] + d} \quad (4.5)$$

where  $SFR_0/(M_\odot \text{yr}^{-1}) = L([\text{OII}])/(2.53 \times 10^{40} \text{erg s}^{-1})$ ,  $x = \log(M_*/M_\odot)$ ,  $a = -1.424$ ,  $b = 9.827$ ,  $c = 0.572$ , and  $d = 1.700$  for a Kroupa (2001) IMF (see Gilbank et al. (2010) for more details). The stellar masses used in this formula are estimated via the Bell et al. (2003) method, as explained below.

Also in this case, our estimate can offer only a rough estimate of the SFR. Indeed, the calibration provided by Gilbank et al. (2010) is calibrated at  $z \sim 0.1$  and there is no way with our data to check whether we should take into account any redshift evolution up to  $z \sim 0.3$ . The spectra used for the [OII] line flux estimate are VIMOS low resolution spectra. Thus, we can not distinguish the doublet line. In addition, the uncertainty of basing the

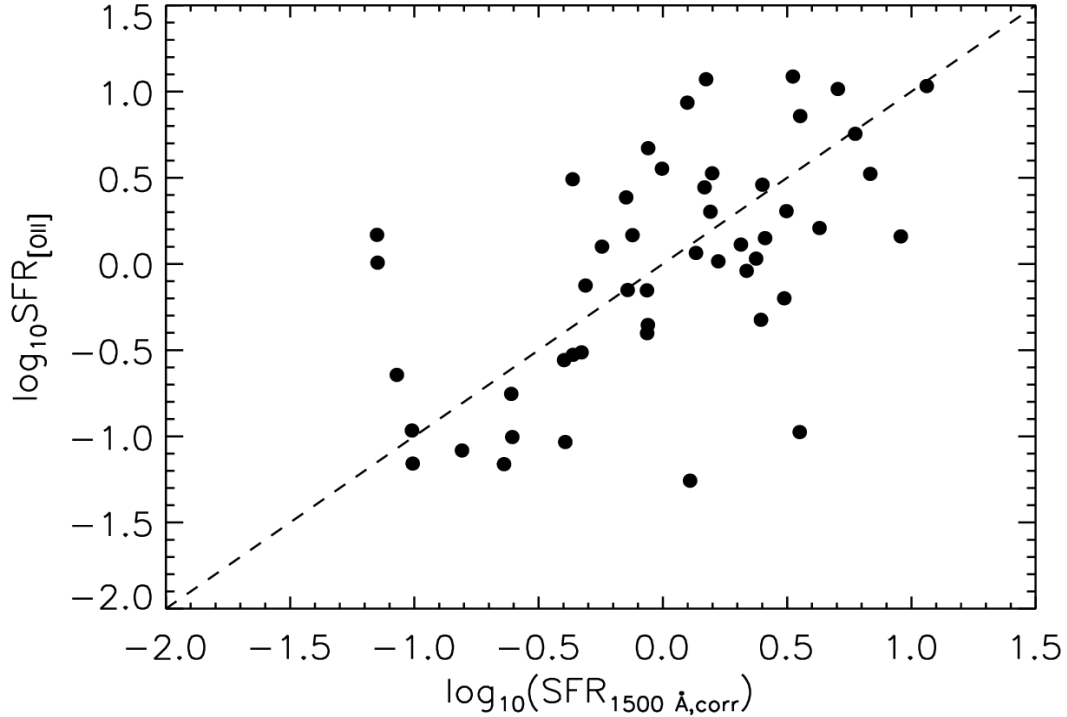


Figure 4.26: Comparison between the SFR derived from the flux at 1500 Å and the SFR derived from the [OII] line flux for all the spectroscopic members of Abell 1300 with an [OII] emission line.

stellar mass estimate on just the B,V and R photometry enters in the SFR estimate. However, we use this SFR measure only as a further check of the SFR based on the UV emission to look for a rough agreement. We compare the SFR derived from the 1500 Å, corrected for the extinction, with the SFR computed using the [OII] line flux. Fig. 4.26 is showing in the log-log space the  $\text{SFR}_{\text{UV}}$  calibrated with  $\text{SFR}_{\text{IR}}$  versus the  $\text{SFR}_{[\text{OII}]}$ . In agreement with previous findings, the  $\text{SFR}_{\text{UV}}$  is underestimated, but the larger scatter with respect to Fig. 4.25 prevents us from obtaining an additional calibration. Thus, in the further analysis, we use the  $\text{SFR}_{\text{UV}}$  calibrated as explained in previous Section.

### Stellar Mass estimate

Since wide photometric coverage is not available for the clusters like it was for the groups, the estimate of stellar mass from the SED fitting would give values with large uncertainties. For this reason, we estimate the stellar masses for all the galaxies in the region of the two clusters as done in Gilbank et al. (2010). Our dataset offers a photometric coverage in B, V, R bands for both the clusters. Thus, we can use the magnitude and color information. We use the B photometric band to measure the galaxy luminosity,  $L_B$ . Given the color (B-R)

of a galaxy and the B absolute magnitude (computed using the k-correction calculator of Chilingarian, Melchior, & Zolotukhin 2010), we are able to estimate its mass-to-light ratio using the tables provided by Bell et al. (2003). We use the following equation:

$$\log_{10}(M/L) = a_B + (b_B \times color) \quad (4.6)$$

where  $a_B = -0.976$  and  $b_B = 1.111$ .

Gilbank et al. (2010) find agreement within 0.21 dex ( $1\sigma$  scatter) when they compare their masses estimated in this way with those estimated using a set of stellar population synthesis models.

## 4.6 The evolution of the total SFR per halo mass in structures

In this section we want to study whether SF activity in dynamically active clusters is enhanced with respect to the relaxed clusters, but still below the SF level of groups. For this purpose we use the same approach of Popesso et al. (2012), by studying the location of the two merging systems in the  $\Sigma(SFR)/M_{halo}$ -redshift plane. We first explain how the total SFR per halo mass is estimated for A1300 and AS0520. Then we compare it to the one of clusters and groups.

### 4.6.1 The $\Sigma(SFR)/M_{halo}$ estimate of A1300 and AS0520

Popesso et al. (2012) define the  $\Sigma(SFR)/M_{halo}$  as the sum of the cluster (group) members with IR luminosity  $L_{IR} > 10^{11}L_{\odot}$  (LIRG regime) and within  $R_{200}$ . For A1300 and AS0520 infrared data are not available. To overcome this problem we adopted the following approach. We derive the SFR limit ( $SFR_{limit}$ ) corresponding to the  $L_{IR} = 10^{11}L_{\odot}$  via the Kennicutt (1998b) relation, by taking care of the correction to the Chabrier IMF adopted in our work. We, thus, sum up the SFR of all galaxy members within  $R_{200}$  and with SFR above  $SFR_{limit} = 17.2 M_{\odot} \text{ yr}^{-1}$  (in Salpeter (1955) IMF). To cope with the spectroscopic incompleteness, which turns out to be very high for AS0520, we proceed in the following way. The lack of infrared data does not allow us to use the same approach adopted in Popesso et al. (2012). Thus, we need to define an optical magnitude limit among the three bands available, B,V and R, to estimate the spectroscopic incompleteness above that limit. We choose the bluest band (B) in order to be closer in wavelength to the physical region used to define the SFR, that is 1500 Å rest frame. We use the galaxies at  $0.28 < z < 0.32$  with  $SFR \sim SFR_{limit}$  in the cluster regions, to define the range of apparent B band magnitude corresponding to the  $L_{IR} = 10^{11}L_{\odot}$  galaxies. The galaxies cover a quite large B magnitude range. We estimate the mean spectroscopic completeness at  $B \leq 21.37$ , which encompasses 70% of the  $L_{IR} = 10^{11}L_{\odot}$  galaxies. The completeness is of 65% in A1300 and 30% for AS0520. We divide the integrated SFR over the LIRG population by 0.65 for A1300 and 0.30 for AS0520 to correct for incompleteness.

This kind of approach is much more prone to uncertainties than the one of Popesso et al. (2012). In that case the infrared selection helps in estimating with much more accuracy the calorimetric SFR and in defining more clearly the MIPS or PACS flux limit to estimate the incompleteness. Thus, to take into account all the uncertainties due to the lack of infrared data and to the spectroscopic incompleteness (in particular for AS0520), we run dedicated simulations. As for the error analysis implemented for our group galaxy studies of previous Chapter, we use the mock catalog of Kitzbichler & White (2007). We use the same approach described in Section 2.5 to randomly extract from the complete Kitzbichler & White (2007) mock catalog, 100 mock catalogs (for each cluster) with the same spectroscopic incompleteness in B band as observed in our systems. Given the large uncertainty in the SFR estimate based on UV emission, we add randomly a noise to the SFR of each galaxy by adding a  $\delta_{\text{SFR}}$  in the range  $-\sigma_{\text{SFR}_{\text{UV}}}, \sigma_{\text{SFR}_{\text{UV}}}$  ( $\sigma_{\text{SFR}_{\text{UV}}} = 0.45$  dex, as found in Section 4.5.1), to take into account also this source of uncertainty. We, then, extract randomly in each catalog 1000 positions (ra, dec). We use these coordinates as the center coordinates of fake clusters with the redshift, velocity dispersion and  $R_{200}$  of our systems. For each fake cluster, in each catalog, we define as cluster members the galaxies with recessional velocity within  $\pm 3\sigma_{\text{CL}}$  (where  $\sigma_{\text{CL}}$  is the velocity dispersion of the considered cluster) and within  $R_{200}$ . Given the good agreement between the Kitzbichler & White (2007) mock galaxy properties and the local universe, we use the same value of  $\text{SFR}_{\text{limit}}$  used in the real dataset to identify the LIRG population. We apply the same method used for the real data to estimate the B band limit for the incompleteness correction estimate. We, then, calculate the total SFR for each fake cluster region by summing up the SFR of all galaxies with SFR above  $\text{SFR}_{\text{limit}}$ , within  $R_{200}$  and by correcting for incompleteness as done for the real data.

We estimate also the “true” total SFR in the same “fake” cluster regions in the complete Kitzbichler & White (2007) mock catalog and without adding any noise to the original SFR. The total SFR is calculated by simply summing up the SFR of all galaxies within  $\pm 3\sigma_{\text{CL}}$ , within  $R_{200}$  and with SFR above the  $\text{SFR}_{\text{limit}}$ . We measure, then, the  $\Delta(\Sigma(\text{SFR})) = \Sigma(\text{SFR})_{\text{observed}} - \Sigma(\text{SFR})_{\text{true}}$ , where  $\Sigma(\text{SFR})_{\text{observed}}$  is the one obtained as explained above in the “incomplete” catalog and  $\Sigma(\text{SFR})_{\text{true}}$  is the total SFR estimated in the original complete Kitzbichler & White (2007) mock catalog. We end up with 100000 (100 catalogs  $\times$  1000 fake cluster regions) estimates of  $\Delta(\Sigma(\text{SFR}))$  for each cluster. As already done for the group galaxy study, we analyze the distribution of  $\Delta(\Sigma(\text{SFR}))$  to estimate biases and uncertainties. The mean of the distribution is zero even in the case of AS0520, which has very low spectroscopic completeness. This confirms that, despite the rough estimate of the SFR via UV emission and SED fitting with only 3 bands, and despite the spectroscopic incompleteness, we do not over- or underestimate, on average, the total SFR. The dispersion of the distribution provides us, instead, a robust estimate of the uncertainty of our estimate of the  $\Sigma(\text{SFR})$ . It is clear that the error of this total SFR estimate is much larger than the one based on purely infrared derived SFR. Indeed we observe a dispersion of 0.31 dex for A1300 and 0.42 dex for AS0520. We use these error estimates for the estimation of the total SFR per halo mass.



### 4.6.2 The $\Sigma(SFR)/M_{halo}$ estimate for groups and relaxed clusters

In order to compare the  $\Sigma(SFR)/M_{halo}$  of the merging systems with the one of groups at lower masses and relaxed cluster at the same mass, we use the sample and  $\Sigma(SFR)/M_{halo}$  estimates of Popesso et al. (2012). Indeed, our group sample comprises the group sample studied by Popesso et al. (2012). Thus, we add the groups of our sample, not included in Popesso et al. (2012), to populate the galaxy group region in the  $\Sigma(SFR)/M_{halo}$ -redshift diagram. In addition Popesso et al. (2012) consider also a sample of 9 relaxed clusters observed in the PEP survey Lutz et al. (2010) and a merging system, the “Bullet” cluster, for which Spitzer MIPS 24  $\mu m$  data are publicly available (Chung et al. 2010).

As in Popesso et al. (2012), we estimate  $\Sigma(SFR)$ , the total SFR of each system and we then correct  $\Sigma(SFR)$  for spectroscopic incompleteness in the following way. For all systems where the PACS data reach the  $10^{11}L_{\odot}$  limit at the system redshift, we take as a reference the PACS 100  $\mu m$  catalog. We plot the 100  $\mu m$  flux density vs.  $L_{IR}$  of system member galaxies in narrow redshift bins to estimate the 100  $\mu m$  flux density that corresponds to the LIRG  $L_{IR}$  at each redshift,  $f_{LIRG}(z)$ . The spectroscopic incompleteness is defined as the fraction of PACS sources with  $z$ , among all those with flux  $> f_{LIRG}(z)$  within  $r_{200}$ . The inverse of this fraction is the correction factor that we apply to the  $\Sigma(SFR)$  estimates to correct for incompleteness.

To test the reliability of this method at least on our galaxy group sample, we apply the same error analysis described in the previous Section in the case of A1300 and A0520. For this purpose we use the catalogs generated as explained in Section 2.5). The only difference with respect to the error analysis described above is that we do not add any noise to the galaxy SFR of the incomplete mock catalogs. Indeed, the SFR of the LIRG population of our group sample is entirely based on PACS or MIPS data, thus, with an uncertainties of  $\sim 10\%$  (see Lutz et al. 2010). The error ranges from 0.1 to 0.24 dex depending on the spectroscopic completeness.

We use the estimates of  $M_{200}$  as measure of the dark matter halo mass within  $R_{200}$  for our groups. The  $\Sigma(SFR)/M_{halo}$  is obtained by dividing the total SFR by  $M_{200}$ . The final error in  $\Sigma(SFR)/M_{halo}$  is obtained by propagating the error in  $\Sigma(SFR)$  and  $M_{200}$ . For the cluster sample and the Bullet cluster, instead, we use the  $\Sigma(SFR)/M_{halo}$  estimates and uncertainties provided by Popesso et al. (2012). In this work we express all new estimates of the SFR and total SFR with a Salpeter IMF in order to compare them with the analysis of Popesso et al. (2012).

### 4.6.3 The $\Sigma(SFR)/M_{halo}$ redshift relation

#### Clusters versus groups

The  $\Sigma(SFR)/M$ -redshift relation is shown in Fig. 4.27. Black, magenta and green symbols show the  $\Sigma(SFR)/M$ -redshift relation for the clusters, massive groups ( $8 \times 10^{13} < M_{200}/M_{\odot} < 2 \times 10^{13}$ ), and low mass groups ( $8 \times 10^{12} < M_{200}/M_{\odot} < 8 \times 10^{13}$ ), respectively. For all samples there is evidence for a significant  $\Sigma(SFR)/M$  vs.  $z$  correlation, 99% significant according to a Spearman rank correlation test. On the other hand, we do not

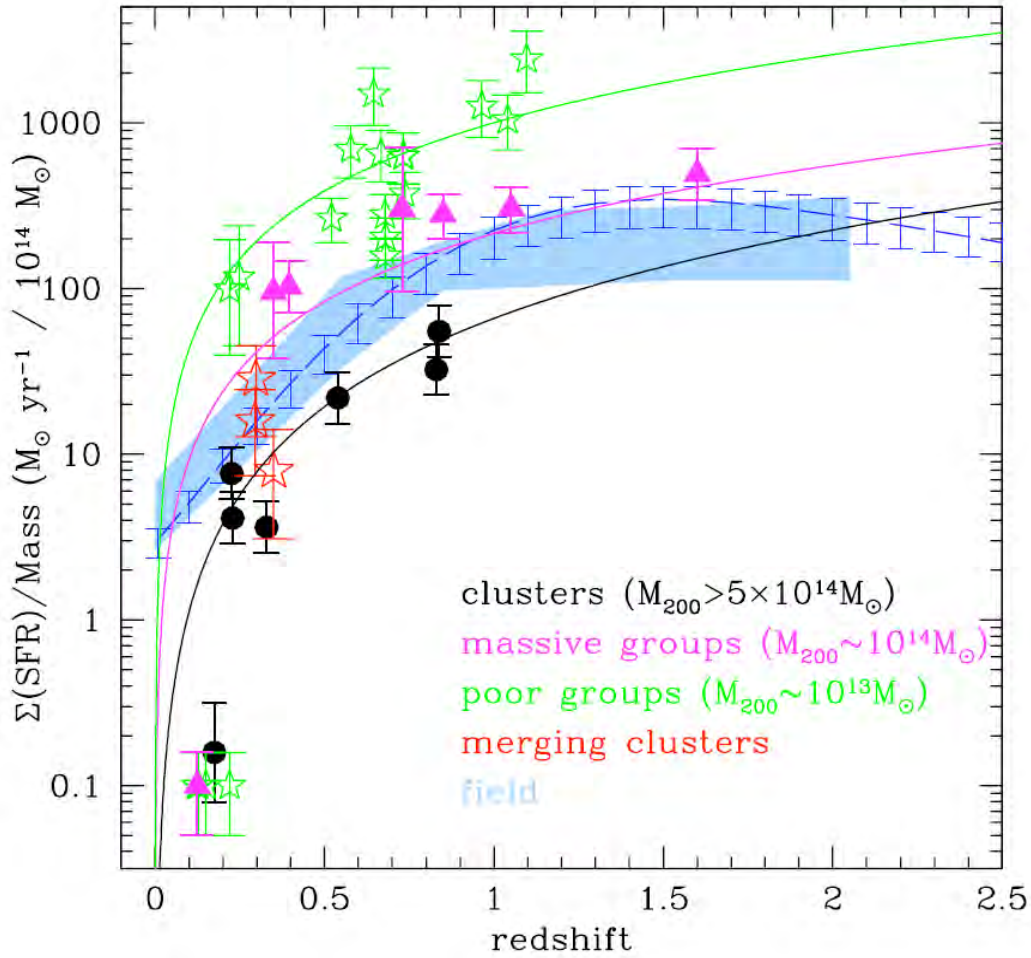


Figure 4.27:  $\Sigma(\text{SFR})/M$ - redshift relation for clusters (black symbols, from Popesso et al. 2012), massive groups (magenta triangles, of Popesso et al. 2012), poor groups (green stars), and (post-)merging systems (red stars). The black, magenta and green solid lines show the best fit  $\Sigma(\text{SFR})/M$ - $z$  relation for the clusters, massive groups, and poor groups, respectively. The light blue shaded region represents the field  $\Sigma(\text{SFR})/M$ -redshift relation from Magnelli et al. (2011) the dashed blue line the same relation of Gruppioni et al. (2011). The shading and error bars represent  $1\sigma$  confidence levels.

find evidence for significant  $\Sigma(\text{SFR})/M$ - $M_{200}$  or  $M_{200}$ - $z$  correlations within the group and cluster samples separately. Hence the observed  $\Sigma(\text{SFR})/M$ - $z$  relation within each sample must be interpreted as a genuine redshift evolution of the  $\Sigma(\text{SFR})/M$  of galaxy systems.

With respect to Popesso et al. (2012) we see a first clear difference. The inclusion of lower mass groups, not done in the previous sample, shows clearly that at least up to redshift  $z \sim 1$  (where we still have low mass groups), there is a strong  $\Sigma(\text{SFR})/M_{\text{halo}}$  vs.  $M_{200}$  anti-correlation. Indeed low mass groups tend to have higher  $\Sigma(\text{SFR})/M$  than

massive groups and clusters. This extends to much lower dark halo masses and confirms the findings of other works in the literature (Finn, Zaritsky, & McCarthy 2004; Finn et al. 2005; Homeier et al. 2005; Koyama et al. 2010).

The black and magenta solid curves in Fig. 4.27 represent best-fit models to the observed  $\Sigma(\text{SFR})/M$ - $z$  relations obtained by Popesso et al. (2012),  $\Sigma(\text{SFR})/M = (66 \pm 23) \times z^{1.77 \pm 0.36}$  for the cluster sample and  $\Sigma(\text{SFR})/M = (213 \pm 44) \times z^{1.33 \pm 0.34}$  for the massive group sample. The green line shows instead the best fit obtained in this work by fitting the low mass groups. Given the lower redshift range covered by the low mass groups, we fix the slope of the relation and we fit only the normalization. The best fit of the  $\Sigma(\text{SFR})/M$ - $z$  relation is  $\Sigma(\text{SFR})/M = (305 \pm 37) \times z^{1.33}$ . According the best fit the evolution is fast below redshift 0.2 for both groups and clusters where almost no LIRGs are detected, despite the very high spectroscopic coverage observed for these systems at the PACS or MIPS flux corresponding to  $L_{\text{IR}} = 10^{11} L_{\odot}$ .

### Structures versus field

In Fig. 4.27 we compare the  $\Sigma(\text{SFR})/M$ - $z$  relation of galaxy systems with the corresponding relation for field galaxies (light blue shaded region and blue dashed line). The  $\Sigma(\text{SFR})/M$ - $z$  relation of field galaxies is obtained by dividing the observed Star Formation Rate Density (SFRD) of Magnelli et al. (2011, triangles) and the modeled SFRD of Gruppioni et al. (2011, dashed line), by the mean comoving density of the universe ( $\Omega_m \times \rho_c$  where  $\Omega_m = 0.3$  and  $\rho_c$  is the critical density of the Universe). Both SFRD have been evaluated only down to the SFR corresponding to the LIRG  $L_{\text{IR}}$ , via the Kennicutt (1998b) relation.

The field SFRD has been estimated in large comoving volumes that include galaxy systems, voids, and isolated galaxies, thus it is representative of the general field galaxy population. According to the dark halo mass function of Jenkins et al. (2001), halos of  $10^{11} - 10^{12} M_{\odot}$  give the main contribution to the dark matter budget at all redshifts. Thus, the  $\Sigma(\text{SFR})/M$  of Fig. 4.27 can be considered as an effective estimate of the  $\Sigma(\text{SFR})/M$  of galaxy-sized dark matter halos.

Observed and modeled  $\Sigma(\text{SFR})/M$  are in very good agreement within the error bars. They increase from  $z = 0$  to  $z \sim 1$  where they reach a plateau. The field  $\Sigma(\text{SFR})/M$ - $z$  relation lies above both the group and the cluster relations at  $z < 0.2$ . The field  $\Sigma(\text{SFR})/M$  is more than an order of magnitude higher than those of the structures at  $z \sim 0.1$ . At higher redshifts, massive group and field galaxy halos show comparable  $\Sigma(\text{SFR})/M$ . Instead, low mass groups tend to have much higher  $\Sigma(\text{SFR})/M$  than the field and the more massive structures. Since the halo mass is proportional to the volume, this indicates that, despite the differences in the IR luminosity function shape and normalization, LIRGs are much more concentrated in the low massive groups than, on average, in more massive structures and in the field.

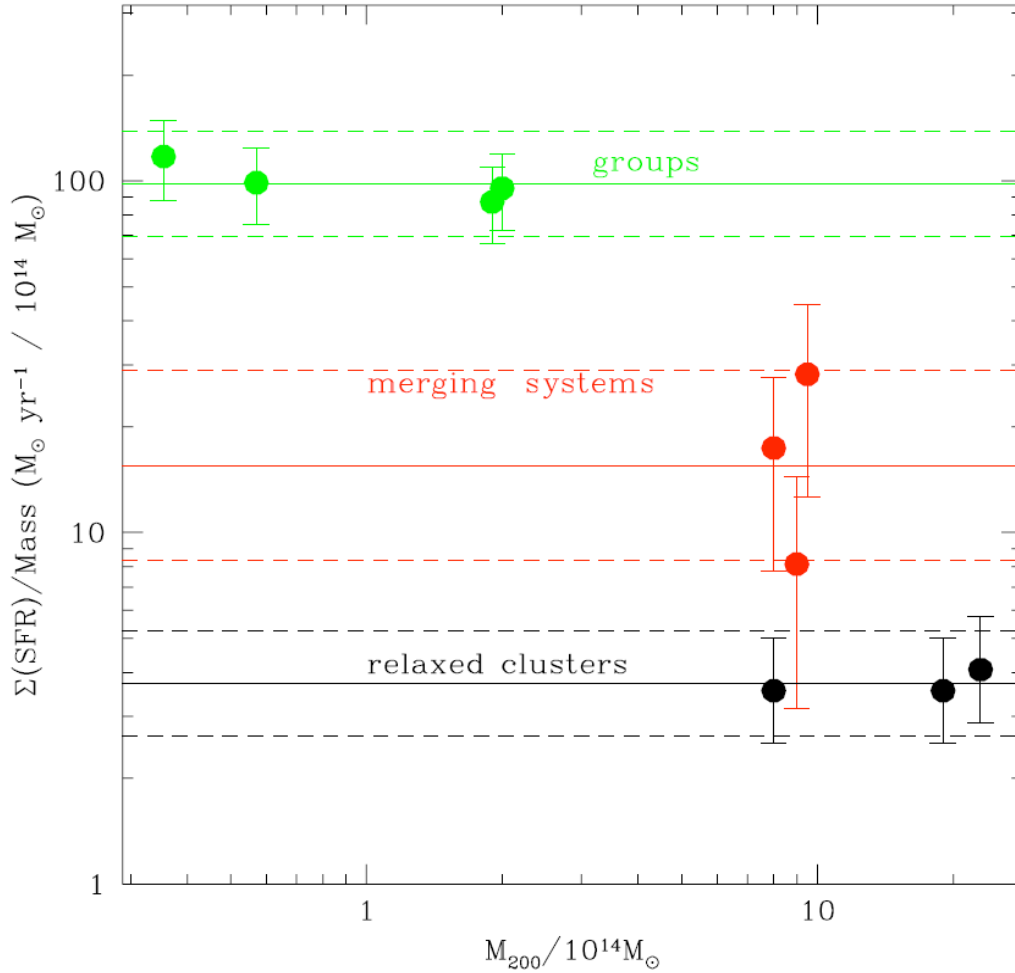


Figure 4.28:  $\Sigma(\text{SFR})/M$  vs  $M_{200}$  for different mass bins occupied by the systems of Fig. 4.27. The colors are the same as in Fig.4.27.

### Merging systems

Given the large error bars, the three merging systems (the Bullet clusters, A1300 and AS0520, red stars in Fig. 4.27) are not located clearly above the cluster  $\Sigma(\text{SFR})/M$ - $z$  relation. To have a better look at the location of the merging systems with respect to the other structures, we zoom into the redshift range of the considered systems. Fig. 4.28 shows the structures of Fig. 4.27 after zooming in to the  $0.25 < z < 0.45$  redshift range. The relative location of systems of different masses is more clearly visible. First, despite the low statistics, we see a significant anti-correlation. The average of the group  $\Sigma(\text{SFR})/M$  is  $7\sigma$  higher than the one of clusters. The merging systems, all at similar masses, show a much larger spread and the mean  $\Sigma(\text{SFR})/M$  is only  $2\sigma$  higher than the one of clusters. This could be due to several reasons. First, given the anti-correlation  $\Sigma(\text{SFR})/M$ -mass, the merging

systems, that cover roughly an intermediate mass range between groups and clusters, could just scatter “around” the linear fit between groups and clusters. Alternatively, the merging systems could really scatter “above” the linear fit, by following a sequence of times elapsed since the merger. Indeed the Bullet cluster is at  $\sim 250$  Myr after the merger event (the highest in  $\Sigma(\text{SFR})/M$ ), while A1300 is at 3 Gyr since the main merger (the intermediate in  $\Sigma(\text{SFR})/M$ ) and AS0520 is the most relaxed (consistent with the  $\Sigma(\text{SFR})/M$  shown by relaxed clusters). The low statistics and the large uncertainty due to our estimate of the SFR, do not lead to a conclusive results about the role of the merging activity in quenching or enhancing the SF activity in structures. In order to clarify this issue, we need either to collect a much larger sample of merging systems to create a composite cluster as we did for the galaxy group analysis, or we need a much more accurate estimate of the SFR to lower the error bars of the individual clusters. Nevertheless, this exercise shows clearly how powerful this kind of analysis can be. Indeed, with better statistics, we could identify if there is really a sequence of times since the merger event in the location of the  $\Sigma(\text{SFR})/M$ , to constrain for the first time the timescale of the quenching processes.

# Discussion and Conclusions

The goal of this thesis is to shed light on the role of the environment and the merging time of clusters in the evolution of the star formation activity. We first analyzed the properties of group and cluster galaxy separately, and then we combined them to investigate the star formation rate per halo mass of the systems. In the next sections we summarize the main results achieved (Sec. 5.1) and we discuss our findings comparing them with other work in the literature (Sec. 5.2). We present our conclusions in Sec. 5.3.

## 5.1 Summary

### 5.1.1 Galaxy groups

In the hierarchical scenario of structure formation, galaxy groups are the “building blocks” of galaxy clusters, thus these systems are a fundamental object of study. In addition to this aspect, from the observational point of view, galaxy groups are also the most common environment of galaxies in the present day universe, hosting up to 70% of the galaxy population (Eke et al. 2005; Geller & Huchra 1983). Hence, given that most galaxies will encounter the group environment during their lifetime, an understanding of groups is critical to follow galaxy evolution in general.

In order to follow the evolution of the relation between SF activity and environment, we divided our galaxy sample in four redshift bins,  $0 < z \leq 0.4$ ,  $0.4 < z \leq 0.8$ ,  $0.8 < z \leq 1.2$ ,  $1.2 < z \leq 1.7$ , according to the redshift distribution of our group sample (see Fig. 2.18). We note that the last redshift bin is populated by just one structure at  $z \sim 1.6$  (Kurk et al. 2009), which is likely a super-group or a cluster in formation (see discussion of Section 2.4.1). With the aim of limiting the selection effects and of taking into account the different level of spectroscopic completeness per physical properties in the different redshift bins, we applied a mass cut at  $M = 10^{10.3} M_{\odot}$ . The uncertainties were evaluated case by

case with dedicated Monte Carlo simulations based on the mock catalog of Kitzbichler & White (2007) drawn from the Millennium simulation (Springel et al. 2005). We tackled mainly three issues:

- the SFR–group-centric distance relation together with the stellar mass– and specific SFR–group-centric distance relation, to study the evolution of the SF activity within the group environment
- the SFR–galaxy local density relation with two approaches (see below)
- the location of galaxies of different environment in the SFR–stellar mass plane

We analyzed the dependence of the SF activity, stellar mass and specific SFR on the group-centric distance of the composite groups in each redshift bin. In addition we studied, for the very first time, the evolution of this dependence up to redshift  $\sim 1.6$ . We did not find any correlation between SFR and group centric distance (as confirmed by the Spearman test) at any redshift. This is consistent with previous findings and confirms the different distribution of the SF galaxies within the group region with respect to the cluster region. The mean SFR in group galaxies increases with redshift, in agreement with the picture of Noeske et al. (2007a) and Elbaz et al. (2007), who argue that the universe was more active in forming stars in the past (see also Lilly et al. 1996). Consistently with the flat SFR–distance relation, we did not observed any strong mass segregation in groups at any redshift. This could indicate a very long relaxation or dynamical friction timescale, which are usually responsible for creating mass segregation.

The main issue about the evolution of the SFR–density relation is whether it reverses or not at high redshift. It is well known that the SFR–density relation of the bulk of the galaxy population in the local universe is an anti-correlation (Gomez et al. 2003). Elbaz et al. (2007) and Cooper et al. (2008) claim that this relation reverses at high redshift indicating that the bulk of the SF activity at  $z \sim 1$  could take place in the high density regions. To shed light on this topic we followed the evolution of the SFR–density relation up to redshift  $\sim 1.6$  in the ECDFS and in the GOODS-N field. First we analyzed the SFR–density relation simply studying the statistical correlation between the SFR and galaxy local density parameters as usually done in the literature. As a second approach we used a “dynamical” definition of environment by differentiating between massive bound structures, less massive bound or unbound structures and relatively isolated galaxies. We followed the evolution of the relation in both cases up to redshift 1.6 and we tested and compared our results with the predictions of simulations.

By studying the SFR–density relation in the standard way, we found an anti-correlation up to  $z \sim 0.8$  and no correlation at higher redshift. Although the significance found by the Spearman test decreased as the redshift increased, we did not observe any reversal of the SFR–density relation. We checked the presence of biases using the mock catalogs of Kitzbichler & White (2007), as shown in Fig. 3.13. Although we constantly overestimated the values of SFR at all redshifts, due to the spectroscopic incompleteness of our catalogs, the slope of our SFR–density relation was not affected by any bias. This allowed us to



confirm the robustness of our result. We checked that the role of AGNs is rather marginal in shaping the relation, probably due to the fraction of AGNs diluted in a big area. On the other hand, the group members appeared to drive the trend on the SFR–density relation at  $z < 0.8$ . We checked if the SFR–density relation could be driven by a strong mass segregation. However, our galaxy sample shows only a very mild mass segregation at any redshift bin.

We extensively investigated the SFR–density relation at  $z \sim 1$  to understand the disagreement with previous findings. We concluded that previously observed reversal of the SFR–density relations is most likely due to the combination of different selection effects. In fact, the galaxy sample selection, a rather high fraction of AGNs in the selected sample (due to the cosmic variance) and a possibly biased definition of the density parameter, can hide a redshift dependence.

By using the “dynamical” definition of environment, we saw more clearly, for the first time and in a robust way, that the bulk of quenching happens in the groups. We found that group spectroscopic members show a much lower mean SFR than galaxies at similar density (but not belonging to bound structures of the same mass) at least up to  $z \sim 1$ . On the other hand, galaxies in less massive bound or unbound structures exhibit the same level of SFR as field isolated galaxies. Group galaxies reach the same level of SF activity as field galaxies only at  $z > 1$ . However, even with this alternative approach, we did not see any significant SFR–density reversal. The dynamical approach allowed us also to detect a mild mass segregation in groups, with the filaments representing a somewhat intermediate environment. In particular, the ratio of the mean galaxy properties with respect to the field in the different redshift bins, revealed no big variation in the mass segregation with redshift, but a strong evolution in SFR and sSFR. Thus, we conclude that group galaxies experience a much faster evolution with respect to galaxies in other environments. In addition, the strong difference in the evolution of the group galaxies with respect to non-group galaxies at similar density reveals that processes related to the presence of a rather massive dark matter halo, rather than purely density-related processes, must be dominant in the suppression of the SF activity in group galaxies below redshift 1.

In order to understand the cause of the faster evolution in group galaxies, we studied also the location of the groups, intermediate and low density galaxies in the SFR–stellar mass plane. This was done to identify if the lower mean SFR in groups at  $z < 1$  with respect to field galaxies is due to a general quenching of the SFR in all galaxies or to a faster evolution of the galaxy type mix. We found that the so called star forming galaxy Main Sequence of the groups is offset with respect to the field galaxies up to  $z \sim 0.8$ , i.e. it is shifted towards less star forming galaxies. At higher redshift the star forming group galaxies are on sequence. The intermediate density galaxies occupy at every redshift a halfway position between groups and field. This suggests that both density- and halo-related processes play a role in quenching the star formation activity of active star forming galaxies. Interestingly, the quiescent galaxy (QG) fraction evolves much faster in the groups than in the other two environments up to  $z \sim 0.8$ , beyond which the fractions are comparable. This suggests that the different type mix in groups is likely the driver of the strong evolution observed in the SFR–density relation analyzed in the dynamical approach.

### 5.1.2 Galaxy Clusters

In this section we summarize the main results obtained on the two galaxy clusters analyzed in this work: Abell 1300 and Abell S0520.

#### Abell 1300

We investigated the recent assembly history of the REFLEX-DXL post-merging cluster A1300 through the X-ray and optical (spectroscopy and photometry) data. Our main results are summarized as follows:

- The galaxy distribution of red sequence galaxies reveals a filamentary structure departing from the inner area of the cluster which extends beyond  $R_{200}$ . This suggests that galaxies could be pre-processed in the groups that we identify embedded in the filaments surrounding A1300.
- The distribution of the red galaxies of the cluster (mostly concentrated at the center) exhibits a marked correspondence with the entropy (and temperature) features, suggesting that the galaxies track the information provided by the gas in the central region out to larger cluster-centric radii.
- The study of the hydrodynamical details of the merger reveals that the X-ray surface brightness distribution is clearly affected by the presence of filamentary structures through which the groups enter the virial radius of the cluster.
- A possible forward shock (consistent with a Mach number  $\mathcal{M} = 1.20 \pm 0.10$ ) is identified in the southern part of the cluster coincident with a candidate relic (Reid et al. 1999 and Giacintucci 2011) found in the radio bands. Surprisingly also the galaxy distribution presents a sharp edge in the SW.
- A comparison with simulations suggests that  $3 (\pm 1)$  Gyr elapsed since the two cluster progenitors (still visible in the entropy map) started merging with a likely projected impact parameter between 462 and 932 kpc.

A1300 could have been disturbed by another cluster of similar mass. The collision happened most likely with a small impact parameter. The resulting shock heated the gas, yielding all the features visible in X-rays.

#### Abell AS0520

Combining X-ray, Optical and UV data we were able to investigate the mass assembly history of AS0520. The elongation of the elliptical morphology is reflected in the position of the four central brightest galaxies which are connected by a stream of diffuse stellar light. The colors of the ICL and the absence of NUV emission suggest that the diffuse light comes from an old stellar population, consistent with the build up of the BCG through

dissipationless merging (De Lucia & Blaizot 2007). Furthermore, the comparison of our analysis to the simulations of Dubinski (1998) points towards the identification of the ICL with the primordial filament of dark matter which collapsed when the cluster formed, followed by the distribution of ICM (Pierini et al. 2008).

The alignment of the brightest galaxies with the X-ray surface brightness axis finds correspondence with a filament in the South in the galaxy distribution (Fig. 4.10), characterized by faint blue galaxies. Conversely, the main body of the cluster is composed by bright red galaxies. The combination of the X-ray morphological analysis and the galaxy distribution analysis, reveals that the system is dynamically active and in accretion.

Smith et al. (2010) shows that the amplitude of the magnitude gap between the BCG and the second brightest galaxy can be related to the dynamical state of the system. Namely, very large magnitude gap are typical of relaxed system where the galaxy merger activity leads to the formation of a super-bright BCG and the lack of bright galaxies in the core. Small magnitude gaps are, instead, typical of dynamically active clusters. Thus, the amplitude of the luminosity gap is a function of both the cluster formation epoch and the recent infall history of the cluster. We used the magnitude gap observed in AS0520 to date its merger. AS0520 exhibits a slightly larger magnitude gap than A1300. This suggests that the time elapsed since the merger event of AS0520 should be slightly longer than the case of A1300. This is supported also by the lack of shocks observed in the X-ray emission of the cluster.

### 5.1.3 SFR per halo mass

In order to look at the evolution of the SF activity in galaxy systems, we considered a global quantity such as the star formation rate per unit of halo mass, that is the sum of the SFRs of all the galaxies in a system divided by the system total mass,  $\Sigma(\text{SFR})/M$  (e.g. Popesso et al. 2012). We limited the measure of  $\Sigma(\text{SFR})/M$  to the most star forming galaxies (LIRG). We built a  $\Sigma(\text{SFR})/M$ - $z$  relation up to  $z \sim 1.6$  using all the groups and clusters studied in this work and the systems previously investigated by Popesso et al. (2012). The group sample considered in this work allowed us to extend the work of Popesso et al. (2012) to a lower halo mass range. The inclusion of lower mass groups shows clearly that, at least up to  $z \sim 1$ , there is a strong  $\Sigma(\text{SFR})/M_{\text{halo}}$  vs.  $M_{200}$  anti-correlation at any redshift. Indeed low mass groups tend to have higher  $\Sigma(\text{SFR})/M$  than massive groups and clusters.

The field  $\Sigma(\text{SFR})/M$ - $z$  relation lies above both the group and the cluster relations only at  $z < 0.2$ . The field  $\Sigma(\text{SFR})/M$  is more than an order of magnitude higher than those of the structures at  $z \sim 0.1$ . At higher redshifts, massive group and field galaxy halos show comparable  $\Sigma(\text{SFR})/M$ . Instead, low mass groups tend to have much higher  $\Sigma(\text{SFR})/M$  than the field and the more massive structures. Since the halo mass is proportional to the volume, this indicates that, despite the differences in the IR luminosity function shape and normalization, LIRGs are much more concentrated in the low massive groups than, on average, in more massive structures and in the field.

By zooming into the  $0.25 < z < 0.45$  redshift range of A1300 and AS0520, we built

the  $\Sigma(SFR)/M_{halo} - M_{200}$  relation. We saw, despite the low statistics, a significant anti-correlation. The average of the group  $\Sigma(SFR)/M$  is  $7\sigma$  higher than the one of clusters. The merging systems, all at similar masses, show a much larger spread. Indeed, the mean  $\Sigma(SFR)/M$  is only  $2\sigma$  higher than the one of clusters. This could be due to several reasons. First, given the anti-correlation  $\Sigma(SFR)/M$ –mass, the merging systems, that cover roughly an intermediate mass range between groups and clusters, could just scatter “around” the linear fit between groups and clusters. Alternatively, the merging systems could really scatter “above” the linear fit, by following a sequence of times elapsed since the merger. Indeed the Bullet cluster is at  $\sim 250$  Myr after the merger event (the highest in  $\Sigma(SFR)/M$ ), while A1300 is at 3 Gyr since the main merger (the intermediate in  $\Sigma(SFR)/M$ ) and AS0520 is the most relaxed (consistent with the  $\Sigma(SFR)/M$  shown by relaxed clusters). The low statistics and the large uncertainty due to our estimate of the SFR, do not lead to conclusive results about the role of the merging activity in quenching or enhancing the SF activity in structures. However, our analysis suggests that the merging event could play an important role in the “revival” of the SF in clusters, and the time elapsed after the merging could draw a sequence in the location of the  $\Sigma(SFR)/M$ . A better statistics and a larger sample are key parameters for confirming our analysis.

## 5.2 Discussion

### 5.2.1 SFR, Mass and sSFR as a function of group-centric distance

Since  $z \sim 2$  galaxy evolution is characterized, generally speaking, by the quenching of the star formation. In order to shed light on the processes that affect the star formation of galaxies in different environments and at different cosmic epochs, we have investigated how SFR, stellar mass and sSFR are distributed as a function of the distance from the group centers. Our main results see the absence of gradients in SFR and sSFR and a mild mass segregation within the systems of our sample. We discuss in this section the implication of these two results and the comparison with other works.

The weak dependence of SFR group global properties, such as group-centric distance, might be an indication that the SF properties of group galaxies are more affected by their immediate environment, e.g., local galaxy density or presence of substructures (Wilman et al. 2005), rather than the global environment. It could also suggest that the SF properties of the group members are not directly related to their present environment (Balogh et al. 2004). This does not usually happen for relaxed clusters where the local SF fraction increases linearly from the cluster core to large radii in nearby rich clusters (e.g. Bai et al. 2009; Balogh, Navarro, & Morris 2000; Chung et al. 2010; Mahajan, Haines, & Raychaudhury 2010). In particular, Balogh, Navarro, & Morris (2000), in a study of the CNOC1 cluster sample, find that although the SFR increases towards the cluster outskirts ( $\sim 2R_{200}$ ), it remains suppressed by almost a factor of two relative to the field. Moreover, Balogh, Navarro, & Morris (2000) reproduce qualitative and quantitative dif-

ferences in the mean star formation rates and colors between clusters and the field using N-body simulations. Their model assumes that the cluster galaxy population is built by the ongoing accretion of field galaxies which are sustained by regular accretion of gas from their surroundings, and reservoirs of fresh star formation fuel are lost as galaxies enter the cluster potential. Thus, the origin of radial gradients in these properties is the natural consequence of the strong correlation between radius and accretion times which results from the hierarchical assembly of the cluster. According to this model, the absence of anti-correlation between mean galaxy SFR and the group-centric distance that we observe could reflect the much smaller spread in accretion times of low mass objects such as the groups considered in our analysis. Recent studies have extended this conclusion to even larger radii. For example, Chung et al. (2010), studying a sample of local clusters using WISE (IR) data, observe a steep increase in the mean sSFR from the central bin to  $R_{200}$ , then a monotonically increment till a flattening out below the field value at larger radii ( $\sim 3R_{200}$ ).

Recent results of Rasmussen et al. (2012) and Wetzel, Tinker, & Conroy (2012) show that a dependence of the SF activity on the distance from the center is established also in groups. However, both works use an optical selection which could introduce some biases in the identification of the groups themselves. In more detail, Rasmussen et al. (2012) analyze a sample of group galaxies at  $z \approx 0.06$  with deep UV observations. They detect a SF gradient within  $2 R_{200}$  for galaxies less massive than  $10^{10} M_{\odot}$  (similarly to Presotto et al. 2012), while they do not find any environmental effect for massive galaxies. The authors argue that the difference in the result with respect to previous works is due to a higher mass cut applied to the other samples. In their opinion, it is in principle possible to observe such a gradient with a higher mass completeness. A similar conclusion is reached by Wetzel, Tinker, & Conroy (2012) who study the fraction of quenched galaxies as a function of group-centric distance in a sample of groups in the SDSS. They find that the fraction of quenched galaxies increases towards the halo center, with a strong trend for the low mass galaxies. According to this scenario, our mass cut at  $M = 10^{10.3} M_{\odot}$  does not allow us to see the ongoing quenching of the SF. However, analyzing the behavior of galaxies less massive than  $10^{10} M_{\odot}$  we do not see any dependence in SFR and sSFR with group-centric distance, even in our lowest redshift bin. The divergence in the result might be due to the different range in the group-centric distance considered in the two works. In particular, Rasmussen et al. (2012) consider in their analysis also the group infalling regions (up to  $10 R_{200}$ ), where several authors find enhanced star formation (e.g. Haines et al. 2010; Pereira et al. 2010). On the other hand, our analysis centers on the study of galaxy properties within  $\sim 1.5 R_{200}$ , thus investigate a region more directly affected by the gravitational potential of the group.

A conclusion similar to our results is reached by Bai et al. (2010). In this work the authors analyze the Spitzer MIPS observations of a subsample of 9 groups at  $z \approx 0.06$  optically selected in the 2dF spectroscopic survey and detected with XMM observations. They compare the mean SF galaxy (with  $\text{SFR} > 0.1 M_{\odot} \text{ yr}^{-1}$ ) fraction of groups to other two clusters with similar data. In contrast to the rich clusters, SF fractions in groups show no clear dependence on the distance from the group centers and remain at a level

higher than the outer region of the rich clusters. They propose as interpretation a possible breakdown of the correlation between the galaxy density and projected distance rather than a breakdown of the correlation between SF galaxy fractions and galaxy density. However, we do not find any significant correlation between SF activity and density within the group environment. This strengthens the interpretation that the SF properties of the group members are not directly related to their present environment Balogh, Navarro, & Morris (2000).

Presotto et al. (2012) use a sample of optically selected groups at  $0 < z < 0.8$  drawn from the *zCOSMOS* survey (Lilly et al. 2005). They observe that the blue fraction of most massive group galaxies ( $\log(M_{\text{gal}}) \geq 10.56$ ) does not reveal a strong group-centric dependence, despite displaying a clear lower blue fraction in groups than in the field. Conversely, they find a radial dependence in the changing mix of red and blue galaxies for less massive galaxies ( $0.8 \leq \log(M_{\text{gal}}/M_{\odot}) < 10.56$ ), with red galaxies being found preferentially in the group center. They note that this trend is stronger for poorer groups, while it disappears for richer groups. Their definition of richness is based on an absolute magnitude cut and does not give any indication of the group halo mass. Thus we are not able to directly compare the results based on our group sample with their results. Moreover, Presotto et al. (2012) add photometric members to their groups in order to increase the statistics. This could introduce a contamination of field galaxies, in particular in the group outskirts and in the poor groups.

A comparison at higher redshift is offered by Tran et al. (2010). They analyze the dependence of the SF activity as a function of the density in a super-group at  $z = 1.6$ . Their *Spitzer* MIPS data reveals a very high level of star formation activity which increases with density. According to their estimate, the highest level of star formation happens in the system core. This is apparently in contrast with our results, according which there is no dependence between SFR and group-centric distance. However, Tran et al. (2010) detect a correlation with a significance of only  $> 2\sigma$ . Furthermore, they consider strong IR emitting galaxies for which the luminosity could be the result of a boosting due to the luminosity extrapolated by the  $24 \mu\text{m}$  (Elbaz et al. 2011, see also Sec. 1.4.2).

Our interpretation of the flat relation between mean SFR and group-centric distance up to redshift 1.6 is more linked to the very little mass segregation observed in our groups at any redshift. Indeed, we find only a mild and poorly significant ( $\sim 2.5\text{-}3\sigma$  significance level) anti-correlation between mass and distance from the center in the two lowest redshift bins and no correlation at all at  $z > 0.8$ . In general, the presence of a strong mass segregation is expected to be found in massive clusters as the result of violent relaxation or dynamical friction. In the first case, mass segregation occurs with an exchange of kinetic energy among group member galaxies with the lighter galaxies having larger velocity than the heavier galaxies. After the energy is exchanged, most massive galaxies set in the core of the cluster while the lighter galaxies preferentially reside in the outer regions. This scenario is particularly efficient for groups, where the galaxy encounters are very common. Dynamical friction, instead, represents a kind of frictional drag which causes the galaxy motion to slow down. If the galaxy is on an orbit that makes repeated passages through the cluster or group halo, its orbit will decay over time and it will spiral in and be accreted by the larger

object, thus causing the larger object to grow in mass and size. Since the timescale of dynamical friction varies as  $\sigma/\rho^3$  (where  $\sigma$  is the velocity dispersion and  $\rho$  the density of the halo), high velocity dispersion clusters do not suffer much internal dynamical evolution of their galaxy populations after their primary formation phase. Conversely, relatively low velocity dispersion groups could produce interactions and mergers on a cosmologically short timescale, even at low redshifts. Both violent relaxation and dynamical friction would support the picture for which the mass gradient in groups should be evident. Thus, if a correlation between the group-centric distance and time since the galaxy infall is expected (Gao et al. 2004; Weinmann, van den Bosch, & Pasquali 2011), radial gradients should translate into an evolutionary sequence of star formation and mass segregation. However, we do not observe such a scenario. The lack of mass segregation, together with a constant fraction of blue galaxies observed by Bai et al. (2010), would suggest that the galaxy type mix and the stellar mass function does not depend on the location within the groups. This alone would explain the flat relation between SFR and distance from the center.

The lack of mass segregation in groups is observed also in other works in the literature. For example, Presotto et al. (2012) find a constant mix of galaxy stellar masses irrespective of the radial distance from group center for poor groups, although they do see significant mass segregation for rich groups. However, the arbitrary definition of group richness adopted by Presotto et al. (2012), does not allow us to fairly compare the two results. A similar conclusion is reached by Tal, Wake, & van Dokkum (2012) for a sample of Luminous Red Galaxies (LRGs) at redshift  $0.28 < z < 0.4$ . Indeed, LRGs are the most massive galaxies ( $M > 10^{11} M_{\odot}$ ) in the nearby universe and 90% of them are expected to be the central galaxy in halos of  $M_{\text{halo}} > 10^{13} M_{\odot}$ . Similarly to our result, the authors find a mild mass segregation in LRGs environments (up to 700 kpc from the LRG). It must be noted, however, that Tal, Wake, & van Dokkum (2012) use luminosity segregation to assess mass segregation. The absence of mass gradient is assessed also by Wetzel, Tinker, & Conroy (2012) who study a sample of optically selected groups in SDSS. In particular, the authors do not find any satellite mass segregation at any group halo mass.

We point out that mass segregation is a matter of debate also in case of galaxy clusters. Indeed, not all galaxy clusters show a significant sign of mass segregation within the virial radius (e.g. von der Linden et al. 2010). One typical example is represented by the Coma cluster. White (1977) compare the galaxy distribution observed in Coma with the one obtained from N-body simulations. The main argument of White (1977) to explain the disagreement between their model and the observation is that the most of the cluster mass could not be bound to the galaxies (as known as “the missing mass” problem), since in their model the most massive galaxies end up always in the center of the cluster. Another plausible explanation can be related to the dynamical state of the cluster. The perturbations due to accretions or merging can delay the relaxation times, since more galaxy encounters are expected. According to this picture, the relaxation or the dynamical friction timescales are not short enough to lead to a significant mass segregation at any of the considered redshifts in our study. Moreover, according to the hierarchical scenario of galaxy formation, groups are a rather “unstable” environment since the time necessary for heavy galaxies to sink to the center of the potential well is too long compared to the



lifetime of the group itself, i.e. the relaxation time is longer than the group crossing time.

### 5.2.2 SFR–density relation

#### The “environmental approach”

The local SFR–density relation (Gómez et al. 2003) shows an anti-correlation, where the cores of massive clusters are galaxy graveyards full of massive spheroidal systems, dominated by old stellar populations. However, it has been argued that as we approach the epoch at which the early type galaxies should be forming the bulk of their stars at  $z \gtrsim 1.5$  (e.g. Rettura et al. 2010), the relation between star formation activity and environment should progressively reverse.

Our results shows that the SFR–density relation is progressively flattening towards high redshift but it does not reverse. In addition a careful analysis of the biases due to the spectroscopic selection, leads us to the conclusion that we can not exclude even an anti-correlation at  $z > 0.8$ . The observed SFR–density anti-correlation at  $z < 0.8$  is not simply ascribable to mass segregation (most massive galaxies are generally passive galaxies, low mass galaxies are on average star forming). Indeed, we observe only a mild mass segregation at any redshift bin. Our results seem to be at odds with Kauffmann et al. (2004) who find strong mass segregation at least in the local universe. At higher redshift the effect has never been thoroughly analyzed, except for the recent results of Scodeggio et al. (2009) who show that already at  $z \sim 1$  mass and galaxy density are coupled with the most massive galaxies segregated in the most dense environment. However, we must note that our stellar mass cut ( $M > 10^{10.3} M_{\odot}$ ) is rather high. Indeed, applying a lower mass cut ( $M > 10^9 M_{\odot}$ ) in the low redshift bin leads to a much stronger mass segregation although of small amplitude. This would be in agreement with recent finding of Rasmussen et al. (2012) who, as mentioned above, observe that mass segregation can be observed within  $10 R_{200}$  from the groups only by considering low mass galaxies.

Given, the further flattening of the SFR–density relation observed after excluding group galaxies from the sample, we conclude that group galaxies are mostly responsible for the observed anti-correlation at  $z < 0.8$ . Thus, galaxies living in relatively massive dark matter halos must have a suppressed mean SFR with respect to the field at least up to  $z \sim 0.8$ . This will be confirmed by the SFR–density relation analyzed with our “dynamical” approach (see the discussion below).

One of the most striking findings in our analysis is the lack of reversal of the SFR–density relation at  $z \sim 1$ . This result is at odds with recent findings. In particular, Elbaz et al. (2007) and Cooper et al. (2008) observe the reversal of the SFR–density relation at  $z \sim 1$  in the GOODS and the DEEP2 fields, respectively, using a spectroscopically defined density parameter. In the discussion of our results in Section 3.3, we compare extensively our analysis with the one of Elbaz et al. (2007). Indeed, the most fair comparison is with Elbaz et al. (2007) since our dataset include the sky regions covered by their dataset. We argue that the possible source of disagreement can be either a different galaxy sample definition, or a different recipe for the estimate of the SFR or of the density parameter.

Popesso et al. (2011) show that the use of PACS data provide the big advantage, with respect to the MIPS data or [OII] doublet, for measuring without biases the SFR of AGN, whose SFR could be enhanced with respect to non active galaxies of similar stellar mass (Santini et al. 2012). Thus, given the high fraction of AGN (17%) measured at least in the highly star forming population of the GOODS-S and GOODS-N population, Popesso et al. (2011) conclude that the reversal of the SFR observed by Elbaz et al. (2007) could be due to a bias introduced by the AGN SFR. However, using the AGN sample of Shao et al. (2010) for the GOODS-N region and the AGN sample of Lutz et al. (2010) for the ECDFS, we observe that AGN play a marginal role in shaping the SFR-density relation. A further source of disagreement could be in the different approach in measuring the density parameter. As explain in Section 2.6, our density estimate is based on a constant mass cut. Popesso et al. (2012) show also that the density definition adopted by Elbaz et al. (2007), based on a simple galaxy apparent magnitude cut ( $z_{AB} < 23.5$  mag), could lead to a strong redshift bias. Thus, we conclude that the previously observed reversal of the SFR-density relations is most likely due to the combination of different selection effects due to the galaxy sample selection, a rather high fraction of AGNs in the selected sample and a possibly biased definition of the density parameter, which can hide a redshift dependence.

Our result is, instead, in agreement with Feruglio et al. (2010) who find no dependence of the SFR and LIRG fraction on environment, arguing that the reversal, if any, must occur at  $z > 1$ . According to Feruglio et al. (2010) the reversal found by Elbaz et al. (2007) and Cooper et al. (2008) might be due to the contribution of galaxies at lower stellar mass and SFR comprised in Elbaz et al. (2007) and Cooper et al. (2008) galaxy sample. However, since we consider a wide range of SFR and stellar masses, we disagree with this conclusion. The advantage of Feruglio et al. (2010) is the use of a wide field such as COSMOS, thus they are less affected by cosmic variance. However, they use sources with both spectroscopic and photometric redshifts to define the density field. This could dilute somehow any overdensity present in the field. Our approach is more rigorous in this sense. In addition, we check for biases in our analysis using the mock catalogs of Kitzbichler & White (2007). This comparison assures us that we are not suffering from any bias in the slope of the SFR-density relation and, thus, that our result is reliable.

### The “dynamical approach”

The use of the standard approach for the study of the SFR-density relation, can be poorly effective if the galaxy local density is not directly connected to the SF activity, either via mass segregation or due to SF quenching processes linked to the galaxy-galaxy interactions. This is the reason why we analyze the SFR-density relation with a “dynamical” approach. This is done by distinguishing environments on the basis of the parent halo mass rather than density. In other words, we distinguish between group members, as identified via dynamical analysis, and galaxies at intermediate environments (“filament-like” environment), which is at the same density but not belonging to any of the detected X-ray sources. Field isolated galaxies are, instead, identified as the systems with galaxy local density in the range of values where no group galaxies are found. The “dynamical approach” allows us to separate

the contribution to the highest galaxy density bins of groups and filament-like galaxies, respectively. This is not possible in a more classical “environmental approach”.

Our results show that the bulk of the SF is quenched in groups, which actually drive the trend of the SFR–density relation. The high density environment has a slower evolution in SF compared to the groups, thus the density (galaxy-galaxy interaction) itself can not be responsible for the bulk of the quenching. We are showing, for the first time and in a robust way, that the SFR–density relation, as generally intended in the “environmental approach” (Cooper et al. 2008; Elbaz et al. 2007; Feruglio et al. 2010), is not enough to separate the contribution of dynamically bound systems with respect to high density environments in a different dynamical state.

The high SFR in the “filament-like” galaxies, more consistent with the field mean SFR than with the group SFR, is in agreement, at least at low redshift, with the recent finding of Fadda et al. (2008) and Biviano et al. (2011). They show that the filament around the supercluster A1763 hosts the highest fraction of IR-emitting galaxies. Similarly, the filament region contains the highest total SFR per unit galaxy. The findings are also consistent with those of Porter & Raychaudhury (2007), who have used optical data to discover an enhanced star-forming activity among galaxies associated with filaments in the nearby Pisces-Cetus supercluster. They also claim that the SFR in the filament galaxies peaks at 3-4 Mpc from the cluster center, consistently with Biviano et al. (2011).

### 5.2.3 The SFR-Mass plane in different environments

In order to investigate what is the cause of the strong evolution of star formation in the systems of our sample, we study the position of group galaxies with respect to the main sequence population (Daddi et al. 2007a; Elbaz et al. 2007; Noeske et al. 2007a; Peng et al. 2010).

Many works focused mainly on the study of the MS in field galaxies. For example, according to Noeske et al. (2007a), this smooth sequence suggests that the same set of few physical processes governs the SF activity in galaxies. If “mass quenching” is the dominant mechanism for moving a galaxy across the MS, the location of the star forming galaxies in high density environments should not be different from the bulk of the star forming galaxies regardless of their environment. If, instead, the environment plays a role in the evolution of the galaxy SF activity, the position of the group galaxies along or across the main sequence should be different with respect to the bulk of the star forming galaxies.

This last point reflects our main result on the analysis of the SFR-Mass relation. In particular, we have studied, for the first time, the location in the SFR- $M_\star$  plane of groups, filaments and field galaxies. The evolution of  $\Delta_{\text{MS}}$  shows that, at least below redshift  $\sim 0.8$ , the star formation activity in group galaxies is quenched with respect to the bulk of the SF galaxies. At earlier epochs, groups, filaments, and field have comparable star formation. Interestingly, the density seems to play a role in the distance from the MS, since the filaments represent a somewhat intermediate environment also in the evolution of  $\Delta_{\text{MS}}$ . Thus, we show, for the first time and with high significance, that the speed of the evolution of the SF activity in star forming galaxies depends, at least since  $z \sim 1$ ,

on the galaxy environment, defined according to our “dynamical” approach. In addition, we find also that the fraction of quiescent galaxies decreases more steeply as the redshift increases for groups than for filaments and field. The latter two environments show a very similar evolution of quiescent galaxy fraction. This confirms once again that the galaxy membership to a rather massive halo ( $2 \times 10^{13} M_{\odot}$ ) is a cause for a rapid evolution and for a rapid quenching of the SF activity much more than the membership to a generally dense region. Thus, quenching processes happening in massive halos (strangulation, ram pressure stripping) are likely to be much more effective than the simple galaxy-galaxy interaction.

Our result is in contrast with the analysis of Peng et al. (2011). Peng et al. (2011) argue that the central star forming galaxies are equivalent to field galaxies. They claim that there is no difference in the main sequence relation of central and satellite galaxies. However, it is not clear how they discern between star forming and passive galaxies. In fact, over their whole study, Peng et al. (2011) use the red/blue galaxy dichotomy to distinguish between passive/SF galaxies respectively. However, as argued by Woo et al. (2012), about 30% of the SDSS red sequence galaxies, identified in the color-magnitude diagram, lies on the MS sequence. This is confirmed also by Whitaker et al. (2012) who find 2 different MS for blue and star forming galaxies. This implies that selecting blue galaxies leads to missing many red dusty star forming sources. Moreover, Peng et al. (2011) use the catalog of Yang et al. (2007) (based on a Friend of Friend algorithm) to explore the properties of group galaxies. As we already mentioned, the optical selection is much more prone to projection effects than the X-ray selection and it can lead to highly contaminated catalogs.

Our findings show that we can not rule out completely the pre-processing scenario (galaxies age in groups before entering in clusters) as proposed by Popesso et al. (2012). This is consistent with the result of an analogous analysis done by Bai et al. (2010) on the sample of 2dF groups already mentioned in previous discussion. Interestingly, they show that the group SF galaxies are located below the field MS, but above the location of the bulk of cluster star forming galaxies. This suggests that a certain amount of pre-processing is happening in groups but a further quenching must happen even in the more dense cluster environment. Here we show that a certain amount of pre-processing happens even before the star forming galaxies enter in the group environment when they are falling along the filaments. Recently, Rasmussen et al. (2012), computing the SFR from UV emission for nearby group galaxies, find a MS broadly consistent but flatter than the MS of field galaxies at the same redshift. They argue that the flattening could be expected if the SFR of low mass galaxies is suppressed in groups. At a median mass of  $\log(M_{\star}/M_{\odot}) = 9.63$  their MS predicts a mean sSFR which is  $\sim 40\%$  lower than that expected for the field. This could be consistent with our results although we do not cover the same mass range.

The pre-processing is supported also by models. De Lucia et al. (2012), using semi-analytic models, show that the fraction of galaxies that can be pre-processed in a group-size halo of mass  $\sim 10^{13} M_{\odot}$  is significant ( $\sim 27\%$  which raise to  $\sim 44\%$  for galaxies with  $M \sim 10^{11} M_{\odot}$ ). Furthermore, comparing observations with their theoretical predictions, they argue that satellite galaxies become passive after they have spent 5-7 Gyr in halos more massive than  $M_{\text{halo}} \sim 10^{13} M_{\odot}$ . Similarly, McGee et al. (2009), using the stellar mass and merger trees produced by the semi-analytic galaxy catalogs, find that clusters

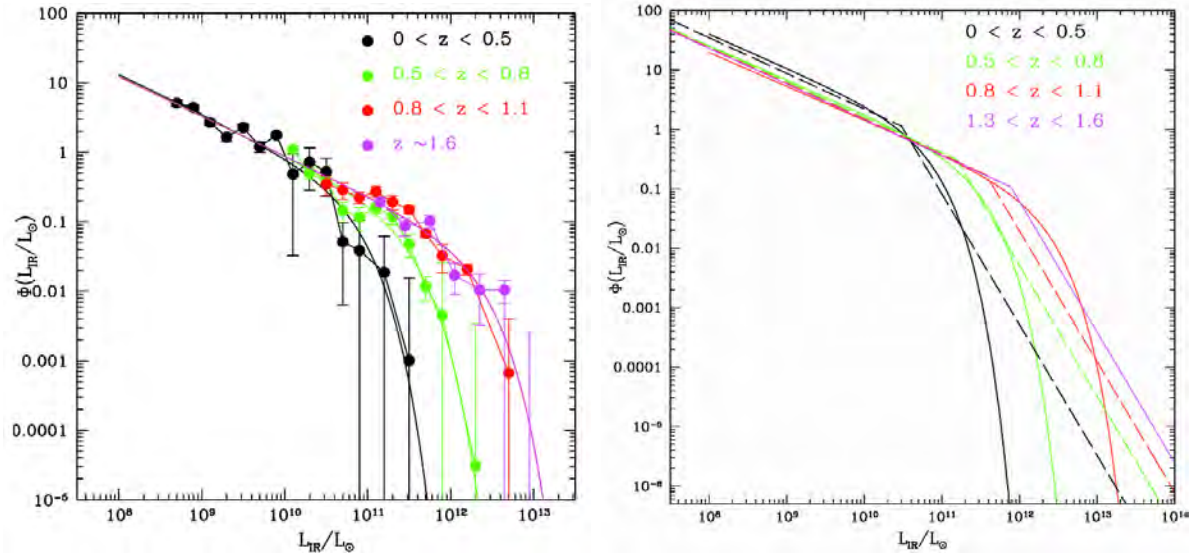


Figure 5.1: Left panel: Infrared luminosity function for the X-ray detected groups in ECDFS (Popesso & Ziparo in prep.). Right panel: comparison of the best fits for the group (left panel, solid lines) and field (dashed lines) IR luminosity functions. The group LF is fitted with a Schechter function and renormalized to the LF of the field which is best fitted with a double power law.

at all redshifts examined exhibit a significant fraction of their galaxies accreted through galaxy groups. For instance,  $10^{14.5} M_{\odot}$  mass clusters at  $z = 0$  have had  $\sim 40\%$  of their galaxies accreted through group halos. At higher redshifts ( $z \sim 1.5$ ) this fraction is only  $\sim 25\%$ . Our results show qualitative agreement with this prediction. Conversely, Berrier et al. (2009), using cosmological  $\Lambda$ CDM N-body simulations, find that on average,  $\sim 70\%$  of cluster galaxies fall into the cluster potential directly from the field, with no luminous companions in their host halos at the time of accretion; and less than  $\sim 12\%$  are accreted as members of groups with five or more galaxies.

This scenario is also reflected in our analysis on the QG fraction in groups, intermediate density environments and the field. Our findings suggest that these environments have a different type mix up to  $z \sim 1$ , with groups being the most efficient locus for quenching the SF. At higher redshift the galaxy population of groups, filaments and field is similar. Our results find support in several works in the literature. For example, Kovač et al. (2010) show that galaxy star-formation and color transformation rates are higher in the group regions than in lower density areas at  $z \sim 1$ . In addition, Iovino et al. (2010) show that the group galaxy population becomes bluer as redshift increases, but it maintains a systematic difference with respect to the global galaxy population, and an even larger difference with respect to the isolated galaxy population.

Recently, Popesso & Ziparo (in prep.) analyze the IR composite luminosity function of the group sample presented in this work. Fig. 5.1 shows the evolution of the group luminosity function (the LF are normalized for an easy comparison). The characteristic

luminosity at which the luminosity function has an exponential cut-off, shifts to brighter luminosities as the redshift increases. Interestingly, this is consistent with what Magnelli et al. (2009, 2011) find for the field. Indeed, once the best-fit for groups and field are superposed (right panel of Fig. 5.1), the bright ends become more and more similar, in perfect agreement with our results.

### 5.2.4 Star formation rate per halo mass

The cluster  $\Sigma(\text{SFR})/M$  evolution we find, appears to be faster, at least in the range  $0 < z < 1$ , compared to the evolutionary relation suggested by Bai et al. (2007); Bai et al. (2009); Geach et al. (2006); Koyama et al. (2010). This might be due to our higher- $L_{\text{IR}}$  cut, if LIRGs evolve faster than less luminous IR-emitting galaxies. A faster evolution has already been suggested by Biviano et al. (2011), but only in the  $z < 0.5$  range, while in our data there is no sign of a flattening of the  $\Sigma(\text{SFR})/M$ - $z$  relation for clusters above that redshift.

We confirm earlier indications (Bai et al. 2007; Finn et al. 2005; Koyama et al. 2010) that  $\Sigma(\text{SFR})/M$  is lower for systems of higher mass, and we extend this analysis, for the first time, to low mass X-ray groups with masses of  $M_{200} \sim 10^{13} M_{\odot}$ . Bound systems of any mass lie below the field relation only at  $z < 0.2$ . At higher redshifts, the massive group and the field  $\Sigma(\text{SFR})/M$  become comparable, while low mass group lie always above the field and the massive group relation. This indicates that, despite the difference in luminosity function shape and normalization, the spatial concentration of group SF galaxies is higher in systems of lower masses. This is due to the fact that the halo mass is a proxy of the volume.

As already proposed by Popesso et al. (2012), our results appear to support a scenario in which the quenching of SF occurs earlier in galaxies embedded in more massive halos, i.e. first in clusters, then in groups, and finally in the field. This would be consistent with a “halo downsizing” effect, whereby massive halos evolve more rapidly than low mass halos (Neistein, van der Bosch & Dekel 2006). Although in a narrow range of halo masses, the “halo downsizing” effect has already been observed in the stellar-to-total mass ratio vs. redshift relation by Foucaud et al. (2010).

Our analysis suggests that the time elapsed after the merging event in clusters and the dynamical state could play an important role in the SF activity of a system. Indeed, the merging systems exhibit, although with marginal significance, a SF activity per unit of halo mass intermediate between the groups and the relaxed clusters at the same redshift. However, given the large error bars, we could not constrain with high significance the role of the merging activity in the evolution of the  $\Sigma(\text{SFR})/M$ . In order to clarify this issue, we need either to collect a much larger sample of merging systems to create a composite cluster, as we did for the galaxy group analysis, or we need a much more accurate estimate of the SFR to lower the error bars of the individual clusters. Nevertheless, this exercise shows clearly how powerful this kind of analysis can be. All these results suggest that the total mass and dynamical state of a system are key parameters for the understanding of galaxy formation and evolution.

### 5.3 Conclusions: the big picture

In this work we have investigated the role of the environment and merging activity in the evolution of the star formation up to  $z \sim 1.6$ . A clear picture emerges from this analysis: X-ray groups are fundamental laboratories to study galaxy formation and evolution and they are not a simple scaled down version of the clusters. We summarize the main results in the following:

- The absence of any gradient of star formation within the group environment could reflect the much smaller spread in accretion times of groups with respect to the clusters. This result is not affected by the mild mass segregation that we observe up to  $z \sim 0.8$ ;
- The mild mass segregation indicates that the relaxation or the dynamical friction timescales of group galaxies is longer than the group crossing time;
- The SFR–density relation shows anti-correlation up to  $z \sim 0.8$ , but no reversal is observed up to  $z \sim 1.6$ . Anyhow the flattening of the SFR–density relation towards higher redshift indicates that at  $z > 0.8$  group galaxies are highly contributing to the star formation rate density of the universe. We expect that at even higher redshift the mean SFR in groups should be higher than in lower density regimes. Indeed at higher redshift, where generally clusters do not exist (at least in a significant number), massive galaxies should live in groups and should be in the starbursting phase (De Lucia et al. 2006).
- Although the trend of the SFR–density is driven by the galaxy groups at  $z < 0.8$ , the SFR–density relation, in its standard definition, is not able to separate the contribution of dynamically bound systems from simply high density environments such as filaments and overdense regions. This is much better highlighted in the SFR–density analyzed with our novel “dynamical approach”. This implies that the galaxy membership to a massive dark matter halo is a much more efficient way to quench the SF activity than the membership to an overdense but not gravitationally bounded region (such as a filament) or to a lower mass halo ( $M_{200} \sim 5 \times 10^{12} M_{\odot}$ ).
- The evolution of  $\Delta_{\text{MS}}$  shows that at least below redshift  $\sim 0.8$  the star formation activity in group galaxies is damped with respect to the bulk of the SF galaxies. Thus, the lower mean SF level of group galaxies with respect to the field does not depend only on the different type mix (evolution of the quiescent galaxy fraction) but also to a lower SF activity in Main Sequence galaxies. This is the strong evidence for the efficiency of a quenching process that is not internal to the galaxy (simply mass dependent), but external and particularly efficient in massive dark matter halos. Such process can be either strangulation or ram pressure stripping, which can take place mainly in massive halos. At earlier epochs, groups, filaments, and field have comparable star formation.

- The total SF budget is not only dependent on the damped star formation in systems, but also on the different type mix in groups with respect to the lower density environments. In fact, our analysis reveals that the fraction of quiescent galaxies decreases steeply as the redshift increases, while filaments and field have a more similar behavior. This confirms that other processes, rather than the simple galaxy-galaxy interaction, must play an important role, in quenching the SF activity and thus leading to the observed galaxy type mix.
- The evolution of star formation per halo mass suggests that the time elapsed after the merging event in clusters and the dynamical state could play an important role in the SF activity of a system. Indeed, the merging systems exhibit, although with marginal significance, a higher SF activity per unit of halo mass intermediate between the groups and the relaxed clusters at the same redshift. All these results suggest that the total mass and dynamical state of a system are key parameters for the understanding of galaxy formation and evolution. We demonstrate that a certain amount of pre-processing is happening in groups at least below  $z \sim 0.8$  but a further quenching must happen even in the more dense or, better, more massive cluster environment.

In order to shed light on the role of the dark matter halo properties in affecting the galaxy SF activity evolution, we surely need to enlarge our group and cluster sample. The ideal next step of our project would be to extend the group sample to much lower dynamical masses in order to perform the same analysis not only per redshift bin but also per group mass bin as suggested by Presotto et al. (2012) and Yang et al. (2012). Only with this approach we would be able to identify at which halo masses the SF activity below  $z \sim 0.8$  start to be quenched. In addition, enlarging the sample of merging clusters, possibly at different merger stage, would let us understand if and at what time since the merger the SF activity is quenched in massive halos. These two steps would be already sufficient to completely follow the whole structure evolutionary path and to link the evolution of the SF activity to the structure formation process.





# Bibliography

- Abadi M. G., Moore B., Bower R. G., 1999, MNRAS, 308, 947
- Abraham R. G., van den Bergh S., 2001, Sci, 293, 1273
- Alcalá J. M., Pannella, M., Puddu, E., Radovich, M., Silvotti, R., Arnaboldi, M., Capaccioli, M., Covone, G., et al., 2004, A&A, 428, 339
- Alexander D. M., et al., 2003, AJ, 126, 539
- Alonso-Herrero A., Rieke G. H., Rieke M. J., Colina L., Pérez-González P. G., Ryder S. D., 2006, ApJ, 650, 835
- Altieri B., et al., 2010, A&A, 518, L17
- Andreon S., Lobo C., Iovino A., 2004, MNRAS, 349, 889
- Angulo R. E., Springel V., White S. D. M., Jenkins A., Baugh C. M., Frenk C. S., 2012, arXiv, arXiv:1203.3216
- Arnouts S., Cristiani S., Moscardini L., Matarrese S., Lucchin F., Fontana A., Giallongo E., 1999, MNRAS, 310, 540
- Arnouts S., et al., 2001, A&A, 379, 740
- Baade D., et al., 1999, Msngr, 95, 15
- Bai L., Rieke G. H., Rieke M. J., Hinz J. L., Kelly D. M., Blaylock M., 2006, ApJ, 639, 827
- Bai, L. et al. 2007, ApJ, 664, 181
- Bai L., Rieke G. H., Rieke M. J., Christlein D., Zabludoff A. I., 2009, ApJ, 693, 1840

- Bai L., Rasmussen J., Mulchaey J. S., Dariush A., Raychaudhury S., Ponman T. J., 2010, *ApJ*, 713, 637
- Balestra I., et al., 2010, *A&A*, 512, A12
- Balogh M. L., Morris S. L., Yee H. K. C., Carlberg R. G., Ellingson E., 1999, *ApJ*, 527, 54
- Balogh M. L., Navarro J. F., Morris S. L., 2000, *ApJ*, 540, 113
- Balogh M., Eke V., Miller C., Lewis I., Bower R., Couch W., Nichol R., Bland-Hawthorn J., et al. 2004, *MNRAS*, 348, 1355
- Balogh M. L., et al., 2011, *MNRAS*, 412, 2303
- Barger A. J., Cowie L. L., Wang W.-H., 2008, *ApJ*, 689, 687
- Bauer, F. E., et al. 2002, *AJ*, 123, 1163
- Baugh C. M., Cole S., Frenk C. S., 1996, *MNRAS*, 283, 1361
- Baugh C. M., 2006, *RPPh*, 69, 3101
- Beers T. C., Flynn K., Gebhardt K., 1990, *AJ*, 100, 32
- Bekki K., 2009, *MNRAS*, 399, 2221
- Bell, E. F., McIntosh, D. H., Katz, N., & Weinberg, M. D. 2003, *ApJs*, 149, 289
- Berrier J. C., Stewart K. R., Bullock J. S., Purcell C. W., Barton E. J., Wechsler R. H., 2009, *ApJ*, 690, 1292
- Berta S., et al., 2010, *A&A*, 518, L30
- Berta S., et al., 2011, *A&A*, 532, A49
- Bertin E., Arnouts S., 1996, *A&AS*, 117, 393
- Birnboim Y., Dekel A., 2003, *MNRAS*, 345, 349
- Biviano A., Murante G., Borgani S., Diaferio A., Dolag K., Girardi M., 2006, *A&A*, 456, 23
- Biviano A., Fadda D., Durret F., Edwards L. O. V., Marleau F., 2011, *A&A*, 532, A77
- Böhringer H., et al., 2001, *A&A*, 369, 826
- Borgani S., Kravtsov A., 2009, *arXiv*, arXiv:0906.4370
- Boselli A., Gavazzi G., Sanvito G., 2003, *A&A*, 402, 37

- Boselli A., Lequeux J., Gavazzi G., 2004, *A&A*, 428, 409
- Boselli A., Gavazzi G., 2006, *PASP*, 118, 517
- Boselli A., Gavazzi G., 2009, *A&A*, 508, 201
- Bower R. G., Castander F. J., Ellis R. S., Couch W. J., Bohringer H., 1997, *MNRAS*, 291, 353
- Braglia F., Pierini D., Böhringer H., 2007, *A&A*, 470, 425
- Braglia F. G., Pierini D., Biviano A., Böhringer H., 2009, *A&A*, 500, 947
- Brammer G. B., van Dokkum P. G., Coppi P., 2008, *ApJ*, 686, 1503
- Brunetti G., 2011, *arXiv*, arXiv:1106.0591
- Bruzual G., Charlot S., 2003, *MNRAS*, 344, 1000
- Busarello G., Merluzzi P., La Barbera F., Massarotti M., Capaccioli M., 2002, *A&A*, 389, 787
- Butcher H., Oemler A., Jr., 1978a, *ApJ*, 219, 18
- Butcher H., Oemler A., Jr., 1978b, *ApJ*, 226, 559
- Butcher H., Oemler A., Jr., 1984a, *ApJ*, 285, 426
- Butcher H. R., Oemler A., Jr., 1984b, *Natur*, 310, 31
- Calzetti D., Armus L., Bohlin R. C., Kinney A. L., Koornneef J., Storchi-Bergmann T., 2000, *ApJ*, 533, 682
- Calzetti D., et al., 2005, *ApJ*, 633, 871
- Calzetti D., et al., 2007, *ApJ*, 666, 870
- Capak P., et al., 2004, *AJ*, 127, 180
- Capak P., et al., 2007, *ApJS*, 172, 99
- Capak P. L., 2009, *AAS*, 214, #200.06
- Caputi K. I., et al., 2007, *ApJ*, 660, 97
- Caputi K. I., et al., 2009, *ApJ*, 691, 91
- Cardamone C. N., et al., 2010, *ApJS*, 189, 270
- Cardelli J. A., Clayton G. C., Mathis J. S., 1989, *ApJ*, 345, 245

- Carollo C. M., et al., 2012, arXiv, arXiv:1206.5807
- Cayatte V., van Gorkom J. H., Balkowski C., Kotanyi C., 1990, AJ, 100, 604
- Chabrier G., 2003, PASP, 115, 763
- Chary R., Elbaz D., 2001, ApJ, 556, 562
- Chilingarian I. V., Melchior A.-L., Zolotukhin I. Y., 2010, MNRAS, 405, 1409
- Chung S. M., Gonzalez A. H., Clowe D., Markevitch M., Zaritsky D., 2010, ApJ, 725, 1536
- Cimatti A., et al., 2002, A&A, 392, 395
- Cimatti A., et al., 2008, A&A, 482, 21
- Cohn J. D., 2012, MNRAS, 419, 1017
- Coia D., et al., 2005, A&A, 431, 433
- Cole S., Aragon-Salamanca A., Frenk C. S., Navarro J. F., Zepf S. E., 1994, MNRAS, 271, 781
- Colless M., Dunn A. M., 1996, ApJ, 458, 435
- Comastri A., et al., 2011, A&A, 526, L9
- Connelly J. L., et al., 2012, ApJ, 756, 139
- Cooper M. C., et al., 2006, MNRAS, 370, 198
- Cooper M. C., et al., 2008, MNRAS, 383, 1058
- Cooper M. C., et al., 2011a, arXiv, arXiv:1112.0312
- Cooper M. C., et al., 2011b, ApJS, 193, 14
- Couch W. J., Barger A. J., Smail I., Ellis R. S., Sharples R. M., 1998, ApJ, 497, 188
- Cristiani S., et al., 2000, A&A, 359, 489
- Croom S. M., Warren S. J., Glazebrook K., 2001, MNRAS, 328, 150
- Croton, D. J., Springel, V., White, S. D. M., et al. 2006, MNRAS, 365, 11
- Cucciati O., et al. 2006, A&A, 458, 39
- Daddi E., Cimatti A., Renzini A., Fontana A., Mignoli M., Pozzetti L., Tozzi P., Zamorani G., 2004, ApJ, 617, 746
- Daddi E., et al., 2007a, ApJ, 670, 156

- Daddi E., et al., 2007b, ApJ, 670, 173
- Dale D. A., Helou G., 2002, ApJ, 576, 159
- Damen M., et al., 2011, ApJ, 727, 1
- Danese L., de Zotti G., di Tullio G., 1980, A&A, 82, 322
- Davies J. I., et al., 2010, A&A, 518, L48
- De Lucia, G., Kauffmann, G., & White, S. D. M. 2004, MNRAS, 349, 1101
- De Lucia G., Springel V., White S. D. M., Croton D., Kauffmann G., 2006, MNRAS, 366, 499
- De Lucia G., Blaizot J., 2007, MNRAS, 375, 2
- De Lucia G., Weinmann S., Poggianti B. M., Aragón-Salamanca A., Zaritsky D., 2012, MNRAS, 3042
- den Hartog R., Katgert P., 1996, MNRAS, 279, 349
- Diaferio A., Ramella M., Geller M. J., Ferrari A., 1993, AJ, 105, 2035
- Dole H., Lagache G., Puget J.-L., 2003, ApJ, 585, 617
- Dressler A., 1980, ApJ, 236, 351
- Dressler A., Gunn J. E., Schneider D. P., 1985, ApJ, 294, 70
- Dressler A., Shectman S. A., 1988, AJ, 95, 985
- Dressler A., et al., 1997, ApJ, 490, 577
- Dressler A., Rigby J., Oemler A., Jr., Fritz J., Poggianti B. M., Rieke G., Bai L., 2009, ApJ, 693, 140
- Driver S., 2004, PASA, 21, 344
- Dubinski J., 1998, ApJ, 502, 141
- Eales S., et al., 2010, PASP, 122, 499
- Egami E., et al., 2010, A&A, 518, L12
- Elbaz D., Cesarsky C. J., Chantal P., Aussel H., Franceschini A., Fadda D., Chary R. R., 2002, A&A, 384, 848
- Elbaz D., et al., 2007, A&A, 468, 33

- Elbaz D., et al., 2010, *A&A*, 518, L29
- Elbaz D., et al., 2011, *A&A*, 533, A119
- Ellingson E., Lin H., Yee H. K. C., Carlberg R. G., 2001, *ApJ*, 547, 609
- Elvis, M., et al., 2009 *ApJS* 185, 158
- Eke V. R., Baugh C. M., Cole S., Frenk C. S., King H. M., Peacock J. A., 2005, *MNRAS*, 362, 1233
- Faber S. M., et al., 2003, *SPIE*, 4841, 1657
- Fadda D., Biviano A., Marleau F. R., Storrie-Lombardi L. J., Durret F., 2008, *ApJ*, 672, L9
- Fadda, D., Yan, L., Lagache, G., et al., 2010, *ApJ*, 719, 425
- Fazio G. G., et al., 2004, *ApJS*, 154, 10
- Feruglio C., et al., 2010, *ApJ*, 721, 607
- Finn R. A., Zaritsky D., McCarthy D. W., Jr., 2004, *ApJ*, 604, 141
- Finn R. A., et al., 2005, *ApJ*, 630, 206
- Finn R. A., et al., 2010, *ApJ*, 720, 87
- Finoguenov A., Böhringer H., Zhang Y.-Y., 2005, *A&A*, 442, 827
- Finoguenov A., et al., 2007, *ApJS*, 172, 182
- Finoguenov A., et al., 2009, *ApJ*, 704, 564
- Finoguenov A., Sarazin C. L., Nakazawa K., Wik D. R., Clarke T. E., 2010, *ApJ*, 715, 1143
- Förster Schreiber N. M., Roussel H., Sauvage M., Charmandaris V., 2004, *A&A*, 419, 501
- Fontana A., et al., 2004, *A&A*, 424, 23
- Fontana A., et al., 2006, *A&A*, 459, 745
- Forman W., Jones C., 1982, *ARA&A*, 20, 547
- Foucaud S., Conselice C. J., Hartley W. G., Lane K. P., Bamford S. P., Almaini O., Bundy K., 2010, *MNRAS*, 406, 147
- Franceschini A., Aussel H., Cesarsky C. J., Elbaz D., Fadda D., 2001, *A&A*, 378, 1

- Franx M., et al., 2003, *ApJ*, 587, L79
- Frederic J. J., 1995, *ApJS*, 97, 259
- Frenk C. S., White S. D. M., Efstathiou G., Davis M., 1985, *Natur*, 317, 595
- Frenk C. S., White S. D. M., Davis M., Efstathiou G., 1988, *ApJ*, 327, 507
- Fujita Y., 2004, *PASJ*, 56, 29
- Gao L., White S. D. M., Jenkins A., Stoehr F., Springel V., 2004, *MNRAS*, 355, 819
- Garilli B., Fumana M., Franzetti P., Paiono L., Scodreggio M., Le Fèvre O., Paltani S., Scaramella R., 2010, *PASP*, 122, 827
- Gavazzi G., Boselli A., Pedotti P., Gallazzi A., Carrasco L., 2002, *A&A*, 396, 449
- Gawiser E., et al., 2006a, *ApJ*, 642, L13
- Gawiser E., et al., 2006b, *ApJS*, 162
- Geach J. E., et al., 2006, *ApJ*, 649, 661
- Gehrels N., 1986, *ApJ*, 303, 336
- Geller M. J., Huchra J. P., 1983, *ApJS*, 52, 61
- Gerke B. F., et al., 2005, *ApJ*, 625, 6
- Giacintucci S., 2011, *MmSAI*, 82, 541
- Gialalisco M., et al., 2004, *ApJ*, 600, L93
- Gilbank D. G., Baldry I. K., Balogh M. L., Glazebrook K., Bower R. G., 2010, *MNRAS*, 405, 2594
- Giodini S., et al., 2012, *A&A*, 538, A104
- Giovanelli R., Haynes M. P., 1985, *ApJ*, 292, 404
- Giovannini G., Feretti L., 2002, *ASSL*, 272, 197
- Girardi M., Biviano A., Giuricin G., Mardirossian F., Mezzetti M., 1993, *ApJ*, 404, 38
- Gómez P. L., et al., 2003, *ApJ*, 584, 210
- Goto T., et al., 2003, *PASJ*, 55, 739
- Grazian A., et al., 2006, *A&A*, 449, 951, 1
- Gruppioni C., Pozzi F., Zamorani G., Vignali C., 2011, *MNRAS*, 416, 70



- Gunn J. E., Gott J. R., III, 1972, *ApJ*, 176, 1
- Guzzo L., et al., 2009, *A&A*, 499, 357
- Haines C. P., Smith G. P., Pereira M. J., Egami E., Moran S. M., Hardegree-Ullman E., Rawle T. D., Rex M., 2010, *A&A*, 518, L19
- Haines C. P., et al., 2011, *MNRAS*, 417, 2831
- Hayashi M., Kodama T., Koyama Y., Tadaki K.-I., Tanaka I., 2011, *MNRAS*, 415, 2670
- Harrison E. R., Noonan T. W., 1979, *ApJ*, 232, 18
- Hasinger G., et al., 2007, *ApJS*, 172, 29
- Hickson P., Kindl E., Huchra J. P., 1988, *ApJ*, 331, 64
- Hernquist L., Katz N., Weinberg D. H., 1995, *ApJ*, 442, 57
- Hildebrandt H., et al., 2006, *A&A*, 452, 1121
- Homeier N. L., et al., 2005, *ApJ*, 621, 651
- Hubble E. P., 1926, *ApJ*, 64, 321
- Hubble E., Humason M. L., 1931, *ApJ*, 74, 43
- Huynh M. T., Frayer D. T., Mobasher B., Dickinson M., Chary R.-R., Morrison G., 2007, *ApJ*, 667, L9
- Ilbert O., et al., 2006, *A&A*, 457, 841
- Ilbert O., et al., 2009, *ApJ*, 690, 1236
- Ilbert O., et al., 2010, *ApJ*, 709, 644
- Iovino A., et al., 2010, *A&A*, 509, A40
- Jenkins A., Frenk C. S., White S. D. M., Colberg J. M., Cole S., Evrard A. E., Couchman H. M. P., Yoshida N., 2001, *MNRAS*, 321, 372
- Jones C., Forman W., 1984, *ApJ*, 276, 38
- Jones, C. & Forman, W. 1992, in *Clusters and superclusters of galaxies*, ed. A. C. Fabian, NATO ASI Series, 366, 49
- Katgert P., Biviano A., Mazure A., 2004, *ApJ*, 600, 657
- Kauffmann, G., White, S. D. M., & Guiderdoni, B. 1993, *MNRAS*, 264, 201

- Kauffmann G., Charlot S., White S. D. M., 1996, MNRAS, 283, L117
- Kauffmann, G. & Charlot, S. 1998, MNRAS, 294, 705
- Kauffmann, G., Colberg, J. M., Diaferio, A., & White, S. D. M. 1999, MNRAS, 303, 188
- Kauffmann, G. & Haehnelt, M. 2000, MNRAS, 311, 576
- Kauffmann G., White S. D. M., Heckman T. M., Ménard B., Brinchmann J., Charlot S., Tremonti C., Brinkmann J., 2004, MNRAS, 353, 713
- Kawata D., Mulchaey J. S., 2008, ApJ, 672, L103
- Kennicutt R. C., Jr., 1983, ApJ, 272, 54
- Kennicutt R. C., Jr., 1998a, ARA&A, 36, 189
- Kennicutt R. C., Jr., 1998b, ApJ, 498, 541
- King I., 1962, AJ, 67, 471
- Kitzbichler M. G., White S. D. M., 2007, MNRAS, 376, 2
- Knobel C., et al., 2012, ApJ, 753, 121
- Kodama T., Smail I., Nakata F., Okamura S., Bower R. G., 2001, ApJ, 562, L9
- Kodama T., Balogh M. L., Smail I., Bower R. G., Nakata F., 2004, MNRAS, 354, 1103
- Koyama Y., Kodama T., Shimasaku K., Hayashi M., Okamura S., Tanaka I., Tokoku C., 2010, MNRAS, 403, 1611
- Kovač K., et al., 2010, ApJ, 708, 505
- Kriek M., et al., 2008, ApJ, 677, 219
- Kriek M., van Dokkum P. G., Labbé I., Franx M., Illingworth G. D., Marchesini D., Quadri R. F., 2009, ApJ, 700, 221
- Kron R. G., 1980, ApJS, 43, 305
- Kroupa P., 2001, MNRAS, 322, 231
- Kurk J. D., et al., 2008, ASPC, 381, 303
- Kurk J., et al., 2009, A&A, 504, 331
- Lagache G., Dole H., Puget J.-L., 2003, MNRAS, 338, 555
- Lagache G., et al., 2004, ApJS, 154, 112

- Landolt A. U., 1992, *AJ*, 104, 340
- Larson R. B., Tinsley B. M., Caldwell C. N., 1980, *ApJ*, 237, 692
- Lavery R. J., Henry J. P., 1988, *ApJ*, 330, 596
- Le Fèvre O., et al., 2003, *SPIE*, 4841, 1670
- Le Fèvre O., et al., 2004, *A&A*, 428, 1043
- Le Floc'h E., et al., 2005, *ApJ*, 632, 169
- Leauthaud A., et al., 2010, *ApJ*, 709, 97
- Lehmer B. D., et al., 2005, *ApJS*, 161, 21
- Lemonon L., Pierre M., Hunstead R., Reid A., Mellier Y., Boehringer H., 1997, *A&A*, 326, 34
- Lemson, G. et al. 2006, *ArXiv Astrophysics*: astro-ph/0608019
- Li I. H., Yee H. K. C., Ellingson E., Laurent G., 2004, *ogci.conf*, 426
- Lilly S. J., Le Fevre O., Hammer F., Crampton D., 1996, *ApJ*, 460, L1
- Lilly S. J., et al., 2007, *ApJS*, 172, 70
- Luo B., et al., 2008, *ApJS*, 179, 19
- Lutz D., et al., 2010, *ApJ*, 712, 1287
- Lutz D., et al., 2011, *A&A*, 532, A90
- Macario G., Markevitch M., Giacintucci S., Brunetti G., Venturi T., Murray S. S., 2011, *ApJ*, 728, 82
- Madau P., Ferguson H. C., Dickinson M. E., Giavalisco M., Steidel C. C., Fruchter A., 1996, *MNRAS*, 283, 1388
- Magnelli B., Elbaz D., Chary R. R., Dickinson M., Le Borgne D., Frayer D. T., Willmer C. N. A., 2009, *A&A*, 496, 57
- Magnelli B., Elbaz D., Chary R. R., Dickinson M., Le Borgne D., Frayer D. T., Willmer C. N. A., 2011, *A&A*, 528, A35
- Mahajan S., Haines C. P., Raychaudhury S., 2010, *MNRAS*, 404, 1745
- Mamon G. A., Biviano A., Murante G., 2010, *A&A*, 520, A30

- Markevitch M., Gonzalez A. H., David L., Vikhlinin A., Murray S., Forman W., Jones C., Tucker W., 2002, *ApJ*, 567, L27
- Markevitch M., Vikhlinin A., 2007, *PhR*, 443, 1
- Martin D. C., et al., 2005, *ApJ*, 619, L1
- Mauduit J.-C., Mamon G. A., 2007, *A&A*, 475, 169
- McCracken H. J., et al., 2003, *A&A*, 410, 17
- McGee S. L., Balogh M. L., Bower R. G., Font A. S., McCarthy I. G., 2009, *MNRAS*, 400, 937
- Menanteau F., Hughes J. P., 2009, *ApJ*, 694, L136
- Merritt D., 1984, *ApJ*, 276, 26
- Metcalfe L., et al., 2003, *A&A*, 407, 791
- Miller N. A., Fomalont E. B., Kellermann K. I., Mainieri V., Norman C., Padovani P., Rosati P., Tozzi P., 2008, *ApJS*, 179, 114
- Mittaz J. P. D., et al., 2001, *A&A*, 365, L93
- Moore B., Katz N., Lake G., Dressler A., Oemler A., 1996, *Natur*, 379, 613
- Morrison G. E., Owen F. N., Dickinson M., Ivison R. J., Ibar E., 2010, *ApJS*, 188, 178
- Moy E., Barmby P., Rigopoulou D., Huang J.-S., Willner S. P., Fazio G. G., 2003, *A&A*, 403, 493
- Mulchaey J. S., Zabludoff A. I., 1996, *AAS*, 28, 1386
- Mulchaey J. S., Zabludoff A. I., 1998, *ApJ*, 496, 73
- Mulchaey J. S., 2000, *ARA&A*, 38, 289
- Mulchaey J. S., Davis D. S., Mushotzky R. F., Burstein D., 2003, *ApJS*, 145, 39
- Muller G. P., Reed R., Armandroff T., Boroson T. A., Jacoby G. H., 1998, *SPIE*, 3355, 577
- Murphy, E.J., Chary, R.-R., Alexander, D.M., et al., 2009, *ApJ*, 698, 1380
- Muzzin A., et al., 2012, *ApJ*, 746, 188
- Navarro J. F., Frenk C. S., White S. D. M., 1995, *MNRAS*, 275, 720
- Navarro J. F., Frenk C. S., White S. D. M., 1997, *ApJ*, 490, 493

- Neistein, E., van den Bosch, F. C., & Dekel, A. 2006, MNRAS, 372, 933
- Noeske K. G., et al., 2007a, ApJ, 660, L43
- Noeske K. G., et al., 2007b, ApJ, 660, L47
- Nordon R., et al., 2010, A&A, 518, L24
- Nordon R., et al., 2012, ApJ, 745, 182
- O'Donnell J. E., 1994, ApJ, 422, 158
- Oemler Jr. A., 1974, ApJ, 194, 1
- Oemler A., Jr., Dressler A., Butcher H. R., 1997, ApJ, 474, 561
- Oliver S. J., et al., 2010, A&A, 518, L21
- Ostriker J. P., Hausman M. A., 1977, ApJ, 217, L125
- Ostriker J. P., Steinhardt P. J., 1995, Natur, 377, 600
- Padovani P., Mainieri V., Tozzi P., Kellermann K. I., Fomalont E. B., Miller N., Rosati P., Shaver P., 2009, ApJ, 694, 235
- Papovich C., Dickinson M., Ferguson H. C., 2001, ApJ, 559, 620
- Papovich C., et al., 2007, ApJ, 668, 45
- Peng Y., et al., 2010, ApJ, 721, 193
- Peng Y., Lilly S. J., Renzini A., Carollo M., 2011, arXiv, arXiv:1106.2546
- Pereira M. J., et al., 2010, A&A, 518, L40
- Pérez-González P. G., et al., 2006, ApJ, 648, 987
- Pickles A. J., 1998, PASP, 110, 863
- Pierini D., Zibetti S., Braglia F., Böhringer H., Finoguenov A., Lynam P. D., Zhang Y.-Y., 2008, A&A, 483, 727
- Pierre M., Oukbir J., Dubreuil D., Soucail G., Sauvageot J.-L., Mellier Y., 1997, A&AS, 124, 283
- Pilbratt, G., et al. 2010, A&A, 518, L1
- Pipino A., Matteucci F., 2011, A&A, 530, A98

- Poggianti B. M., Bridges T. J., Komiyama Y., Yagi M., Carter D., Mobasher B., Okamura S., Kashikawa N., 2004, *ApJ*, 601, 197
- Poglitsch, A., et al. 2010, *A&A*, 518, L2
- Ponman T. J., Cannon D. B., Navarro J. F., 1999, *Natur*, 397, 135
- Popesso P., et al., 2009, *A&A*, 494, 443
- Popesso P., et al., 2011, *A&A*, 532, A145
- Popesso P., et al., 2012, *A&A*, 537, A58
- Porter S. C., Raychaudhury S., 2007, *MNRAS*, 375, 1409
- Presotto V., et al., 2012, *A&A*, 539, A55
- Press W. H., Schechter P., 1974, *ApJ*, 187, 425
- Prevot M. L., Lequeux J., Prevot L., Maurice E., Rocca-Volmerange B., 1984, *A&A*, 132, 389
- Quadri R., et al., 2007, *AJ*, 134, 1103
- Rakos K., Schombert J., 2004, *AJ*, 127, 1502
- Ramella M., Pisani A., Geller M. J., 1997, *AJ*, 113, 483
- Reid A. D., Hunstead R. W., Lemonon L., Pierre M. M., 1999, *MNRAS*, 302, 571
- Relaño M., Lisenfeld U., Battaner E., Vilchez J. M., Pérez-González P., 2008, *ASPC*, 381, 185
- Renzini A., da Costa L. N., 1997, *Msngr*, 87, 23
- Rasmussen J., Ponman T. J., Mulchaey J. S., Miles T. A., Raychaudhury S., 2006, *MNRAS*, 373, 653
- Rasmussen J., Mulchaey J. S., Bai L., Ponman T. J., Raychaudhury S., Dariush A., 2010, *ApJ*, 717, 958
- Rasmussen J., Mulchaey J. S., Bai L., Ponman T. J., Raychaudhury S., Dariush A., 2012, *arXiv*, arXiv:1208.1762
- Rettura A., et al., 2010, *ApJ*, 709, 512
- Rieke G. H., et al., 2004, *SPIE*, 5487, 50
- Rieke G. H., Alonso-Herrero A., Weiner B. J., Pérez-González P. G., Blaylock M., Donley J. L., Marcillac D., 2009, *ApJ*, 692, 556

- Rix H.-W., et al., 2004, *ApJS*, 152, 163
- Rodighiero, G., et al., 2010, *A&A*, 518, L25
- Roussel H., Sauvage M., Vigroux L., Bosma A., 2001, *A&A*, 372, 427
- Saintonge A., Tran K.-V. H., Holden B. P., 2008, *ApJ*, 685, L113
- Salim S., et al., 2009, *ApJ*, 700, 161
- Salmi F., Daddi E., Elbaz D., Sargent M. T., Dickinson M., Renzini A., Bethermin M., Le Borgne D., 2012, *ApJ*, 754, L14
- Salpeter E. E., 1955, *ApJ*, 121, 161
- Salvato M., et al., 2009, *ApJ*, 690, 1250
- Sanders D. B., Mazzarella J. M., Kim D.-C., Surace J. A., Soifer B. T., 2003, *AJ*, 126, 1607
- Sanders D. B., et al., 2007, *ApJS*, 172, 86
- Santini P., et al., 2009, *A&A*, 504, 751
- Santini P., et al., 2012, *A&A*, 540, A109
- Sarazin, C. L. 2002, in *The Physics of Cluster Mergers*, ed. L. Feretti, I. M. Gioia & G. Giovannini, 272, 1-38
- Schechter P., 1976, *ApJ*, 203, 297
- Schlegel D. J., Finkbeiner D. P., Davis M., 1998, *ApJ*, 500, 525
- Schombert J. M., 1987, *ApJS*, 64, 643
- Schombert J. M., 1988, *ApJ*, 328, 475
- Scodeggio M., et al., 2005, *PASP*, 117, 1284
- Scodeggio M., Franzetti P., Garilli B., Fumana M., Paiono L., Zanicelli A., 2008, *eic..work*, 95
- Scodeggio M., et al., 2009, *A&A*, 501, 21
- Scoville N., et al., 2007, *ApJS*, 172, 1
- Shao L., et al., 2010, *A&A*, 518, L26
- Shapley A. E., Steidel C. C., Adelberger K. L., Dickinson M., Giavalisco M., Pettini M., 2001, *ApJ*, 562, 95

- Shapley A. E., Steidel C. C., Erb D. K., Reddy N. A., Adelberger K. L., Pettini M., Barmby P., Huang J., 2005, *ApJ*, 626, 698
- Silverman J. D., et al., 2010, *ApJS*, 191, 124
- Smith G. P., et al., 2010, *MNRAS*, 409, 169
- Smoot G. F., et al., 1992, *ApJ*, 396, L1
- Springel, V., White, S. D. M., Tormen, G., & Kauffmann, G. 2001, *MNRAS*, 328, 726
- Springel V., Hernquist L., 2003, *MNRAS*, 339, 312
- Springel V., et al., 2005, *Natur*, 435, 629
- Springel V., Farrar G. R., 2007, *MNRAS*, 380, 911
- Strateva I., et al., 2001, *AJ*, 122, 1861
- Strolger L.-G., et al., 2004, *ApJ*, 613, 200
- Sutherland W., Saunders W., 1992, *MNRAS*, 259, 413
- Szokoly G. P., et al., 2004, *ApJS*, 155, 271
- Tal T., Wake D. A., van Dokkum P. G., 2012, *ApJ*, 751, L5
- Tanaka M., Finoguenov A., Ueda Y., 2010, *ApJ*, 716, L152
- Taniguchi Y., et al., 2007, *ApJS*, 172, 9
- Taylor E. N., et al., 2009, *ApJS*, 183, 295
- Toomre A., Toomre J., 1972, *ApJ*, 178, 623
- Tran K.-V. H., Saintonge A., Moustakas J., Bai L., Gonzalez A. H., Holden B. P., Zaritsky D., Kautsch S. J., 2009, *ApJ*, 705, 809
- Tran K.-V. H., et al., 2010, *ApJ*, 719, L126
- Treister E., et al., 2009, *ApJ*, 693, 1713
- Treu T., Ellis R. S., Kneib J.-P., Dressler A., Smail I., Czoske O., Oemler A., Natarajan P., 2003, *ApJ*, 591, 53
- van der Wel A., Franx M., van Dokkum P. G., Rix H.-W., 2004, *ApJ*, 601, L5
- van Dokkum P. G., Franx M., Fabricant D., Illingworth G. D., Kelson D. D., 2000, *ApJ*, 541, 95



- Vanzella E., et al., 2008, *A&A*, 478, 83
- Venturi T., 2011, *MmSAI*, 82, 499
- von der Linden A., Wild V., Kauffmann G., White S. D. M., Weinmann S., 2010, *MNRAS*, 404, 1231
- Voit G. M., 2005, *RvMP*, 77, 207
- Weinmann S. M., van den Bosch F. C., Pasquali A., 2011, *efgt.book*, 29
- Wetzel A. R., Tinker J. L., Conroy C., 2012, *MNRAS*, 424, 232
- Whitaker K. E., van Dokkum P. G., Brammer G., Franx M., 2012, *ApJ*, 754, L29
- White S. D. M., 1977, *MNRAS*, 179, 33
- White S. D. M., Rees M. J., 1978, *MNRAS*, 183, 341
- White S. D. M., Frenk C. S., Davis M., Efstathiou G., 1987, *ApJ*, 313, 505
- White, S. D. M. & Frenk, C. S. 1991, *ApJ*, 379, 52
- Wilman D. J., Balogh M. L., Bower R. G., Mulchaey J. S., Oemler A., Carlberg R. G., Morris S. L., Whitaker R. J., 2005, *MNRAS*, 358, 71
- Wolf C., et al., 2004, *A&A*, 421, 913
- Woo J., et al., 2012, *arXiv*, arXiv:1203.1625
- Worthey G., 1994, *ApJS*, 95, 107
- Wu H., Cao C., Hao C.-N., Liu F.-S., Wang J.-L., Xia X.-Y., Deng Z.-G., Young C. K.-S., 2005, *ApJ*, 632, L79
- Wuyts S., et al., 2011, *ApJ*, 742, 96
- Xue Y. Q., et al., 2011, *ApJS*, 195, 10
- Yahil A., Vidal N. V., 1977, *ApJ*, 214, 347
- Yang X., Mo H. J., van den Bosch F. C., Weinmann S. M., Li C., Jing Y. P., 2005, *MNRAS*, 362, 711
- Yang X., Mo H. J., van den Bosch F. C., Pasquali A., Li C., Barden M., 2007, *ApJ*, 671, 153
- Yasuda N., et al., 2001, *AJ*, 122, 1104
- Zabludoff A. I., Mulchaey J. S., 1998, *ApJ*, 496, 39

- Zhang Y. -, Finoguenov A., Boehringer H., Ikebe Y., Matsushita K., Schuecker P., Guzzo L., Collins C. A., 2004a, astro, arXiv:astro-ph/0402533
- Zhang Y.-Y., Finoguenov A., Böhringer H., Ikebe Y., Matsushita K., Schuecker P., 2004b, A&A, 413, 49
- Zhang Y.-Y., Böhringer H., Finoguenov A., Ikebe Y., Matsushita K., Schuecker P., Guzzo L., Collins C. A., 2005, AdSpR, 36, 667
- Zhang Y.-Y., Böhringer H., Finoguenov A., Ikebe Y., Matsushita K., Schuecker P., Guzzo L., Collins C. A., 2006, A&A, 456, 55
- Zhu Y.-N., Wu H., Cao C., Li H.-N., 2008, ApJ, 686, 155
- Zibetti S., White S. D. M., Schneider D. P., Brinkmann J., 2005, MNRAS, 358, 949
- Ziparo F., Braglia F. G., Pierini D., Finoguenov A., Böhringer H., Bongiorno A., 2012, MNRAS, 420, 2480
- ZuHone J. A., 2011, ApJ, 728, 54



# Acknowledgements

I would like to thank all the people who made this thesis possible. I would like to thank my supervisor, Paul Nandra, who accepted to represent me at the university and encouraged me to finish my thesis (on time). All my gratitude goes to my project supervisors, Alexis Finoguenov and Paola Popesso. Thank you Alexis for supporting me and offering me the possibility to be part of exciting scientific projects. Thank you for your constant presence and sponsoring me around the world. Thank you for believing in me and never let me down. Special thanks to Paola, well all this thesis would not be enough to thank you. Thank you for believing in me and for the continuous support, your enthusiasm is contagious! Thank you for your patience and for demonstrating me that nothing is impossible, you just need “forza di volontà”. Thank you for being just what you are. Thank you, Alexis and Paola, you made this happening, it is not easy to find supervisors like you.

I would like to thank Mara Salvato, for all the useful discussions we had and for supporting me when the things were not so easy. You made me understand things that count. Thank you Daniele Pierini, for your patience and all the things you taught me. Thank you for your presence and for caring about my scientific knowledge. Thanks to Filiberto Braglia, a precious collaborator with a lot of patience. Thank you Andrea Biviano, for your great patience and the nice atmosphere, it is an honor to collaborate with you. Thanks to Dave Wilman, for precious advices, useful discussion and comparison in the analysis. Thank you Peter Predehl, for listening, understanding, caring, and supporting me. Thanks to Dieter Lutz and the PEP team for an excellent collaboration and relaxing atmosphere. Thanks to Hans Böhringer, who contributed to the beginning of this thesis, for giving me the possibility to meet so many inspiring people. Thank you Birgit Boller, for all your patience and encouragement, MPE would not be the same without you.

Thanks to the guys of the “galaxy groups” group, Jen, Ghazaleh, Mohammad, Viola, just for being a real group. Thank you Alex for chatting, helping and...for the translation of the abstract in German! Thank you Miguel for very good advices and last-minute solutions. Thank you Rene for supporting and caring. Thank you Angela, for listening and sharing. Thank you Benjamin, for encouraging, chatting, listening. Thank you Marcella, Andrea, and Piero for listening and caring. Thanks to the Romaniellos for the great patience. Thanks to all the Garching volley lovers-players for the amazing Friday nights.

Thanks to my friends, Emmanuel, Sotiria, Gilles, Alice, Betta for nice life and mutual

support. Thank you Enrico, for listening, understanding, encouraging, supporting...being there always, even in the most difficult moments. Thank you for being what you are. Thank you Harla, for just being my *favorite* sister (not that easy). Thank you for supporting and encouraging me, being there in the most difficult moments and... entertain me with nice recent “stories”. Thanks to my parents for help, support, patience and encouragement. *Grazie mamma e papà, tutto questo non sarebbe possibile senza di voi!*

I probably forgot somebody, thus I would like to thank all the people who made this thesis possible.

# Curriculum Vitae

**Felicia Ziparo**

## **Present Address:**

Max-Planck-Institut für Extraterrestrische Physik  
Giessenbachstraße 1,  
85741 Garching bei Muenchen  
Tel.: +49 176 38204411  
felicia.ziparo@mpe.mpg.de

## **Personal Data**

*Date of birth:* 21/10/1983  
*Place of birth:* Catanzaro (Italy)  
*Citizenship:* Italian  
*Gender:* Female

## **Languages**

Italian – Native Speaker  
English – Fluent  
German – Basic  
French – Basic

## Education

**2009–2012: PhD in Astrophysics**

*Thesis subject:* “The role of environment and the merging activity in the evolution of star formation up to  $z \sim 1.6$ ”

*Advisors:* K. Nandra, A. Finoguenov, P. Popesso  
Max Planck Institute for Extraterrestrial Physics  
Garching bei München, Germany

**2006–2009: Master of Science in Astrophysics and Cosmology**

*Thesis title:* “A Multiwavelength characterization of high redshift Extremely Red Objects”

*Advisors:* A. Cimatti, C. Gruppioni  
“Alma Mater Studiorum” Bologna University, Italy

**2002–2006 Bachelor degree in Astronomy**

*Thesis title:* “The problem of AGN underluminosity”

*Advisors:* L. Ciotti, S. Pellegrini  
“Alma Mater Studiorum” Bologna University, Italy

## Peer Reviewed Publications

“In the whirlpool’s coils: tracing substructure from combined optical/X-ray data in the galaxy cluster A1300”. **Ziparo, F.**; Braglia, F. G.; Pierini, D.; Finoguenov, A.; Böhringer, H.; Bongiorno, A.; 2012, MNRAS, 420, 2480

“First simultaneous optical/near-infrared imaging of an X-ray selected, high-redshift cluster of galaxies with GROND”. Pierini, D.; Suhada, R.; Fassbender, R.; Nastasi, A.; Böhringer, H.; Salvato, M.; Pratt, G. W.; Lerchster, M.; Rosati, P.; Santos, J. S.; de Hoon, A.; Kohnert, J.; Lamer, G.; Mohr, J. J.; Muehleger, M.; Quintana, H.; Schwöpe, A.; Biffi, V.; Chon, G.; Giodini, S.; Koppenhoefer, J.; Verdugo, M.; **Ziparo, F.**; Afonso, P. M. J.; Clemens, C.; Greiner, J.; Kruehler, T.; Kupcu Yoldas, A.; Olivares E., F.; Rossi, A.; Yoldas, A. ; 2012, A&A, 540, 45

“Two fossil groups of galaxies at  $z \approx 0.4$  in the Cosmic Evolution Survey: accelerated stellar-mass build-up, different progenitors”. Pierini, D.; Giodini, S.; Finoguenov, A.; Böhringer, H.; D’Onghia, E.; Pratt, G. W.; Dmoch, J.; Pannella, M.; Zibetti, S.; Braglia, F. G.; Verdugo, M.; **Ziparo, F.**; Koekemoer, A. M.; Salvato, M.; 2011, MNRAS, 417, 2927